MENDEL UNIVERSITY IN BRNO
FACULTY OF FORESTRY AND WOOD TECHNOLOGY
DEPARTMENT OF WOOD SCIENCE

ANALYSIS OF THE MECHANICAL BEHAVIOUR OF WOOD BY MEANS OF DIGITAL IMAGE CORRELATION

DOCTORAL THESIS

Author: Ing. Martin Brabec
Supervisor: Ing. Václav Sebera, Ph.D.

2016

DECLARATION

I declare I have written the presented doctoral thesis titled "Analysis of the Mechanical Behaviour of Wood by means of Digital Image Correlation" independently and that I have listed all references. I agree that my thesis will be published in accordance with § 47b of Act No. 111/1998 Coll., on higher education as amended thereafter and in accordance with the Guidelines on the Publishing of University Student Theses.

I am aware of the fact that my thesis is subject to Act. No. 121/2000 Coll., the copyright act and that the Mendel University in Brno is entitled to close a licence agreement and use the results of my thesis as the "School Work" under the terms of § 60 par. 1 of the copyright act.

Before closing a licence agreement on the use of my thesis with another person (subject) I undertake to request for a written statement of the university that the licence agreement in question is not in conflict with the legitimate interests of the university, and undertake to pay any contribution, if eligible, to the costs associated with the creation of the thesis, up to their actual amount.

Brno 15. 10. 2016 Martin Brabec

PREFACE AND ACKNOWLEDGMENTS

The dissertation was accomplished during the years 2012 – 2016 at the Department of Wood Science at the Faculty of Forestry and Wood Technology, Mendel University in Brno (Czech Republic). Experimental measurements were mainly performed at the Josef Ressel Research Centre in Brno-Útěchov and partly at the Technical University in Zvolen (Slovakia) during the scientific placement at the Department of Wood Science at the Faculty of Wood Sciences and Technology.

This work was supported by the European Social Fund and the state budget of the Czech Republic within the project "The Establishment of an International Research Team for the Development of New Wood-based Materials" (Reg. No. CZ.1.07/2.3.00/20.0269) as well as by the Internal Grant Agency of Faculty of Forestry and Wood Technology at Mendel University in Brno within two IGA-I projects such as "The Complex Stress State of Wooden Sample during the Compression Loading Parallel to the Grain" (Grant No. 62/2013) and the project "Utilization of Digital Image Correlation in Determining of Both Longitudinal Shear Moduli of Wood at Single Torsion Test" (Grant No. 17/2015) and also within two IGA-V projects such as "Combined Processes of Beech Wood Modification for Floorings- Influence on Properties, Durability and Health Aspects" (Grant No. 79/2013) and the project "Modification of Hardwoods for Outdoor Applications: Influence of Abiotic and Biotic Factors on Its Aging" (Grant No. LDF_PSV_2016015). This work was also partly supported by the Ministry of Education, Science, Research and Sport of the Slovak Republic within the project "Building Constructions from Beech Wood as a Strategic Source, Quality Parameters Prediction and Their Implementation within the Diagnostic Methods" (Grant No. VEGA 1/0395/16).

My sincere thanks belong to all those, who contributed to accomplish this work, namely first of all to Ing. Václav Sebera, Ph.D. and Ing. Jan Tippner, Ph.D. for a professional supervision of my work and for a selfless giving of their knowledge and experience to me. I also appreciate the willing assistance from Ing. Jaromír Milch during my laboratory measurements, and also our let say "mutual competitive approach" to research, which raced me forward and to finish this work. Further, I am grateful to doc. Ing. Vladimír Gryc, Ph.D. for the opportunity to be part of the research team at the Department of Wood Science. Finally, I express my heartfelt gratitude to my family for their great dedication for me as well as for financial and moral support during my study.

ABSTRACT

Brabec M. (2016) Analysis of the mechanical behaviour of wood by means of digital image correlation, Doctoral thesis, Mendel University in Brno, 161 p.

The full-field optical techniques such as e.g. a digital image correlation are capable to fully reflect the natural wood heterogeneity. Therefore, this thesis aspires to contribute to the experimental mechanics of wood and wood-based composites by the implementation of the full-field optical technique based on the digital image correlation to the standard mechanical tests. A supplementation of the conventional displacement sensors should help to obtain more precise mechanical characteristics and to do more sophisticated analyses of the deformation behaviour of wood and wood-based composites.

The experimental part of the thesis is divided into the five independent case studies listed as the original papers. The measurements were carried out on the most wide-spread wood species in central Europe such as European beech (*Fagus sylvatica*, L.) and Norway spruce (*Picea abies*, L. Karst). Beside the solid wood, the new wood-based sandwich structure, which consists of a core made from birch plywood and the particleboard facings, was investigated too. The loading of the samples was carried out using of the standard mechanical tests such as tension, compression, three-point bending and torsion test.

In the first study, the full-field deformation data were used to indentify reasons for the non-standard deformation behaviour of spruce and beech wood during compression parallel to grain. Reason for this was recognized in the abrubt compression of damage zones located near the compression plates, which induced the expansion of the middle zone located between them. The second study aimed to find out neutral axis position in native and thermally modified beech wood during the conventional three-point bending test. The relative neutral axis position was obtained from mutual position of the neutral axis and centroidal axis, which was determined based on the appropriate image processing methods. It was found that the neutral axis and centroidal sample axis are almost coincident. Objective of the third study was to determine both longitudinal shear moduli of beech wood with help of the full-field shear strains, obtained from a single torsion test, together with use of the appropriate analytical solutions for the calculation of the stress distribution within the radial and tangential direction on the longitudinal-

radial and longitudinal-tangential sample surfaces. Both longitudinal shear moduli increasingly mutually differed as the load increases. Within the fourth study, verification of the elastic material model used in finite-element analyses was carried out with help of full-field deformations induced around notches within dog-bone shaped sample during the uniaxial tension. Great correlation was found between numerically predicted and experimentally measured strain data sets for both longitudinal-radial and longitudinal-tangential shear planes. The fifth study dealed with the characterization of elastic deformation behaviour of newly developed wood-based composite with a sandwich structure. Based on the full-field strain analysis the local strain concentrations were identified. They took place within the core during flatwise compression, and within the facings, when the edgewise compression test was done.

A variety of presented results confirmed widespread applicability of optical methods in the mechanics of materials. Therefore, the utilization of full-field optical method based on digital image correlation in experimental mechanics of wood and wood-based composites can be highly recommended.

KEYWORDS: Mechanics; Digital Image Correlation (DIC); Full-field; Deformation; Displacement; Strain; Stress-strain behaviour; Young's modulus; Shear modulus; Poisson's ratio; Mechanical testing; Compression test; Tension test; Bending test; Torsion test; Wood

ABSTRAKT

Brabec M. (2016) Analýza mechanického chování dřeva metodou korelace obrazu, Disertační práce, Mendelova Univerzita v Brně, 161 s.

Plnopolní optické metody snímání deformací jako je např. digitální korelace obrazu jsou schopny plně zachytit přirozenou heterogenitu dřeva. Proto se předkládaná práce snaží přispět k tomu, aby se metoda korelace obrazu stala běžnou součástí klasických mechanických zkoušek dřeva. Doplnění standardních snímačů posunutí plno-polními optickými metodami by mělo vést k získání přesnějších mechanických vlastností a umožnit vykonávání i pokročilejších analýz deformačního chování dřeva a kompozitů na bázi dřeva.

Experimentální část práce je rozdělena do pěti víceméně nezávislých studií, které jsou zpracovány ve formě vědeckých publikací nebo manuskriptů. Měření byla prováděna na nejpoužívanějších druzích středoevropských dřev, a to na dřevě buku lesního (*Fagus sylvatica*, L.) a smrku ztepilého (*Picea abies*, L. Karst). Kromě masivního dřeva, byly mechanické zkoušky prováděny také na nově vyvinutém kompozitním materiálu na bázi dřeva se sendvičovou strukturou. Tento materiál je tvořen jádrem z břízové překližky, které oboustranně oplášťováno tenkou dřevotřískovou deskou. Zkušební tělesa byla zatěžována pomocí klasických mechanických zkoušek jako je prostý tlak, prostý tah, tříbodý ohyb a krut.

V první případové studii byla plno-polní deformační data použita pro odhalení příčiny nestandardního deformačního chování smrku a buku během tlakového zatížení podél vláken. Příčina nestandardního chování byla spatřena v náhlém kolapsu (stlačení) kontaktních zón, které jsou ve styku s tlačnými deskami, které způsobilo nulovou až zápornou deformaci (rozpínání) středové části zkušebního tělesa. Cílem druhé případové studie bylo identifikovat pozici neutrální osy v deformačním poli přírodního a tepelně upraveného dřeva buku v průběhu klasické tříbodé ohybové zkoušky. Relativní pozice neutrální osy byla stanovena ze vzájemné polohy neutrální osy a geometrické osy zkušebního tělesa. Geometrická osa byla získána pomocí několika kroků v rámci zpracování digitálního obrazu. Z výsledků je patrné, že netrální osa a geometrická zkušebního tělesa se téměř překrývají, což paltí jak pro přírodní tak i tepelně upravené dřevo buku. Třetí případová studie byla zaměřena na stanovení obou podélných smykových modulů dřeva buku pomocí plno-polních smykových deformací,

získaných z jedné krutové zkoušky, v kmbinaci s analytickým řešením pro výpočet distribuce smykového napětí v radiálním a tangenciálním směru na podélně-radiální a podélně-tangenciální rovině dřeva. Oba podélné smykové moduly se vzájemně lišily, přičemž se vzrůstajícím zatížením se rozdíl zvyšoval. V rámci čtvrté případové studie byla provedena verifikace (ověření) elastického materiálového modelu používaného při konečně-prvkových analýzách pomocí plno-polních smykových deformací v okolí zářezů na zkušebních tělesech ve tvaru psí kosti, které byly zatíženy jednoosým tahem. Byla nalezena velmi dobrá shoda mezi numericky predikovanými a experimentálně naměřenými deformacemi pro podélně-radiální i podélně-tangenciální smykovou rovinu. Pátá případová studie se zabývá charakteristikou elastického deformačního chování nově vyvinutého kompozitního materiálu na bázi dřeva se sendvičovou strukturou. Na základě plno-polní analýzy deformací byla identifikována místa, kde dochází k lokální koncetraci deformací. Tyto místa se nacházela v jádře při zatížení kolmo na plochu desky, resp. na krycích deskách při zatížení rovnoběžně s plochou desky.

Rozmanitost prezentovaných výsledků potvrdila širokou aplikovatelnost optických metod v materiálové mechanice. Z toho důvodu, lze použití plno-polní optické metody založené na principu korelace digitálního obrazu v rámci experimentální mechaniky dřeva a materiálů na bázi dřeva vřele doporučit.

KLÍČOVÁ SLOVA: Mechanika; Korelace digitálního obrazu (DIC); Plno-polní; Deformace; Posunutí; Poměrná deformace; Napěťově-deformační chování; Youngův modul pružnosti; Smykový modul pružnosti; Poissonovo číslo; Mechanické zkoušky; Tlaková zkouška; Tahová zkouška; Ohybová zkouška; Krutová zkouška; Dřevo

TABLE OF CONTENT

LIST OF FIGURES

LITERATURE REVIEW

MATERIALS AND METHODS

PAPER I

PAPER II

PAPER III

PAPER IV

PAPER V

LIST OF TABLES

LITERATURE REVIEW

MATERIALS AND METHODS

PAPER I

PAPER II

PAPER III

PAPER IV

PAPER V

1. INTRODUCTION

1.1 BACKGROUND

An appropriate utilization of the wood, mainly in the timber engineering, requires the knowledge of its mechanical behaviour. Moreover, the mechanical behaviour of wood plays the main role also in the machining such as cutting, planning, bending or compression when the wood is preparing for the other non-structural utilization. In a distant past, the assessment of the mechanical behaviour of wood was based on the practical experiences only. As a science and technology became historically more and more sophisticated, the practical experiences were supplemented by the exact strength and stiffness mechanical properties of the wood. In order to determine the mechanical properties, the mechanical loading ("action") and corresponding deformations ("reaction") of wood have to be quantified.

The methods for the measurement of the applied force were historically developed from the loading by a piece of a metal with an exactly defined weight, through the simple load gauge equipped with springs, up to the modern tensometric load cell with a digital output. A similar development through the time can be recognized also for the deformation measurement apparatus. The first step in the development of these devices was the replacing of the manual discontinuous recording of the data from the dial scale by the continuous data acquiring system based on the mechanical converter with a dial finger. It was still not enough accurate for the very small deformations because of the relatively high bias caused by the low sensitivity of this analogue system to the small displacements. The second step consisted in the employment of the electronic continuous data recording, which increased the measurement accuracy on the appropriate level.

The apparatus of the displacement recording was developed together with the position of the displacement sensor. The basic version of the testing machines includes the displacement sensor into the crosshead. It implies that the deformation of the loaded sample is identified as a change of the mutual testing jaws position. Unfortunately, the measured displacement includes the undesirable clearances within the testing jaws. Therefore, the displacement sensor was separated from the crosshead and placed directly onto the sample surface. The position of the displacement sensor can be fixed with help of a spring system or by gluing. The spring external displacement sensor is

well known as an extensometer, meanwhile, the glued one is known as strain gauge or rosette. The concurrently utilization of the internal displacement sensor placed in the crosshead and some the external ones is not uncommon. The change of crosshead position represents the active displacement in the load direction and the passive displacement perpendicularly to the load direction is measured by the external sensor. Subsequently, the Poisson's ratio can be calculated.

Nevertheless, the external displacements sensors are capable to measure the displacement only within the small area on the sample surface or even as a point-wise data which are reliable only for the homogenous deformation field. As the wood is highly heterogeneous material on all of observation levels, the homogeneous deformation field cannot be assumed. Therefore, the displacement data and consequently mechanical properties may vary depending on the sensor position within the sample surface, which introduces into the measurement results some kind of uncertainty. This issue could be treated by the great amount of testing samples for various sensor positions within the sample surface together with the subsequent averaging of the results.

The more sophisticated alternative way is based on the utilization of the full-field optique methods for displacement measurement, which are based on the digital image processing. Today, the image-based measurement methods such as Digital image correlation (DIC), Moiré interferometry, Photoelasticity, Holography, Thermoelastic stress analysis, Photoacoustic, etc., are wide-spread used in the experimental mechanics. On the contrary to the advantage of the full-field data character, the displacement and strains cannot be usually obtained in a real time as by the conventional displacement sensors. This drawback can be partially overcome by a compromise solution when the area of interest on the sample surface is reduced to a necessary minimum consists of few pixels. A smaller area of interest requires the smaller computer performance and subsequently a shorter time for the displacement and strains calculations, which can be carried out in the real time. This variant of the full-field optique methods can be considered as the optical analogy to the conventional extensometer, which is well known as the videoextensometer. Despite the mentioned advantages of the full-field optique methods, the conventional displacement sensors such as internal crosshead sensors, extensometers and strain gauges are still used in the experimental mechanics.

1.2 MOTIVATION

The motivation to accomplish this work stems from a big potential, which can be recognized in the wide-spread and diverse utilization of the full-field displacement and strain data within the experimental mechanics of the anisotropic materials. Based on the literature survey, three scenarios, how to fully exploit the full-field data potential, can be summarized. The first scenario aims to search the undesirable sub-region(s) within the entire full-field area, which should be excluded from the stress-strain analysis. On the contrary, the objective of the second scenario is to search the sub-region(s), which are desirable for the stress-strain analysis. Meanwhile, in the third scenario the utilization of the entire full-field area is required. It was challenge to find the application of these three different ways of the full-field potential utilization within the determination of the mechanical properties of wood and wood-based composites.

The first scenario was applied within the Paper I, which deals with the analysis of the standard and non-standard compression behaviour of spruce and beech wood. The application of the second scenario can be found in the Paper II, IV and V, where the neutral axis of bended beech wood was localized (Paper II), resp. the elastic shear characteristics of wood were determined (Paper IV), resp. the elastic behaviour of the new wood-based sandwich composite was characterized. Finally, the third scenario is fitted by the Paper III, which is focused on the determination of both longitudinal shear moduli of beech wood with help of the full-field shear data from torsion test.

1.3 OBJECTIVES

The general objective of this work was to exploit the potential of the full-field displacement and strain data obtained by a digital image correlation (DIC) in order to enhance the possibilities and increase the accuracy and efficiency of the standard mechanical tests of wood and wood-based composites. In order to fulfil the general objective, the effort was to utilize the full-field displacement and strain data:

1) to analyse reasons for the non-standard deformation behaviour of spruce and beech wood during the compression parallel to grain (Paper I),

2) to find out the neutral axis position in the native and thermally modified beech wood during the conventional three-point bending test (Paper II),

3) to determine both longitudinal shear moduli of beech wood with help of the full-field shear strains obtained from a single torsion test (Paper III),

4) to quantify the shear strains of beech and spruce wood from the uniaxial tension test of the double-notched "dog-bone" shaped samples (Paper IV),

5) to characterize the elastic behaviour of the new wood-based sandwich composite subjected to compression, tension and bending loading (Paper V)

2. LITERATURE REVIEW

2.1 MECHANICS OF WOOD

2.1.1 ANISOTROPY & ORTHOTROPY

The anisotropy implies that the mechanical properties depend upon the infinite number of directions (Kollmann and Côté 1968). An orientation of the covalent and hydrogen bonds and an arrangement of the anatomical elements in a wood volume are the crucial factors, which determines a strong dependency of the mechanical behaviour of wood upon the directions (Bodig and Jayne 1993). A plenty of experiments on the wood samples revealed the diversibility of the mechanical characteristics within the three principal directions such as a longitudinal (*L*), radial (*R*) and tangential (*T*) direction. Based on these directions, three mutually perpendicular planes of a material symmetry such as radial-tangential (*RT*), longitudinal-radial (*LR*) and longitudinal-tangential (*LT*) can be recognized. When a variability of the mechanical properties is neglected within the *RT* plane along the stem as well as within the *LR* plane for a growth ring curvature greater than 100 mm, and finally within the *LT* plane along the stem radius, the wood can be considered as an "orthogonal anisotropic", shortly "orthotropic" material. While applying the static non-cyclic loading, the ratio between the mechanical characteristics of wood measured in the different directions implies that the wood behaves as one of the most orthotropic materials (Tab. 2.1.1-1). If the *R* and *T* mechanical characteristics are assumed equal, which is required in many design situations, the wood classifies as a "transverse isotropic" material.

Tab. 2.1.1-1: General mechanical strength (σ, τ) and stiffness (E, G) characteristics of wood in the longitudinal ($\parallel$) and transversal ($\perp$) principal direction according to Kollmann and Côté (1968), Wagenführ (2007), Ugolev (2007) and Požgaj et al. (1997)

LOADING TYPE	$\sigma_u^{\parallel}$ $\tau_u^{\parallel}$	$\sigma_{u\perp}$ $\tau_{u\perp}$	$\sigma_u^{\parallel} : \sigma_{u\perp}$ $\tau_u^{\parallel} : \tau_{u\perp}$	$E_{\parallel}$ $G_{\parallel}$	$E_{\perp}$ $G_{\perp}$	$E_{\parallel} : E_{\perp}$ $G_{\parallel} : G_{\perp}$
	MPa	MPa	MPa	MPa	MPa	-
Tension	100	5	20 : 1	10000	500	20 : 1
Compression	50	5	10 : 1	10000	1000	10 : 1
Bending	80	5	10 : 1	10000	1000	10 : 1
Longitudinal shear	10	5	2 : 1	1000	1000	1 : 1
Torsion	15	7	2 : 1	1500	1000	1.5 : 1

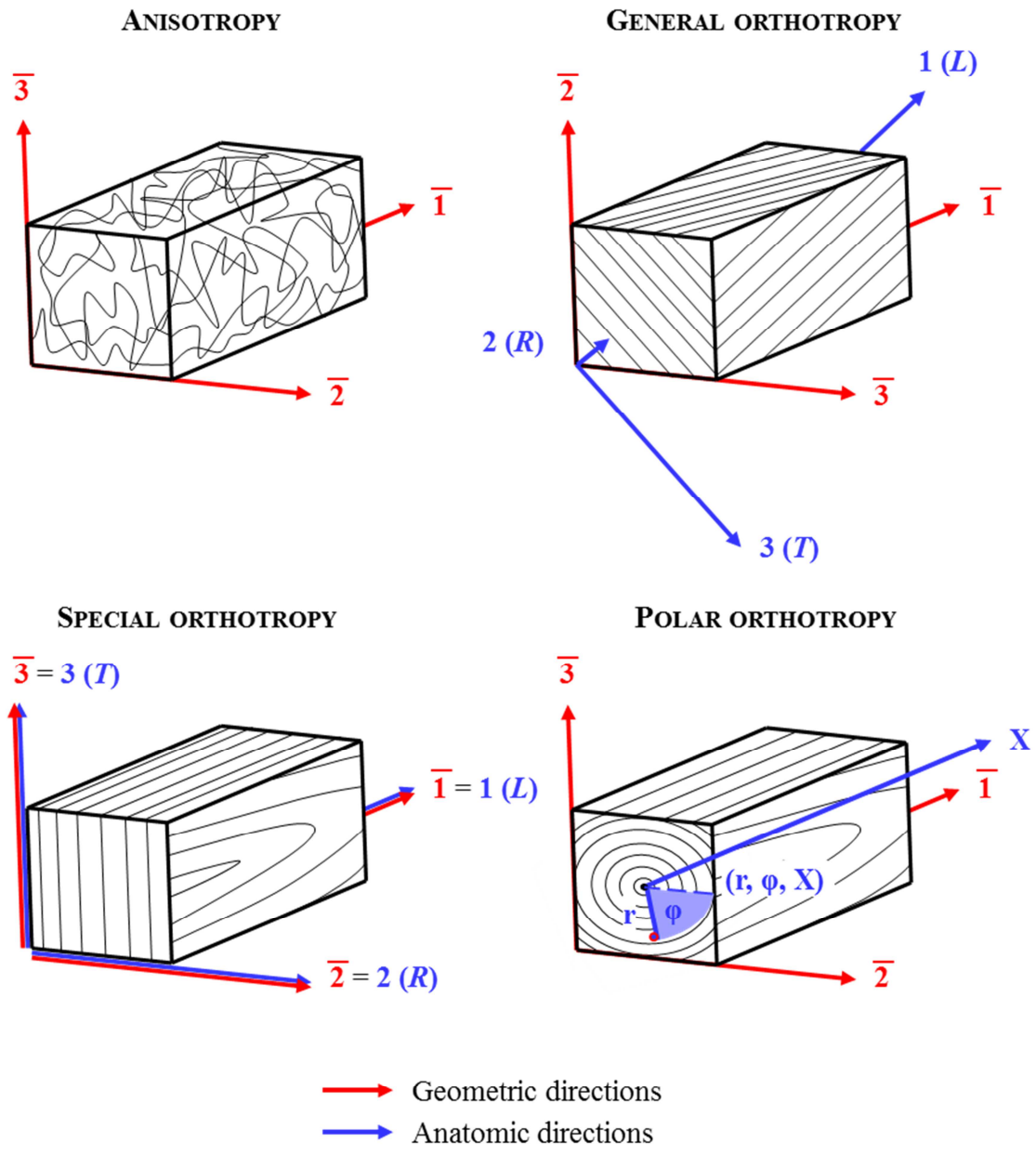

Fig. 2.1.1-1: The possible configuratios of the wood structure

The position of each point within the orthotropic sample of wood can be described with help of two Cartesian coordinate systems. One of them known as "internal anatomic" coordinate system (1, 2, 3) refers to the principal anatomic directions of a wood structure and another known as "external geometric" coordinate system ($\bar{1}$, $\bar{2}$, $\bar{3}$) is related to the geometric directions of a wood sample. When the internal anatomic and external geometric coordinate axes are coincident ($1 = \bar{1}$, $2 = \bar{2}$, $3 = \bar{3}$), the configuration of the wood structure can be referred as a "special orthotropic" structure (Fig. 2.1.1-1). Although special orthotropic structure is desired for a wood properties measurement as well as for most of the timber engineering applications, it is rather an

exception than a rule. The incoincidence of both sets of the external geometric and internal anatomic coordinate axes ($1 \neq \bar{1}, 2 \neq \bar{2}, 3 \neq \bar{3}$) can be referred as "general orthotropic" structure (Fig. **2.1.1-1**).

If a wood sample is cut at a position, which is closer than 100 mm to the pith, the growth ring structure of wood is known as a "polar orthotropic" structure. Within this structure, the polar (cylindrical) coordinate system is usually applied (Požgaj et al. 1997). The position of each point can be described by two polar coordinates such as a radius (r) and angle (φ) and one orthogonal (O). The polar coordinates describe the position within the *RT* plane and the orthogonal coordinate the position of the *RT* plane along the longitudinal axis of the stem (Fig. **2.1.1-1**). A polar coordinate system is naturally not capable of comprising local perturbations such as knots or growth ring irregularities, but offers a more detailed representation than the transversely isotropic model. It distinguishes between the two perpendicular directions *R* and *T*. According to Shipsha and Berglund (2007), simple uniaxial loading induces a shear coupling effects within the polar orthotropic structure, which can cause an inhomogeneous and complex stress state of a wood sample similar as in case of the general orthotropic structure. Hence, the assumption of the polar orthotropy can be important for prediction of the stresses in wood. This has also been proved by Aicher et al. (2001), who found good correspondence between experimental and numerical results in the *RT* plane by assuming the polar orthotropy. It should be noted that the experimental determination of the orthotropic mechanical characteristics based on the polar system seems to be complicated, as an inhomogeneous strain field may occur just because of polar orthotropy.

2.1.2 STRESSES IN WOOD

The normal stresses ($\bar{\sigma}_{qq}$) can be defined according to Eq. (2.1.2-1) based on the elementary normal force ($\Delta\bar{F}_q$) acting perpendicular to the elementary planar surface ($\Delta\bar{S}_q$) of the elementary cube of wood. The shear stresses ($\bar{\tau}_{qr}$) can be defined by Eq. (2.1.2-2) where $\Delta\bar{F}_r$ is the elementary shear force and $\Delta\bar{S}_q$ is the elementary planar surface of the elementary cube of wood, to which the shear force acts parallelly. The surfaces of an elementary cube of wood are oriented consistently with the external geometric coordinate system ($\bar{1}, \bar{2}, \bar{3}$), and therefore, the indices $\{q, r\} = \{\bar{1}, \bar{2}, \bar{3}\}$.

$$\bar{\sigma}_{qq} = \lim_{\Delta \bar{S}_q \to 0} \frac{\Delta \bar{F}_q}{\Delta \bar{S}_q} \tag{2.1.2-1}$$

$$\bar{\tau}_{qr} = \lim_{\Delta \bar{S}_q \to 0} \frac{\Delta \bar{F}_r}{\Delta \bar{S}_q} \tag{2.1.2-2}$$

In order to describe the complex stress state of an elementary cube of wood while the stress vector, consisted of 3 basic components, is acting on all of 6 cube surfaces, a total 18 stress components are needed. Assuming the static stability of the cube, i.e. $\bar{\sigma}_{qq} = -\bar{\sigma}_{qq}$ and $\bar{\tau}_{qr} = -\bar{\tau}_{qr}$, then 9 stress components (3 $\bar{\sigma}_{qq}$ and 6 $\bar{\tau}_{qr}$) are sufficient (Požgaj et al. 1997, Vable 2012). All 9 stress components can be written in a tensor form as

$$[\bar{\sigma}] = \begin{bmatrix} \bar{\sigma}_{11} & \bar{\tau}_{12} & \bar{\tau}_{13} \\ \bar{\tau}_{21} & \bar{\sigma}_{22} & \bar{\tau}_{23} \\ \bar{\tau}_{31} & \bar{\tau}_{32} & \bar{\sigma}_{33} \end{bmatrix} \tag{2.1.2-3}$$

However, it is known from the basic mechanics that the mutual shear stresses are equal in magnitude, which approximately applies also for wood (Bodig and Jayne 1993). It implies a minor symmetry (compatibility of the mutually related shear stresses), i.e. $\bar{\tau}_{qr} = \bar{\tau}_{rq}$ where $q \neq r$ (Boresi and Schmidt 2003, Riley et al. 2007). Subsequently, the number of stress components is reduced again, which results in 6 independent stress components needed for the description of the complex stress state of the elementary cube of wood. These 6 stress components can be expressed in the vector form as

$$[\bar{\sigma}] = \begin{bmatrix} \bar{\sigma}_{11} & \bar{\tau}_{12} & \bar{\tau}_{13} \\ & \bar{\sigma}_{22} & \bar{\tau}_{23} \\ sym & & \bar{\sigma}_{33} \end{bmatrix} = \begin{Bmatrix} \bar{\sigma}_{11} \\ \bar{\sigma}_{22} \\ \bar{\sigma}_{33} \\ \bar{\tau}_{23} \\ \bar{\tau}_{13} \\ \bar{\tau}_{12} \end{Bmatrix} = \{\bar{\sigma}\} \tag{2.1.2-4}$$

2.1.3 STRAINS IN WOOD

Within the "small-scale strain theory", the strain components can be expressed by the "geometric equations". For the normal strains ($\bar{\varepsilon}_{ss}$), it is written as

$$\bar{\varepsilon}_{ss} = \lim_{\Delta\bar{x}_s \to 0} \frac{\Delta\bar{u}_s}{\Delta\bar{x}_s} \tag{2.1.3-1}$$

where $\Delta\bar{u}_s$ is the elementary increment of the displacement and $\Delta\bar{x}_s$ is the elementary initial length and the indices $\{s, t\} = \{\bar{1}, \bar{2}, \bar{3}\}$. The shear strains ($\bar{\delta}_{st}$) can be calculated as the distortion angle in radians according to Eq. (2.1.3-2).

$$\bar{\delta}_{st} = \lim_{\Delta\bar{x}_t \to 0} \tan\frac{\Delta\bar{u}_s}{\Delta\bar{x}_t} \tag{2.1.3-2}$$

where the indices $\{s, t\} = \{\bar{1}, \bar{2}, \bar{3}\}$. For a wood, the equality of two adjacent distortion angles (α_1) and (α_2) cannot be assumed; therefore, the resulted strain tensor is asymmetric. However, it can be readily decomposed into the symmetrical and asymmetrical matrices by taking one-half the sum and one-half the difference of components in identical positions on opposite sides of the principal diagonal (Bodig and Jayne 1993, Požgaj et al. 1997). The symmetrical matrix is called as a strain matrix [ε], meanwhile, the asymmetrical one is called a rotation matrix [ω]. The rotation matrix rotates the distorted elementary cube of wood by a one-half of difference between the two adjacent distortion angles, thus, it makes them equal ($\alpha_1 = \alpha_2$). The rotation of the distorted elementary cube of wood has no direct effect on the stress-strain relationship; therefore, the rotation matrix is not taken into account in the calculation of the shear strains. As a consequence, the symmetrical shear strains ($\bar{\varepsilon}_{st}$) can be obtained as an one-half sum of two adjacent distortion angles. For a small shear strains can be a tangens neglected, then the symmetrical shear strains can be calculated as

$$\bar{\varepsilon}_{st} = \lim_{\substack{\Delta\bar{x}_s \to 0 \\ \Delta\bar{x}_t \to 0}} \frac{1}{2}\left(\frac{\Delta\bar{u}_s}{\Delta\bar{x}_t} + \frac{\Delta\bar{u}_t}{\Delta\bar{x}_s}\right) \tag{2.1.3-3}$$

where the indices $\{s, t\} = \{\bar{1}, \bar{2}, \bar{3}\}$. Nevertheless, for an engineering elastic shear characteristics calculation the engineering shear strains ($\bar{\gamma}_{st}$) are needed. They are calculated as a simple sum of α_1 and α_2 according to Eq. (2.1.3-4).

$$\bar{\gamma}_{st} = \lim_{\substack{\Delta\bar{x}_s \to 0 \\ \Delta\bar{x}_t \to 0}} \left(\frac{\Delta\bar{u}_s}{\Delta\bar{x}_t} + \frac{\Delta\bar{u}_t}{\Delta\bar{x}_s}\right) \tag{2.1.3-4}$$

where the indices $\{s, t\} = \{\bar{1}, \bar{2}, \bar{3}\}$. Then, assuming the static stability of the cube, i.e. $\bar{\varepsilon}_{ss} = -\bar{\varepsilon}_{ss}$ and $\bar{\gamma}_{st} = -\bar{\gamma}_{st}$ similarly to the stresses components, the resulted strain tensor is formed by 9 strain components as

$$[\bar{\varepsilon}] = \begin{bmatrix} \bar{\varepsilon}_{11} & \bar{\gamma}_{12} & \bar{\gamma}_{13} \\ \bar{\gamma}_{21} & \bar{\varepsilon}_{22} & \bar{\gamma}_{23} \\ \bar{\gamma}_{31} & \bar{\gamma}_{32} & \bar{\varepsilon}_{33} \end{bmatrix} \tag{2.1.3-5}$$

The minor symmetry (compatibility of the mutually related shear strains) applies also for the engineering shear strains, i.e. $\bar{\gamma}_{st} = \bar{\gamma}_{ts}$ where $s \neq t$ (Boresi and Schmidt 2003, Vable 2007). Similarly to stress tensor, the number of strain components is reduced to 6 independent ones needed for the description of the complex strain state of the elementary cube of wood. These 6 strain components can be expressed in the vector form as

$$[\bar{\varepsilon}] = \begin{bmatrix} \bar{\varepsilon}_{11} & \bar{\gamma}_{12} & \bar{\gamma}_{13} \\ & \bar{\varepsilon}_{22} & \bar{\gamma}_{23} \\ sym & & \bar{\varepsilon}_{33} \end{bmatrix} = \begin{Bmatrix} \bar{\varepsilon}_{11} \\ \bar{\varepsilon}_{22} \\ \bar{\varepsilon}_{33} \\ \bar{\gamma}_{23} \\ \bar{\gamma}_{13} \\ \bar{\gamma}_{12} \end{Bmatrix} = \begin{Bmatrix} \bar{\varepsilon}_{11} \\ \bar{\varepsilon}_{22} \\ \bar{\varepsilon}_{33} \\ \bar{\varepsilon}_{23} + \bar{\varepsilon}_{32} \\ \bar{\varepsilon}_{13} + \bar{\varepsilon}_{31} \\ \bar{\varepsilon}_{12} + \bar{\varepsilon}_{21} \end{Bmatrix} \{\bar{\varepsilon}\} \tag{2.1.3-6}$$

2.1.4 STRESS-STRAIN BEHAVIOUR OF WOOD

A stress-strain behaviour of wood characterises the wood response to the mechanical loading. This relation could be quantified by the mechanical properties of wood. The mechanical loading induces the stresses within the wood structure, which reacts by the internal displacements coupled with the dimensional, volume and shape changes of the wood sample (Brdička et al. 2000, Vable 2015). The mechanical loading can be applied on wood either by the external forces induced by tension, compression, shear, bending and torsion load or by the internal forces induced due to the hygro-expansion or thermo-expansion of wood (Kollmann and Côté 1968).

In the course of the mechanical loading, the composition of the total normal, shear or combined strain varies depending on the actual load level. There is a proportional limit of the stresses known as "yield stress" (σ_y or τ_y), which divides the stress-strain behaviour of the wood into two phases. In the first phase starting from zero stresses and

ending at the proportional limit only the elastic strains (ε_{el} or γ_{el}) appear. These strains appear immediately after inducing the stresses as well as disappear together with the stresses if the mechanical loading stops (Betherlot 1998, Vable 2007). Within the second phase, which starts from the proportional limit and ends at the maximum limit of stresses known as "ultimate stress" (σ_u or τ_u) where the wood fails, beside the elastic strains are present the viscous (ε_v or γ_v) and plastic (ε_p or γ_p) strains. The viscous strains are gradualy formed, i.e. they are delayed in respect to the actual induced stresses, which applies for both loading and un-loading modes. As a consequence, when the mechanical loading is stopped, the gradually disappearing viscous strains temporary keep the corresponding stress level within the wood structure while no external forces are applied. In the contrary, the plastic strains follow the actual stresses without delay but they are formed as fixed ones accompanied by the stress relaxation (Brdička et al. 2000, Riley et al. 2007). Therefore, the wood can be characterised as a hygroscopic, heterogeneous and anisotropic continuum exhibits the elasto-visco-plastic mechanical behaviour (Kollmann nad Côté 1968).

The percentages of the elastic, viscous and plastic strains from the total strain as well as the mechanical properties themselves vary for a lot of reasons such as a type of loading, loading time, moisture content, temperature, anatomic structure, chemical composition, etc. (Perelygin 1965, Kollmann and Côté 1968, Gerhards 1982, Bodig and Jayne 1993, Požgaj et al. 1997).

Tab. 2.1.4-1: Generalized characteristics of the elasto-visco-plastic behaviour of wood loaded by a different mechanical loading in longitudinal (||) and transversal (⊥) principal direction according to Kollmann and Côté (1968) and Požgaj et al. (1997)

LOADING TYPE	$\sigma_y^{\parallel,\perp}/\sigma_u^{\parallel,\perp}$ $\tau_y^{\parallel,\perp}/\tau_u^{\parallel,\perp}$	ε_t γ_t	$\varepsilon_{el}/\varepsilon_t$ γ_{el}/γ_t	$(\varepsilon_v + \varepsilon_p)/\varepsilon_t$ $(\gamma_v + \gamma_p)/\gamma_t$
	-	%, °	-	-
Tension	0.9	<1%	0.9	0.1
Compression	0.7	<1%	0.7	0.3
Bending	0.7		0.7	0.3
Longitudinal shear	0.9	<1°	0.9	0.1
Torsion	0.9	<1°	0.9	0.1

Based on the literature survey, the type and time of the mechanical loading together with the synergy of the temperature and moisture seem to be crucial factors, which

substantially vary the elasto-visco-plastic behaviour of wood. The generalized different elasto-visco-plastic behaviour of wood for the static non-cyclic loading was summarized in Tab. 2.1.4-1.

The generalized elasto-visco-plastic behaviour of wood can be transformed by using of the data from Tab. 2.1.1-1 to the generalized stress-strain curves in Fig. 2.1.4-1.

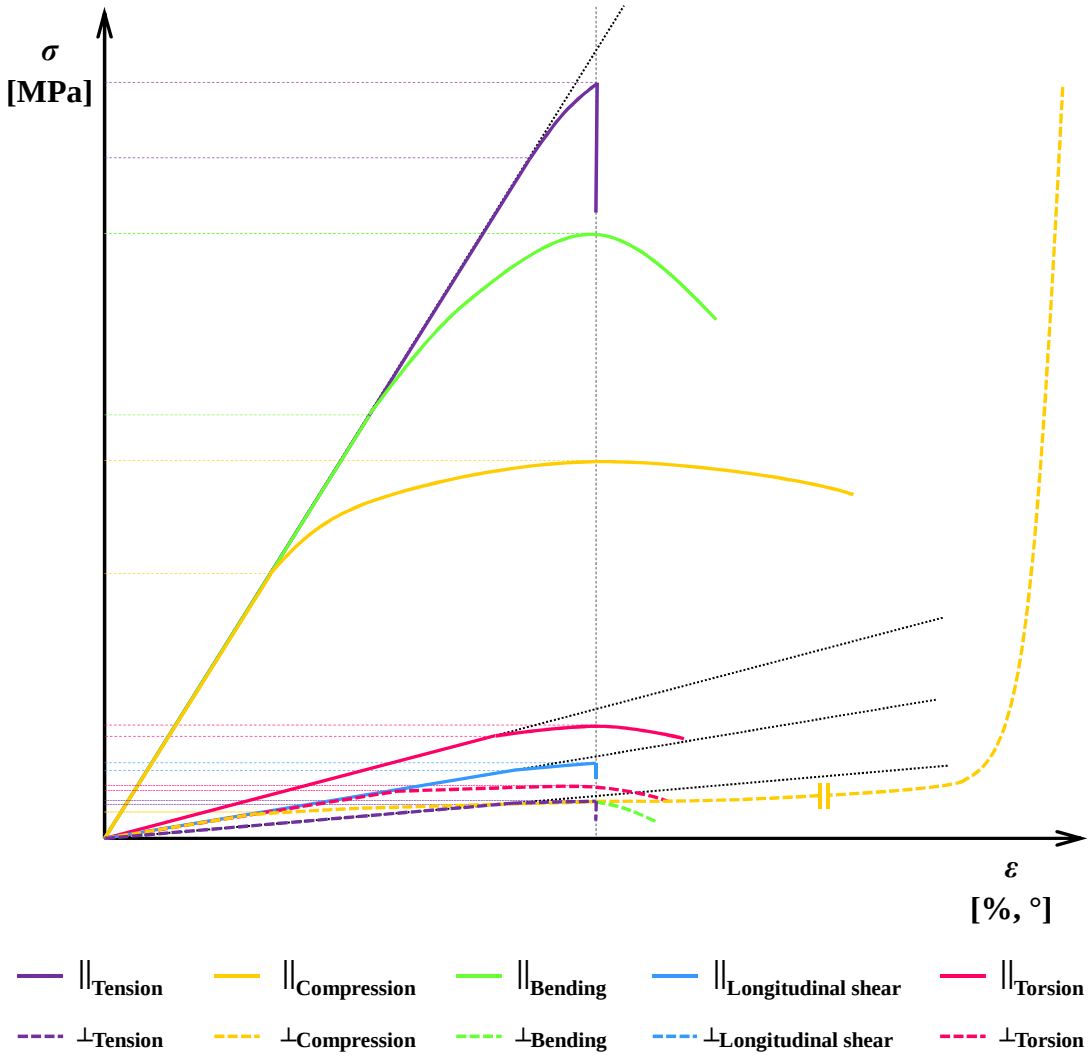

Fig. 2.1.4-1: The generalized stress-strain curves obtained by the different mechanical loading of wood

2.1.5 ELASTICITY OF WOOD

2.1.5.1 GENERAL ORTHOTROPY

Wood can be assumed to behave approximately linearly elastic up to certain stress level for short-term loading (Bodig and Jayne 1993). In this case, each component of stress and strain can be mutually linearly related through the stiffness or compliance

coeficient by Hooke's law (Betherlot 1998, Vable 2002). The mutual relation of stress and strain tensors can be written using of the internal anatomic coordinate system (1, 2, 3) of wood in tensorial stiffnes form as

$$\left[\sigma_{qr}\right] = \left[C_{qrst}\right] \cdot \left[\varepsilon_{st}\right] \tag{2.1.5-1}$$

or in the tensorial compliance form as

$$\left[\varepsilon_{qr}\right] = \left[S_{qrst}\right] \cdot \left[\sigma_{st}\right] \tag{2.1.5-2}$$

where the indices $\{q, r, s, t\} = \{1, 2, 3\}$, $[C_{qrst}]$ is a tensor of the stiffness coefficients and $[S_{qrst}]$ is a tensor of the compliance coefficients. The inverse relationship between the $[C_{qrst}]$ and $[S_{qrst}]$ is apparent as $[C_{qrst}] = [S_{qrst}]^{-1}$ and, vice versa. For the general orthotropic wood structure where the external geometric axes $(\bar{1}, \bar{2}, \bar{3})$ and the internal anatomic coordinate axes (1, 2, 3) are not coincident $(1 \neq \bar{1}, 2 \neq \bar{2}, 3 \neq \bar{3})$, each fourth order tensor $[C_{qrst}]$ and $[S_{qrst}]$ contains 3^4 components (Bodig and Jayne 1993). A total number of 81 elastic parameters would thus be required to characterise the anisotropic material completely. However, when the above mentioned minor symmetry (compatibility of the mutually related shear stresses and strains), i.e. $[C_{qrst}] = [C_{rqst}] = [C_{qrts}]$ applies, then the number of the elastic parameters is reduced to 36 (Daniel and Ishai 2006). An additional reducing of that number stems from the invariance of a general strain energy potential (w) for any linear elastic material, which is for a volume unit defined by

$$w = \int \left[\sigma_{qr}\right] d\left[\varepsilon_{qr}\right] = \int \left[C_{qrst}\right] \cdot \left[\varepsilon_{st}\right] d\varepsilon_{qr} = \frac{1}{2} \left[C_{qrst}\right] \cdot \left[\varepsilon_{qr}\right] \cdot \left[\varepsilon_{st}\right] \geq 0 \tag{2.1.5-3}$$

Assuming the sufficiently smooth w, it is true that

$$\frac{\partial^2 w}{\partial\left[\varepsilon_{qr}\right] \cdot \partial\left[\varepsilon_{st}\right]} = \left[C_{qrst}\right] = \frac{\partial^2 w}{\partial\left[\varepsilon_{st}\right] \cdot \partial\left[\varepsilon_{qr}\right]} = \left[C_{stqr}\right] \tag{2.1.5-4}$$

where $q \neq s$ and $r \neq t$. This implies a major symmetry of the shear components in the stiffness tensor. When the minor and major symmetry is combined such as $[C_{qrst}] = [C_{rqst}] = [C_{qrts}] = [C_{stqr}]$, then the stiffness tensor is reduced to 21 independent elastic parameters of the wood stiffness (Betherlot 1998). Consequently, the expanded tensorial stiffness form of the Hooke's law for a general orthotropic elementary cube of wood can be written using of the internal anatomic coordinate axes (1, 2, 3) as

$$\begin{bmatrix} \sigma_{11} \\ \sigma_{22} \\ \sigma_{33} \\ \hdashline \tau_{23} \\ \tau_{13} \\ \tau_{12} \end{bmatrix} = \left[\begin{array}{ccc:ccc} C_{1111} & C_{1122} & C_{1133} & C_{1123} & C_{1113} & C_{1112} \\ & C_{2222} & C_{2233} & C_{2223} & C_{2213} & C_{2212} \\ & & C_{3333} & C_{3323} & C_{3313} & C_{3312} \\ \hdashline & & & C_{2323} & C_{2313} & C_{2312} \\ & & & & C_{1313} & C_{1312} \\ sym & & & & & C_{1212} \end{array}\right] \cdot \begin{bmatrix} \varepsilon_{11} \\ \varepsilon_{22} \\ \varepsilon_{33} \\ \hdashline \gamma_{23} \\ \gamma_{13} \\ \gamma_{12} \end{bmatrix} \tag{2.1.5-5}$$

or using of the external geometric coordinate axes ($\bar{1}$, $\bar{2}$, $\bar{3}$)

$$\begin{bmatrix} \bar{\sigma}_{11} \\ \bar{\sigma}_{22} \\ \bar{\sigma}_{33} \\ \hdashline \bar{\tau}_{23} \\ \bar{\tau}_{13} \\ \bar{\tau}_{12} \end{bmatrix} = \left[\begin{array}{ccc:ccc} \bar{C}_{1111} & \bar{C}_{1122} & \bar{C}_{1133} & \bar{C}_{1123} & \bar{C}_{1113} & \bar{C}_{1112} \\ & \bar{C}_{2222} & \bar{C}_{2233} & \bar{C}_{2223} & \bar{C}_{2213} & \bar{C}_{2212} \\ & & \bar{C}_{3333} & \bar{C}_{3323} & \bar{C}_{3313} & \bar{C}_{3312} \\ \hdashline & & & \bar{C}_{2323} & \bar{C}_{2313} & \bar{C}_{2312} \\ & & & & \bar{C}_{1313} & \bar{C}_{1312} \\ sym & & & & & \bar{C}_{1212} \end{array}\right] \cdot \begin{bmatrix} \bar{\varepsilon}_{11} \\ \bar{\varepsilon}_{22} \\ \bar{\varepsilon}_{33} \\ \hdashline \bar{\gamma}_{23} \\ \bar{\gamma}_{13} \\ \bar{\gamma}_{12} \end{bmatrix} \tag{2.1.5-6}$$

According to Daniel and Ishai (2006), it can be proved that the minor and major symmetry applies analogically for the elastic parameters of the wood compliance. Subsequently, the expanded tensorial compliance form of the Hooke's law for a general orthotropic elementary cube of wood can be written using of the internal anatomic coordinate axes (1, 2, 3) as

$$\begin{bmatrix} \varepsilon_{11} \\ \varepsilon_{22} \\ \varepsilon_{33} \\ \hdashline \gamma_{23} \\ \gamma_{13} \\ \gamma_{12} \end{bmatrix} = \left[\begin{array}{ccc:ccc} S_{1111} & S_{1122} & S_{1133} & S_{1123} & S_{1113} & S_{1112} \\ & S_{2222} & S_{2233} & S_{2223} & S_{2213} & S_{2212} \\ & & S_{3333} & S_{3323} & S_{3313} & S_{3312} \\ \hdashline & & & S_{2323} & S_{2313} & S_{2312} \\ & & & & S_{1313} & S_{1312} \\ sym & & & & & S_{1212} \end{array}\right] \cdot \begin{bmatrix} \sigma_{11} \\ \sigma_{22} \\ \sigma_{33} \\ \hdashline \tau_{23} \\ \tau_{13} \\ \tau_{12} \end{bmatrix} \tag{2.1.5-7}$$

or using of the external geometric coordinate axes ($\bar{1}$, $\bar{2}$, $\bar{3}$)

$$\begin{bmatrix} \bar{\varepsilon}_{11} \\ \bar{\varepsilon}_{22} \\ \bar{\varepsilon}_{33} \\ \hdashline \bar{\gamma}_{23} \\ \bar{\gamma}_{13} \\ \bar{\gamma}_{12} \end{bmatrix} = \left[\begin{array}{ccc:ccc} \bar{S}_{1111} & \bar{S}_{1122} & \bar{S}_{1133} & \bar{S}_{1123} & \bar{S}_{1113} & \bar{S}_{1112} \\ & \bar{S}_{2222} & \bar{S}_{2233} & \bar{S}_{2223} & \bar{S}_{2213} & \bar{S}_{2212} \\ & & \bar{S}_{3333} & \bar{S}_{3323} & \bar{S}_{3313} & \bar{S}_{3312} \\ \hdashline & & & \bar{S}_{2323} & \bar{S}_{2313} & \bar{S}_{2312} \\ & & & & \bar{S}_{1313} & \bar{S}_{1312} \\ sym & & & & & \bar{S}_{1212} \end{array}\right] \cdot \begin{bmatrix} \bar{\sigma}_{11} \\ \bar{\sigma}_{22} \\ \bar{\sigma}_{33} \\ \hdashline \bar{\tau}_{23} \\ \bar{\tau}_{13} \\ \bar{\tau}_{12} \end{bmatrix} \tag{2.1.5-8}$$

As is apparent from the Eqs. (2.1.5-5) and (2.1.5-6), the normal stresses induce beside the normal strains also the shear strains, and conversely, the shear stresses induce

the shear strains and the normal strains too (Kollmann and Côté 1968). Nevertheless, in a practise the incoicidence of the both sets of axes ($\bar{1}$, $\bar{2}$, $\bar{3}$) and (1, 2, 3) is not uncommon and their misalignment is likely to occur. Therefore, mainly within the structural designing, there is often a need of a transformation of the stresses but also strains as well as the elastic parameters from the external geometric coordinate system ($\bar{1}$, $\bar{2}$, $\bar{3}$) to the internal anatomic coordinate system (1, 2, 3) and vice versa. In order to assess the load carrying capacity of the general orthotropic wood element, the internal stresses acting in the anatomical directions of wood to be known. However, the measurement of the internal stresses is very complicated and practically inapplicable. Therefore, the transformation of the external stresses measured at the geometrical axes to the internal ones is suitable. On the contrary, for the assessment of the usability of the structural element in a wooden truss the external deformations are needed. The measurement of the external deformations is possible but useless in a structural designing. Therefore, the transformation of the internal strains to the external ones seems to be a better solution.

There is a couple of the transformation methods such as a matrix method (Bodig and Jayne 1993, Požgaj et al. 1997, Betherlot 1998, Boresi and Schmidt 2003, Laš 2004, Dahl 2009), an equilibrium method (Bodig and Jayne 1993, Vable 2015) or a Mohr's circle method (Vable 2002, Boresi and Schmidt 2003, Riley et al. 2007), which are able to recalculate the stresses, strains and elastic parameters of wood stiffness or compliance from the external geometric coordinate system ($\bar{1}$, $\bar{2}$, $\bar{3}$) to the internal anatomic coordinate system (1, 2, 3) and, vice versa. All methods are based on the utilization of the various goniometric functions and a rotation angle (θ) defined between the axes of both coordinate systems.

As the stresses and strains are expressed in the matrix form, the matrix transformation method proved to be the most efficient method. This method uses the set of the direction cosines (a_{iq}) defined as

$$a_{iq} = \cos\theta = \cos(\overline{X}, X) \tag{2.1.5-9}$$

where the indices $\{q\} = \{1, 2, 3\}$, $\{i\} = \{\bar{1}, \bar{2}, \bar{3}\}$ and each axis ($\overline{X}$) of the external geometric coordinate system ($\bar{1}$, $\bar{2}$, $\bar{3}$) is related to each axis (X) of the internal anatomic coordinate system (1, 2, 3). The magnitude of the rotation angle is established by a rotating the positive $\overline{X}$ axis into the positive X axis in a clockwise direction. Considering the tensor character of the stresses, strains and elastic parameters of the

wood stiffness and compliance the a_{iq} are arranged into the transformation matrix [A] for each pair of the related indices. Thus, the transformation of the stress tensor can be written as

$$[\bar{\sigma}_{ij}] = [A_{iq}] \cdot [A_{jr}] \cdot [\sigma_{qr}] \tag{2.1.5-10}$$

$$[\sigma_{qr}] = [A_{qi}] \cdot [A_{rj}] \cdot [\bar{\sigma}_{ij}] \tag{2.1.5-11}$$

analogically, the transformation of the strain tensor as

$$[\bar{\varepsilon}_{ij}] = [A_{iq}] \cdot [A_{jr}] \cdot [\varepsilon_{qr}] \tag{2.1.5-12}$$

$$[\varepsilon_{qr}] = [A_{qi}] \cdot [A_{rj}] \cdot [\bar{\varepsilon}_{ij}] \tag{2.1.5-13}$$

and finally, the transformation of the stiffness or compliance tensor as

$$[\bar{C}_{ijkl}] = [A_{iq}] \cdot [A_{jr}] \cdot [A_{ks}] \cdot [A_{lt}] \cdot [C_{qrst}] \tag{2.1.5-14}$$

$$[C_{qrst}] = [A_{qi}] \cdot [A_{rj}] \cdot [A_{sk}] \cdot [A_{tl}] \cdot [\bar{C}_{ijkl}] \tag{2.1.5-15}$$

where the indices $\{q, r, s, t\} = \{1, 2, 3\}$ and $\{i, j, k, l\} = \{\bar{1}, \bar{2}, \bar{3}\}$. The number of the transformation matrices [A] corresponding to the number of the related pairs of the indices, i.e. to the order of each tensor (Dahl 2009). However, the transformation equations (2.1.5-10) and (2.1.5-11) are more often expressed with no indices and with help of the transposed transformation matrices $[A]^T$ (Požgaj et al. 1997) as

$$\bar{\sigma} = A \cdot \sigma \cdot A^T \tag{2.1.5-16}$$

$$\sigma = A^T \cdot \bar{\sigma} \cdot A \tag{2.1.5-17}$$

For the strain tensor, when transforming the symmetrical shear strains ($\varepsilon_{qr} = \gamma_{qr}/2$), the same transformation matrices [A] as apply for the transformation of the stress tensor can be used in the transformation equations (2.1.5-12) and (2.1.5-13), which are then expressed as

$$\bar{\varepsilon} = A \cdot \varepsilon \cdot A^T \tag{2.1.5-18}$$

$$\varepsilon = A^T \cdot \bar{\varepsilon} \cdot A \tag{2.1.5-19}$$

and for the stiffness and compliance tensor as

$$\bar{C} = A \cdot A^T \cdot C \cdot A^T \cdot A \tag{2.1.5-20}$$

$$C = A^T \cdot A \cdot \overline{C} \cdot A \cdot A^T \tag{2.1.5-21}$$

$$\overline{S} = A \cdot A^T \cdot S \cdot A^T \cdot A \tag{2.1.5-22}$$

$$S = A^T \cdot A \cdot \overline{S} \cdot A \cdot A^T \tag{2.1.5-23}$$

For the transformation of the stress tensor within a volume (3D transformation), the transformation equation (2.1.5-16) can be written in the expanded form as

$$\begin{bmatrix} \overline{\sigma}_{11} & \overline{\sigma}_{12} & \overline{\sigma}_{13} \\ \overline{\sigma}_{21} & \overline{\sigma}_{22} & \overline{\sigma}_{23} \\ \overline{\sigma}_{31} & \overline{\sigma}_{32} & \overline{\sigma}_{33} \end{bmatrix} = \begin{bmatrix} a_{\bar{1}1} & a_{\bar{1}2} & a_{\bar{1}3} \\ a_{\bar{2}1} & a_{\bar{2}2} & a_{\bar{2}3} \\ a_{\bar{3}1} & a_{\bar{3}2} & a_{\bar{3}3} \end{bmatrix} \cdot \begin{bmatrix} \sigma_{11} & \sigma_{12} & \sigma_{13} \\ \sigma_{21} & \sigma_{22} & \sigma_{23} \\ \sigma_{31} & \sigma_{32} & \sigma_{33} \end{bmatrix} \cdot \begin{bmatrix} a_{\bar{1}1} & a_{\bar{2}1} & a_{\bar{3}1} \\ a_{\bar{1}2} & a_{\bar{2}2} & a_{\bar{3}2} \\ a_{\bar{1}3} & a_{\bar{2}3} & a_{\bar{3}3} \end{bmatrix} \tag{2.1.5-24}$$

The matrices can be expanded analogically in (2.1.5-17) as well as in the strain transformation equations (2.1.5-18) and (2.1.5-19) and also in the stiffness and compliance transformation equations (2.1.5-20), (2.1.5-21), (2.1.5-22) and (2.1.5-23). Taking the minor symmetry (compatibility of the mutually related shear stresses and strains) and the major symmetry of the shear components in the stiffness and compliance tensors into account, a simple proof can be used to establish that only 6 direction cosines (a_{iq}) are independent within the stress and strain tensor transformations, resp. 21 ones within the stiffness and compliance tensor transformations (Betherlot 1998).

For the transformation of the stress tensor in a plane (2D transformation), the expanded transformation equation (2.1.5-24) is reduced for a $\overline{12}$ plane to

$$\begin{bmatrix} \overline{\sigma}_{11} & \overline{\sigma}_{12} \\ \overline{\sigma}_{21} & \overline{\sigma}_{22} \end{bmatrix} = \begin{bmatrix} a_{\bar{1}1} & a_{\bar{1}2} \\ a_{\bar{2}1} & a_{\bar{2}2} \end{bmatrix} \cdot \begin{bmatrix} \sigma_{11} & \sigma_{12} \\ \sigma_{21} & \sigma_{22} \end{bmatrix} \cdot \begin{bmatrix} a_{\bar{1}1} & a_{\bar{2}1} \\ a_{\bar{1}2} & a_{\bar{2}2} \end{bmatrix} \tag{2.1.5-25}$$

A similar reducing can be done for $\overline{13}$ or $\overline{23}$ plane as well as for the strain, stiffness and compliance tensors. The minor and major symmetry implies 3, resp. 6 independent direction cosines (a_{iq}) within the stress and strain tensor transformation, resp. within the stiffness and compliance tensor transformation (Požgaj et al 1997).

The transformation equations for the in-plane transformations are often additionaly simplified by a grouping of the transformation matrix [A] with its transpose [A]$^{-1}$ to one general transformation matrix [T] (Bodig and Jayne 1993), as

$$A \cdot A^T = T \tag{2.1.5-26}$$

$$A^T \cdot A = T^{-1} \tag{2.1.5-27}$$

Subsequently, the stress transformation equations (2.1.5-16) and (2.1.5-17) can be expressed as

$$\overline{\sigma} = T_\sigma \cdot \sigma \tag{2.1.5-28}$$

$$\sigma = T_\sigma^{-1} \cdot \overline{\sigma} \tag{2.1.5-29}$$

The transformation equations (2.1.5-28) and (2.1.5-29) can be written in the expanded form for the $\overline{1}\overline{2}$ plane as

$$\begin{bmatrix} \overline{\sigma}_{11} \\ \overline{\sigma}_{22} \\ \overline{\sigma}_{12} \end{bmatrix} = \begin{bmatrix} \cos^2\theta & \sin^2\theta & 2\cdot\sin\theta\cdot\cos\theta \\ \sin^2\theta & \cos^2\theta & -2\cdot\sin\theta\cdot\cos\theta \\ -\sin\theta\cdot\cos\theta & \sin\theta\cdot\cos\theta & \cos^2\theta-\sin^2\theta \end{bmatrix} \cdot \begin{bmatrix} \sigma_{11} \\ \sigma_{22} \\ \sigma_{12} \end{bmatrix} \tag{2.1.5-30}$$

$$\begin{bmatrix} \sigma_{11} \\ \sigma_{22} \\ \sigma_{12} \end{bmatrix} = \begin{bmatrix} \cos^2\theta & \sin^2\theta & -2\cdot\sin\theta\cdot\cos\theta \\ \sin^2\theta & \cos^2\theta & 2\cdot\sin\theta\cdot\cos\theta \\ \sin\theta\cdot\cos\theta & -\sin\theta\cdot\cos\theta & \cos^2\theta-\sin^2\theta \end{bmatrix} \cdot \begin{bmatrix} \overline{\sigma}_{11} \\ \overline{\sigma}_{22} \\ \overline{\sigma}_{12} \end{bmatrix} \tag{2.1.5-31}$$

where each transformation component was defined within an equilibrium transformation method (Betherlot 1998, Laš 2004). The replacing direction cosines a_{iq} by the other goniometric functions allows to use the same rotation angle θ for all transformation components, which can be defined by a rotating the positive $\overline{X}$ axis into the positive X axis in a clockwise direction, when $\overline{X} = \{1, 2\} = X$.

Analogically to Eqs. (2.1.5-28) and (2.1.5-29), the Eqs. (2.1.5-18) and (2.1.5-19) can be expressed using of the general transformnation matrix [T] as

$$\overline{\varepsilon} = T_\varepsilon \cdot \varepsilon \tag{2.1.5-32}$$

$$\varepsilon = T_\varepsilon^{-1} \cdot \overline{\varepsilon} \tag{2.1.5-33}$$

Bodig and Jayne (1993) states that when transforming the symmetrical shear strains ($\varepsilon_{qr} = \gamma_{qr}/2$), the general transformation matrix for the strain tensor transformation (T_ε) and its transpose (T_ε^{-1}) are equal to those for the strain tensor transformation (T_σ and T_σ^{-1}), it means that

$$T_\sigma = T_\varepsilon \tag{2.1.5-34}$$

$$T_\sigma^{-1} = T_\varepsilon^{-1} \tag{2.1.5-35}$$

If the transformation of the enginnering shear strain (γ_{ij}) is required, the transformation equations (2.1.5-32) and (2.1.5-33) can be written in the expanded form for $\overline{1}\overline{2}$ plane as

$$\begin{bmatrix} \overline{\varepsilon}_{11} \\ \overline{\varepsilon}_{22} \\ \overline{\gamma}_{12} \end{bmatrix} = \begin{bmatrix} \cos^2\theta & \sin^2\theta & \sin\theta\cdot\cos\theta \\ \sin^2\theta & \cos^2\theta & -\sin\theta\cdot\cos\theta \\ -2\cdot\sin\theta\cdot\cos\theta & 2\cdot\sin\theta\cdot\cos\theta & \cos^2\theta-\sin^2\theta \end{bmatrix} \cdot \begin{bmatrix} \varepsilon_{11} \\ \varepsilon_{22} \\ \gamma_{12} \end{bmatrix} \tag{2.1.5-36}$$

$$\begin{bmatrix} \varepsilon_{11} \\ \varepsilon_{22} \\ \gamma_{12} \end{bmatrix} = \begin{bmatrix} \cos^2\theta & \sin^2\theta & -\sin\theta\cdot\cos\theta \\ \sin^2\theta & \cos^2\theta & \sin\theta\cdot\cos\theta \\ 2\cdot\sin\theta\cdot\cos\theta & -2\cdot\sin\theta\cdot\cos\theta & \cos^2\theta-\sin^2\theta \end{bmatrix} \cdot \begin{bmatrix} \overline{\varepsilon}_{11} \\ \overline{\varepsilon}_{22} \\ \overline{\gamma}_{12} \end{bmatrix} \tag{2.1.5-37}$$

If the stress tensor [σ] in the stiffness form of the Hooke's law is replaced by the Eq. (2.1.5-29), the following expression can be obtained

$$T_\sigma^{-1}\cdot\overline{\sigma} = C\cdot\varepsilon \tag{2.1.5-38}$$

Further appropriate replacement of $\overline{\sigma}$ leads to

$$T_\sigma^{-1}\cdot\overline{C}\cdot\overline{\varepsilon} = C\cdot\varepsilon \tag{2.1.5-39}$$

and additional appropriate replacement of $\overline{\varepsilon}$ gives

$$T_\sigma^{-1}\cdot\overline{C}\cdot T_\varepsilon\cdot\varepsilon = C\cdot\varepsilon \tag{2.1.5-40}$$

By re-arranging the final transformation equation for the stiffness tensor can be obtained

$$\overline{C} = T_\sigma\cdot C\cdot T_\varepsilon^{-1} \tag{2.1.5-41}$$

Taking the engineering shear strains into account, the transformation equation (2.1.5-41) can be written in the expanded form for $\overline{1}\overline{2}$ plane as

$$\begin{bmatrix} \overline{C}_{11} & \overline{C}_{12} & \overline{C}_{16} \\ \overline{C}_{21} & \overline{C}_{22} & \overline{C}_{26} \\ \overline{C}_{61} & \overline{C}_{62} & \overline{C}_{66} \end{bmatrix} = \begin{bmatrix} \cos^2\theta & \sin^2\theta & 2\cdot\sin\theta\cdot\cos\theta \\ \sin^2\theta & \cos^2\theta & -2\cdot\sin\theta\cdot\cos\theta \\ -\sin\theta\cdot\cos\theta & \sin\theta\cdot\cos\theta & \cos^2\theta-\sin^2\theta \end{bmatrix} \cdot \begin{bmatrix} C_{11} & C_{12} & C_{16} \\ C_{21} & C_{22} & C_{26} \\ C_{61} & C_{62} & C_{66} \end{bmatrix} \cdot \begin{bmatrix} \cos^2\theta & \sin^2\theta & -\sin\theta\cdot\cos\theta \\ \sin^2\theta & \cos^2\theta & \sin\theta\cdot\cos\theta \\ 2\cdot\sin\theta\cdot\cos\theta & -2\cdot\sin\theta\cdot\cos\theta & \cos^2\theta-\sin^2\theta \end{bmatrix} \tag{2.1.5-42}$$

The transformation equation for the compliance tensor can be derived in a similar manner as for the stiffness tensor (Požgaj et al. 1997) and it is expressed as

$$\overline{S} = T_{\varepsilon} \cdot S \cdot T_{\sigma}^{-1} \tag{2.1.5-43}$$

Taking the engineering shear strains into account, the transformation equation (2.1.5-43) can be written in the expanded form for $\overline{1}\overline{2}$ plane as

$$\begin{bmatrix} \overline{S}_{11} & \overline{S}_{12} & \overline{S}_{16} \\ \overline{S}_{21} & \overline{S}_{22} & \overline{S}_{26} \\ \overline{S}_{61} & \overline{S}_{62} & \overline{S}_{66} \end{bmatrix} = \begin{bmatrix} \cos^2\theta & \sin^2\theta & \sin\theta\cdot\cos\theta \\ \sin^2\theta & \cos^2\theta & -\sin\theta\cdot\cos\theta \\ -2\cdot\sin\theta\cdot\cos\theta & 2\cdot\sin\theta\cdot\cos\theta & \cos^2\theta-\sin^2\theta \end{bmatrix} \cdot \begin{bmatrix} S_{11} & S_{12} & S_{16} \\ S_{21} & S_{22} & S_{26} \\ S_{61} & S_{62} & S_{66} \end{bmatrix} \cdot \begin{bmatrix} \cos^2\theta & \sin^2\theta & -2\cdot\sin\theta\cdot\cos\theta \\ \sin^2\theta & \cos^2\theta & 2\cdot\sin\theta\cdot\cos\theta \\ \sin\theta\cdot\cos\theta & -\sin\theta\cdot\cos\theta & \cos^2\theta-\sin^2\theta \end{bmatrix} \tag{2.1.5-44}$$

2.1.5.2 SPECIAL ORTHOTROPY

The shear coupling and consequently the issue of a complex stress state within the determination of the engineering elastic characteristics, such as normal elastic moduli (E), shear elastic moduli (G) and Poisson's ratios (v), can be partially overcome by using of the special orthotropic samples with a coincidence of the external geometrical axes and internal anatomical axes ($1 = \overline{1}$, $2 = \overline{2}$, $3 = \overline{3}$). In such a structure it is assuming that the normal stresses induce only the normal strains and the shear stresses induce only the shear strains (Hopperstad 2003). Therefore, further reduction of the 21 elastic independent parameters of the wood stiffness and compliance applying for the general orthotropic samples of wood can be expected. It is highly desirable in order to simplify the application of the Hooke's law. As can be derived by applying of the transformation matrices $[A]$ for zero rotation angle (θ) and the minor and major symmetry of the shear components to the general orthotropic system (Dahl 2009), the expanded tensorial stiffness form of the Hooke's law for a special orthotropic elementary cube of wood can be written using of the internal anatomic coordinate axes (1, 2, 3) as

$$\begin{bmatrix}\sigma_{11}\\ \sigma_{22}\\ \sigma_{33}\\ \hline \tau_{23}\\ \tau_{13}\\ \tau_{12}\end{bmatrix} = \left[\begin{array}{ccc:ccc} C_{1111} & C_{1122} & C_{1133} & 0 & 0 & 0 \\ & C_{2222} & C_{2233} & 0 & 0 & 0 \\ & & C_{3333} & 0 & 0 & 0 \\ \hdashline & & & C_{2323} & 0 & 0 \\ & & & & C_{1313} & 0 \\ sym & & & & & C_{1212} \end{array}\right] \cdot \begin{bmatrix}\varepsilon_{11}\\ \varepsilon_{22}\\ \varepsilon_{33}\\ \hline \gamma_{23}\\ \gamma_{13}\\ \gamma_{12}\end{bmatrix} \tag{2.1.5-45}$$

Analogically, the Hooke's law in the expanded tensorial compliance form for a special orthotropic elementary cube of wood can be written using of the internal anatomic coordinate axes (1, 2, 3) as

$$\begin{bmatrix}\varepsilon_{11}\\ \varepsilon_{22}\\ \varepsilon_{33}\\ \hline \gamma_{23}\\ \gamma_{13}\\ \gamma_{12}\end{bmatrix} = \left[\begin{array}{ccc:ccc} S_{1111} & S_{1122} & S_{1133} & 0 & 0 & 0 \\ & S_{2222} & S_{2233} & 0 & 0 & 0 \\ & & S_{3333} & 0 & 0 & 0 \\ \hdashline & & & S_{2323} & 0 & 0 \\ & & & & S_{1313} & 0 \\ sym & & & & & S_{1212} \end{array}\right] \cdot \begin{bmatrix}\sigma_{11}\\ \sigma_{22}\\ \sigma_{33}\\ \hline \tau_{23}\\ \tau_{13}\\ \tau_{12}\end{bmatrix} \tag{2.1.5-46}$$

In order to quantify each component of the stiffness $[C_{qrst}]$ and compliance $[S_{qrst}]$ tensor in Eqs. (2.1.5-45) and (2.1.5-46), the set of 9 engineering elastic characteristics comprising 3 normal moduli of elasticity (E_{qq}), 3 shear moduli of elasticity (G_{qr}) and 3 Poisson's ratios (v_{qr}) should be used (Kaw 1997, Požgaj et al 1997, Daniel and Ishai 2006). This stems from the major symmetry of the shear components in the stiffness and compliance tensors, i.e. $C_{qqrr} = C_{rrqq}$ and $S_{qqrr} = S_{rrqq}$ where $q \neq r$. If each elastic parameter of the wood stiffness is replaced by a linear relationship of the engineering elastic characteristics (E_{qq}, G_{qr} and v_{qr} where the indices $q, r, t = L, R, T$), then the stiffness tensor is changed as

$$[C_{qrst}] = \left[\begin{array}{ccc:ccc} \frac{1-\nu_{RT}\nu_{TR}}{E_{RR}E_{TT}|S|} & \frac{\nu_{RL}+\nu_{RT}\nu_{TL}}{E_{RR}E_{TT}|S|} & \frac{\nu_{TL}+\nu_{RL}\nu_{TR}}{E_{RR}E_{TT}|S|} & 0 & 0 & 0 \\ & \frac{1-\nu_{TL}\nu_{LT}}{E_{LL}E_{TT}|S|} & \frac{\nu_{RT}+\nu_{RL}\nu_{LT}}{E_{RR}E_{TT}|S|} & 0 & 0 & 0 \\ & & \frac{1-\nu_{RL}\nu_{LR}}{E_{LL}E_{RR}|S|} & 0 & 0 & 0 \\ \hdashline & & & \frac{1}{G_{RT}} & 0 & 0 \\ & & & & \frac{1}{G_{LT}} & 0 \\ sym & & & & & \frac{1}{G_{LR}} \end{array}\right] \tag{2.1.5-47}$$

where |S| is defined as

$$|S| = \frac{1}{E_{LL} \cdot E_{RR} \cdot E_{TT}} \cdot \left(1 - 2\nu_{RL}\nu_{TR}\nu_{LT} - \nu_{LT}\nu_{TL} - \nu_{RT}\nu_{TR} - \nu_{LR}\nu_{RL}\right) \tag{2.1.5-48}$$

The compliance tensor supplemented by the engineering elastic characteristics could be obtained by the inversion of the stiffness tensor and it is defined as

$$\left[S_{qrst}\right] = \left[\begin{array}{ccc:ccc} \frac{1}{E_{LL}} & -\frac{\nu_{LR}}{E_{LL}} & -\frac{\nu_{LT}}{E_{LL}} & 0 & 0 & 0 \\ & \frac{1}{E_{RR}} & -\frac{\nu_{RT}}{E_{RR}} & 0 & 0 & 0 \\ & & \frac{1}{E_{TT}} & 0 & 0 & 0 \\ \hdashline & & & \frac{1}{G_{RT}} & 0 & 0 \\ & & & & \frac{1}{G_{LT}} & 0 \\ sym & & & & & \frac{1}{G_{LR}} \end{array}\right] \tag{2.1.5-49}$$

When the linear range prevails, the engineering elastic characteristics can be determined experimentally by the measurement of the stress and strain increments according to (Boresi and Schmidt 2003, Riley et al. 2007, Vable 2007) as

$$E_{qq} = \frac{\Delta\sigma_{qq}}{\Delta\varepsilon_{qq}} \tag{2.1.5-50}$$

$$G_{qr} = \frac{\Delta\tau_{qr}}{\Delta\gamma_{qr}} \tag{2.1.5-51}$$

$$\nu_{qr} = -\frac{\Delta\varepsilon_{qr}}{\Delta\varepsilon_{qr}} \tag{2.1.5-52}$$

where $\Delta\sigma_{qq}$ is the increment of the normal stresses, $\Delta\tau_{qr}$ is the increment of the shear stresses, $\Delta\varepsilon_{qq}$, resp. $\Delta\varepsilon_{rr}$ are the increments of the normal strains corresponding to $\Delta\sigma_{qq}$, resp. $\Delta\sigma_{rr}$, $\Delta\gamma_{qr}$ is the increment of the engineering shear strains corresponding to $\Delta\tau_{qr}$ and the indices $\{q, r\} = \{L, R, T\}$ where $q \neq r$. A minor symmetry (compatibility of the mutually related shear stresses and strains) implies that

$$\Delta\tau_{qr} = \Delta\tau_{rq} \text{ and } \Delta\gamma_{qr} = \Delta\varepsilon_{qr} + \Delta\varepsilon_{rq} = \Delta\tau_{rq} \tag{2.1.5-53}$$

$$\text{which gives } G_{qr} = G_{rq} \tag{2.1.5-54}$$

2.1.5.3 TRANSVERSE ISOTROPY

A material is transversely isotropic if there is a plane that every plane perpendicular to it is a material symmetry plane. This assumption applies for most of the wood-based composites such as particle boards, structural composite lumber, etc. (Gustaffson 2003, Riley et al. 2007). Nevertheless, some of the solid wood mechanical characteristics are almost equal within the *RT* plane, therefore, the transverse isotropy could be usefully applied, mainly in a timber engineering. The stiffness tensor can be defined as

$$\left[C_{qrst}\right]=\left[\begin{array}{ccc:ccc} C_{1111} & C_{1144} & C_{1144} & 0 & 0 & 0 \\ & C_{4444} & C_{4444} & 0 & 0 & 0 \\ & & C_{4444} & 0 & 0 & 0 \\ \hdashline & & & \frac{C_{4444}-C_{4444}}{2} & 0 & 0 \\ & & & & C_{1414} & 0 \\ & & & & & C_{1414} \end{array}\right] \tag{2.1.5-55}$$

where the indices $\{q, r, s, t\} = \{1, 4\}$. An indice *1* refers to the longitudinal direction and indice *4* refers to the transverse direction. The transversely isotropic material is thus characterized by 5 independent elastic parameters of the material stiffness (Kaw 1997, Betherlot 1998, Vable 2015). If each parameter of the material compliance is replaced by a linear relationship of the engineering elastic characteristics (E_{qq}, G_{qr} and v_{qr} where the indices $q, r, t = L, P$), then the compliance tensor can be expressed as follows

$$\left[S_{qrst}\right]=\left[\begin{array}{ccc:ccc} \frac{1}{E_{LL}} & -\frac{\nu_{LP}}{E_{LL}} & -\frac{\nu_{LP}}{E_{LL}} & 0 & 0 & 0 \\ & \frac{1}{E_{PP}} & -\frac{\nu_{PP}}{E_{PP}} & 0 & 0 & 0 \\ & & \frac{1}{E_{PP}} & 0 & 0 & 0 \\ \hdashline & & & \frac{1+\nu_{PP}}{2\cdot E_{PP}} & 0 & 0 \\ & & & & \frac{1}{G_{LP}} & 0 \\ \textit{sym} & & & & & \frac{1}{G_{LP}} \end{array}\right] \tag{2.1.5-56}$$

where E_{LL} and E_{PP} are the normal elastic moduli in the L and P directions, respectively, G_{LP} and v_{LP} are the in-plane shear modulus and Poisson's ratio, respectively, v_{PP} is the out-of-plane Poisson's ratio corresponding to the *RT* plane in wood.

2.2 DIGITAL IMAGE CORRELATION

2.2.1 HISTORY

In the past, optical methods for measuring of deformations applying the principle of digital image correlation were referred to in various ways, e.g. "Digital Speckle Correlation Method" (Zhang et al. 1999, Zhou and Goodson 2001), "Texture Correlation" (Bay 1995), "Computer-aided Speckle Interferometry" (Chen et al. 1993, Gaudette et al. 2001), "Electronic Speckle Photography" (Sjödahl and Benckert 1993, 1994, Sjödahl 1994, 1997). According to Pan et al. (2009), the method of image correlation is currently known in the wider scientific community as the "Digital Image Correlation" (DIC).

The DIC has its basis in the photogrammetric methods used for the analysis of aerial photographs and to a large extent it is also linked with the development of the image digitization technology (Reu 2009). Its practical use came with the affordable computing performance in the form of a personal computer. The successful development of this method is mainly a result of work of a group of scientists from the University of South Carolina (USA). Peters and Ranson (1982) published the first use of the DIC for 2D application. They were able to measure displacements and strains of a planar surface of a sample in two spatial axes (x and y) under tensile load. The investigated surface of the measured object had a random speckle pattern, which was applied using a laser and captured using a single camera. Displacement was defined based on the analysis of images with the speckle pattern changing during the loading. However, the technology used by Peters and Ranson (1982) was not yet applicable for most cases, in which the points on the surface captured move in the third spatial axis (z) as well due to the loading. As stated in Sutton (2008), the hardest challenge of the DIC extension to 3D applications was to develop a calibration procedure for two cameras so that they were able to work in a stereoscopic system, and capture even the movement of points on the z axis. The first to calibrate the stereo system for the reconstruction of the captured object surface in all three spatial axes (x; y; z) was McNeill et al. (1988). By

moving the camera in one direction, the shape of an oblique plane object was measured. This experiment initiated the development of the measurement of displacements and strains of curved surfaces using the DIC (Luo et al. 1993). Another substantial step in the DIC was introduced by Bay et al. (1999), who expanded the correlation algorithms used for surface applications to volumetric ones. This extended DIC version was called the method of "Digital Volume Correlation" (DVC). They used X-ray computer tomography as a source of digital volumetric data called as "voxels". The DIC method in its current form provides the topography of an object, full-field data of displacements, strains and curvature for surfaces, in the case of DVC also for volumes.

In the area of numerical calculations and programming, the development of the DIC method is related with the application of newly developed correlation algorithms for full-pixel and sub-pixel displacements. In the context of technological progress, white diffuse light started to be used instead of the laser. In the field of experimental data acquisition, analog recording units have been replaced with digital high-speed cameras with high resolution (Rastogi 2000). In general, progress in science and technology minimizes the computational complexity of the DIC method and improves the accuracy of the results, which allows still a wider range of applications, for example, in real time – production control (Sutton 2008).

2.2.2 BASIC PRINCIPLES

The basic principle of the DIC method consists in finding the correlation between individual points (pixels) of two digital images. One image is always the reference, i.e., an image of the undeformed object surface; the other image is the image of the deformed object surface. In addition to the total deformation, it is usually desirable to describe the deformation behaviour, i.e. the deformation increments during loading. For this reason, images of the deformed surface are taken continuously in particular time intervals during the loading. Subsequently, the correlation of pixels is performed incrementally, i.e., the correlation between the pixels in two consecutive images is searched for. Out of a couple of consecutive images, the image taken earlier from the beginning of the load is always considered the reference. According to Sutton (2008), searching for the correlation between the pixels in two images can be understood as the search for a match, "matching" of pixels. After the identical pixel is found in the image of the object surface before and after deformation, the pixel is assigned spatial

coordinates which define its position. The same position of the matched pixel in both images corresponds to zero pixel displacement or zero surface deformation of the object at the given point, while a different position of the matched pixel indicates the displacement or non-zero deformation of the object at the given point. The relative difference between the coordinates of the pixel in the object surface image before deformation and after deformation corresponds to an absolute displacement of the given point on the surface of the deformed object (Hild and Roux 2006). The position of the pixel in the image aligns with the position on the actual object surface. To express the displacement in physical units of length instead of pixel units, it is necessary to find out how many pixels in the image correspond to a length unit on the actual object surface. This and the other parameters are obtained during calibration of the recording units (Pan et al. 2009). This transformation of displacement between the image and the real surface is based on the assumption that the movement of the points on the real object surface is truthfully transmitted to the image by the recording device (Rastogi 2000).

In order to obtain full-field data (determination of the displacement at any point of the object surface), each image of the deformed and undeformed surface has to be divided into the same number of points that can be matched mutually. This requirement is fully met in the structure of the digital image, which can be defined as a set of a finite number of points (pixels) with discretely distributed brightness values (Gonzalez et al. 2004). However, the image cannot be taken in digital form directly. Photosensitive sensors first capture the incident photons reflected from the surface of the captured object as the electrical charge continuously changing its intensity within the sensor surface area. The charge is then sampled and quantized to the final number of intensities of electric charge, i.e. brightness. The maximum number of pixels of the digital image is given by the number of photosensitive cells on the sensor, i.e. by sensor resolution (Pratt 2007). Each pixel of the digital image is thus characterized by a quantum (level) of brightness. The brightness level is hence used as a correlation variable. Pixels with the same brightness level in two images could theoretically be regarded as the same pixel. Jin et al. (2006) pointed out that with increasing deformation of the object surface some of the points on the surface may disappear (in the case of the surface shrinking), or vice versa, new points on the surface may arise (in the case of surface enlargement). As a result, when matching the pixels, it is not possible to find the pixels representing points that have disappeared in the image of the deformed surface and, vice versa, pixels representing newly created points in the image of the undeformed object surface.

However, it cannot be excluded that a greater number of pixels in one image will have the same level of brightness, which can lead to incorrect pixel matching, i.e. different pixels are considered identical. This problem is largely solved by using the surrounding pixels to identify each pixel in both images uniquely (Pan et al. 2009). The probability that two pixels in one image will have exactly the same surroundings is significantly lower than the probability of identical brightness level of two different pixels in the same image. In addition, the probability of multiple occurrence of the identification surroundings is decreased with its growing size. In this way, the pixel whose brightness level has changed during the object deformation due to local changes in the light intensity or large local deformation of the object surface, etc. can also be found. Identifical pixel surrounding is known as a "subset" or "facet". The subset size depends on several variables, especially the image resolution, magnitude and character of the deformation and the contrast of the object surface. Most commonly, rectangular subsets of size 10×10 to 50×50 pixels are used (Sutton 2008). A matched pixel is usually located in the middle of the subset. Pixels less than half of the subset far from the edge of the image may be placed on the edge of the subset and thus extend the correlated area up to the edges of the image.

The experimental procedure for the application of the DIC method corresponds to the following sections. Usually, first the experimental stage is built and the recording units are calibrated. The treatment increasing the contrast of the object surface follows. Then, the load cycle is launched and images of the deforming object surface are acquired continuously. After the end of the cycle, the same steps are repeated for other objects. Several sub-steps are performed to process the images.

2.2.3 ACQUISITION SYSTEM

2.2.3.1 APPARATUS

According to Sutton (2008), to determine the displacement and strain on a planar surface which is deformed by load only in the *x* and *y* directions, which are parallel to the sensor plane, and there is no movement of the surface perpendicular to the *xy* plane (in the *z* direction), only one digital recording unit (camera or camcorder fitted with a CCD or CMOS sensor), a lens, a tripod with a fully adjustable clamping head, a source of white diffuse light, software for the acquisition of images and their processing (calculation of correlation coefficients, displacement, strain), a computer unit with

adequate computing power and cabling for high data flow, or an additional power supply for the recording unit, are sufficient. If it is necessary to increase the contrast pattern on the surface of the captured object, the acquisition set also needs to include spray or another application device.

However, in most cases the originally planar surface captured becomes non-planar during loading, or its position in the direction perpendicular to the sensor plane changes due to the Poisson's effect. This movement of the surface is mistakenly interpreted as displacement in *x* and *y* directions within the 2D DIC. Therefore, it is necessary to enlarge the set with at least one more digital recording unit and create a stereoscopic system able to distinguish the movement in the *z* direction from the strain in the *x* and *y* directions. The assembly of the units into the stereoscopic system is performed to the common arm and by calibration using calibration grids (standardization samples), which become an integral part of the acquisition set for 3D application together with the appropriate software. Usually, a separate light source is used for each recording unit.

2.2.3.2 EXPERIMENTAL SET-UP

For 2D measurements, the recording unit must be located so that the sensor plane is parallel to the planar surface to be captured (Peters and Ranson 1982). For 3D measurements, the recording units are placed according to the principles of the stereoscopy (Mandát 2012). For successful correlation of the points, both recording units should provide as identical image as possible (Luo et al. 1993). For this purpose it is necessary to put both recording units to the common arm, to the same distance from the captured surface so that the center of the line connecting the two recording units corresponds with the center of the captured surface. The maximum distance between the two recording units derives from the maximum stereoscopic parallax (30°), while at a larger parallax the images of the captured surface are deformed to an unacceptable extent (Sutton et al. 2000). In addition, some parts of the captured surface can fall outside the lens depth of field (DOF), and thus appear as blurry in the image. Pixels located in the deformed and blurry parts of the image usually cannot be matched by the correlation algorithm, and so the displacements and strains cannot be determined.

The setting of the recording units for both 2D and 3D measurements should be such that the centers of the sensors are linked to the center of the captured surface with the shortest possible virtual link. After the calibration of the acquisition set, the recording

units must be fixed in their positions throughout the entire measurement process (Pan et al. 2009). A relative movement of the recording units would render calibration parameters unusable and along with the unwanted deformation of the images would prevent the determination of the actual displacement and strain of the captured object surface. The solution may be re-calibration of the recording units in the new position. However, in some experimental conditions the acquisition set cannot be assembled and calibrated directly on the experiment site (lack of space, closure of captured object in the conditioning chamber, etc.). In this case, it is necessary to assemble the acquisition set in another place and set the position of the recording units relative to an arbitrary object; this implies that the condition of fixed position of recording units after calibration cannot be met. The solution was brought by Sutton (2008), who added a laser beam to the acquisition set. This allows setting the acquisition set exactly in the position to the captured object as it was calibrated relative to an arbitrary object. The laser beam was placed in the center of the line linking the recording units to indicate the center of the captured object surface. Once the center of the virtual cross of live image and the point created on the surface by the laser beam match in the images from both recording units, the correct position of the pre-calibrated set relative to the captured object has been found. No additional calibration procedure is required to process the images.

2.2.3.3 CALIBRATION PROCEDURE

The calibration is a procedure through which the external and internal calibration parameters of recording units are gained. These are then used to transform the displacement and curvature of the object surface from pixel units to the appropriate physical units (Sutton 2008). When one recording unit is used (2D measurement), the calibration sets parameters such as the aspect ratio of sensor, the conversion factor (ratio indicating the number of pixels per a physical unit of length of the captured surface in the given direction – in the case of square sampling of the image it is the same for x and y directions), the location of the center of the lens, and the lens distortion coefficient. In the case of high-quality lenses, the lens distortion coefficient can be neglected. When a recording unit is first used, the calibration is done using calibration grid (Sutton 2008, Sutton et al. 2000). The grid is characterized by a known distance between the lines intersections (nodes) and by three special calibration points (markers), which are usually located in the corners of the grid (Sutton 2008). The special calibration points

are used to determine the coordinate system of the calibration grid, which is put in relation with the global coordinate system of the sensor. The calibration grid must be set plan-parallel relative to the sensor and at the same time, it should be exactly in the distance where the object surface will be captured. During the calibration, several images are acquired, and, and between image acquiring, the calibration grid must be slightly moved or turned in the plane of the sensor (*xy*). Then the calibration images are used to obtain the calibration parameters using the appropriate algorithms. Sutton et al. (2000) stated that successful calibration can be achieved using a calibration plate with random high-contrast pattern instead of the plate with a grid. Sutton (2008) as well as Sutton et al. (2000) agree that when the same recording unit is repeatedly used, it is possible to use some of the calibration parameters from the previous measurement and only re-calibrate the conversion factor in the given direction. A new conversion factor can be easily obtained using a single image of the captured surface with the included standard distance (e.g. a ruler). The standard is attached directly to the captured object surface in the position that coincides with the global coordinate system of the sensor. When processing, two markers are placed on the image, the distance between them being known in physical length units determined by the standard. The direct pixel distance between the markers is determined by edge filters and the conversion factor is calculated.

Sutton et al. (2000) noted that several calibration parameters of the recording unit are added in the 3D version of the DIC method; for example, the mutual position of the recording units, the perpendicular distance of the sensor from the surface captured, etc. Calibration of stereoscopic system is carried out in two steps using the triangulation principles (Mandát 2012). At the first step, which is similar to the calibration procedure using calibration grid within the 2D DIC, external calibration parameters of recording units are obtained. The calibration grid is again moved and turned, with the difference that it is required to move and turn the grid in the *z* direction as well. The images are acquired synchronously by both of the two recording units. At the second step, when each recording unit is calibrated separately, internal calibration parameters of the recording units are obtained. If two same recording units are used to take the images, the internal calibration parameters can be transferred from one to the other. Calibration procedures developed in the framework of commercially available software for DIC slightly differ. Some of them even allow setting of all the internal and external

calibration parameters in one step only, when the images of calibration grid are acquired by both recording units synchronously.

2.2.4 DATA ACQUISITION (PRE-PROCESSING)

2.2.4.1 PREPARATION OF CAPTURED SURFACES

The surface needs to be prepared if it is not sufficiently contrasting and pixels cannot be matched with sufficiently high probability of finding the right match. It applies that the larger are the differences in the brightness levels of the individual pixels in the subset, i.e. the more contrasting surface, the more clearly the pixels can be matched (Pan et al. 2009). Luo et al. (1993) stated that a contrasting pattern ("Speckle Pattern") additionally applied to the surface of the object must have randomly distributed brightness intensity without any repetition; otherwise it has no effect. The pattern on a naturally contrasting surface moves in accordance with the surface of the loaded object, therefore, it is referred to as the carrier of the information about the displacement. This function is to be transferred to the artificially applied high-contrast speckle pattern. Since the first use of the DIC method in the experimental mechanics, several ways for application of the high-contrast speckle pattern have been developed, see Tab. 2.2.4-1.

Tab. 2.2.4-1: Methods for application of random high-contrast speckle pattern according to Sutton (2008)

MATERIAL AND APPLICATION METHOD	APPROXIMATE SPECKLE SIZE
Paint sprayed by gun or spray (B&W)	50 μm
Unfiltered Xerox toner dry coating	30 – 50 μm
Filtered Xerox toner wet coating	15 μm
Color sprinkled from the brush	0.25 – 5 mm
Vinyl with high-contrast speckle pattern, temporarily attached	0.25 – 5 mm
Indelible marker manually	0.25 – 5 mm
Chemical etching of the metal surface	1 – 200 μm
Photolithography on metal surface	1 – 20 μm
Chalk and pepper	0.5 – 1 mm

2.2.4.2 IMAGE ACQUISITION

The data characterizing the load (force, moisture, temperature) as well as data characterizing the deformation (images) are variable in time. For the description of stress-strain, hygro-expansion or thermo-expansion behaviour, the data of loading and deformations must be coupled. To this end, time is used as the only common variable for both types of experimental data. For the correct determination of stress-strain characteristics, synchronous recording of the load and deformations is required. The acquisition interval depends on the loading rate and the magnitude of the total deformation until the ultimate strength of the material (Luo et al. 1993, Helm et al. 1996). In the cases of impact or vibration loading, a regular interval cannot be set for the data recording. It is necessary to record the data at the right time (e.g. at amplitudes of material vibration) using a trigger and busbar of signals, which synchronizes the incoming impulses from the vibration exciter and the outgoing impulses transmitted to the recording units and the loading device.

2.2.5 IMAGE DATA EVALUATION (POST-PROCESSING)

2.2.5.1 CORRELATION ALGORITHMS FOR FULL-PIXEL DISPLACEMENTS (SUBSET PAIRING)

When matching the pixels, the correlation algorithm processes the image of the undeformed and deformed surface gradually, i.e. point by point, which may, particularly for images with high resolution, prove to be a disadvantage as this is highly time-consuming (Pan et al. 2009). Hild and Roux (2006) described their own method for matching pixels: first, in the undeformed image an area is defined where the displacement and strain is to be determined ("Area of Interest" – AOI). Subsequently, a random pixel is selected to be matched and its brightness level is recorded together with the level of brightness of all pixels in the subset. Often the weight of subset positions adjacent to the matched pixel is strengthened using filters, e.g. Gaussian filter (Tong 2005). In the following step, the correlation algorithm records brightness levels of all pixels at the same position but in the image of the deformed object surface. The brightness levels with coordinates of the individual pixels from both images are the variables that are used in the correlation function (criteria) to calculate the correlation score. According to Giachetti (2000), the most often used correlation function for the DIC is the multiplication type of summations, e.g. the sum of multiplied brightness

levels of the subset in the image of the undeformed and deformed surface ("Cross Correlation Criterion"). However, Tong (2005) stated that also the differential type of summations can be used, e.g. the sum of the squares of differences of brightness levels of the subset in the image of the undeformed and deformed surface ("Sum of Squared Differences Correlation Criterion"). The correlation score has to be calculated for all pixels in the image of the deformed surface located in the AOI. It is necessary to find the matching pixel in the resulting map of correlation score within the individual pixels of the image of the deformed surface. In the case of multiplication summation, the absolute maximum is searched; vice versa, in the case of differential summation, the absolute minimum of the correlation score is wanted. After the absolute extreme is found, the correlation score calculation is repeated for all the pixels in the image of the deformed surface located in the AOI, with the difference that brightness levels of another subset in the image of the undeformed surface are used. Since, such procedure for all pixels in the image of the undeformed surface would unduly prolong the computing time and the noise could be amplified in the resulting field of displacements and strains, the correlation scores are calculated for each pixel in the image of the deformed surface located in AOI, but not for each pixel located in AOI in the image of the undeformed surface (Tong 2005). The subset moves in AOI in the image of the undeformed surface with a step that should not be greater than half-size of the subset. To reduce the number of correlation calculations in the image of the deformed surface, the DIC software has an implemented algorithm which uses the position of the matched pixel determined during the previous level of loading as the initial estimation of the position of the matched pixel during the following loading level. Known coordinates of matched pixels are used to calculate displacement in pixels in the image of the deformed surface and it is converted to physical length units using the calibration parameters (Zhang et al. 2006). The result is a discrete field of displacement in selected pixels in the AOI, which is extended to standard full-field information (for all pixels in the AOI) using shape functions and various interpolation schemes. The whole process is carried out gradually for all the images of the deformed surface of the object.

2.2.5.2 SHAPE FUNCTIONS

Shape functions are used to estimate the position of the other pixels located between the matched pixels in the image of deformed surface, and thus to obtain the full-field

data of the displacements and strains (Schreier and Sutton 2002). The shape function of zero order works with the identical position of pixels within a subset or it establishes the same direct displacement or the same angle of rotation around the central pixel for all subset pixels. The result is a simple displacement or rotation of the subset, which corresponds to the term "Rigid Body Motion" in material mechanics. However, this type of deformation hardly ever occurs separately. In the vast majority of cases, a more complex deformation of the object surface occurs and it causes not only the displacement but also rotation or distortion and rippling of subset edges. The shape function of first order operates with gradients of pixel displacements in direct directions within a subset. The result is a distorted subset. The shape function of second order operates with gradients of displacements of subset pixels in curves. A subset that was originally square in an image of undeformed surface can correspond to a distorted subset with rippling edges (Lu and Cary 2000).

The practical use of shape functions to estimate the position of unmatched pixels is based on the principle of triangulation. The position of the unmatched pixels is always estimated in triangular area demarked by three matched pixels. However, full-field data cannot be used directly because there may be considerable differences in the displacement of the pixels between adjacent triangular regions. In order to smooth the transitions between the areas with different displacement values, the average value of the displacement within the triangular area is counted and assigned to the central pixel within the triangle. This procedure is repeated several times until the density of the network of discrete points is so great that the displacement values of the remaining pixels can be interpolated (Sutton et al. 2000).

2.2.5.3 INTERPOLATION SCHEMES FOR BRITHGNESS LEVELS AND DISPLACEMENT

A digital image is a set of discrete values of brightness levels (Gonzalez et al. 2004). When loading an object, we cannot assume regarding the basic principles of solid mechanics that the resulting displacement of the contrasting points on the real object surface captured will exactly match the full-pixel distance in the image. If a real point with the maximum brightness level on the captured surface is driven by the load to make a displacement, which in the image corresponds to a half-pixel distance towards the adjacent point with the minimum level of brightness, the brightness level of the originally bright pixel will be reduced to 50 % and the brightness level of the originally

minimum bright pixel will increase to 50 % as well. As a result, there will be two neighbouring pixels with the same (average) brightness value. If only a few isolated points made the sub-pixel displacement, the subset correlation technique would be able to match them. However, in a real situation sub-pixel displacement of almost all points of the captured area can be expected and a few isolated points will perform a full-pixel displacement. The transformed brightness levels of the vast majority of pixels cannot be matched with the corresponding pixels in the undeformed surface image using the correlation algorithm. According to Sutton et al. (2000), the solution is to insert mid-levels of brightness between adjacent pixels by interpolation of adjacent intensities. The interpolation provides the smoothing of the transitions between the brightness levels of adjacent pixels, and the resulting image thus approaches the continuous distribution of brightness on the real surface. For this purpose several interpolation schemes are used, from simple ones, such as the bilinear bicubic interpolation, up to time consuming and computation demanding ones, like the bicubic or biquintic interpolation using the "Spline" function (Schreier et al. 2000, Knaus et al. 2003). Similar interpolation techniques are also used to obtain full-field data of displacement and strain from the discrete network of points concentrated using shape functions. A graphical interpretation of the different interpolation schemes is provided in e.g. Sutton et al. (2000). Mathematical relationships for the use of these interpolation schemes can be found in e.g. Press (2003). However, it is not possible to work further with the almost continuous image within correlation algorithms. The image has to be re-sampled into the discrete distribution of brightness levels but with a higher number of samples and lower differences in the level of brightness between adjacent pixels compared to the original image. According to Sutton (2008), it is additionally recommendable to increase the number of quantizing levels to 10 – 12 bits. The result is an image with artificially increased resolution with almost a gradient distribution of brightness levels. The task of calculating the sub-pixel displacement is through the interpolation converted to the task of calculating full-pixel displacement.

2.2.5.4 REGISTRATION ALGORITHMS FOR SUB-PIXEL DISPLACEMENTS

These are optimization (numerical) methods that are used in the context of DIC for precise localization of the correlation score extreme within the AOI in the image of the deformed surface. The most used version is the Newton-Raphson method (Bruck et al.

1989), which was significantly improved by Vendroux and Knauss (1998). A very popular algorithm used by many scientists for the calculations associated with DIC is "Iterative Spatial Domain Cross-Correlation Algorithm". Peters and Ranson (1982) and Yang et al. (2006) state that also "Coarse-fine Search Algorithm" can be used. Further, according to Chen et al. (1993) and Sjödahl and Benckert (1993), the "Peak-finding Algorithm" is applicable. "Spatial-gradient-based Algorithm" was developed by Davis and Dennis (1998), the improvement was made by Zhang and Jin (2003). "Genetic Algorithm" was used for example by Hwang et al. (2008) and "Finite Element Method" and "B-spline Algorithm" were developed by Besnard et al. (2006).

2.2.6 ASPECTS OF MEASUREMENT ACCURACY

2.2.6.1 EXPERIMENTAL SET-UP

When capturing the image with one recording unit, the plane of the sensor must be oriented plan-parallel to the captured surface of the object and the sensor distance from the captured surface must be constant. This condition is not met if the sensor unit is placed incorrectly, the deformation of the object surface is not planar, the surface is not worked to be planar, or if there are imperfections of the loading system. If the condition of parallel position is not met, some parts of the captured surface can get beyond the DOF of the lens. A similar effect will appear if the parallax is greater than 30° during the stereoscopic imaging. A change in the distance between the sensor and the captured surface within 2D measurement is mistakenly interpreted as displacement and strain of the surface in the *x* and *y* direction. Meng et al. (2006) stated that when the parallelism of the sensor and captured surface is wrong by up to 5°, the results manifest a maximum error of 0.01 pixels. Helm and Deanner (2004) numerically proved that calibration by the calibration grid can almost remove the experimental measurement errors caused by violation of parallelism between the sensor and the captured surface in the range of up to 30°. The magnitude of the experimental error of this type decreases with increasing DOF. The extension of DOF is possible using the telecentric lens or by extending the distance (Sutton et al. 2000).

2.2.6.2 TECHNICAL PARAMETERS OF MEASUREMENT APPARATUS

It is known that cheaper optical lenses suffers from a spheric defect that distorts the image taken into the barrel or cushion shape. Schreier et al. (2004) stated that to determine and reduce the effect of lens defect on the image distortion, it is necessary to reconstruct the deformation function of the display system. For this, they proposed to use a flat plate with a contrast speckle pattern for the calibration of the display system. The same procedure was also used for high-speed sensor units. A little different way of calibration was published by Zhang et al. (2006). The coefficients for the deformation function were obtained by comparing the positions of the nodes in the real calibration grid with the positions of the calibration nodes in the images. Yoneyama et al. (2006) proposed two methods for the determination of the radial and tangential distortion caused by the use of zoom when taking an image. One of them is based on measuring multiple types of planar displacement of contrast speckle patterns; the other on the analysis of the calibration grid distortion by a technique using Fourier transformation. Also technologies have been developed to minimize the image distortion when taking them using microscopic techniques.

Additionally, the accuracy of the calculated displacement and strain is largely affected by the image resolution, resp. the conversion factor. The image resolution depends on the number of photosensitive cells of the sensor. With an increasing resolution, the results get more accurate, but only to a point where the disadvantage of an unfavorable noise/useful signal ratio captured by the photosensitive cell starts to outweigh the advantage of high resolution. An important factor is also the focal length of the lens, which determines the DOF, or the sensitivity of the image sharpness to relative movements of the object or the recording unit perpendicular to the plane of the sensor (direction z) during capturing. The element of recording units significantly affecting the measurement accuracy is also the A/D converter, which, besides bringing an error while amplifying the analog signal, determines the bit depth of the image (number of brightness levels).

2.2.6.3 EXPOSURE CONDITIONS

The light intensity of the captured surface is a key exposure parameter. The light intensity has to be within a particular range. Weak or strong light reduces the contrast between the individual points of the captured surface and subsequently between the

pixels in the image, which prevents the successful matching of individual pixels between the images. The reflections of light from the captured surface or shiny areas around the surface can produce "over-exposed spots", which can significantly affect the correlation, even if they do not occur directly on the captured surface (Wang et al. 2007). In order to prevent the over-exposed spots in the image, it is recommended to apply matte high-contrast speckle pattern to the reflective surface of the object captured and an overlay matte layer (e.g. paper tape) to the other reflective surfaces in the surroundings. Due to unfavorable exposure conditions, noise gets into the images. The term noise is used for all changes to the pixel brightness level caused by another source than the electromagnetic radiation in the visible spectrum reflected from the captured surface. The sources of the noise are most often high temperature, strong electromagnetic background (e.g. MW, UV), non-constant light intensity (flashing of light sources powered by alternating current), damaged photosensitive cells of the sensor, dirt on the sensor, etc.). Besides the exposure conditions, the noise can be caused by the movement of the sensor or the captured surface beyond the effect of the investigated loading. This unwanted auxiliary movement can be induced by vibrations of the loading device during loading, vibrations of the acquisition set transmitted from the floor, or strong audio signals. Gonzales et al. (2004) recommended reducing the noise in the image using a light source powered with direct current, vibration and sound insulation of the laboratory, maintaining the ambient temperature at 20° C or use of cooled sensors.

2.2.6.4 PATTERN QUALITY

To evaluate the quality of the high-contrast speckle pattern, various parameters have been proposed, such as the average pattern size (Lecompte et al. 2006), subset entropy (randomness) (Yaofeng and Pang 2007), and according to Pan et al. (2008) the "Sum of Square of Subset Intensity Gradients". An ideal contrast speckle pattern, according to Sutton (2008), should have a flat brightness histogram, in other words, all the brightness levels should be represented in the same proportion. In practice, according to the same author, the maximum shot width is achieved between the 50^{th} and 220^{th} brightness level out of the total range 0 – 255 at 8-bit color depth of image. The ideal average size of the pattern corresponds to the width of the peak at the value of autocorrelation of 0.5 (Sutton 2008). However, the size of the captured surface, or the distance of the

recording units to the captured surface, the size of displacement and the subset are significant.

2.2.6.5 SUBSET SIZE

Usually, the DIC users have to choose the size of the subset using their own experience with the particular acquisition set. It ranges from a few pixels to over 100 pixels. With the increasing size of the subset the certainty of matching the right pixels in an image of undeformed and deformed surface grows but the reliability of the shape functions and interpolation schemes for the identification of the position of the other subset pixels decreases. The experience of a wide scientific community suggests that a compromise that will be closer to smaller sizes of subsets is necessary. Pan et al. (2008) derived the theoretical model for the estimation of the displacement measurement accuracy by DIC and described a new parameter - the "Sum of Square of Subset Intensity Gradients" - to determine the optimum size of a subset. The same parameter is also associated with the evaluation of the quality of the high-contrast speckle pattern.

2.2.6.6 CORRELATION CRITERION, SHAPE FUNCTION AND INTERPOLATE SCHEME

Tong (2005) assessed the suitability of various correlation functions (criteria) to calculate the correlation score. Zero-mean Normalized Sum of Squared Differences (ZNSSD) and Zero-mean Normalized Cross-Correlation (ZNCC) appeared as the most stable and the most reliable for images with variable light intensity. The mathematical derivation also indicates that the correlation criteria are resistant to displacement and linear change of light.

The shape function, when it is used for a small subset, easily and accurately approximates the position of subset pixels. Systematic errors with regard to the order of the shape functions were examined by Schreier and Sutton (2002). Theoretical and experimental results published by Lu and Cary (2000) and Pan et al. (2008) showed that the shape functions of the second order bring a lower systematic error than the shape functions of the first order at approximately the same levels of random error. After comparison of various interpolation schemes, Schreier et al. (2000) recommended the use of bicubic or biquintic interpolation using the "Spline" function of higher order,

despite the increased computational complexity. Image interpolation can lead, according to Sutton (2008), to accuracy of up to ± 0.02 pixels.

2.2.7 OTHER IMAGE-BASED METHODS

2.2.7.1 INTERFEROMETRY

This technique began to be used in experimental mechanics to determine surface full-field displacement of rigid objects in plane (2D) and beyond the plane (3D). Superposition of two grids, each of which consists of regularly arranged light and dark strips, forms Moiré contours (Post and Han 2008). The name Moiré comes from the French labelling of fabrics from dipped silk and mohair, which are characterized by light and dark strips (Walker 1994). Using parameters of Moiré contours, the mutual displacement of the two overlapping grids can be reconstructed retrospectively. One of the grids, which is referred to as a reference (static), is placed immediately in front of the sample (Han and Post 2008). This is typically a transparent plastic plate with a stripped texture. The other grid (measuring) is placed on the surface of the sample and moves according to its deformation during the load by the external force. There are several ways of the grid application to the surface. For the analysis of planar deformations in the *x* and *y* directions, the stripped texture is printed over the surface of the specimen or sprayed through a template (Post et al. 2000). Han (2005) presented the method for the mapping of the object surface movement in the *z* direction in which the stripped pattern was only projected onto the surface as a shadow of the reference grid ("Shadow moiré") or it is generated directly in the light source ("Projection moiré"). In the case of transparent samples, the partial reflection of laser beams from their surfaces is used to create the stripped structure. Each beam that hits the surface of the specimen at an angle lower than 90°, i.e. is not perpendicular to the surface, is due to the different angle of reflection from the obverse and reverse surfaces divided into two weaker reflected beams and one stronger beam that passes through. The distance between the two reflected beams indicates the thickness of the specimen. After the specimen is loaded with external forces, its thickness and along with that the density of stripping of the reflected beams change. The superposition image is obtained from the reflected beams before loading and after loading. Superposition of the two grids is captured using a camcorder or a camera with a time-lapse function. The images captured are processed in software (Post et al. 2000).

Superposition images resulting from the displacement of the measuring grid against the reference in one direction (e.g., the *x* direction) again manifest the stripped texture in the accordant direction with the stripping of the original grids. If only a rotation of the measuring grid occurs, the result is the superposition with rhomboids or even squares (Han and Post 2008). However, in real-world conditions the movement of the measuring grid to the reference is usually combined (several directions at the same time, or with rotation included). Subsequently, the superposition image is characterized by non-linear stripping, i.e. contour lines (Takasaki 1970). The displacement of the specimen under load is reconstructed using the geometry laws. Mathematical combinations of parameters are used such as the defined distance of the strips (grid stripping frequency), the degree of gridding in the superposition, the angles of the reflections and the impacts of light beams when projecting the pattern onto the sample surface, etc. (Han and Post 2008). A more detailed description of the ways of displacement calculation has been published by Han and Post (2008), Post et al. (2000), Han (2005). More information about advanced concepts of interferometric measurements of surface displacement of solids can be found in e.g. Han (1993), Han and Han (2006), Huntley (1998), Post et al. (1994) and Testorf et al. (1996). Minster et al. (2006) demonstrated the application of Moiré interferometry in wood science for the prediction of mechanical properties of timber structures.

2.2.7.2 PHOTOELASTICITY

This optical method has undergone an extensive development from conventional to digital photoelasticity. The phenomenon of the temporary birefringence, on which it is based, was discovered by Brewster (1816). Thanks to the work of Coker and Filon (1930) in the UK, the method has gained popularity. A big boom was related with the beginnings of the production of epoxy resin (Ramesh 2008). A number of versions for various applications have been developed. "Dynamic Photoelasticity" was introduced for the study of dynamic properties of solid materials. This modified method was used in e.g. Rossamanith and Shukla (1981). Pih and Knight (1969) modified the photoelasticity for orthotropic stress analysis of composites ("Photo-orthotropic Elasticity"). Burger (1980) stated that the displacement and strain of solids above the proportional limit can be analysed using "Photoplasticity". Ramesh et al. (2011) mentioned that with the development of digital data processing, digital photoelasticity

started to be more intensively used. Full-field results are presented in the form of contour maps of the displacement, strain, stress, or a combination of these variables directly on the object surface, or using computer graphics. Each contour encloses the area in which the output variable achieves values in a specific interval. The type of the output variable is determined by the physical principle on which the experimental method is based. The possibility to obtain directly the distribution maps of stress on the object surface under the load is the biggest advantage of photoelasticity (Ramesh 2008).

The principle of this method lies in the variability of the optical properties of some transparent amorphous polymers at different stress conditions. When the polymer is not loaded, it manifests isotropic optical properties, i.e., it does not affect the direction of light vectors passing through its structure. Under the load, the internal structure of the polymer temporarily changes so that it is able to split the light beam into two perpendicular directions (Ramesh 2008). In addition, the resulting beams are turned in the axis of propagation of the original beam (2D), or even in the axis perpendicular to the axis of propagation (3D). The changed orientation of the light beams corresponds to the direction of the loading. Non-homogeneous stress distribution in the polymer under the load has a consequence similar to Moiré interferometry - formation of a non-linear stripped optical structure (contour lines). After the load is removed from the polymer, its original isotropic optical properties return.

In the experimental set-up of the measuring device, the amorphous polymer is used in the form of spray or coating on the surface of the sample ("Reflection Photoelasticity"). The surface of the object should reflect the incident light beams passing through the polymeric film and be clingy, so that stress induction in the polymer may occur due to the object deformation. Under these conditions, the polymeric film is able to provide information about stress-strain behaviour of the loaded object (Zandman et al. 1962). Polarized light with a defined orientation of light vectors is used as the light source for easy determination of the loading direction (Trebuna 1990). Modified polarized light beams reflect from the surface of the specimen and are analyzed by an optical device. If the specimen is made directly from the amorphous polymer with the mentioned optical properties, it can itself perform the role of optically active interface (Ramesh 2008). In this case, it is necessary to catch the passing beams from the reverse side of the measured surface (behind the specimen). Application of photoelasticity in combination with conventional extensometers and numerical procedures for aluminum, composite and wood was published by Rowlands (2008).

2.2.7.3 HOLOGRAPHY

At present, the invention of holography is attributed to Prof. D. Gabor of the University of London Imperial College of Science and Technology, who won the Nobel Prize in 1971 for this discovery (Gabor 1948). In reality, he discovered and formulated work by G. Lippmann from the late 19th century focusing on the object color encoding on a thick emulsion photographic plate (Lippmann, 1891). This original work was followed by Y. Denisyuk's reflective holography (Denisyuk, 1962). At this time, when many years have passed since the foundations of holography, there is no generally available method for a reliable quantitative interpretation of holograms (Pryputniewicz 2008). However, a series of methods and systems for specific applications have been developed (Vest and Pryputniewicz 2007). Experimental mechanics uses holographic interferometry in particular (Pryputniewicz 2008). It is an extension of classical interferometry from mirror or optically polished surfaces of specimens on diffuse reflective non-planar surfaces of samples. Holographic interferometry was discovered in 1965 (Stetson and Powell 1965), and it was soon advanced (Brooks et al. 1965). The basic concept of holography in the experimental mechanics is well described in Cloud (2008). According to Pryputniewicz and Stetson (1990), the progress in the technology of lasers, computer technology, optical fibers, etc., which was implemented in holography, led to a technology known as optoelectronic holography. The results are fully compatible with the "computer aided design" (CAD), "computer aided engineering" (CAE) and "computer aided machining" (CAM) formats, which allows a full use of these measurements directly in the design of any industrial components.

The experimental measuring itself consists of the holographic record, its reconstruction, and quantitative interpretation of holographic interferograms. The optical set for the holographic record of the specimen consists of a light source (laser), optical filters, and photosensitive recording surface (Pryputniewicz 2008). In classic photography, only beams from the light source and those reflected from the object surface hit the photosensitive surface. The result is always a 2D image, which can be perceived by the human eye as 3D. For a physically three-dimensional image of an object, it is necessary that not only beams reflected from the light source (object beams), but also the reference beams which pass outside the captured object fall on the photosensitive area (Pryputniewicz 1995). For this reason, the laser beam is divided into two immediately after it is generated. Both types of beams overlap on the photosensitive

area and create a superposition interferogram. The record is unintelligible to the human eye, it does not show the true image of the object and any similarity is coincidental. Conversion of a 2D interferogram to a 3D hologram is performed using the original optical set. The condition is to remove the object and shield the object beams. Only the reference beams fall on the recorded interferogram and they are difracted into wave surfaces, which form the 3D hologram after reflection. The recording medium allows the reconstruction of the hologram at a different place or at a later time. The properties of holographic images are described by Pryputniewicz (2008). The development of quantitative interpretation of holograms shows that the best results are provided by the transformation matrices that allow holographic parameters to be transformed into material parameters of samples (Schumann et al. 1985). The solution of the resulting matrix equations can be obtained through established computing practices (Pryputniewicz 1992). Pryputniewicz et al. (2000) stated that the holographic interferometry is used in experimental mechanics particularly in the area of development and production of micro-electromechanical systems, e.g. high-speed micro-electric motors. Holography was used in the wood processing industry e.g. as a control tool for the production process of veneer-based boards (Sfarra et al. 2013).

2.2.7.4 THERMOELASTIC STRESS ANALYSIS

This full-field optical method is based on the thermoelastic effect of solids. This phenomenon was first mentioned by Weber (1830). It is similar to the consequence of gas state equation, according to which gas temperature increases with its decreasing volume. Similarly, during loading and subsequent deformation of solids, their internal energy, or temperature, changes (Greene et al. 2008). The thermoelastic effect was first described theoretically in 1853 by William Thomson, later known as Lord Kelvin (Thomson 1853). Compton and Webster (1915) confirmed the theory experimentally. In the 1950s, Biot used irreversible thermodynamics for the extension of the theory to anisotropic, viscoelastic and plastic material response to load (Biot 1954, Biot 1955, Biot 1956). The first contactless measurement of full-field temperature changes using the infrared radiometer was performed by Belgen (1967).

Thermoelasticity is practically usable only for the dynamic loading with cyclic course (0.5 Hz to 20 kHz), because only these conditions of sample loading can induce photon emission sufficiently intense for precise measurement (Greene et al. 2008). The

samples need not be prepared in any way, with the exception of metal ones, which are coated in black paint in order to increase and homogenize the surface emissivity (MacKenzie 1989). The main element in the thermo-acquisition set is the infrared thermodetector able to measure very small changes in temperature (photon emission) associated with the thermoelastic effect of solids. The sensors have been commercially manufactured under the name SPATE (Stress Pattern Analysis) since 1982. Currently, photodetectors are used which convert photons radiated by the sample in the infrared spectrum to stress and strain maps on the areas of the sample (Greene et al. 2008). Processing of an infrared image is performed similarly to the processing of a light image using digital cameras. More advanced technologies of thermoelasticity include random vibration excitation of samples presented by Harwood and Cummings (1986). Maldague (2001) considers the infrared background created by the surrounding objects to be the main aspect that affects the accuracy of the thermoelasticity. The influence of the infrared background is particularly evident when the measuring is performed directly in an industrial environment. There are many applications of this optical method, e.g. mechanical analysis of anisotropic materials (Lin and Rowlands 1995), fracture mechanics (Ju and Rowlands 2007), analysis of residual stresses in the material (Quinn et al. 2004). Possible use of thermoelasticity in wood processing was presented by Wolfe et al. (1994).

2.2.7.5 PHOTOACOUSTIC

In photoacoustic measurement of mechanical properties, the samples are loaded mechanically by ultrasonic waves (Krishnaswamy 2008). Ultrasonic waves as mechanical waves cause a periodic dynamic load as they propagate through the specimen. It means dynamic parameters of mechanical behaviour of samples are gained through photoacoustic measurement. Ultrasonic waves are generated by lasers. The impulse for photoacoustics development came in the early 1960s, when White (1963) demonstrated the generation of ultrasonic waves by a laser. Comprehensive overviews of generating ultrasonic waves by a laser are provided by Hutchins (1988) or Scrubs and Drain (1990). Formerly laboratory research tool has become a measuring technology for monitoring of stress and strain in industrial processes in the past 20 years.

Pulse laser is used for the excitation of ultrasonic waves, and the absorbed part of the laser beam energy turns to thermal energy. The result is a rapid local temperature

increase. The tested material immediately responds by increasing the dimensions, i.e., generating an ultrasonic wave (Krishnaswamy 2008). If the optical performance of the laser does not cause melting or vaporization of the sample, the ultrasound is generated in the thermoelastic mode. If a higher optical performance of the laser is needed to generate the ultrasonic wave, which would cause damage to the tested material, protective coating is used. The damage then takes effect only on this cover layer (Krishnaswamy 2008). According to Wagner (1990), optical contactless detection of mechanical response of the specimen to ultrasonic pulses is particularly performed using interferometry and the reference beam ("Reference-Beam Interferometry") or dynamic holographic interferometry. In both methods, first the ultrasonic response is converted to optical parameters and then the optical parameters are decoded to mechanical parameters of the tested material (Mouchalin 1986). The transformation of the motion of an object loaded by ultrasound to optical parameters is done through the interaction with light beams (Dewhurst and Shan 1999). Intensity, frequency and phase of the sample vibration can be converted to optical parameters. There are several ways to do this, e.g. Antonelli et al. (2002) or Adler et al. (1968). For example, the intensity of vibration can be converted into the optical form based on the different angle of the light beam reflection from a diverted surface of the vibrating sample in comparison with angle of beam reflection for the unloaded sample. If the reference beam reflected from the unloaded sample is confined in a precise slit before the impact on the photosensitive area, any large beam deflection causes a decrease in the light intensity on the photosensitive surface (Adler et al. 1968). More information on photoacoustic methods is to be found in e.g. Gusev and Karabutov (1993). Photoacoustic methods have been used many times for the description of anisotropic mechanical behaviour of materials, e.g. Maznev et al. (1999), Hurley et al. (2001), Every and Sachse (1990). Measurement of dynamic viscoelastic properties of wood under heat stress using photoacoustic methods was presented by Kojiro et al. (2008).

2.3 WOOD AND DIGITAL IMAGE CORRELATION

2.3.1 GENERAL APPLICATIONS

An independence of scale (from micrometers to tens of meters), tested material (wood, metal, ceramics, polymers, natural tissues, fruits) and relatively low initial costs (considering the free codes) are the prerequisities for the wide-spread utilization of DIC

in experimental mechanics. Some of its application possibilities are summarized in Fig. **2.3.1-1**. There is a few loading types as mechanical forces acting in compression, tension, bending, shear or torsion mode, futher, moisture and temperature changes, which are capable to induce the dimension changes and shape deformations of wood. The studies dealing with deformation analysis of the variously loaded wood and wood-based composites by means of DIC are roughly introduced in Tab. 2.3.2-1-Tab. 2.3.7-1.

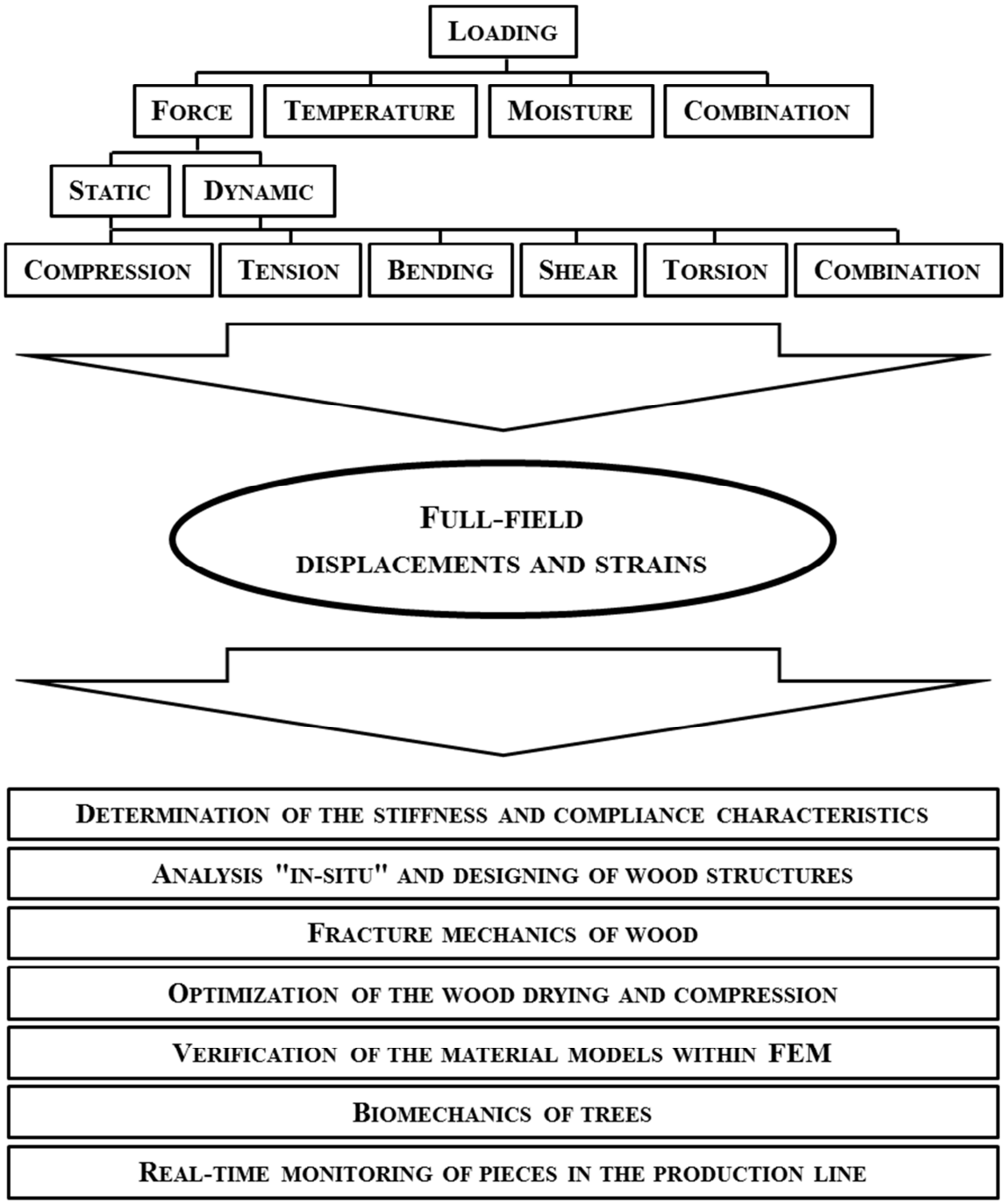

Fig. 2.3.1-1: A summary of the loading types and some of application possibilities of the full-field displacements and strains data sets in the wood research

2.3.2 COMPRESSION LOADING

Tab. 2.3.2-1: A brief list of the studies dealing with the compression loading of wood coupled with DIC

AUTHOR	UTILIZATION OF THE FULL-FIELD DEFORMATION DATA
Zink et al. (1995)	A validation of a new proposed correlation algorithm when the wood is loaded by a compression parallel to the grain. A new algorithm was used for analysis of local deformations in the oriented strand boards (OSB).
Murata et al. (1999)	A determination of a deformation distribution on the micro-scale level within the radial-tangential principal plane of wood loaded perpendicularly to the grain in the radial direction.
Murata and Masuda (2003)	A description of a relationship between the deformation distribution within the annual rings and the anatomic structure, particularly, the earlywood and latewood structure, when the wood is loaded perpendicularly to the grain.
Murata and Nakao (2007)	A comparison of deformation fields induced by transversal loading in softwood and alternately laminated veener lumber on the micro-scale.
Shipsha and Berglund (2007)	A description of the shear coupling effect within the polar orthotropy structure during the transversal loading of wood.
Garab et al. (2010)	An assessment of the orthotropy within the RT plane of wood by means of the off-axis grain angle, which gives the lowest Young's modulus.
Murata and Tanahashi (2010)	A determination of the Young's moduli, shear moduli and Poisson's ratios in the LR plane of wood and their comparison with those determined based on the deformations measured by the extensometers.
Sebera and Muszyński (2011)	A verification of the morphology-based finite-element model of the oriented strand boards (OSB) based on the local deformation behaviour, described also by the synchrotron radiation CT data in more detail.
Xavier et al. (2012)	A quantification of the variability of longitudinal Young's modulus for different lengths and cross-sections of sample and friction coefficients applied onto contact surfaces within the finite-element analysis.
Hering et al. (2012)	A determination of the longitudinal elastic engineering parameters of beech wood as function of a moisture content by using of the dog-bone shaped samples for the application in the finite-element modelling.
Majano-Majano et al. (2012)	A determination of all nine elastic components characterizing the elastic orthotropic behaviour of wood at single test of a double off-axis sample.
Ozyhar et al. (2013)	A description of variability of the visco-elastic (compliance) behaviour of wood during the long-term compression and tension loading.
Zauner and Niemz (2014)	A quantification of the size effect on the ultimate strength and deformation behaviour of the spruce wood in longitudinal direction.
Güntekin et al. (2016)	An investigation of moisture content effect on the orthotropic elastic engineering parameters of beech wood loaded in all principal directions.

2.3.3 TENSION LOADING

Tab. 2.3.3-1: A brief list of the studies dealing with the tension loading of wood coupled with DIC

AUTHOR	UTILIZATION OF THE FULL-FIELD DEFORMATION DATA
Mott et al. (1996)	A determination of the deformation distribution on the surface of a single wood fibres loaded by using of a micro-tensile apparatus while the image data were obtained with help of scanning electron microscope.
Serrano and Enquist (2005)	A determination of deformation distribution in a bond-line in order to predict mechanical properties of glues for various sample dimensions.
Muszyński et al. (2006)	A quantification of the mechano-sorptive effect by a substracting of the deformations, which occurred under constant moisture conditions, together with the moisture-induced deformations from the total deformations caused by the cyclic-changing moisture conditions.
Miyauchi and Murata (2007)	An analysis of the abrupt increase of the deformations at the location where the failure occurs in order to mathematically describe the non-linear part of the stress-strain curve.
Ukyo et al. (2008)	A revealing of the shear strain concentrations within the two standard type of the traditional japan joints, which was supplemented by the finite-element analysis of the shear stress concentrations.
Keunecke et al. (2008, 2012)	A verification of the literally reported low longitudinal Young's moduli of yew wood in relation to its higher density for the different fibre orientations in respect to the loading direction.
Niemz et al. (2009)	An evaluation of the applicability of DIC for the determination of the Young's moduli and for the cracks prediction within the wood and wood-based composites in comparison with acoustic emission method.
Oscarsson et al. (2012)	A revealing of the hidden defects, which cannot be detected by standard visual control or by a scanning method and to analyze the deformation distribution aroung the knots appearing on the various sample surfaces.
Ozyhar et al. (2012)	A quantification of the variability of the strength and stiffness orthotropy of beech wood depending on the moisture content.
Pereira et al. (2014)	A capturing of the variation of the elastic engineering parameters, which characterize the elastic behaviour of pine wood within the RT plane, among the various annual rings, positions in the stem and various trees.
Ritschel et al. (2014)	An analysis of the damage evolution within the plywood materials made from spruce wood and, for comparison, solid spruce wood, a damage evolution was simultaneously monitored by the acoustic emission.
Schwarzkopf and Muszyński (2015)	An analysis of the deformation behaviour across the adhesive bond interfaces in heterogeneous solids described by the empirical methodology, which was developed in a parallel study.
Jeong and Park (2016)	A determination of the orthotropic elastic engineering parameters such as Young's moduli, shear moduli and Poisson's ratios of four different wood species while the off-axis tension samples were used.

2.3.4 FRACTURE MECHANICS

Tab. 2.3.4-1: A brief list of the studies dealing with the fracture mechanics of wood coupled with DIC

AUTHOR	UTILIZATION OF THE FULL-FIELD DEFORMATION DATA
Wang et al. (2002)	An identification of the local plastic zone around the crack tip and calculation of the fracture characteristics of birch wood.
Samarasinghe and Kularisi (2004)	A verification of the fracture characteristics calculated based on the linear elastic fracture theory for the various experimental parameters.
Vasic and Ceccotti (2009)	An investigation of the loading rate effect on the parameters of the local plastic zone aroung the crack tip and to analyze the resistance curves, which characterize the resistance of wood to the crack propagation.
Bigorgne et al. (2011)	A verification of the finite-element model based on the real morphology of wood on the mesoscopic scale, which is capable to predict the crack behaviour on the RT plane of wood in fracture mode I.
Nagai et al. (2011)	An identification of the direction of the crack propagation direction near the knots and analysis of a time-ahead of the non-linear deformations before the crack propagation starts.
Méité et al. (2013)	An evaluation of the applicability of the DIC technique together with finite-element modelling for the determination of a rate of energy release in the orthotropic wood loaded in the fracture mix-mode.
Silva et al. (2014)	A determination of the crack tip shear displacement for the comparison of two equivalent (direct and indirect) methods describing the cohesive laws of wood bonded joints loaded in the fracture mode II.
Xavier et al. (2014)	An establishment of direct method for the identification of the cohesive law in fracture mode II for pine using of crack tip opening displacement.
Xavier et al. (2015)	An establishment of the direct method for the identification of the cohesive law in fracture mode I for pine wood.
Tukiainen and Hughes (2016)	A quantification of the effect of the microstructure and the moisture content (MC) on the local plastic deformations around the crack tip and the crack propagation at the cellular level.

2.3.5 BENDING LOADING

Tab. 2.3.5-1: A brief list of the studies dealing with the bending loading of wood coupled with DIC

AUTHOR	UTILIZATION OF THE FULL-FIELD DEFORMATION DATA
Nagai et al. (2007, 2009)	A reconstruction of the deflection curve and finding of local maximums as a tool for the detection of the internal knots and other hidden structure defects, and finally, the full-field deformation data were used also for the verification of the finite-element model of this new method.
Betts et al. (2010)	An assessment of the influence of the material imperfections on the neutral axis position.
Haldar et al. (2011)	An obtaining of the parameters on the different scales of the hierarchical structure of palm wood for the designing of the polymeric composites.
Davis et al. (2012)	A determination of the size effect and influence of the defects on the neutral axis position.
Haldar and Bruck (2013)	An assignment of deformation behaviour of palm wood loaded by impact bending to its structure for utilization of natural structure of palm wood for hierarchically structured composites with polymeric matrix
Ozarska et al. (2013)	A quantification of the plasticity by means of the neutral axis position.

2.3.6 MOISTURE LOADING

Tab. 2.3.6-1: A brief list of the studies dealing with the moisture loading of wood coupled with DIC

AUTHOR	UTILIZATION OF THE FULL-FIELD DEFORMATION DATA
Murata et al. (2001)	An investigation of the importance of earlywood and latewood within the annual ring as well as longitudinal and transverse orientation of the anatomic elements in the swelling anisotropy of various wood species.
Murata and Masuda (2006)	An assessment of the effect of the surrounding structure of macro vessels during the short-term absorption from the heated water vapor and during the long-term absorption from the saturated solutions.
Larsen et al. (2010)	An assessment of the efficiency of the protection tools against the drying cracks creation and propagation on the RT plane of wood.
Kang et al. (2011a, 2013)	An identification of the time stage in the course of the wood drying when the stress reversal occurs and the localization of this phenomenon on the RT plane of wood.
Kang et al. (2011b)	A quantification of the moisture gradient variability within the RT plane of wood during the drying depending on the drying temperature.
Watanabe et al. (2012)	A determination of the moisture distribution through the wood volume based on the synchrotron radiation CT data.

Keunecke et al. (2012)	A description of the structure-functional relationships for the hygro-expansion within the RT plane of spruce wood in more detail with help of the synchrotron radiation CT data.
Peng et al. (2012, 2013)	A determination of the swelling and shrinkage coefficients for all principal directions of wood as the input data for the other calculations.
Derome et al. (2013)	A modelling of the moisture influence on the mechanical properties of wood within the coupled hygro-mechnical approach to numerical modelling, which collect the high resolution data obtained by DIC, neutron imaging and synchrotron radiation CT techniques.
Lanvermann et al. (2014a)	A study of the perpendicular-to-grain moisture-induced deformations on a growth ring level.
Lanvermann et al. (2014b)	A detection of the local moisture-induced deformations, which were matched to the spatial distribution of water by using of the neutron imaging, subsequently the local gravimetric moisture content and volumetric moisture content were calculated.

2.3.7 COMBINED LOADING

Tab. 2.3.7-1: A brief list of the studies dealing with the combined loading of wood coupled with DIC

AUTHOR	UTILIZATION OF THE FULL-FIELD DEFORMATION DATA
Ukyo and Masuda (2006)	A contribution to the true shear strength characterization.
Vessby et al. (2008)	An analysis of the local deformations of the cover wood-based panels of wooden houses walls around connectors when biaxial loading is applied.
Ukyo et al. (2010)	A finding of the correlation between the shear strength and shear moduli of glue laminated timber determined at single test employing the new shape of the samples.
Clauß et al. (2014)	A characterization of the elastic behaviour of ash wood loaded in tension, compression and shear in the three anatomical directions.
van Beerschoten et al. (2014)	A determination of the Poisson's ratios for the laminated veneer lumber (LVL) when the compression and shear loading was applied
Bachtiar et al. (2016)	A verification of the moisture content effect on the elastic engineering parameters such as Young's moduli, shear moduli and Poisson's ratios of walnut and cherry wood, which were determined with help of the non-destructive ultrasound technique. The destructive testing consisted of the tension, compression and shear loading in all principal directions.
Knorz et al. (2016)	A description of deformation behaviour of the structural wood-adhesive bonds subjected to the mechanical load and moisture content changes.
Ozyhar et al. (2016)	A characterization of the orthotropic hygro-expansion and elastic behaviour of oak wood and quantification of the moisture content effect on the elastic engineering parameters.

3. MATERIALS AND METHODS

3.1 MATERIAL

3.1.1 RAW MATERIAL

A pith wood of European beech (*Fagus sylvatica* L.) (Paper I, II, III, IV), Norway spruce (*Picea abies* L. Karst.) (Paper I, II, IV) grown at the stands in the Czech Republic (Paper I, II, IV), resp. in the Slovakia (Paper III) was collected. The boards were dried in the open air for several weeks from the wet state to wood moisture content (MC) of about 15 %. Two thirds from the pre-dried raw material used in Paper II were separately thermally modified in a laboratory chamber (KATRES s.r.o., Jihlava, Czech Republic) using an atmospheric pressure at a superheated steam environment. A maximum temperature of 180 °C and 200 °C, respectively, was maintained for 3 h. The degree of modification was determined by a mass loss, based on the oven-dry mass before and after the thermal modification process. All boards were finally conditioned in the climate chamber SANYO MTH 2400 (Sanyo Electric Co., Ltd., Osaka-J) or climate room at 20 °C and 65 % relative humidity (RH) until the equilibrium moisture content (EMC) was reached (EMC ~ 12 %). The density and EMC were controlled gravimetrically in compliance with test standard ASTM D2395 (American Society for Testing and Materials 2014).

3.1.2 SAMPLES PREPARATION

The samples were cut from the outer part of board (mature wood) as clear special orthotropic blocks. The dimensions of the samples were derived from the appropriate standards, which are valid for each test method and material such as BS 373 (British Standard Institution 1957) and ASTM D143 (American Society for Testing and Materials 2014) for compression and tension test of small clear samples (Paper I, IV), BS 373 (British Standard Institution 1957) for three-point bending test of small clear samples (Paper II) and ASTM D198 (American Society for Testing and Materials 2014) for torsion test for solid wood samples (Paper III). The sample dimensions for edgewise compression test of new composite (Paper V) followed ASTM C364 (American Society for Testing and Materials 2012), meanwhile for flatwise compression test of new composite ASTM C365 (American Society for Testing and Materials 2011) is valid

(Paper V). Three-point bending samples of new composite (Paper V) followed ASTM C393 (American Society for Testing and Materials 2006) and flatwise tensile samples of new composite (Paper V) followed ASTM C297 (American Society for Testing and Materials 2009). In order to improve the image matching during DIC computation, a stochastic and high-contrast speckle pattern created by a basic matt white paint followed by a finely pigmented black paint was sprayed on the samples' surfaces to be captured. An average speckle size was derived based on the measuring distance, from which the sample surface was captured.

3.2 TESTING OF SAMPLES

3.2.1 LOADING

The compression test parallel to the grain (Paper I – Fig. 3.2.1-1), the tension parallel to grain (Paper IV – Fig. 3.2.1-4), three-point bending test in the tangential direction (Paper II – Fig. 3.2.1-2) as well as all tests of new composite were carried out by the universal testing machine Zwick Z050/TH 3A (Zwick Roell AG, Ulm-DE) with the 50 kN load cell. The experiment procedures were set and controlled by TestXpert v. 11.02 (Zwick Roell AG, Ulm-DE). The samples were accommodated in the testing jaws under a preload of 10 N. The torsion test (Paper III – Fig. 3.2.1-3) was carried out with help of the torsion test machine KM-50-1 (Minpribor, Russia) equipped with one static and one rotary jaw. All samples were loaded until the failure at a quasi-static loading rate loading rate. The failure was defined by a significant drop in the loading force along with the visible sign of the failure.

Fig. 3.2.1-1: The experimental setup for the compression test parallel to the grain (Paper I)

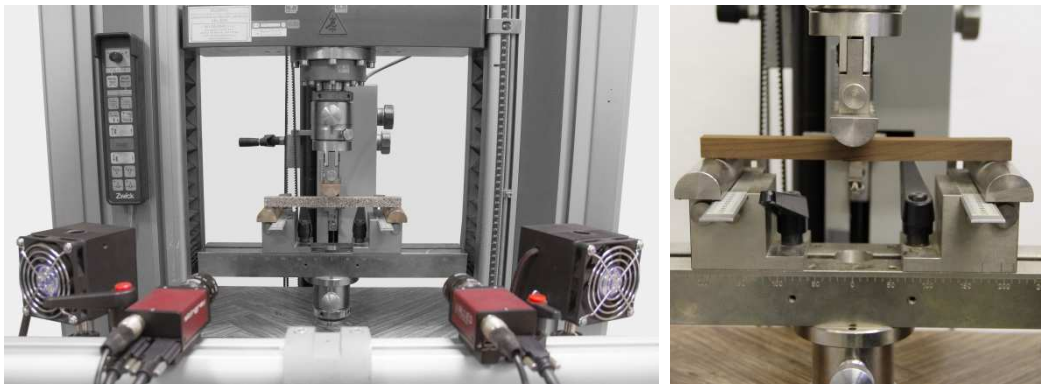

Fig. 3.2.1-2: The experimental setup for the three-point bending test in tangential direction (Paper II)

Fig. 3.2.1-3: The experimental setup for the torsion test around longitudinal axis (Paper III)

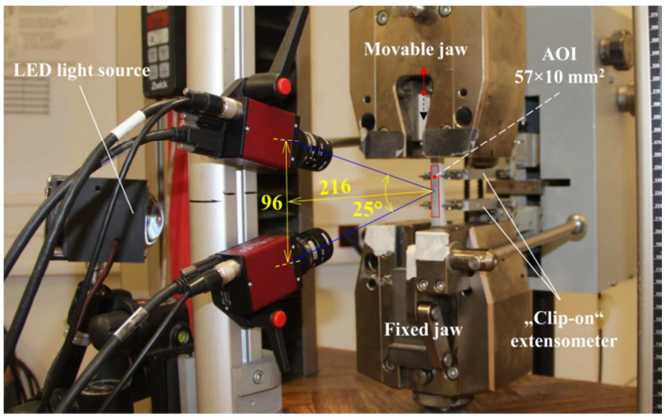

Fig. 3.2.1-4: The experimental setup for the uniaxial tension test of notched "dog-bone" shaped samples (Paper V)

3.2.2 DEFORMATION MEASUREMENT

The deformations were measured by using of the conventional displacement sensors such as an internal crosshead sensor (Paper I), a "clip on" extensometer (Paper I, IV, V), a "clip on" deflectometer (Paper II, V), a linear variable differential transformer (Paper III) and by a full-field optique method based on the digital image correlation (Paper I, II, III, IV, V). The optical stereovision system Vic-3D (Tab. 3.2.2-1) was used for the analysis of a deformation field induced in the compression samples (Paper I, V), in the tension samples (Paper IV) as well as in the bending samples (Paper II, V), meanwhile, for the deformation field induced within the torsion samples (Paper III) the optical stereovision system ARAMIS® 3D 12 M (Tab. 3.2.2-1) was employed. The measurement procedure comprising the systems calibration, setup of the appropriate capture position, data acquisition and image data post-processing (calculations of displacement and strains) was accomplished according to the systems manuals. The loading force together with the displacements from the conventional sensors and optical system was recorded at an acquisition rate appropriately to applied quasi-static loading rate. The average accuracy of the optical systems for setups was estimated based the displacement and strains calculated from images while no loading force was applied.

Tab. 3.2.2-1: The technical parameters of the used optical systems

PARAMETER	Vic-3D	ARAMIS® 3D 12 M
Producer	Correlated Solutions Inc. Columbia-SC, USA	GOM, GmbH Braunschweig, Germany
User	Mendel University in Brno Czech Republic	Technical university in Zvolen
Number of cameras (pcs)	2	2
Sensor type	CCD	CCD
Image resolution (px)	2456 × 2056	4096 × 3072
Bith depth per pixel (bit)	8	8
Focal length (mm)	25	100
Number of light sources (pcs)	2	2
Light source	LED chip	LED diode
Power of light source (W)	90	24
Illumination	Cold white	Cold white
Polarizing filtr	No	Yes

4. RESULTS AND DISCUSSIONS

4.1 LIST OF PAPERS

The results and discussions addressed in this work are divided into the papers I-V, where indice **A** referred to original paper, meanwhile the indice **B** to conference paper:

PAPER IA Brabec M., Tippner J., Sebera V., Milch J., Rademacher P. (2015) Standard and non-standard deformation behaviour of European beech and Norway spruce during compression. *Holzforschung* 69(9): 1107-1116

PAPER IB Brabec M., Tippner J., Sebera V., Milch J., Rademacher P. (2015) Identification of the "non-standard" deformation behaviour of European beech and Norway spruce during the compression loading. *Proceedings of the 58th SWST International Convention*, Grand Teton National Park, Wyoming, USA, 290-299

PAPER IIA Brabec M., Čermák P., Milch J., Sebera V., Tippner J. (2016) Neutral axis location in thermally modified wood during three-point bending by means of digital image correlation. *European Journal of Wood and Wood Products*: Submitted manuscript

PAPER IIB Brabec M., Čermák P., Milch J., Sebera V., Tippner J. (2015) Analysis of deformation distribution and neutral axis location in thermally modified wood by means of digital image correlation. *Proceedings of the InWood2015: Innovations in Wood Materials and Processes*, Brno, Czech Republic, 68-69

PAPER III Brabec M., Lagaňa R., Milch J., Sebera V., Tippner J. (2016) Utilization of digital image correlation in determining of both longitudinal shear moduli of wood at single torsion test. *Wood Science and Technology* (in press) DOI: 10.1007/s00226-016-0848-7

PAPER IV Milch J., Brabec M., Sebera V., Tippner J. (2016) The verification of the elastic material characteristics of Norway spruce and European beech in the field of shear behavior. *Holzforschung*: Submitted manuscript

PAPER V Klímek P. Wimmer R., Brabec M., Sebera V. (2016) Novel sandwich panel with interlocking plywood kagome lattice core and grooved particleboard facings. *BioResources* 11(1): 195-208

4.2 PAPER I

STANDARD AND NON-STANDARD DEFORMATION BEHAVIOUR OF EUROPEAN BEECH AND NORWAY SPRUCE DURING COMPRESSION

Martin Brabec[1,*], Jan Tippner[1], Václav Sebera[1], Jaromír Milch[1], Peter Rademacher[1]

Holzforschung (2015) 69-9: 1107–1116

[1] Department of Wood Science, Faculty of Forestry and Wood Technology, Mendel University in Brno, Zemědělská 3, 613 00 Brno, Czech Republic; phone: +420 545 134 545

*corresponding author: martin.brabec@mendelu.cz

ABSTRACT

The goal of the study is to investigate the "non-standard" deformation behaviour of wood loaded by compression parallel to the grain. This is represented as a negative increment of strain in range of plastic deformations when the load continues to increase. The objectives of this study are to point out this problem and to provide its description based on the deformation fields that have been analysed using three approaches: a) full-field optical technique based on digital image correlation (DIC); b) "clip on" extensometer and its virtual analogy, and c) crosshead displacement method. Further, the negative strain phenomenon was studied depending on the sample length. The samples were made from the European beech (*Fagus sylvatica* L.) and Norway spruce (*Picea abies* L. Karst.). Based on the strain analysis, it can be concluded that the deformation field consists of three sub-regions exhibiting different stiffness values (three-spring model). The failure of less stiff zones near the compression plates during the "non-standard" compression behaviour causes almost zero compression deformation of the stiffer middle zone or even leads to its expansion. The three-zone heterogeneity of deformation field induces a deviation of the displacement and strain measured by the proposed approaches. This phenomenon substantially influences the resulting longitudinal Young's modulus and, therefore, should be of concern when measuring wood in such a mode.

KEYWORDS: Compression test; Damage zone; Digital Image Correlation; Strain; Wood

4.2.1 INTRODUCTION

Stress-strain behaviour of wood is especially important if it is used for structural purposes. Wood anisotropy is often reduced to orthotropy, which makes the determination of reliable wood elastic constants easier, especially by using special orthotropic samples (Bodig and Jayne 1993). However, such samples do not exhibit the homogeneous deformation fields when loaded uniaxially because of wood's heterogeneity and problems of the representative volume element (RVE) determined by sample dimensions (Bodig and Goodmann 1973). There are three approaches for measuring the deformations induced in a material. First, the conventional (contact) methods that allow obtaining point-wise (1D) strain data; second, the visible radiation (optical) methods that provide full-field strain data in an area (2D); and finally, the invisible radiation methods that enable to obtain the volumetric (3D) strain data. The contact methods are local, so they cannot reflect the wood heterogeneity. To reveal this problem, the digital image correlation (DIC) is usually applied (Peters and Ranson 1982; Sutton et al. 2000). The digital volume correlation (DVC) technique seems to be the most suitable method among all those introduced. It provides all six components of strain tensor at each voxel of a sample (Forsberg et al. 2008, 2010).

Scientific papers dealing with the compression of wood perpendicular to grain are often focused on the relationship between the strain distribution in an annual ring on the cross section and the anatomical structure (earlywood and latewood). Reiterer and Stanzl-Tschegg (2001) investigated the wood elastic constants and failure modes during the compression at different loading orientations between the longitudinal (*L*) and the radial (*R*) direction (fibre angles of 0°, 20°, 45°, 70°, and 90°) using videoextensometers. A previous study demonstrated that the dependency of the Young's modulus (*E*) on the loading orientation can be accurately calculated and predicted well based on the simple theory of orthotropic elasticity. More recently, the grain angle dependency of the elastic parameters in the *R-T* plane was again verified (Garab et al. 2010), while the data varied greatly in different wood species. Reiterer and Stanzl-Tschegg (2001) found the concentration of the shear strain near the annual ring boundary at loading angles of 20° and 45° on the *L-R* plane. The same concentration on the *R-T* plane was found by Murata and Masuda (2003). The concentration of the shear strain at these locations leads to the initiation of the cracks at

the samples' edges (Murata and Nakao 2007). Moreover, the deformation field on the cross section may consist of both compression and tension strains (Murata et al. 1999). If the cross section contains the pith region (polar orthotropic material), the shear coupling effects decrease the transverse stiffness and increase the strain field heterogeneity (Shipsha and Berglund 2007). The wood elastic parameters vary depending on the increment of the growth ring number (Xavier et al. 2009; Jeong et al. 2010; Pereira et al. 2014). The variability of the transverse stiffness parameters is reflected differently on varying scales. The heterogeneity is at its maximum at the scale of the cell morphology (Simon et al. 2010).

The heterogeneity of the strains during compression parallel to the grain was also reported (Choi et al. 1991; Dahl and Malo 2009). The largest strains are allocated near the compression plates (Zink et al. 1995), which create a zone often called "damage zone". The zone between them is called "middle zone". Xavier et al. (2012) investigated the influence of the damage zones on the apparent *E*, which they obtained from the displacement of the movable compression plate. The authors proposed the analytical model of sample as a series of three springs, in which two less stiff ones represent the damage zones and the stiff one is for the middle zone. The damage zones decrease the apparent *E*, meanwhile the friction that arises between the sample and the compression plates has a contrary effect. However, the damage zones have a much higher effect than the friction. Both phenomena become more crucial as the sample length decreases. Meanwhile, Bertolini et al. (2012) reported that the sample length in a range of 150–250 mm does not influence the Young's modulus significantly when extensometers are used for measurements. An increase of the sample cross section near the compression plates causes lower strain magnitudes in the damage zones which results in higher apparent *E*. In this context, a dog-bone shape sample was investigated by André et al. (2013). The friction effects induce also the "barrel" deformation mode of the sample (Xavier et al. 2012). The "barrel", "buckling" or "shear" deformation modes complicate the determination of a passive strain needed for calculation the Poisson's ratios. The conditions for the maximal "homogeneous" deformation mode were proposed by Benabou (2008, 2010).

The motivation of this study is the "non-standard" deformation behaviour of the wood when compressed parallel to the grain, which is called "non-standard" compression behaviour. This is represented as a negative increment of strain in the loading direction (ε_L), i.e. decrease of ε_L as the load increases. This behaviour is

observable in a range of plastic deformations of Norway spruce measured by extensometers. In case of European beech, this behaviour was seldom observed.

The underlying hypotheses of the present work is that in an analytical model proposed by Xavier et al. (2012) the middle stiffer spring in a series of three springs can expand due to the failure of the two springs representing the less stiff damage zones of a sample. Therefore, the objectives of this study are to elaborate this problem and to provide data for its description. The amount of the samples behaving in the "non-standard" way should also be determined when sample length variations are investigated together with the elastic modulus (E).

4.2.2 MATERIAL AND METHODS

Wood of European beech (*Fagus sylvatica* L.) and Norway spruce (*Picea abies* L. Karst.) grown at the stands close to Brno (Czech Republic) was collected. The boards were dried in the open air for several weeks from the wet state to a moisture content (MC) of ca. 15 %. The boards were finally conditioned in the climate chamber SANYO MTH 2400 (Sanyo Electric Co., Ltd., Osaka-J) at 20 °C and 65 % relative humidity (RH) until the equilibrium moisture content (EMC) was reached (EMC ~ 12 %). The samples were cut from the outer part of board (mature wood) as clear special orthotropic blocks with a cross section radial (R) × tangential (T) = 20 × 20 mm^2 and different lengths (h = 30, 40, 50 and 60 mm). The sample dimensions were derived from the BS 373 (British Standard Institution 1957) and ASTM D143 (American Society for Testing and Materials 1994). Ten samples were prepared for each h and wood species, so a total 80 samples were tested. One sample side was covered with stochastic and high-contrast speckle pattern needed for the DIC computation. Half of samples in the series (five samples) were patterned on the R plane and the other half on the T plane. A basic white thin paint followed by a finely pigmented black paint was sprayed on the surface. The density of the samples varied from 631 to 708 kg m^{-3} (beech) and from 384 to 628 kg m^{-3} (spruce). These density ranges are typical in this region (Gryc et al. 2011; Čermák et al. 2013).

The loading of the samples parallel to the grain was carried out by the universal testing machine Zwick Z050/TH 3A (Zwick Roell AG, Ulm-DE) with the 50 kN load cell. The experiment procedure was set and controlled by TestXpert v. 11.02 (Zwick Roell AG, Ulm-DE). The samples were loaded until the failure with a loading rate of

2 mm min^{-1} and the proportional limit was reached between 30 and 90 s. The sample was accommodated between the compression plates under a preload of 10 N.

A deformation was measured by three methods: a) full-field optical technique based on DIC; b) "clip on" extensometer and its virtual analogy (videoextensometer), and c) crosshead method. For method a) we used two CCD cameras (AVT Stingray Copper F-504B, Allien Vision Technologies, Osnabrück-DE, cell size of 3.45 µm and resolution of 2452 × 2056 pixels) equipped with the lenses (Pentax C2514-M, Pentax Precision Co., Ltd., Tokyo-J, focal length of 25 mm) at the stereovision configuration (3D) were used (Fig. **4.2.2-1**–left). The patterned sample surface was illuminated by two light sources SobrietyCube 360 (Sobriety s.r.o., Kuřim-CZ) fitted by LED sensors (Luminus Phlatlight CSM-360, 90 W, Luminus Devices Inc., Billerica-MA USA). The stereovision system was centred to the centroid of area of interest (AOI). Prior to the optical measurement, the system was calibrated by 60 pairs of calibration images of a grid with 5.5 mm spacing at various geometric orientations. The resulting scale was 0.08 mm $pixel^{-1}$ for all samples. For method b) we used the "clip on" extensometers (Zwick Roell AG, Ulm-DE) equipped with two pairs of contact sensor arms separated by 10 mm. They were always clamped at the centre of the sample length (Fig. **4.2.2-1**–right). For method c) we used the crosshead displacement was measured by an internal sensor.

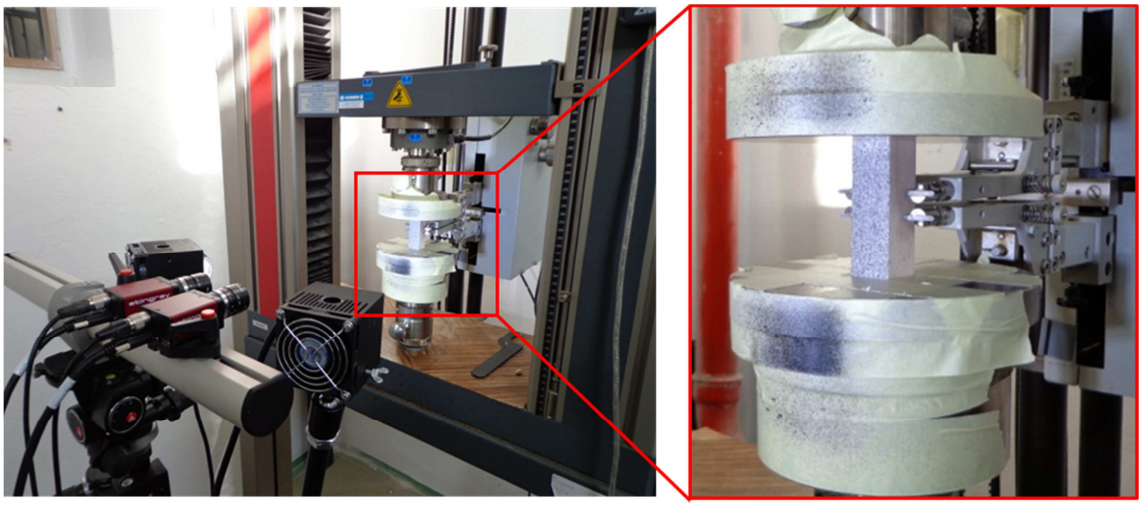

Fig. 4.2.2-1: Experimental set-up: *left* – the optical stereovision system, *right* – the "clip on" extensometers

To verify of the employed measuring methods, it is necessary to measure displacement at the same point on the sample surface. Unfortunately, this prerequisite

cannot be fulfilled. Therefore, the verification test without the sample was carried out by the "clip on" deflection extensometer (Zwick Roell AG, Ulm-DE) used for bending tests. A wooden block (20 × 20 × 20 mm^3) with high-contrast pattern was mounted to the sensor arm tip. The sensor arm was clamped to the movable compression plate. The wooden block was captured during the crosshead movement. The resulting average displacement computed by DIC was correlated with that one measured by the extensometer and the crosshead.

The images were captured in the same acquisition interval (0.25 s = 4 Hz) as well as the displacement from extensometers and crosshead. The force and deformation recording was synchronised by a hardware trigger device. The calculation of the strain from the images was performed by software Vic-3D v. 2010 (Correlated Solutions Inc., Columbia-SC USA). A subset size of 25 × 25 pixels and subset step of 5 pixels were chosen based on the pre-study which examined the optimal amount of the computed points (6 points mm^{-2}). The strain was calculated with an accuracy within the range of 52 – 89 micro strain. The strains were calculated as a Langrangian strain: $\varepsilon=dl/l$ where l is the initial length and dl is the deformation of length. The stress induced in the sample by the compression force was calculated as $\sigma=F/(a\cdot b)$ where F is the compression force and a, b are the dimensions of the sample cross section. The local longitudinal Young's modulus (E_L) was calculated based on the differential stress and strain as $E_L=(\sigma_{60\%}-\sigma_{30\%})/(\varepsilon_{L60\%}-\varepsilon_{L30\%})$ where $\sigma_{60\%}$ and $\sigma_{30\%}$ are compression stresses calculated at the 60% and 30% level of maximal force recorded during test (F_{max}), $\varepsilon_{L60\%}$ and $\varepsilon_{L30\%}$ are strains in the loading direction (i.e. parallel to grain) corresponding to the stresses $\sigma_{60\%}$ and $\sigma_{30\%}$.

4.2.3 RESULTS AND DISCUSSION

4.2.3.1 VERIFICATION TEST OF DISPLACEMENT MEASUREMENT

The coefficients of determination (R^2) and the linear regression models (Tab. **4.2.3-1**) indicated a very good agreement among the data of the three techniques. The best agreement was found between the extensometer and the crosshead methods. The deviations found between the displacements obtained from the DIC compared to the extensometer and crosshead were 2 % and 4 %, respectively. Considering the objectives of this study, the observed deviations did not affect measurements significantly.

Tab. 4.2.3-1: Correlation between the displacements measured by different techniques

VERIFICATION TEST	R^2	y = ax + b
Extensometer × Crosshead	0.999	y = 1.01x + 0.01
DIC × Extensometer	0.999	y = 0.98x + 0.08
DIC × Crosshead	0.999	y = 1.04x – 0.06

4.2.3.2 STRAIN FIELD CHARACTERIZATION

A typical deformation field of strain in the loading direction (ε_L) during compression consists of three sub-regions (springs) (Fig. **4.2.3-1**), which can be identified based on the ε_L values and their location. The horizontal ε_L profile compared to the vertical ε_L profile is flat (Fig. **4.2.3-1**) in agreement with data of Zink et al. (1995). Consequently, the deformation sub-regions are clearly distinguishable only across the sample length (h) which is in agreement with the observations made by André et al. (2013), Xavier et al. (2012), Benabou (2008), and Zink et al. (1995). The boundaries between the sub-regions are apparent on the vertical ε_L profile as well as on the computed ε_L map (Fig. **4.2.3-1**).

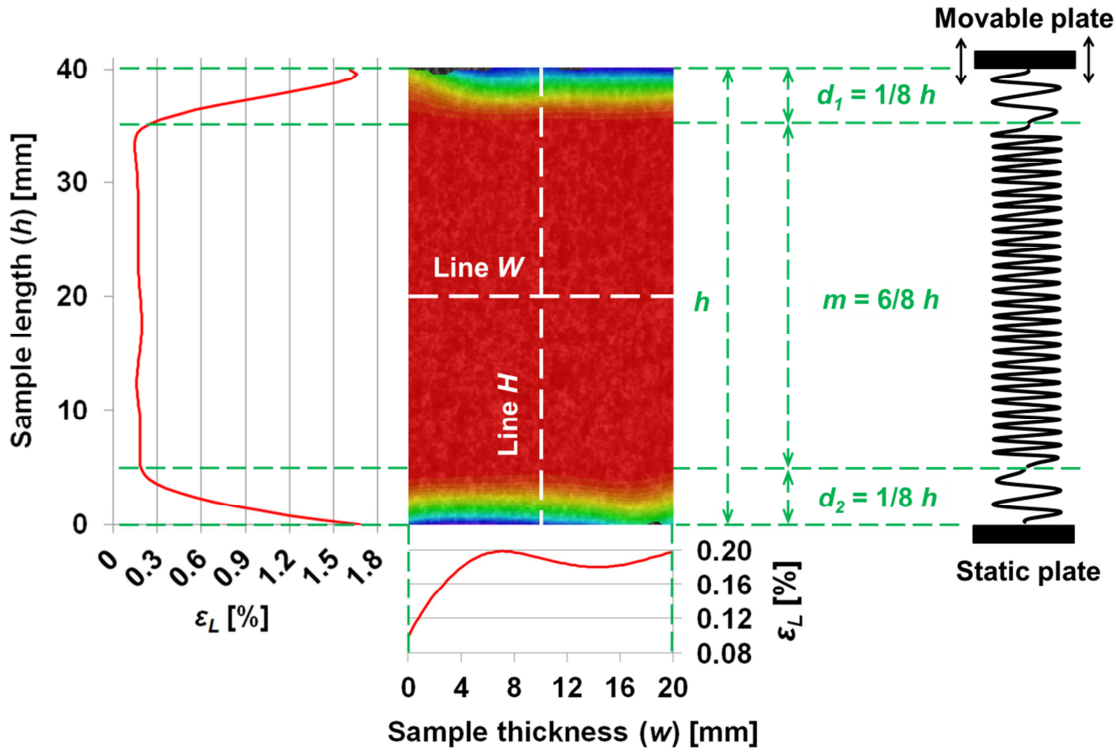

Fig. 4.2.3-1: Typical deformation field of strain in the loading direction (ε_L) and its vertical and horizontal profiles at the $F_{50\%}$ of Norway Spruce (20 × 20 × 40 mm^3) during compression parallel to grain

The sub-regions in contact with compression plates exhibited a high variation of ε_L (0.2 – 1.7 %) and called damage ($d_{1;2}$) zones, according to Xavier et al. (2012). The region between zones d_1 and d_2 (middle (m) zone) exhibited low variation of ε_L (0.1 – 0.2 %). The ε_L in zones $d_{1;2}$ has a gradual distribution along the h. The ε_L value exponentially increased as the distance from the compression plate decreased. The highest ε_L is concentrated on the interface of sample surface and compression plate.

As can be seen at Fig. **4.2.3-2**–up, the "highest-to-lowest" ε_L ratio for spruce increased as h increased; meanwhile, for beech the opposite was true. Zone m of the beech samples with the increasing h became increasingly unstable and subsequently the compression of zones $d_{1;2}$ was stopped by its earlier failure. This phenomenon may be attributed to the shorter anatomical elements and a lower lignin content of beech compared with spruce. The averaged vertical ε_L profiles of spruce samples (Fig. **4.2.3-2**–up) also showed the lower maximum of ε_L within zone d_2 located near the static plate compared to zone d_1 near the movable plate. This phenomenon is apparent only for beech samples of h = 30 and 40 mm. In the case of samples with h = 50 and 60 mm, its development was stopped by the mentioned failure of the unstable zone m.

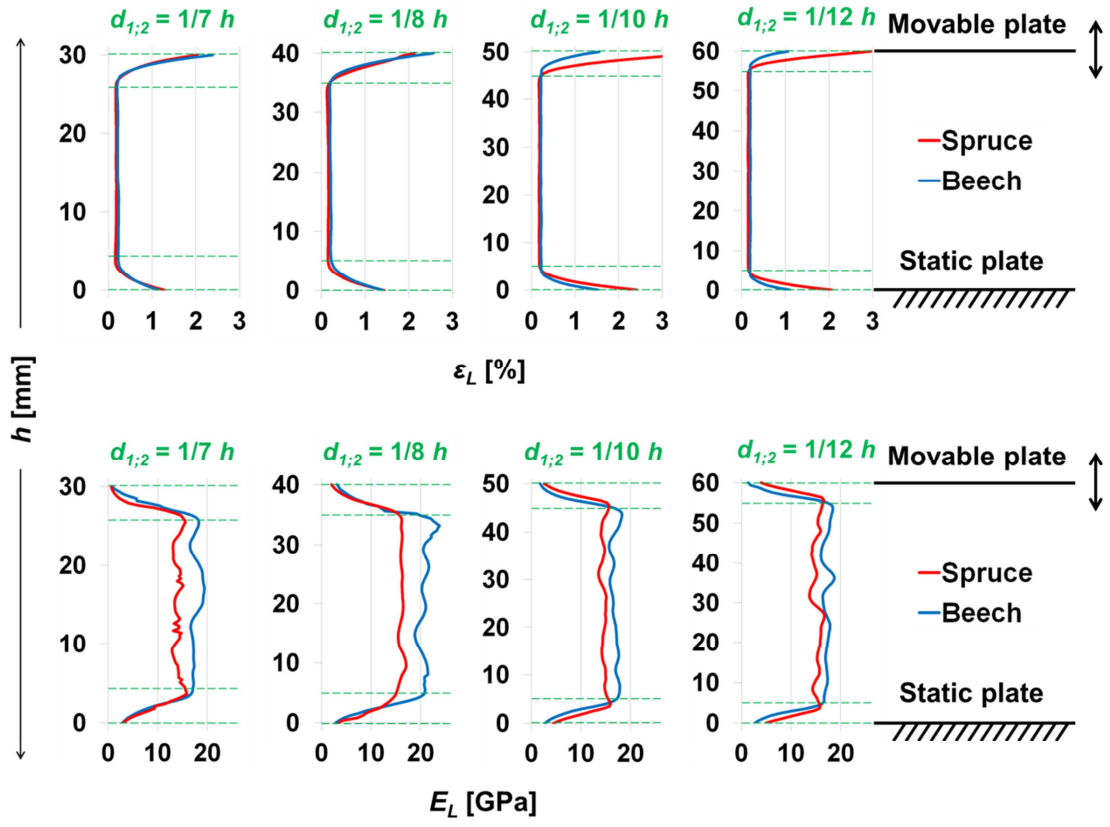

Fig. 4.2.3-2: Influence of the sample length (h) and wood species: *up* – on length of the deformation sub-regions at the $F_{50\%}$, *down* – on the local Young's modules (E_L)

We found that the length of zones $d_{1;2}$ was independent of the h, indicating that only the length of zone m increased as a function of h. The real length of zones $d_{1;2}$ varied by about 5 mm except h = 30 mm, where zones $d_{1;2}$ were about 4 mm. The relative constant length of zones $d_{1;2}$ was reflected in their decreasing proportion of h with an increasing h (Fig. **4.2.3-2**–up and Fig. **4.2.3-2**–down). This finding confirms the decreasing negative influence of zones $d_{1;2}$ on the apparent E_L as h increases, as reported by Xavier et al. (2012). The vertical dimensions of the sub-regions were almost the same for both spruce and beech. The length of zones $d_{1;2}$ and zone m for all samples and species in the course of the elastic part of compression deformation was more or less constant (Fig. 4.2.3-3). In conclusion, the length of zones $d_{1;2}$ was dependent of the surface roughness of contact sample surface and compression plate, etc. The more substantial changes occurred in the range of plastic deformation behaviour of samples. For a few samples, the expansion of zone m was indirectly confirmed by the successive disappearance of one or both zones $d_{1;2}$ from the computed ε_L map (Fig. 4.2.3-3). This corresponds to the stiffening of zones $d_{1;2}$ due to compression.

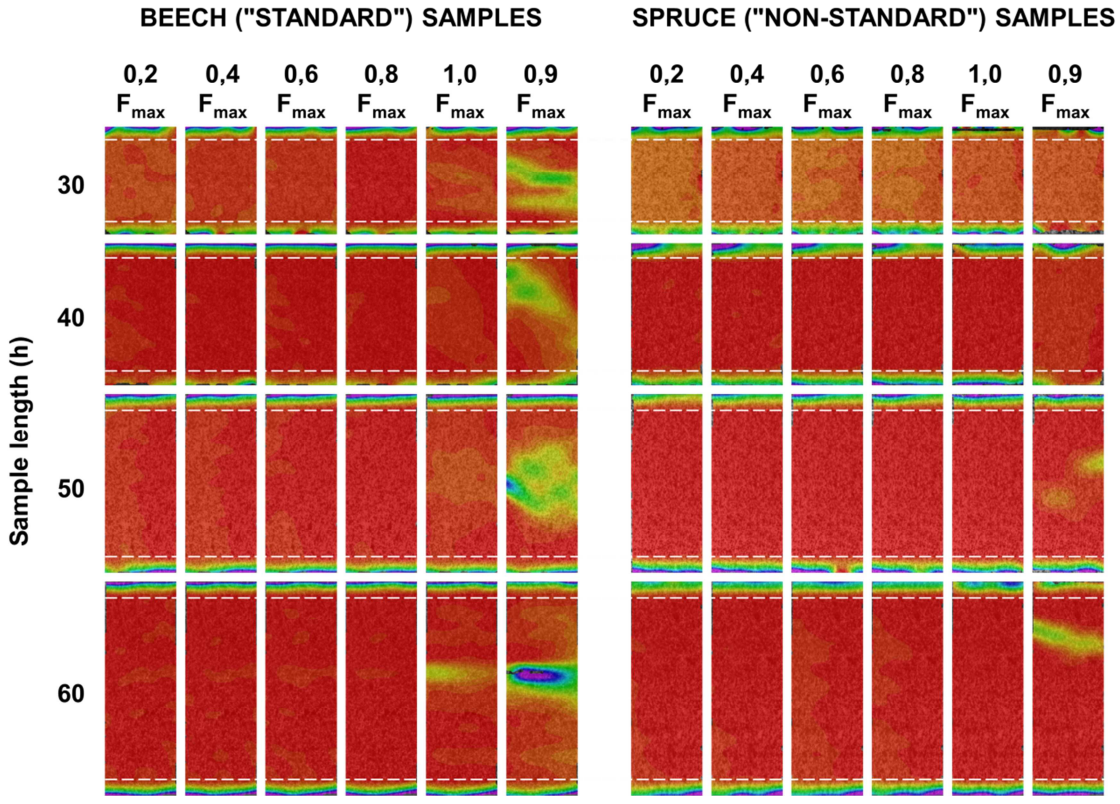

Fig. 4.2.3-3: Deformation sub-regions consisting of strain in the loading direction (ε_L) during "standard" and "non-standard" compression behaviour

The stress-strain curves and vertical E_L profiles presented in Fig. **4.2.3-4** and Fig. **4.2.3-5** are based on the ε_L computed by DIC at points spaced along the h in 1/50 h steps. As can be seen, the accuracy of the curves was reduced by the global compression stress used in the calculation of ε_L. There was a good link between the vertical ε_L and E_L profiles. However, a direct comparison of variability was not possible, mainly because of the differential ε_L ($\varepsilon_{L60\%}$-$\varepsilon_{L30\%}$) used in the calculation of E_L (Fig. **4.2.3-4**) unlike the immediate ε_L ($\varepsilon_{L50\%}$) from which the vertical ε_L profiles were composed (Fig. **4.2.3-1** and Fig. 4.2.3-2–up).

Nevertheless, the variability of the E_L along the white dashed line (Fig. **4.2.3-4**) fairly corresponded to the variability of ε_L along line H (Fig. **4.2.3-1**). A low variation of the E_L across zone m was reflected in the similar slope of the stress-strain curves and in their overlapping (Fig. **4.2.3-4**). Due to the inversely proportional relationship between ε_L and E_L, the E_L was distributed along h in the opposite way to the vertical distribution of the ε_L. Consequently, the lowest E_L was calculated on the interface of the sample surface and the compression plate. As the distance from the compression plate increased, the E_L exponentially increased up to the border of zones $d_{1;2}$. A randomly distributed E_L keeping the low certain limit was observed in zone m (Fig. **4.2.3-4**). Such behaviour may be attributed to the wood heterogeneity. The E_L profile in sub-regions was virtually not influenced by h.

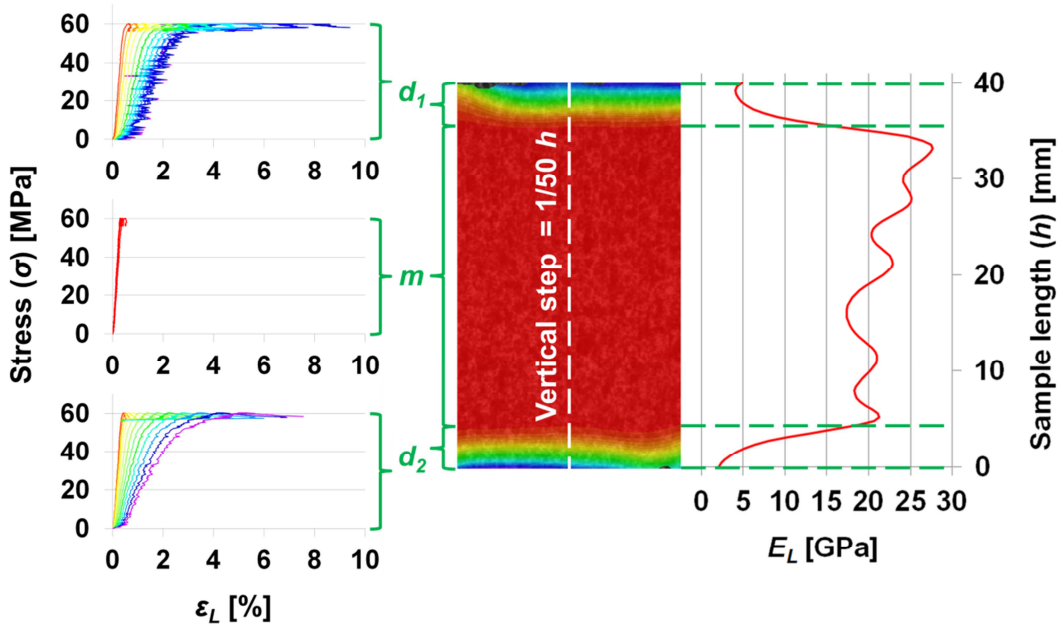

Fig. 4.2.3-4: Development of strain in the loading direction (ε_L) during compression computed by DIC on Norway Spruce samples of 40 mm exhibiting the "non-standard" compression behaviour: *left* – stress-strain curves; *right* – typical Young's modules (E_L) distribution along the sample length (h) at the $F_{50\%}$

In fact, the analytical model of the compression sample should be composed of one middle spring with a constant stiffness along its length and two springs with an exponentially varying stiffness along their lengths. In the analytical approach proposed by Xavier et al. (2012), zones $d_{1;2}$ were modelled in a simplified way as springs with constant stiffness along their lengths, which provides satisfactory results.

In this study, there were differences between E_L within zone *m* of spruce and beech samples which were also observed by Wangaard (1950), Bodig and Goodmann (1973), Kollmann and Côté (1984), Požgaj et al. (1997). Wood density plays the main role in this issue. Due to the ε_L variability along *h*, the three approaches (DIC, extensometers and crosshead) provided different stress-strain curves (correlatively ε_L and E_L) for the same sample (Fig. **4.2.3-5**a and Fig. **4.2.3-5**b). The highest E_L was computed by DIC ("DIC avg-m") in zone *m* and by the extensometers ("E"). Stress-strain curves obtained from zones $d_{1;2}$ based on the ε_L computed by DIC ("DIC avg-d_1, d_2") and crosshead ("C") reveal the lowest E_L. The ε_L averaged over the whole AOI from DIC measurement ("DIC avg") provides the averaged E_L of the sample. As a consequence, E_L calculated from the ε_L measured by the extensometers can be 3-6 times higher when compared to one obtained by the crosshead.

4.2.3.3 DETECTION OF NEGATIVE INCREMENT OF E_L BY VARIOUS METHODS

A complex analysis of wood compression (stress-strain, displacement and velocity curves) showed that each sample deformed differently. Therefore, the curves depicted in Fig. **4.2.3-5**a to Fig. **4.2.3-5**h showed the most frequent cases of deformation behaviour of both beech and spruce samples.

"Clip on" extensometer: The negative increment of ε_L was interpreted in our hypothesis as an expansion of the middle spring in the three-spring model described above. The "non-standard" compression behaviour of the sample was apparent only on the stress-strain curve obtained by the extensometer (Fig. **4.2.3-5**b). This can be explained by the calculation of ε_L. The extensometer provides the ε_L calculated from the relative positions of two mechanically tracked points. The ε_L obtained from the crosshead was also determined from the positions of two points. In contrast to the extensometer, these were located on the sample contact surfaces that moved throughout the compression test only relative to each other.

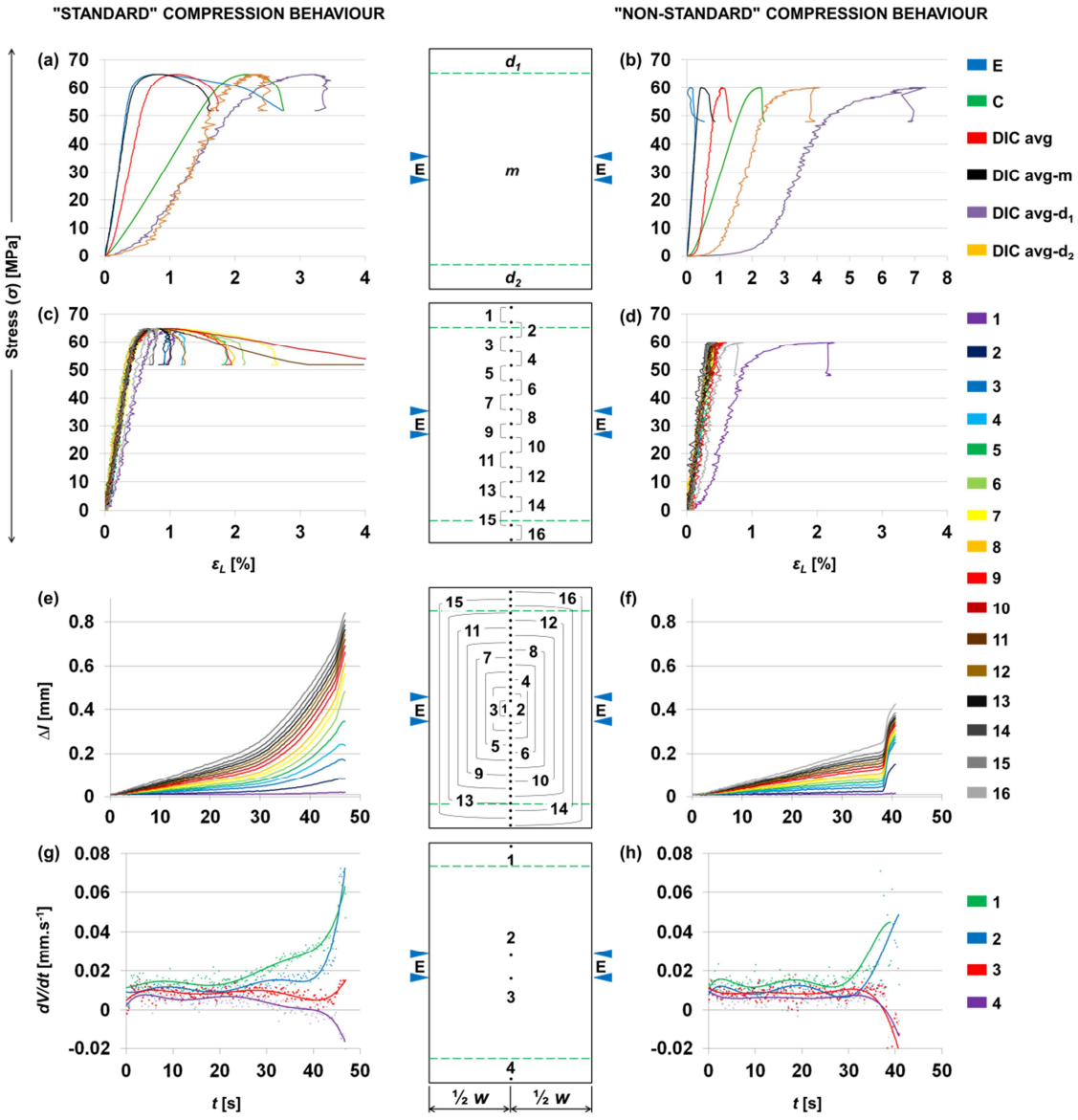

Fig. 4.2.3-5: Comparison of "standard" (selected from beech samples) and "non-standard" (selected from spruce samples) compression behaviour from various perspectives:

a, b – Stress-strain curves obtained using crosshead (C), extensometer (E) and DIC

c, d – Stress-strain curves obtained from DIC between tracked points

e, f – Development of the differences (Δl) between the initial distance (l_0) and the actual distance (l) of the tracked points spaced along the sample length (h) with the increasing initial distance (l_0)

g, h – Development of displacement velocity (dV/dt) at selected points located near the compression plates (no. 1,4) and at the vertical position as the points tracked by the extensometers (no. 2,3)

The strain field obtained by DIC expressed the local ε_L computed from three nodes using triangulation scheme. The stress-strain curves obtained by DIC and based on averaged ε_L over zone m cannot capture the negative increment of ε_L. The sensitivity analysis (omitted here to save space) proved that this also applied to any size of AOI within zone m. The negative increment of ε_L reported by the extensometer can be also

caused by a "barrel" deformation mode of sample, which was reported by Benabou (2008, 2010). Nevertheless, the transverse displacement of points spaced near the vertical edges of AOI exhibited random spatial distribution along *h* in most of the samples.

Videoextensometer analyses: The isolated tracked points were spaced with a constant initial distance (l_0) = 3 mm. The plastic part of stress-strain curves of the samples exhibiting "non-standard" compression behaviour (Fig. **4.2.3-5**d) demonstrated the lower ε_L induced within zone *m* compared with zones $d_{1;2}$. This finding revealed an earlier collapse of zones $d_{1;2}$ before the failure of zone *m*, which was in the contrast to samples behaving in the standard way. The vertical position of shear crack plane in zone *m* within the samples exhibiting standard compression behaviour can be found between the points achieving the highest ε_L (Fig. **4.2.3-5**c).

To detect the vertical boundaries of negative increment of ε_L area, tracked isolated points were symmetrically spaced with respect to the horizontal axis of AOI along *h* with the increasing l_0. The curves display the development of the difference (Δl) between l_0 and the actual distance (l_a) of the tracked points. Owing to various l_0, the Δl were incommensurable at the specific time points. However, the comparison of their development during compression, i.e. the curve's courses, was possible. The Δl increased faster throughout the compression between the points that were initially more distant compared to the points spaced with the lower l_0.

The increase in Δl in the range of the plastic deformation behaviour of the samples exhibiting "non-standard" compression behaviour was reduced by the expansion of zone *m* (Fig. **4.2.3-5**f). The shear crack plane originating in zone *m* within the samples exhibiting standard compression behaviour had a similar effect but to a lesser degree (Fig. **4.2.3-5**e).

Velocity analysis: This approach was based on the velocity analysis in the loading direction of the selected points by DIC (Fig. **4.2.3-5**g and Fig. **4.2.3-5**h). The velocity field reached its maximum where samples came into the contact with the movable compression plate. As the distance from the movable compression plate increased, the velocity decreased down to the other contact zone at the static compression plate where velocity was zero.

The relatively constant velocity of the selected points can be observed in the range of the elastic deformation behaviour of the sample. After exceeding the proportion limit, the points located in the upper half of AOI accelerated; on the contrary, the points located in the lower half of AOI slowed down. Once the shear crack plane was created, the part of the sample volume positioned under it became almost static. Consequently, the velocity induced by the movable plate had to be distributed within the shorter interval of *h*, resulting in a faster movement of the upper sample part.

The velocity curves of point nos. 2 and 3 (Fig. **4.2.3-5**h) contained the short time interval in which point no. 3 achieved a higher velocity than point no. 2. This indicates that those points move away from each other during that interval which is reflected as the expansion of zone *m*. The critical time interval corresponds to the time interval in which the negative increment of ε_L is commonly measured by the extensometer (Fig. **4.2.3-5**b).

4.2.3.4 PERCENTAGE OF "NON-STANDARD" COMPRESSION BEHAVIOUR

We found that the percentage of the samples exhibiting "non-standard" compression behaviour (P_{un}) depends on *h* and wood species (Fig. **4.2.3-6**). When the *h* was 50 mm, the aspect ratio reached its optimum for the compression tests of both beech and spruce samples, i.e. the P_{un} was at its minimum. The spruce and beech exhibited the most "non-standard" compression behaviour when *h* was 60 mm (P_{un} = 70 %) and 30 mm (P_{un} = 10 %), respectively.

Poulsen et al. (1997), Benabou (2008, 2010) and Byskov et al. (2002) reported that the samples compressed parallel to the grain mostly failed due to the shear crack plane. It arises within zone *m* under the specific angle to the longitudinal axis of a sample (~60°). The inclination of the shear crack plane is noticeable on the tangential sample surface. On the radial sample surface it is reflected as a horizontal shear line (Poulsen et al. 1997). In the current study zones $d_{1;2}$ of the samples exhibiting "non-standard" compression behaviour failed earlier than the shear crack plane occurred within zone *m*. The P_{un} of spruce was about 7-10 times higher (Fig. **4.2.3-6**) than that of beech. These differences may be related to the failure modes of spruce and beech when compressed parallel to the grain.

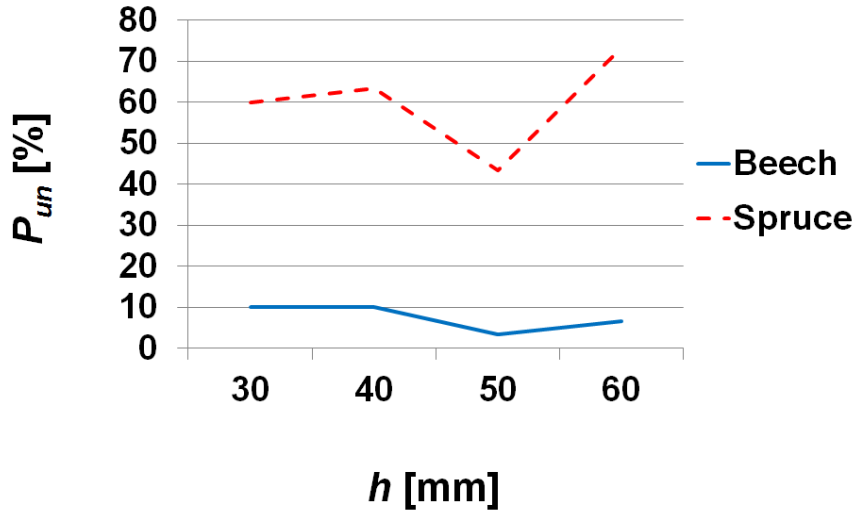

Fig. 4.2.3-6: Influence of sample length (*h*) and wood species on the percentage of samples exhibiting "non-standard" compression behaviour (P_{un})

The longer cellulose fibres and anatomical elements of the spruce samples fail mostly by the local buckling during longitudinal compression (Benabou 2008). The anatomical elements creating the contact sample surface are unilaterally restrained. Therefore, the shear crack plane is often reached earlier within zones $d_{1;2}$. It is created as a horizontal plane. The shear crack plane of the beech, which has shorter cellulose fibres and anatomical elements, more frequently originates by their end fracture. Then it propagates as a slip between the anatomical elements under the specific angle with respect to the longitudinal axis (Reiterer and Stanzl-Tschegg 2001). Therefore, the anatomical elements at the contact sample surface are less susceptible to failure than those located in zone *m*. Compression tests with another sample shape, e.g. a dog bone sample shape used by André et al. (2013) can contribute to the reduction of P_{un}.

4.2.4 CONCLUSION

This paper describes the "non-standard" compression behaviours (when compressed parallel to grain) of Norway spruce (*Picea abies*, L. Karst) and European beech (*Fagus sylvatica*, L.) which were reflected as a negative increment of strain in the loading direction. We found that the deformation field of the samples consisted of two less stiff damage zones near the compression plates and one stiffer zone located between them. Only the length of the middle zone increases as a function of the sample length and it was the same for both wood species. The strain measured at the middle zone gives

3-6 times higher Young's modulus compared with the one obtained based on the strain of the damage zones for both wood species.

The full-field deformation analysis revealed that the negative increment of strain results in an expansion of the middle zone. This corresponds to the earlier collapse of damage zones compared to the middle zone. We also found that the "non-standard" compression behaviour occurred 7-10 times more often within the spruce than within the beech. The amount of the samples behaving in the "non-standard" way also depended on the sample length. The findings of this study can be helpful for the identification of weaknesses of standard compression tests, especially in the choice of the sample length and surface area for the deformation measurement.

Acknoledgments: This work was funded by the of Internal Grant Agency of Faculty of Forestry and Wood Technology at Mendel University in Brno (Grant No. 62/2013) and Ministry of Education, Youth and Sports of the Czech Republic (Grant No. 6215648902) and by the European Social Fund and the state budget of the Czech Republic, project "The Establishment of an International Research Team for the Development of New Wood-based Materials" Reg. No. CZ.1.07/2.3.00/20.0269.

4.2.5 REFERENCES

André, A., Kliger, R., Olsson, R. (2013) Compression failure mechanism in small-scale wood specimens reinforced with CFRP: An experimental study. Constr. Build. Mater. 41:790-800.

ASTM D143 (1994) Standard test methods for small clear specimens of timber. American Society for Testing and Materials, Philadelphia, PA, USA.

Benabou, L. (2008) Kink band formation in wood species under compressive loading. Exp. Mech. 48:647-656.

Benabou, L. (2010) Predictions of compressive strength and kink band orientation for wood species. Mech. Mater. 42:335-343.

Bertolini, M.S., Silva, D.A.L., Souza, A.M., Calil, C., Lahr, F.A.R. (2012) Influência do Comprimento de Corpos-de-prova na Obtenção do Módulo de Elasticidade Ec0. Floresta e Ambiente 19:179-183.

Bodig, J., Goodman, J.R. (1973) Prediction of elastic parameters for wood. Wood Sci. 5(4):249-264.

Bodig, J., Jayne, B.A. Mechanics of wood and wood composites. Krieger Publishing Company, Malabar, 1993.

BS 373 (1957) Methods of testing small clear specimens of timber. British Standard Institution, London, UK.

Byskov, E., Christoffersen, J., Christensen, C.D., Poulsen, J.S. (2002) Kinkband formation in wood and fiber composites – morphology and analysis. Int. J. Solids Struct. 39:3649-3673.

Čermák, P., Horáček, P., Rademacher, P. (2013) Measured temperature and moisture profiles during thermal modification of beech (*Fagus sylvatica* L.) and spruce (*Picea abies* L. Karst.) wood. Holzforschung 68:1-9.

Dahl, K.B., Malo, K.A. (2009) Planar Strain Measurements on Wood Specimens. Exp. Mech. 49:575-586.

Forsberg, F., Mooser, R., Arnold, M., Hack, E., Wyss, P. (2008) 3D micro-scale deformations of wood in bending: Synchrotron radiation μCT data analysed with digital volume correlation. J. Struct. Biol. 164:255-262.

Forsberg, F., Sjödahl, M., Mooser, R., Hack, E., Wyss, P. (2010) Full Three-Dimensional Strain Measurements on Wood Exposed to Three-Point Bending: Analysis by Use of Digital Volume Correlation Applied to Synchrotron Radiation Micro-Computed Tomography Image Data. Strain 46:47-60.

Garab, J., Keunecke, D., Hering, S., Szalai, J., Niemz, P. (2010) Measurement of standard and off-axis elastic moduli and Poisson's ratios of spruce and yew wood in the transverse plane. Wood. Sci. Technol. 44:451-464.

Gryc, V., Horáček, P., Šlezingerová, J., Vavrčík, H. (2011) Basic density of spruce wood, wood with bark and bark of branches in locations in the Czech Republic. Wood Res-Slovakia 56:14-23.

Choi, D., Thorpe, J.L., Hanna, R.B. (1991) Image analysis to measure strain in wood and paper. Wood Sci. Technol. 25:251-262.

Jeong, G.Y., Hindman, D.P., Zink-Sharp, A. (2010) Orthotropic properties of loblolly pine (Pinus taeda) strands. J. Mater. Sci. 45:5820-5830.

Kollmann, F.F.P., Côté, W.A. Principles of wood science and technology. Springer-Verlag, Berlin, 1984.

Murata, K., Masuda, M. (2003) Analysis of strain distribution of softwood in transverse compression measured by digital image correlation method. J. Soc. Mater. Scie. 52:347-352.

Murata, K., Masuda, M., Ichimaru, M. (1999) Analysis of radial compression behavior of wood using digital image correlation method. Mokuzai Gakkaishi 45:375-381.

Murata, K., Nakao, S. (2007) Transverse compression behavior of softwood and alternately laminated lumber of rubberwood veneer and falcata veneer. J. Soc. Mater. Sci. 56:316-320.

Pereira, J., Xavier, J., Morais, J., Lousada, J. (2014) Assessing wood quality by spatial variation of elastic properties within the stem: Case study of Pinus pinaster in the transverse plane. Can. J. Forest Res. 44:107-117.

Peters, W.H., Ranson, W.F. (1982) Digital Imaging Techniques In Experimental Stress Analysis. Opt. Eng. 21:213-227.

Poulsen, J.S., Moran, P.M., Shih, C.F., Byskov, E. (1997) Kink band initiation and band broadening in clear wood under compressive loading. Mech. Mater. 25:67-77.

Požgaj, A., Chovanec, D., Kurjatko, S., Babiak, M. Štruktúra a vlastnosti dreva. Príroda, a. s., Bratislava, 1997.

Reiterer, A. Stanzl-Tschegg, S.E. (2001) Compressive behaviour of softwood under uniaxial loading at different orientations to the grain. Mech. Mater. 33:705-715.

Shipsha, A., Berglund, L. (2007) Shear coupling effects on stress and strain distributions in wood subjected to transverse compression. Compos. Sci. Technol. 67:1362-1369.

Simon, P., Maigre, H., Bigorgne, L., Eyheramendy, D., Jullien, J.F. (2010) Multi-scale study of the variability in softwood transverse elasticity. In: 11th World Conference on Timber Engineering. Trentino, Italy. pp. 988-995.

Sutton, M.A., Mcneill, S.R., Helm, J.D., Chao, Y.J. (2000) Advances in two-dimensional and three-dimensional computer vision. Photomechanics 77:323-372.

Xavier, J., Avril, S., Pierron, F., Morais, J. (2009) Variation of transverse and shear stiffness properties of wood in a tree. Compos. Part A-Appl. S. 40:1953-1960.

Xavier, J., De Jesus, A.M.P., Morais, J.J.L., Pinto, J.M.T. (2012) Stereovision measurements on evaluating the modulus of elasticity of wood by compression tests parallel to the grain. Constr. Build. Mater. 26:207-215.

Wangaard, F.F. The Mechanical Properties of Wood. John Wiley & Sons, New York, 1950.

Zink, A.G., Davidson, R.W., Hanna, R.B. (1995) Strain measurement in wood using a digital image correlation technique. Wood Fiber Sci. 27:346-359.

4.3 PAPER II

NEUTRAL AXIS LOCATION IN THERMALLY MODIFIED WOOD DURING THREE-POINT BENDING BY MEANS OF DIGITAL IMAGE CORRELATION

Martin Brabec[1,*], Petr Čermák[1], Jaromír Milch[1], Václav Sebera[1], Jan Tippner[1]

European Journal of Wood and Wood Products (2016): Submitted manuscript

[1]Department of Wood Science, Faculty of Forestry and Wood Technology, Mendel University in Brno, Zemědělská 3, 613 00 Brno, Czech Republic; phone: +420 545 134 545

*corresponding author: martin.brabec@mendelu.cz

ABSTRACT

The full-field analysis of the deformations during the three-point bending allowed localizing the neutral axis in the sample. In order to obtain comparable value, the determination of the neutral axis position relative to the centroidal sample axis was done. The centroidal sample axis was found with help of the image processing methods such as "edge filtering" and "image subtracting", which finf out the sample outline in the image. Then, the coordinates of the centroidal axis were defined at middle position between upper and lower sample edge. It was found that the neutral axis and centroidal sample axis are almost coincident. This statement applies for native as well as for thermally modified beech wood (*Fagus sylvatica* L.). However, the position of the neutral axis slightly changed; first locally moved to tension side of the bended sample under the loading head as load increases; second globally also towards the tension side of the sample but not significantly. For future step, the fourth-point bending method seems to be able to provide the more accurate neutral axis position.

KEYWORDS: Neutral axis; Digital image correlation (DIC); Three-point bending; Image processing; Thermal modification; Wood

4.3.1 INTRODUCTION

A thermally modified timber (TMT) has been long recognized as efficient and eco-friendly alternative to tropical species or other way treated wood. According to applied process parameters, thermal modification can efficiently improve natural properties such as a colour shade (Johansson and Morén 2006, Hill 2006, Bekhta and Niemz 2003, Čermák and Dejmal 2013), moisture dimensional stability (Seborg et al. 1953, Burmester 1975, Rautkari et al. 2014, Militz and Altgen 2014, Čermák et al. 2015) and natural bio-durability (Hakkou et al. 2006). Nevertheless, the range of feasible applications for TMT is limited by the undesired side effect of thermal modification such as reduction in the mechanical properties of wood (Tjeerdsma 1998, Militz 2002, Hill 2006, Widmann et al. 2012). Therefore, the exploration of the mechanical performance of the TMT has always been a big issue while it was assessing for structural applications.

Mechanical behaviour of wood and its assessment by means of the bending tests is considered to be the most reliable with a high predictive ability (Kollmann and Côté 1968, Bodig and Jayne 1993). According to Bodig and Jayne (1993), Eggert (1994), Bedford and Liechti (2001) and Niemz et al. (2007) the convex side of the bended sample is loaded by the tension stress parallel to grain meanwhile its concave side is loaded by the compression stress parallel to grain. At the interface of tension and compression stresses is a point of zero normal stresses and strains called as a neutral axis (NA). As the distance from the NA increases, the tension or compression stresses increases up to the extreme fibre located on the sample surface. Such distribution of the normal stresses within the transverse sample cross-section leads to the inducing of the shear stresses parallel to the grain between the individual layers through the sample height. Owing to the opposite character of the tension and compression, the shear stress is maximal at the NA (Niemz et al. 2007). According to Malvern (1969), Gere and Timoshenko (1997), Bedford and Liechti (2001) and Betts et al. (2010), the position of the NA can be derived from the ratio of the compression and tension wood stiffness parallel to the grain and it is closer towards the higher value.

As was recently reported by Niemz et al. (2007), Hack and Schumacher (2007), Betts et al. (2010), Davis et al. (2012), Sinha et al. (2012) and Lukacevic et al. (2014), the NA can be successfully localized with help of the full-field strain data obtained by means of the various optical techniques as well as by the finite-element (FE) analyses.

Niemz et al. (2007) proved the concurring position of the NA and centroidal sample axis for an isotropic material such as fibre boards. For the wood as an anisotropic and heterogeneous material the similar axes positions cannot be assumed. According to Betts et al. (2010) as well as Davis et al. (2012), the NA of the small clear samples moderately moved away from the centroidal sample axis towards the tension zone meanwhile for the full-size samples the opposite is true. The wooden knots moved the NA in their vicinity towards the zone opposite the knots (Betts et al. 2010). As the knots approached to the tensile or compressive extreme fibre, the character of the NA deviations became increasingly global. Based on the study reported by Sinha et al. (2012) can be noticed that the random multiple knots pattern affects the NA location dependently on the knots closeness to each other. The tension and compression knots placed close to each other along the sample length had an offsetting effect, which results in the one global movement of the NA away from the centroidal sample axis. Conversely, the sparse multiple knots pattern induced the considerable local deviations of the NA position.

Based on the above review it seems that the NA location knowledge has a potential for the estimation of more than bending mechanical characteristics. Therefore, the goal of this study is to enhance the assessment of the mechanical performance of TMT through the NA localization during the three-point bending. The effort is devoted to estimate the degree of thermal treatment effect on the normal stiffness in tension and compression parallel to the grain as well as the bending stiffness at single test. Based on literature review it is hypothesized that the thermal modification affects the tensile and compressive wood stiffness parallel to the grain in a similar level, thus the initial NA location observed within the untreated samples will be slightly changed.

4.3.2 MATERIAL AND METHODS

4.3.2.1 MATERIAL

A mature pith wood of the European beech (*Fagus sylvatica* L.) grown at the stands close to Brno (Czech Republic) was collected (Fig. 4.3.2-2). The boards with the radial (*R*) × tangential (*T*) × longitudinal (*L*) dimension = 90 × 40 × 700 mm^3 were dried in an open air during the several weeks from the wet state to wood moisture content (MC) about of 15 % and cut into three parts with the length of 230 mm. One part was used to make the control samples. Two other parts were separately thermally

modified in a laboratory chamber (KATRES s.r.o., Jihlava, Czech Republic) using an atmospheric pressure at a superheated steam environment. A maximum temperature of 180 °C and 200 °C, respectively, was maintained for 3 h (Fig. 4.3.2-1).

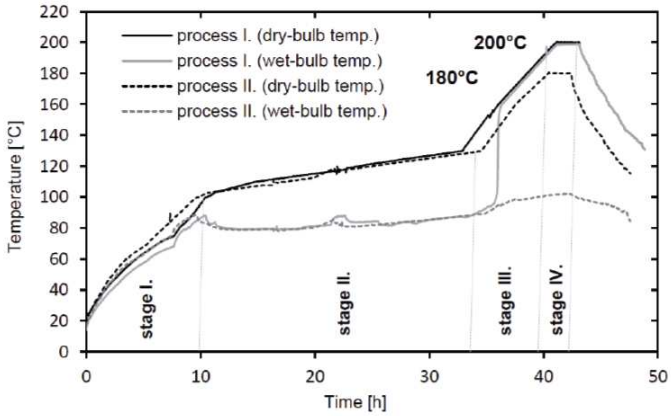

Fig. 4.3.2-1: Thermal modification process schedules – modification temperature at 180°C and 200°C

Fig. 4.3.2-2: Colour changes of the European beech (*Fagus sylvatica* L.) due to the thermal modification

The reference as well as TM blocks were before the sampling conditioned in a climate chamber SANYO MTH 2400 (SANYO Electric Co., Ltd., Osaka, Japan) at 20 °C and 65 % relative humidity until the equilibrium moisture content (EMC) was reached. The final EMC was determined gravimetrically in compliance with test standard ASTM D2395 (American Society for Testing and Materials 2014). Further, the samples were cut into the clear special orthotropic blocks with a square cross section $R \times T = 14 \times 14$ mm^2 and length equal to $15 \times$ depth = 210 mm meeting the requirements of the BS 373 (British Standard Institution 1957). For each wood species and type of treatment 10 samples were prepared, so a total 90 samples were tested. The basic material parameters of the samples as the density and EMC at the measurement time are given in Tab. 4.3.2-1. In order to improve the image matching during DIC computation, a stochastic and high-contrast speckle pattern created by a basic matt white paint followed by a finely pigmented black paint was sprayed on one samples' side (*T* surface).

Tab. 4.3.2-1: The basic materials parameters at the measurement time

TEMPERATURE	EMC	DENSITY
Control	10.6 ±0.1	793 ±23
180 °C	6.8 ±0.1	705 ±20
200 °C	4.9 ±0.1	696 ±23

4.3.2.2 BENDING LOADING

The three-point loading of the samples in the tangential direction was carried out on the universal testing machine Zwick Z050/TH 3A (Zwick Roell AG, Ulm, Germany) equipped with the 50 kN load cell. The samples were supported and loaded using a rounded load heads (with a diameter of 15 mm) mounted on a pivot pin allowing the rotation of the samples about its longitudinal axis but no translation in any direction. The sample was centered in a bending span of 14 × depth = 196 mm with the free sample ends equal to half depth = 7 mm. To avoid any movement of the samples, when the "clip on" deflectometer was clamped, the preload of 10 N was applied. The force was applied at the midspan until the failure at such a loading rate that the proportional limit was reached between 30 and 90 s for all samples. The failure was defined by a significant drop in the force along with the visible sign of the failure.

4.3.2.3 DEFORMATION MEASUREMENT

The deflection of the samples was measured by the "clip on" deflectometer (Zwick Roell AG, Ulm, Germany) clamped to the bottom sample surface at the midspan. The length of a contact sensor arm was set in such a way that the middle point of the transverse sample dimension was measured. The deformation induced in the samples was measured using of the full-field optical system which applies the principles of DIC. The acquisition part of the system includes two CCD cameras AVT Stingray Copper F-504B (Allied Vision Technologies, Osnabrück, Germany, cell size of 3.45 μm and resolution of 2452 × 2056 pixels = 5 MPx) equipped with the lenses Pentax C2514-M (Pentax Precision Co., Ltd., Tokyo, Japan, focal length of 25 mm) at the stereovision (3D) configuration. The contrast between the pattern components on the patterned sample surface was enhanced by two cold light sources SobrietyCube 360

(Sobriety s.r.o., Kuřim, Czech Republic) fitted by LED sensors Luminus Phlatlight CSM-360 (Luminus Devices Inc., Billerica-MA, USA).

4.3.2.4 SYSTEM CALIBRATION AND CAPTURE POSITION

Owing to the objectives of this study, the full-field strains were collected in an area of interest (AOI) fully covered the *LT* samples' surface, i.e. in an area of 210 × 14 mm^2. The cameras mounted on a slider with the span of 228 mm apart were calibrated in the measuring distance of 600 mm, which allowed capturing the AOI under the maximal angle of vision (camera angle of 25°) ensuring the maximal measurement accuracy. The aperture diaphragm of f/4 provided the sufficient depth of field fully covering the out of plane movements during the sample bending. The calibration procedure was carried out with help of 60 left and right calibration images of a grid with 5.5 mm spacing positioned over the whole AOI at various geometric orientations. The described geometry of the optical setup resulted in the magnification of 11 px mm^{-1}. The calibrated stereovision system was placed in such a way that the centre of a captured area corresponded with the AOI centre.

4.3.2.5 DATA ACQUISITION AND MEASUREMENT ACCURACY

All experimental data were synchronically acquired every 0.25 s (4 Hz) using a hardware trigger device, which was appropriate in respect to induced quasi-static loading rate and also to the recognition the speckle pattern by the used software. The strain fields were calculated from the partial derivatives of the displacement using Lagrange notation in Vic-3D v. 2010 (Correlated Solutions Inc., Columbia-SC, USA). In order to obtain the accurate position of the neutral axis (NA) as possible with the appropriate spatial resolution along the sample length, the strains were calculated locally with help of the lowest possible displacement field of 3 × 3 points and strain filter size of 5 × 5 points. A subset size of 19 × 19 pixels and subset step of 5 pixels provided the optimal ratio between the density of the correlated points and the robustness of the image matching. The average accuracy of the measurement was assessed based on the displacement and strain field detected on the 5 images while no loading force was applied. The deflection was measured with the resolution of 1 µm.

4.3.2.6 BENDING STRENGTH AND STIFFNESS CALCULATIONS

The modulus of rupture (*MOR*) was determined based on the ultimate applied moment (*M*), the moment of inertia (*I*) and the distance from the neutral axis to the extreme fibre ($\bar{y}$). For the rectangular cross-section, *MOR* is commonly calculated as

$$MOR = \frac{M}{I} \cdot \bar{y} = \frac{3 \cdot F_{\max} \cdot l}{2 \cdot b \cdot h^2} \tag{4.3.2-1}$$

where F_{max} is the maximal loading force, l is the span of supports, b is the dimension of a cross-section perpendicular to load direction and h is the dimension of a cross-section parallel to the load direction. The modulus of elasticity (*MOE*) was determined based on the forces measured at 10% and 40% of the maximal loading force and corresponding deflections of bended sample as measured by the clip-on deflectometer. The value of *MOE* was calculated using of the following equation:

$$MOE = \frac{\left(F_{40\%} - F_{10\%}\right) \cdot l^3}{4 \cdot b \cdot h^3 \cdot \left(u_{40\%} - u_{10\%}\right)} \tag{4.3.2-2}$$

where $F_{40\%}$ and $F_{10\%}$ are the forces at the 40% and 10% level of the maximal loading force F_{max}, $u_{40\%}$ and $u_{10\%}$ are the deflections at forces $F_{40\%}$ and $F_{10\%}$.

4.3.3 RESULTS AND DISCUSSION

4.3.3.1 PROCEDURE OF NA DETERMINATION AND ITS LOCALIZATION IN A SAMPLE

Based on the underlying bending theory, the NA was determined with help of the zero axial strains (ε_{xx}). The coordinates of the zero ε_{xx}, which can be considered as the NA coordinates, were selected from the full-field matrix of ε_{xx} by an algorithm programmed in Matlab R2008b (MathWorks, Inc., Natick, MA-USA). The preliminary study proved that exactly zero ε_{xx} are insufficient because of their lack and a high variability of their position within a sample height. Therefore, the NA coordinates were found with help of the wider "zero ε_{xx} ranges" of ±0.05 %, ±0.1 %, ±0.5 %, ±1 % and ±2 %. In that case, the NA was determined at the middle position between the coordinates of the minimal and maximal value of the "zero ε_{xx} range". The variability of the NA coordinates decreases as the "zero ε_{xx} ranges" increases, meanwhile the accuracy is reducing. The optimal ratio between the variability and accuracy was found for "zero ε_{xx} range" of ±1 % (Fig. 4.3.3-4).

The NA coordinates define the NA position in an image. Nevertheless, in order to obtain appropriate and comparable results, the NA was related to the sample height, resp. to the centroidal sample axis such as in Betts et al. (2010) and Davis et al. (2012) and the relative NA position (NA_{rel}) was obtained. The centroidal sample axis lying exactly at the middle of the sample height was determined based on the sample outline founded by image processing in ImageJ v. 1.50e (National Institutes of Health, USA). At first, the edges were detected through the whole image. Then, the sample outline was selected from the image and obtained its position in the image. The coordinates of the centroidal axis were defined at middle position between upper and lower sample edge. Finally, the difference between the NA coordinates and the centroidal sample axis coordinates was calculated and related to the sample height. The resulted ratio expresses the NA_{rel} position (Fig. 4.3.3-1).

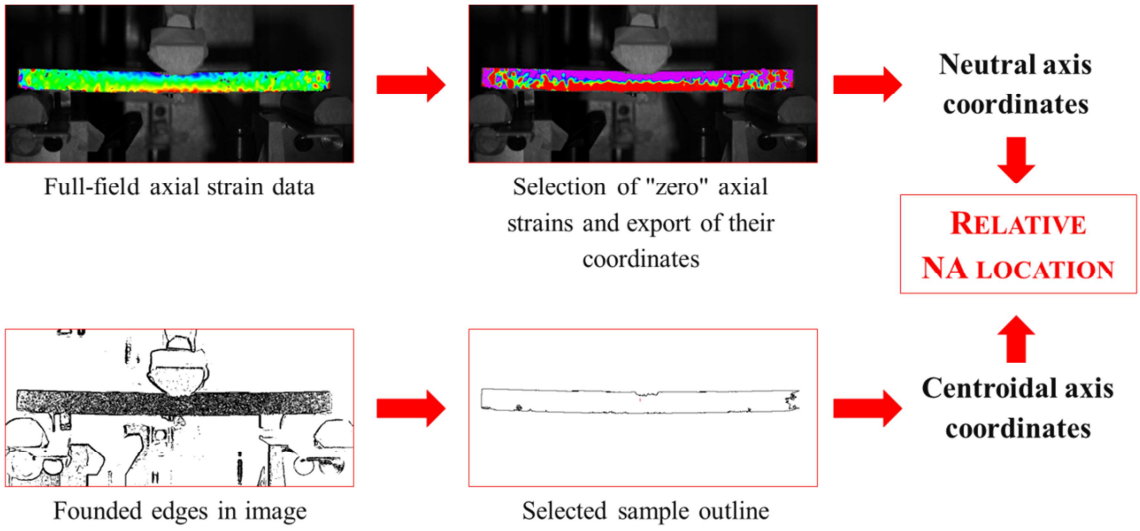

Fig. 4.3.3-1: The procedure used for determination of the relative neutral axis position (NA_{rel})

Fig. 4.3.3-2 and Fig. 4.3.3-3 show that the variety of the zero axial strain position, i.e. NA location within the sample height valid for one elastic load level, which was defined as 50 % of maximal loading force. The NA location is increasingly variable as the distance from the loading point at the midspan increased. This finding is attributable to the decreasing axial strain towards the sample ends that was apparent as the decreasing density of the axial strain contours. As a consequence, the proportion of the noise related to the strain values increased and the NA location became increasingly distorted, if the constant noise throughout the AOI is taken into account. In order to

reduced the variability of the resulted NA position only a middle fourth of the sample length was used to analyse the NA location before and thermall modification (Fig. 4.3.3-3)

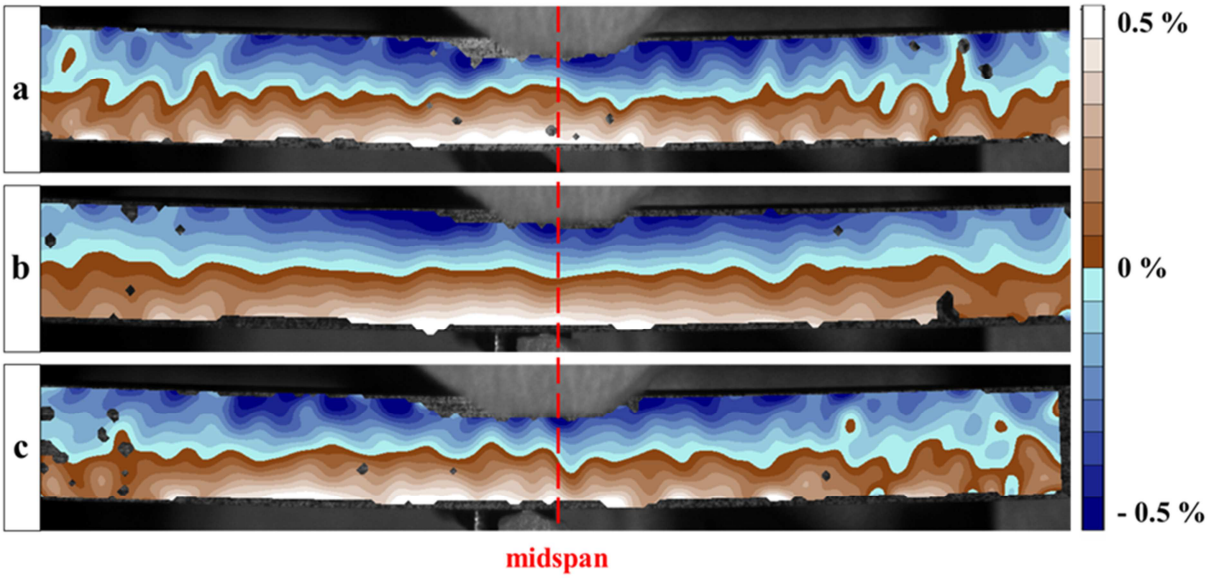

Fig. 4.3.3-2: Axial strain plots before the failure of European beech a) untreated; b) thermally modified at 180°C; and c) thermally modified at 200°C

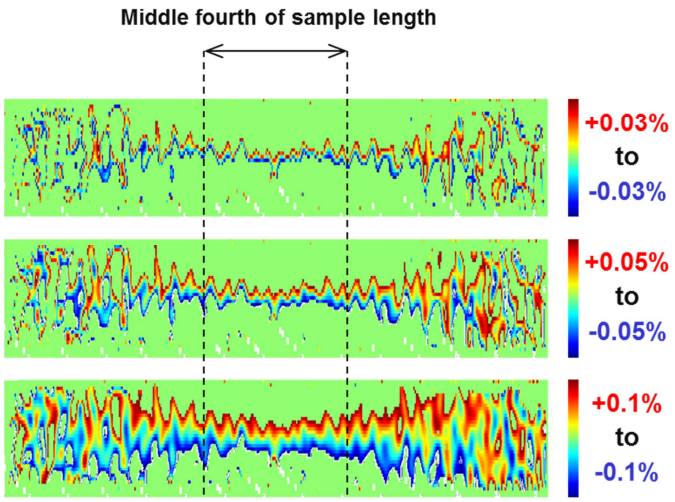

Fig. 4.3.3-3: Range of "zero" axial strain and sample length interval for NA determination

In the Fig. 4.3.3-4 is evaluated the change of relative NA location due to thermal modification. It seems that the thermal modification at 180°C moved the NA closer to the centroidal sample axis in comparison with untreated beech wood. It means that the part of sample cross section loaded by the tension stress in the longitudinal direction became greater, which corresponded to the decrease of deflection due the thermal

modification. In contrary, as the higher temperature was used, the NA moved down approximately into the same position even lower as in case of untreated samples. In order to determine a clear trend of the NA movement due to thermal modification, the more studies at various temperatures are needed. So due to high variability of the NA location, the changes of position are not significant.

In the course of the bending loading the NA slightly moved down (about 1-3 %), i.e. towards the tension side of the bended sample. Moreover, the NA position locally slightly changed (moved to tension side of the bended sample) as load increases, which has a lot of do with the local compression of wood under the loading head. Therefore, the three-point bending is not efficient for the assessment of the neutral axis position.

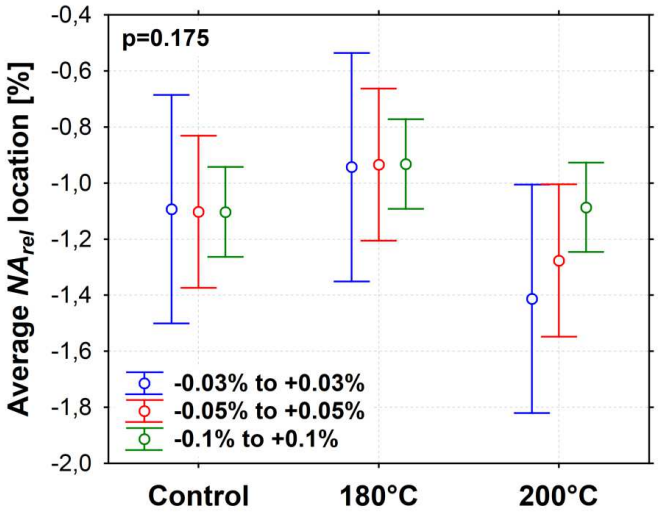

Fig. 4.3.3-4: The variability of the NA_{rel} location depending on the value of the "zero ε_{xx} range"

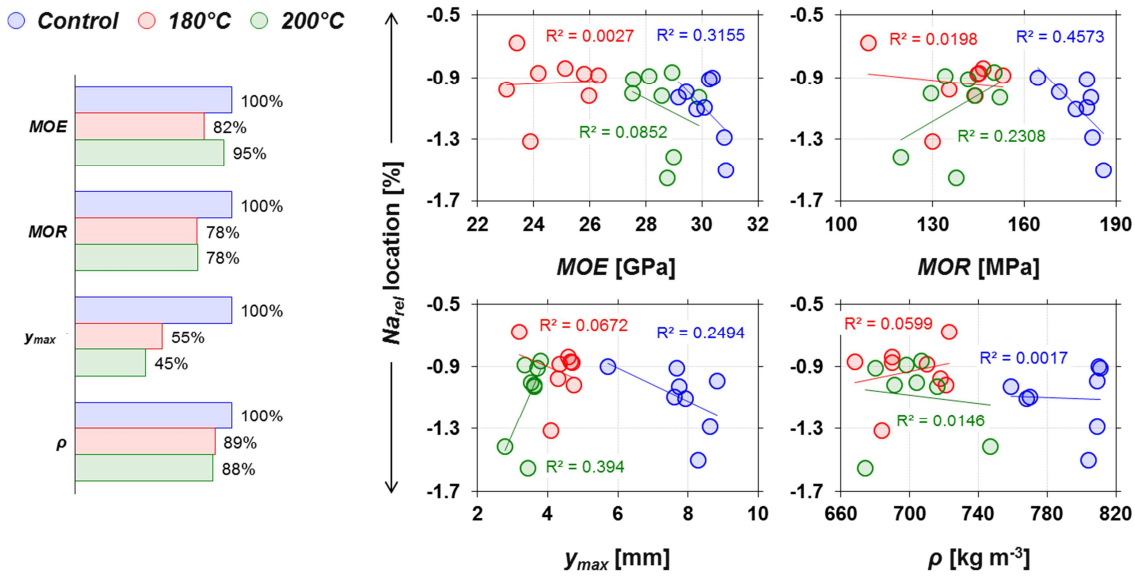

Fig. 4.3.3-5: Correlation of NA_{rel} location with other bending characteristics

As can be seen in Fig. 4.3.3-5, the other bending characteristics such as modulus of elasticity, modulus of rupture and maximal deflection should not be used in order to predict the NA location. Also the density is not good correlated with the NA location in thermally modified beech wood. For the untreated beech wood the relationships of the NA location and the bending characteristics are closer. However, the effect of the thermal modification on the other bending characteristics is well apparent. This effect is described based on the percentage of each characteristic measured after modification in relation to untreated samples, which are considered as 100 %.

4.3.4 CONCLUSION

An effiecient procedure for the NA determination based on the axial strain field obtained by DIC and the sample edges was prepared in Matlab environment.

Although the thermal modification experienced statistically different bending strength and stiffness, the change of the postion of NA was not proved to be significant.

NA location changes slightly with time (load level) towards the tension side of the specimen, however the change is also insignificant. With increasing load becomes more and more visible the local deviation of NA under the loading head. This was attributed to the local compression.

Future work should be focused on more sophisticated filters that will remove the problematic noise. The utilization of the fourth-point bending method seems to be more efficient, mainly because of the pure bending stresses between two loading heads.

Acknowledgments: This work was funded by the Internal Grant Agency of Faculty of Forestry and Wood Technology at Mendel University in Brno (Grant No. LDF_PSV_2016015) and Ministry of Education, Youth and Sports of the Czech Republic (Grant No. 6215648902) and by the European Social Fund and the state budget of the Czech Republic, project "The Establishment of an International Research Team for the Development of New Wood-based Materials" Reg. No. CZ.1.07/2.3.00/20.0269.

4.3.5 REFERENCES

Bekhta, P., Niemz, P. (2003) Effect of high temperature on the change in color, dimensional stability and mechanical properties of spruce wood. Holzforschung. 57:539-546.

Bedford, A., Liechti, K. Mechanics of materials. Prentice Hall, New Jersey, 2000.

Betts, S.C., Miller, T.H., Gupta, R. (2010) Location of the neutral axis in wood beams: A preliminary study. Wood Mater. Sci. Eng. 5:173-180.

Bodig, J., Jayne, B.A. Mechanics of wood and wood composites. Krieger Publishing Company, Malabar, 1993.

BS 373 (1957) Methods of testing small clear specimens of timber. British Standard Institution, London, UK.

Burmester, A. (1975) Zur Dimensionsstabilisierung von Holz. Holz Roh. Werkst. 33:333-335.

Čermák, P., Dejmal A. (2013) The effect of heat and ammonia treatment on colour response of oak wood (*Guercus robur*) and comparison of some physical and mechanical properties. Maderas Cienc. Tecnol. 15:375-389.

Davis, P.M., Gupta, R., Sinha, A. (2012) Revisiting the neutral axis in wood beams. Holzforschung. 66:497-503.

Eggert, O.T. Konstruktion und Fertigung: Untersuchung der Einflußgrößen beim Biegen von Vollholz: Band 7. Institut für Werkzeugmaschinen der Universität Stuttgart, Stuttgart, 1994.

Gere, J.M., Timoshenko, S.P. Mechanics of materials. PWS Publishing Company, Boston, 1997.

Hack, E., Schumacher, A. (2007) ESPI Measurements of strain on a CFRP-reinforced bending beam. Strain. 43:235-239.

Hakkou, M., Pétrissans, M., Gérardin, P., Zoulalian, A. (2006) Investigations of the reasons for fungal durability of heat-treated beech wood. Polym. Degrad. Stabil. 91:393-397.

Hill, C.A. Wood modification: Chemical, Thermal and Other Processes. John Wiley & Sons, Chichester, 2006.

Johansson, D., Morén, T. (2006) The potential of colour measurement for strength prediction of thermally treated wood. Holz Roh. Werkst. 64:104-110.

Kollmann, F.F.P., Côté, W.A. Principles of wood science and technology: I. Solid wood. Springer-Verlag, Berlin, 1968.

Lukacevic, M., Füssl, J., Griessner, J., Eberhardsteiner, J. (2014) Performance assessment of a numerical simulation tool for wooden boards with knots by means of full-field deformation measurements. Strain. 50:301-317.

Malvern, L.E. Introduction to the mechanics of a continuous medium. Prentice-Hall, New Jersey, 1969.

Militz, H. (2002) Heat treatment technologies in Europe: Scientific background and technological state-of-art. In: Proceedings of Conference on “Enhancing the

durability of lumber and engineered wood products". Orlando, Madison, USA. pp. 1-19.

Militz, H., Altgen, M. (2014) Processes and properties of thermally modified wood manufactured in Europe. ACS Symposium Series. 1158:269-285.

Niemz, P., Schreiber, J., Naumann, J., Stockmann, M. (2007) Experimentelle Ermittlung der Dehnungen im Probenquerschnitt bei Biegebelastung von Holzpartikelwerkstoffen. Holz Roh. Werkst. 65:459-468.

Rautkari, L., Honkanen, J., Hill, C.A.S., Ridley-Ellis, D., Hughes, M. (2014) Mechanical and physical properties of thermally modified Scots pine wood in high pressure reactor under saturated steam at 120, 150 and 180 °C. Eur. J. Wood Wood Prod. 72:33-41.

Seborg, R.M., Tarkow, H., Stamm, A.J. (1953) Effect of heat upon the dimensional stabilization of wood. J. Forest Prod. Res. Soc. 3:59-67.

Sinha, A., Voigt, L.R., Miller, T.H., Gupta, R. (2012) Neutral axis of full-size lumber with multiple knots. ACEM. 1:1-15.

Tjeerdsma, B.F., Boonstra, M., Pizzi, A., Tekely, P., Militz, H. (1998) Characterisation of thermally modified wood: molecular reasons for wood performance improvement. Holz Roh. Werkst. 56:149-153.

Widmann, R., Fernandez-Cabo, J.L., Steiger, R. (2012) Mechanical properties of thermally modified beech timber for structural purposes. Eur. J. Wood Wood Prod. 70:775-784.

4.4 PAPER III

UTILIZATION OF DIGITAL IMAGE CORRELATION IN DETERMINING OF BOTH LONGITUDINAL SHEAR MODULI OF WOOD AT SINGLE TORSION TEST

Martin Brabec[1,*], Rastislav Lagaňa[2], Jaromír Milch[1], Jan Tippner[1], Václav Sebera[1]

Wood Science and Technology (2016): Article in press

DOI: 10.1007/s00226-016-0848-7

[1] Department of Wood Science, Faculty of Forestry and Wood Technology, Mendel University in Brno, Zemědělská 3, 613 00 Brno, Czech Republic; phone: +420 545 134 545

*corresponding author: martin.brabec@mendelu.cz

[2] Department of Wood Science, Faculty of Wood Sciences and Technology, Technical University in Zvolen, 960 53 Zvolen, Slovakia; phone: +421 455 206 364

ABSTRACT

A sophisticated approach for the precise determination of both longitudinal shear moduli of wood at single test is introduced. The method is based on the combination of the torsion test inducing pure shear stresses in sample and an optical method providing the full-field strain data of such stress state. The proposed procedure of the longitudinal shear moduli determination consists of two main steps. In the first step, the apparent longitudinal shear modulus following the standardized procedure (EN 408+A1) was determined. Secondly, both longitudinal shear moduli were derived based on the apparent longitudinal shear modulus and the shear strain distribution on the radial and tangential sample surfaces. The wood of European beech (*Fagus sylvatica* L.) was used as material for the experiments. The exploratory analysis revealed the increasing difference between the longitudinal shear moduli determined in the longitudinal-radial plane and in the longitudinal-tangential plane as the total torsion angle increased as well as with the increase in the average torsion stiffness. Further, the longitudinal shear moduli and the torsional longitudinal shear strength did not correlate well. Therefore, they cannot be used in order to predict each other. Although such findings need more detailed studies, they should be taken into account when designing wood structures.

KEYWORDS: Shear moduli; Torsion test; Digital Image Correlation; Strain; Wood

4.4.1 INTRODUCTION

The shear characteristics are one of the fundamental parameters describing the mechanical behaviour of construction materials. The shear characteristics are obtained by mechanical tests either as a "by-product" when measuring other mechanical properties (combined tests) or as a "main product" of the specific shear tests. The bending tests are typical combined tests. When bending a sample, the load is coupled with shear stresses induced in the sample. Vafai and Pincus (1973) and Yoshihara et al. (1998) showed the inaccuracy of the shear strength determined by the three-point bending test when compared with values from the torsion test inducing pure shear stress and strain in the sample. Riyanto and Gupta (1998) and Siller (2002) found that four-point and five-point bending tests also provide distorted shear strength values. According to Riyanto and Gupta (1998), there are also differences between the shear strength obtained by the variously configured bending tests. Harrison (2006) points that the bending tests do not even provide the correct shear moduli. Yoshihara and Kubojima (2002) tried to determine the more reliable shear moduli by the asymmetric four-point loading method. They obtained the correct shear moduli when the span support was equal to twenty times of the sample width. Burdzik and Nkwera (2003) and Hindman et al. (2005a, b) proved a poor correlation between the Young's moduli (E) from the bending tests and the shear moduli (G) obtained by the torsion test. Therefore, the ratio $E:G$ is not suitable for the reliable prediction of the shear moduli. Chui (1991) and Divos et al. (1998) used the frequency resonance method and obtained both shear moduli with a large scatter; therefore, it can be considered as an approximate method. The most of the findings related to shear strength and shear moduli determination obtained using the bending tests have recently been confirmed by Khokhar (2011).

The specific shear test described in the ASTM D143 (1994) and well known as "shear block test" does not induce the pure shear stresses in the sample, which was demonstrated by Ukyo et al. (2008, 2010) and Moses and Prion (2002) by means of the full-field strain measurement and the finite-element (FE) plastic model, respectively. As a consequence, the shear block test provides a significantly different shear strength compared to the one obtained by torsion test (Heck 1998; Gupta et al. 2002a; Gupta and Siller 2002a). The complex strain field occurring within the Iosipescu test was proved by Pierron and Vautrin (1998), Yoshihara et al. (1999, 2001) and

Xavier et al. (2004). The almost pure shear strain and consequently the true shear moduli were obtained by this method only when the samples fractured in brittle way and the strain gauges were glued at the centre of narrow shear area between the notches. Sretenovic et al. (2004) numerically analysed the well-known one-rail shear test improved by Müller et al. (2004a, b) and they proved the almost pure shear stresses in the sample glued and additionally screwed between the two shear grips loaded under tilt angle of 8°. Liu (1984) measured the true shear strength in the longitudinal-tangential plane by using the tensile jaws made by Arcan et al. (1978). Liu et al. (1996), Dahl and Malo (2009a, b) and Xavier et al. (2009) modified the fixture part of the Arcan's jaws together with the determination of the correction factors, which take into account the non-shear strains occurring within the measured area. Thus, they broadened its usage for the determination of the true shear moduli in all anatomic planes.

Further, the specific shear tests are accomplished even without any special jaws by the uniaxial "off-axis" tension or compression at an orientation to the grain in the interval of (0°; 90°). Yoshihara and Ohta (2000) measured true shear strength by the "off-axis" tensile test when the grain angle was in the range of 15–30°. Koerber et al. (2010) and Majano-Majano et al. (2012) successfully used the 45° "off-axis" compression test to determine the shear characteristics.

Based on the multipoint-wise deformation measurement (Davalos et al. 2002; Gupta and Siller 2005b) and FE analyses of the shear stresses (Gupta et al. 2002b; Gupta and Siller 2005c; Hsieh 2007), the pure shear stress-strain state of the twisted sample was confirmed. Authors reported the homogeneous distribution of the shear stress and strain, i.e. constant values, within the span beginning and ending at a distance of two sample widths from both jaws. Gupta et al. (2002b) and Gupta and Siller (2005c) revealed the nonlinear decreasing in the shear stress and strain out of this span towards jaws caused by the clamping of the sample. This phenomenon is well known as St. Venant principle, sometimes denoted as grip end effect. Zero shear stresses were found in the torsion (sample) axis and on the sample edges. The maximal shear stress is induced at the centre of the lateral sample surfaces along the sample length within the homogeneous shear stress distribution span. The practical evidence of such shear stress distribution was provided by Yang (2012) who found an increase in the maximal torsion angle as the sample width decreases. According to Nafa and Araar (2003) and Günay and Orçan (2007) who examined cyclic twisting test, the maximal torsion angle has a lot to do with the amount of cycles, torsion direction, angle of reversion for the

duplex torsion and amplitude. Chen et al. (2006) reported more micro-cracks in the sample twisted in cycles compared to the non-cyclic twisting. Gupta and Siller (2005b, c) and Yang (2012) proved the high correlation between the ratio of both longitudinal shear moduli and shear strength determined by the torsion test. Since 2012, the torsion test is recommended by the European Standard (EN 408+A1 2012) for the determination of the average longitudinal shear modulus of structural lumber.

Up to now, the shear strain is determined either point-wise with help of strain gauges glued onto the sample surface or as the total torsion angle following EN 408+A1 (2012). Based on these strain data, only local or apparent longitudinal shear moduli may be obtained. The hypothesis of this study here stems from the potential for obtaining more reliable and robust longitudinal shear moduli by means of full-field optical methods. Therefore, the objectives of this study are to (a) supply the standard torsion test (EN 408+A1) by the full-field strain measurement based on the digital image correlation (DIC) together with an appropriate analytical stress functions and (b) obtain both true longitudinal shear moduli from the single torsion test.

4.4.2 MATERIAL AND METHODS

4.4.2.1 MATERIAL

Pith wood of European beech (*Fagus sylvatica* L.) grown at Slovakia was used. The boards were dried in open air for several weeks from the wet state to wood moisture content (MC) of about 15 %. The boards were finally conditioned in a climate room at 20 °C and 65 % relative humidity until the equilibrium moisture content (EMC) was reached (EMC ~ 12 %). The samples were cut from the outer part of the board (matured wood) as clear special orthotropic blocks with a square cross section radial (R) × tangential (T) = 20 × 20 mm^2 and length (L) = 500 mm. The cross sectional dimensions of the sample were derived from the width clamping limits of the torsion machine ($R_{max} = T_{max} = 20$ mm). The sample length fulfils the requirements of the ASTM D198 (2014) ($L_{min} = 8 \times R = 8 \times T$ for the square cross section) and consists of the clamping length of 50 mm necessary to securely hold the sample in the torsion machine, the distance of $2 \times R = 2 \times T = 40$ mm on both ends of the sample to take into account the grip end effects on the shear distribution (Davalos et al. 2002; Gupta et al. 2002b; Gupta and Siller 2005b, c; Hsieh 2007) and the pure shear span

of 16 × R = 16 × T = 320 mm. In total, 10 samples were tested. The density of the samples varied from 631 to 708 kg m^{-3}. In order to increase image correlations' score of the DIC computation, two adjacent sample sides (R + T surfaces) were covered by stochastic and high-contrast speckle pattern with an average speckle size of 0.012 mm^2. A basic matt white thin paint followed by a finely pigmented black paint was applied by spraying.

4.4.2.2 TORSION LOADING

The loading of the samples until failure was carried out on the torsion test machine KM-50-1 (Minpribor, Russia) equipped with one static and one rotary jaw (Fig. **4.4.2-1**–middle). The torque was applied by the rotary jaw at the motor's lowest speed of 0.3 rpm corresponding to approx. 1.9° s^{-1}. The applied torque measured by the linear mechanical converter of the torsion test machine was transformed to the digital output by the linear variable differential transformer FWA025T (Ahlborn Mess- und Regelungstechnik, GmbH, Holzkirchen, Germany) connected to a personal computer via data logger Almemo2690-8AKSU (Ahlborn Mess- und Regelungstechnik, GmbH, Holzkirchen, Germany). The failure was defined by a significant drop in the torque along with the visible sign of the failure. A gap of 5 mm between the grip end and the sample end was provided for the unrestrained warping and to avoid any build-up of the compression stress. The sample was clamped into the torsion machine in such a way that the deformation field at two adjacent sample surfaces could be captured at the same time.

4.4.2.3 DEFORMATION MEASUREMENT

A shear deformation induced in the samples was measured using the full-field optical system ARAMIS® 3D 12 M (GOM, GmbH, Braunschweig, Germany) which applies the principles of DIC. The system incorporated two CCD cameras with a resolution of 4096 × 3072 pixels = 12 MPx equipped with lenses with a focal length of 100 mm at the stereovision (3D) configuration. In order to enhance contrast between the pattern components, the patterned sample surface was illuminated by two integrated cold light sources fitted by LED diodes KSP0459 with a power of 24 W (Schneider Optische Werke, GmbH, Bad Kreuznach, Germany). In order to obtain the appropriate

spatial resolution across the transverse sample dimensions, the area of interest (AOI) was defined only within the 60 mm of the shear span; meanwhile, the transverse sample dimensions, i.e. $R + T = 20 + 20$ mm were fully covered. When projecting the transverse dimensions into 2D plane, the AOI occupies an area of 60×28 mm^2. The AOI is subjected to out-of-plane movements due to torsion, and therefore, it was located at the nearest possible position of the static jaw with respect to the grip end effect (Fig. **4.4.2-1**–left).

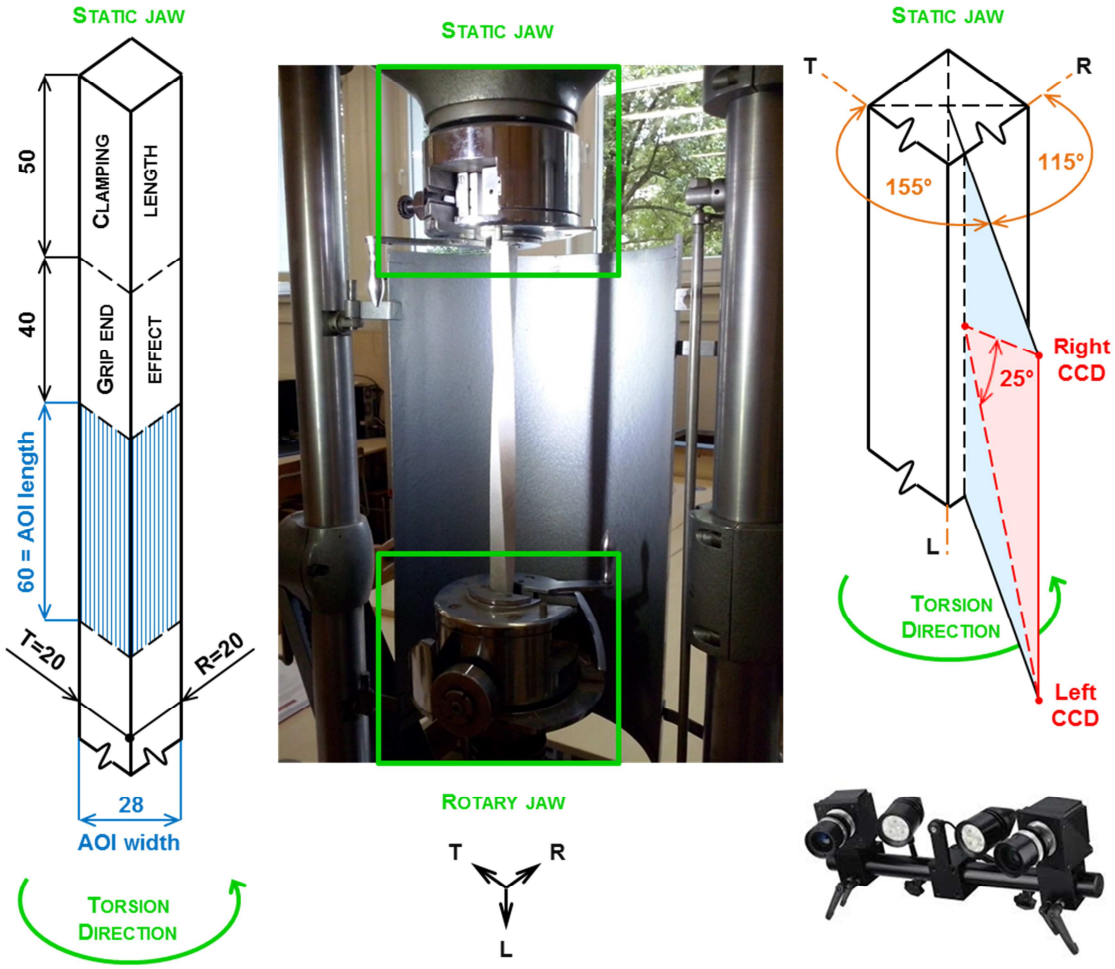

Fig. 4.4.2-1: Experimental set-up: *left* – AOI definition, *middle* – torsion machine, *right* – stereovision set-up

4.4.2.4 SYSTEM CALIBRATION

In order to capture the AOI under maximal angle of vision (camera angle of 25°) ensuring the maximal measurement accuracy, the cameras were mounted on a slider with a span of 182 mm and calibrated in the measuring distance of 495 mm and each camera makes exactly a half camera angle. The chosen aperture diaphragm of f/32

provided the maximal depth of field (17 mm), which fully covered the out-of-plane movements of the twisted AOI. The calibration procedure was carried out according to the User Manual of ARAMIS® 3D 12 M by using 13 left and right calibration images of the calibration object CQ/CP20 55 × 44 at various geometric orientations. The deformed sample surfaces were captured with a scale of 31.5 px mm^{-1}.

4.4.2.5 CAPTURE POSITION OF SYSTEM

The position of the calibrated stereovision system was set with the help of an incorporated laser pointer indicating the centre of the actually displayed area. The slider with the cameras was placed vertically in such a way that both cameras make the same angle with the vertical axis of the sample. Then, the system was placed on a circle with a diameter of the calibrated measuring distance in such position that one half of AOI was seen under 40° greater angle than the other one (Fig. **4.4.2-1**–right). These different vision angles sufficiently increased the time interval for useful capture of the AOI half, which was subjected to the size reducing in an image as torsion angle increased. Its vertical position was adjusted with the help of the markers on the sample surfaces bounding the AOI.

4.4.2.6 DATA ACQUISITION AND MEASUREMENT ACCURACY

The images and the torque were captured appropriately with respect to induced quasi-static loading rate (0.3 rpm) in an acquisition interval of 1 s using a built-in hardware trigger device. The calculation of the strain fields from the partial derivatives of the displacement using Lagrange notation was performed by software included in the system. The local strains needed for the robust determination of the shear moduli were calculated with the help of the lowest possible displacement field of 3 × 3 points and strain filter size of 3 × 3 points. A subset size of 19 × 19 pixels and subset step of 15 pixels were chosen based on the pre-study examining the optimal ratio between the density of the correlated points (14.5 points mm^{-2}) and the robustness of the image matching. The average measurement accuracy was estimated based on the noise on the five images acquired while no loading force was applied. The shear strain was determined with the average accuracy of 0.004969 %, i.e. 50 micro strains.

4.4.2.7 CALCULATIONS OF THE TORSIONAL STRENGTH, APPARENT SHEAR MODULUS AND SHEAR STRAIN DISTRIBUTION

The torsional strength in longitudinal direction (σ_L) was calculated according to Kollmann and Côté (1968) as:

$$\sigma_L = \frac{M_{\max}}{k_2 \cdot (2b) \cdot (2h)^2} \tag{4.4.2-1}$$

where M_{max} is the maximal applied torque, k_2 is the torsional parameter for rectangular cross section (Boresi and Schmidt 2003) and b and h are the half of the longer and shorter dimension of the cross section, respectively.

The apparent shear modulus (G_a) was calculated according to Kollmann and Côté (1968) as:

$$G_a = \frac{M}{\theta \cdot J} \tag{4.4.2-2}$$

where M is the applied torque, J is the torsional constant called as a quadratic cross-sectional moment of inertia. For the rectangular cross section, J is commonly calculated as $J=k_1 \cdot (2b) \cdot (2h)^3$ where k_1 is the torsional parameter expressing the closeness of the rectangular cross section to square shape. A parameter θ is the torsion angle per unit length determined as $\theta = \alpha/l$, i.e. a total torsion angle of the sample (α) measured in the certain distance (l) from the static clamping jaw. The ratio M/θ is the slope of the linear part of the stress-strain curve (Fig. 4.4.2-2). This ratio was obtained using Eq. (4.4.2-3) approximating the first-order derivation for the discrete distributed data of the M and θ within the linear elastic deformations.

$$SLOPE = \frac{\sum \left(\theta - \bar{\theta}\right) \cdot \left(M - \bar{M}\right)}{\sum \left(\theta - \bar{\theta}\right)^2} \tag{4.4.2-3}$$

where $\bar{\theta}$ represents the mean value of θ and $\bar{M}$ represents the mean value of M. The α was determined based on the 3D coordinates of the computed points processed by the software analysis tool, which provided the pure value without the undesirable increment of α when the torque kept the minimal value closed to zero, i.e. during the sample accommodation in the clamping jaws (Fig. 4.4.2-2). Therefore, α obtained by

the analogue counter mounted on the rotary jaw was overestimated by about 7°–12° and was not suitable for the calculation of the shear modulus.

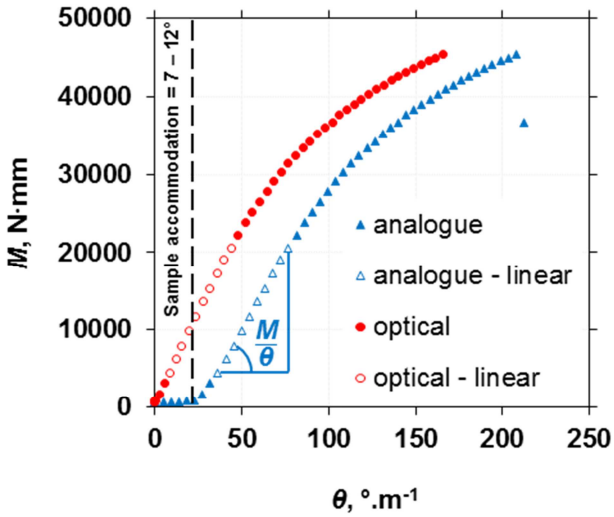

Fig. 4.4.2-2: Stress-strain curves obtained based on the torque (M) and torsion angle per unit length (θ) measured by analogue counter and image processing within optical measurement

The theoretical distribution of the shear strain was calculated with the help of a torsion stress function (ϕ) derived from St. Venant's torsion theory for orthotropic materials:

$$\frac{\partial^2 \phi}{\partial R^2} + \frac{\partial^2 \phi}{\partial T^2} = (G_{LR} + G_{LT})\theta + (G_{LT} - G_{LR})\frac{\partial^2 w}{\partial R \partial T} \qquad (4.4.2\text{-}4)$$

Assuming similarities between the longitudinal shear modulus in the LR plane (G_{LR}) and in the LT plane (G_{LT}) and neglecting displacement changes (w) in longitudinal direction due to torsion, the Eq. (4.4.2-2) can be simplified to well-known Poisson's equation:

$$\frac{\partial^2 \phi}{\partial R^2} + \frac{\partial^2 \phi}{\partial T^2} = 2G_a\theta \qquad (4.4.2\text{-}5)$$

Apparent shear modulus is consequently defined as the average of both longitudinal shear moduli:

$$G_a = (G_{LR} + G_{LT})/2 \qquad (4.4.2\text{-}6)$$

The solution of the differential Eq. (4.4.2-5) for a rectangular cross section by means of the Prandtl membrane analogy gives the distribution of shear stresses σ_{LR} and σ_{LT} in RT plane (Boresi and Schmidt 2003). The stresses at the very surface are calculated as:

$$\sigma_{LR}\big|_{T=-b} = -\frac{16G_a\theta h}{\pi^2}\sum_{n=1,3,5,..}^{\infty}(-1)^{(n-1)/2}\cos\frac{n\pi R}{2h}\sinh\frac{-n\pi b}{2h}/n^2/\cosh\frac{n\pi b}{2h} \quad (4.4.2\text{-}7)$$

$$\sigma_{LT}\big|_{R=-h} = 2G_a\theta R - \frac{16G_a\theta h}{\pi^2}\sum_{n=1,3,5,..}^{\infty}(-1)^{(n-1)/2}\sin\frac{-n\pi}{2}\cosh\frac{n\pi T}{2h}/n^2/\cosh\frac{n\pi b}{2h} \quad (4.4.2\text{-}8)$$

Shear strain follows Hooke's law; thus, local strain distribution at the surface can be calculated as:

$$\varepsilon_{LR,cal} = \sigma_{LR}/G_{LR} \text{ and } \varepsilon_{LT,cal} = \sigma_{LT}/G_{LT} \quad (4.4.2\text{-}9)$$

4.4.2.8 DETERMINATION OF BOTH LONGITUDINAL SHEAR MODULI

The longitudinal shear modulus in the longitudinal-radial plane (G_{LR}) and in the longitudinal-tangential plane (G_{LT}) was determined based on the apparent longitudinal shear modulus (G_a) and the theoretical and experimental distribution of the shear strain on the *R* and *T* sample surfaces in the transverse direction. The apparent shear modulus was determined by using Eqs. (4.4.2-2) and (4.4.2-3). The distribution of the shear strain on the *R* and *T* sample surfaces in the transverse direction was described by the distribution curves.

The experimental distribution curves were obtained based on the strain data located along the sample length in the 30 columns evenly spaced from each other on each AOI half. The strains were averaged within the columns so both radial (*R*) and tangential (*T*) distribution curves were built using 30 values, which ensured the appropriate spatial resolution (1.5 points mm^{-1}) with respect to the shear strain heterogeneity in the *RT* plane (Fig. 4.4.2-3). Both distribution curves were determined for each load level within the elastic deformations. Owing to the data acquisition interval (1 s) and the natural variability of beech wood, the amount of elastic load levels per sample varied from 8 to 14 ones. For example, the elastic deformation behaviour of the sample presented in Fig. 4.4.2-3 was captured on 10 images and therefore was described by 10 *R* and 10 *T* distribution curves. The shear strain profiles in the *RT* plane were in agreement with shear strain data of twisted sample reported by Davalos et al. (2002), Gupta et al. (2002b), Gupta and Siller (2005b) and Yang (2012). The highest strain was concentrated at the centre of each measured surface along the longitudinal sample axis;

meanwhile, the minimal strains were induced at the sample edges. The average shear strain within the *T* sample surface was about 20–40 % higher compared to *R* sample surface. Assuming the same *R* and *T* sample dimension, such shear strain ratio leads to a higher G_{LR} compared to G_{LT}, which is valid for most of the wood species (Kollmann and Côté 1968).

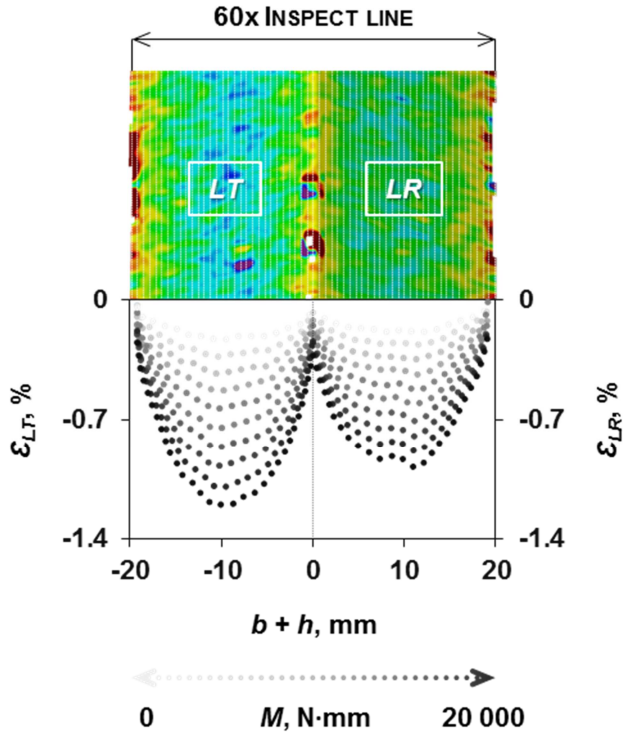

Fig. 4.4.2-3: Shear strain field on the radial (*LR*) and tangential (*LT*) sample surface of twisted sample with square cross section and its transverse strain profile throughout elastic deformations

The theoretical distribution curves for the *LR* and *LT* surfaces ($\varepsilon_{LR,cal}$, $\varepsilon_{LT,cal}$) at any torsion angle were calculated using Eqs. (4.4.2-7), (4.4.2-8) and (4.4.2-9) and then fitted (Fig. 4.4.2-4) to the experimental distribution curves ($\varepsilon_{LR,exp}$, $\varepsilon_{LT,exp}$) using a least square method based on the objective function (Q):

$$Q(G_{LR}) = \sum_{i=1}^{m_1}\left(\varepsilon_{LR,cal,i}(G_{LR}) - \varepsilon_{LR,\exp,i}\right)^2 + \sum_{j=1}^{m_2}\left(\varepsilon_{LT,cal,j}(G_{LT}) - \varepsilon_{LT,\exp,j}\right)^2 \quad (4.4.2\text{-}10)$$

The function was minimized by changing G_{LR} with the help of "fminsearch" function (Matlab R2008b, MathWorks, Inc., Natick, MA-USA) which utilizes a simplex search method. The estimation of G_{LR} in the first iteration was defined as G_a while G_{LT} followed Eq. (4.4.2-6). When Q achieved its minimum, the actual values of G_{LR} and G_{LT} were considered as the resulting longitudinal shear moduli.

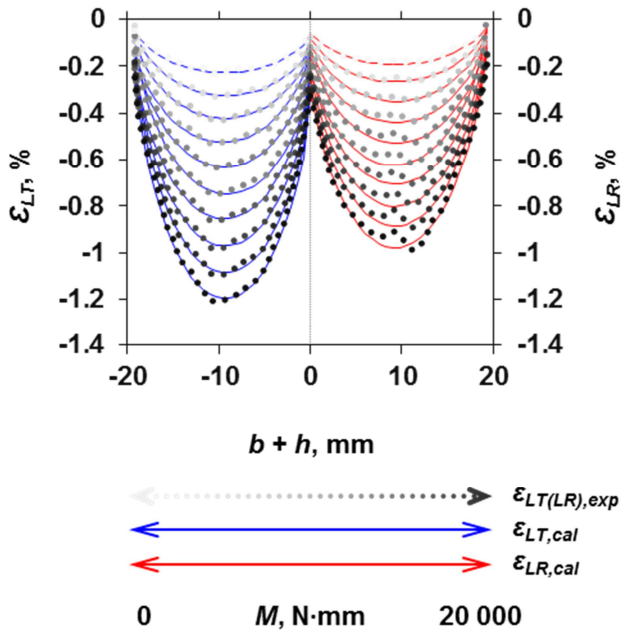

Fig. 4.4.2-4: Fitting of the theoretical distribution curves of shear strain on the radial (*R*) and tangential (*T*) sample surfaces ($\varepsilon_{LT,cal}$, $\varepsilon_{LR,cal}$) to the experimental ones ($\varepsilon_{LT,exp}$, $\varepsilon_{LR,exp}$) throughout elastic deformations

4.4.3 RESULTS AND DISCUSSION

4.4.3.1 EXPLORATORY ANALYSIS OF RESULTED G_{LR} AND G_{LT}

As was assumed based on the ratio of the shear strain determined on the *R* and *T* sample surfaces, the G_{LR} was higher compared to G_{LT}. It seems that the pith rays play the main role in this issue. When the shear stress is induced in the longitudinal direction, the pith rays are loaded in the *RT* plane. The shear stiffness of wood in *RT* plane is only about one-third or one-fourth of that one measured in the *LR* and *LT* plane (Huber 1928; Hearmon and Barkas 1941; Bodig and Goodman 1973; Neumann 1988). On that basis, the pith rays are the elements reducing the longitudinal shear stiffness. The magnitude of the reducing effect may be attributed to the pith rays orientation with respect to the induced shear plane. When the shear stress is induced in the *LT* plane, the pith rays are loaded in their whole volume, meanwhile for the *LR* plane, in their cross section. This is likely the reason for the lower value of G_{LT} compared to G_{LR}.

Although the elastic part of the stress-strain curve (Fig. 4.4.2-2) seems to be directly linear, both G_{LR} and G_{LT} vary throughout the elastic behaviour in the range of about 4 % (Fig. 4.4.3-1–left). Such variability may partially be related to the resolution and noise of the optical measurement. The vertical distance between the G_{LR} and G_{LT} curves

(i.e. a ratio G_{LR}/G_{LT}) is derived from the ratio of the shear strain determined on the *R* and *T* sample surfaces. Its development points to the increase in G_{LR} and decrease in G_{LT} as the applied torque (*M*) increases for most of the samples (Fig. 4.4.3-1–right). As a consequence, the inconsistent elastic load level used for the shear deformations determination might affect the shear moduli values. Whereas the standard procedure according to EN 408+A1 is intended to obtain an average shear modulus using the slope of the linear part from the torque-angle curve, the variability of G_{LR} and G_{LT} throughout the elastic behaviour cannot be reflected. In that case, the total torsion angle is used as an interval of the values in the whole elastic deformation range. A similar principle of the shear moduli determination was reported by many authors carrying out the torsion test (Gupta et al. 2002a; Günay and Orçan 2007; Ukyo et al. 2008, etc.). This procedure was also used partially in this study for G_a determination described above by Eqs. (4.4.2-2) and (4.4.2-3).

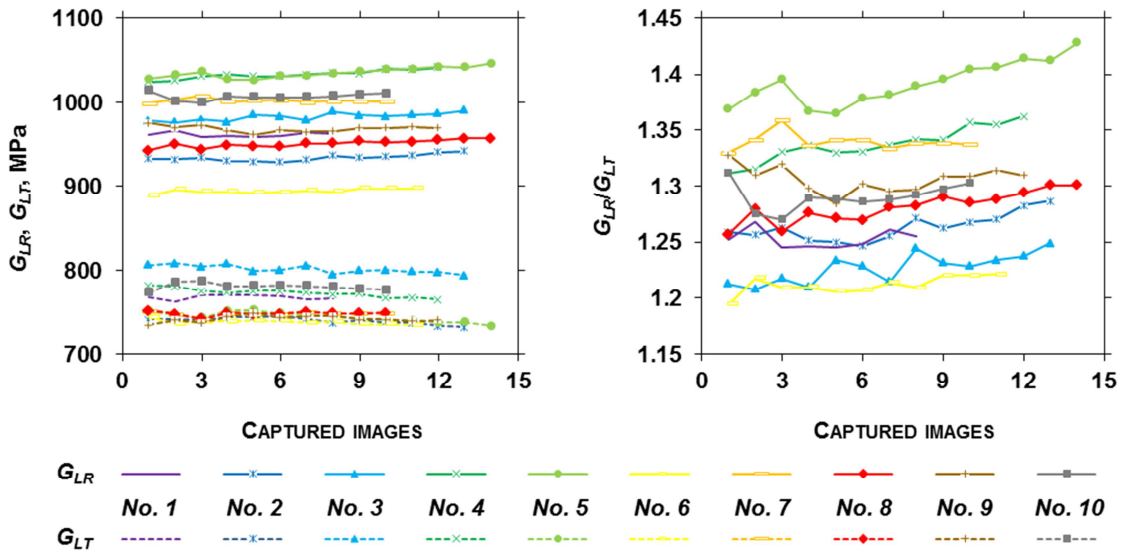

Fig. 4.4.3-1: Longitudinal shear moduli throughout elastic deformations: *left* –.shear modulus in the longitudinal-radial plane (G_{LR}) and longitudinal-tangential plane (G_{LT}), *right* – ratio of both longitudinal shear moduli (G_{LR}/G_{LT})

In order to compare obtained data with the literature ones, the G_{LR} and G_{LT} were averaged through all elastic load levels for each sample as showed in Tab. 4.4.3-1. The introduced procedure of averaging of all local slopes provided G_{LR} and G_{LT} values giving good agreement with the literature (Tab. 4.4.3-2). Owing to the use of G_a as the parameter estimation in the first iteration of the curve fitting, the accuracy of the procedure presented for the shear moduli determination is largely dependent on the

correctness of the G_a. In perspective to the objectives of this study, such fact can be considered as a limiting factor of the optical measurement performance.

Tab. 4.4.3-1: Descriptive statistics of measured longitudinal shear properties of beech wood (*Fagus sylvatica* L.)

NO.	G_a	G_{LR}	G_{LT}	G_{LR}/G_{LT}	σ_L
	MPa	MPa	MPa	-	MPa
1	865	961	768	1.25	21
2	837	934	739	1.26	23
3	892	983	801	1.23	25
4	903	1034	773	1.34	22
5	890	1035	744	1.39	21
6	816	894	738	1.21	21
7	875	1002	748	1.34	22
8	847	951	742	1.28	22
9	855	969	742	1.31	23
10	894	1007	781	1.29	23
x̄	**867**	**977**	**757**	**1.29**	**22**
SD	**28.6**	**44.7**	**21.7**	**0.06**	**1.2**
CV	**3.3**	**4.6**	**2.9**	**4.3**	**5.5**

A slight increase in ratio G_{LR}/G_{LT} as G_a increases was proved (Fig. **4.4.3-2**–right). In fact, this phenomenon is caused by higher increase in G_{LR} compared to G_{LT}. As a consequence, two samples with the different apparent torsion stiffness (G_a) may have the same G_{LT} or even the sample with a higher G_a may exhibit a lower G_{LT} (Tab. **4.4.3-1** and Fig. **4.4.3-2**–left). This phenomenon is not incorporated in the standardized procedure of the G_a determination. In order to confirm and describe this phenomenon in more detail, a further study analysing more samples is needed. Nevertheless, this phenomenon should be taken into account when G_a is used for the stiffness assessment in the structural design.

Müller et al. (2004a, b) stated that, when the sample is uniaxially and diagonally loaded under tilt angle of 5°–8°, the longitudinal shear moduli and average longitudinal shear strength (σ_a) correlate each other closely. However, this does not apply for the shear characteristics obtained by the current torsion tests, which is in agreement with the finding by Khokhar (2011).

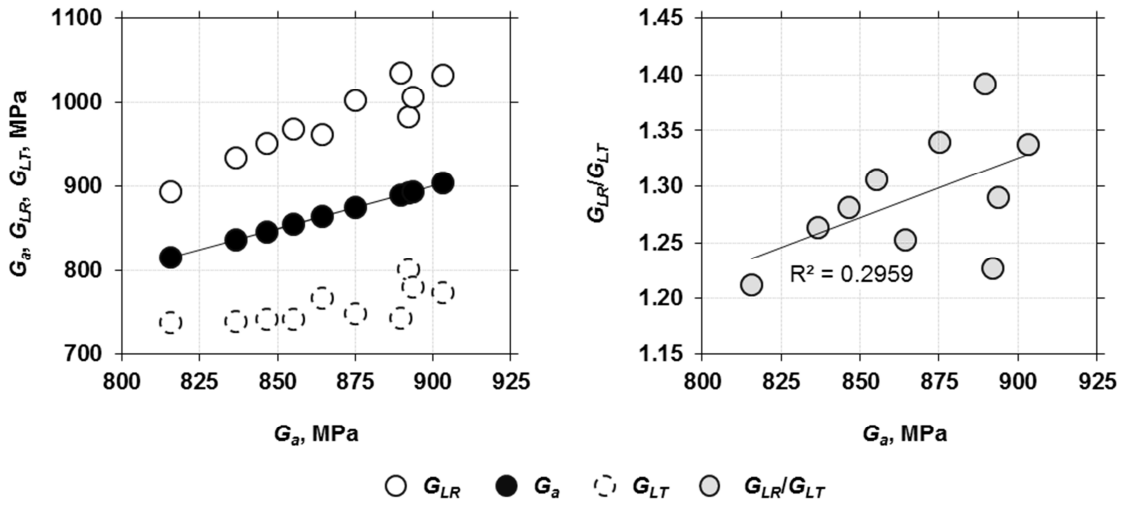

Fig. 4.4.3-2: Relations between all shear moduli: *left* – symmetry of the longitudinal shear moduli in the longitudinal-radial plane (G_{LR}) and longitudinal-tangential plane (G_{LT}) with respect to the apparent longitudinal shear moduli (G_a), *right* – linear correlation between ratio of both longitudinal shear moduli (G_{LR}/G_{LT}) and apparent longitudinal shear modulus (G_a)

The correlation tightness was different for each longitudinal shear modulus (Fig. **4.4.3-3**–left). Highest correlation was observed for G_{LT}, which may be attributed to its lowest variation. However, only about 35 % of G_{LT} variability can be explained by the torsional strength in the longitudinal direction (σ_L), which is still not enough for a good prediction of G_{LT} for beech wood.

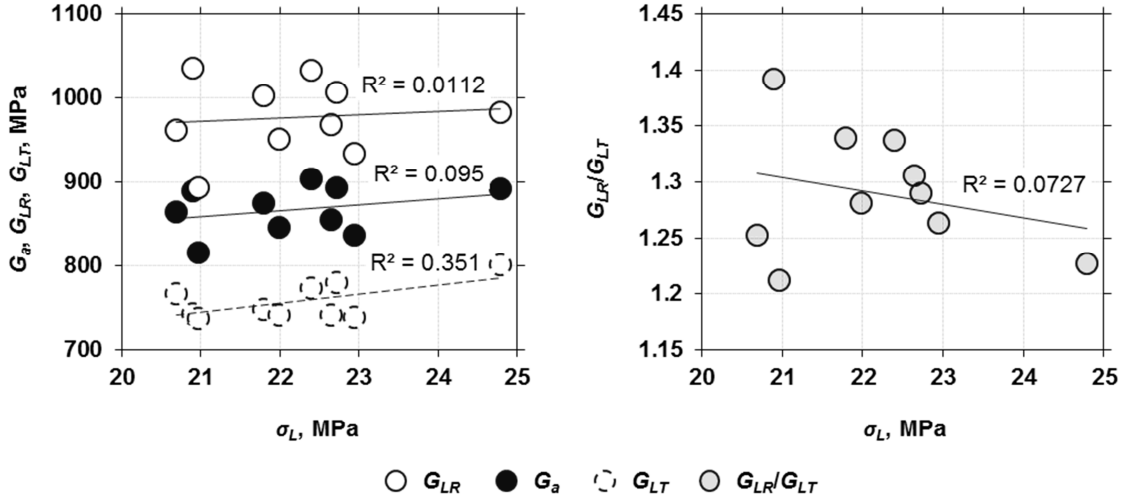

Fig. 4.4.3-3: Linear correlations of the longitudinal shear moduli and torsional strength: *left* – apparent longitudinal shear modulus (G_a), longitudinal shear modulus in the longitudinal-radial plane (G_{LR}) and longitudinal-tangential plane (G_{LT}), *right* – ratio of both longitudinal shear moduli (G_{LR}/G_{LT})

Gupta and Siller (2005b, c) and Yang (2012) found that σ_L of a structural composite lumber is highly dependent on the ratio G_{LR}/G_{LT}. The low determination coefficient of

the linear regression proved that for the solid wood samples it is not true (Fig. **4.4.3-3**–right). Although the linear correlation is poor, the negative slope of the linear regression model is well apparent, so the σ_L increases as the ratio G_{LR}/G_{LT} decreases.

Tab. 4.4.3-2: Measured longitudinal shear properties of beech wood (*Fagus sylvatica* L.) and literature references

METHOD	WOOD SPECIES	MC %	G_a MPa	G_{LR} MPa	G_{LT} MPa	G_{LR}/G_{LT}	σ_L MPa	AUTHOR
TORSION	*F. purpurea* Dum. C.	10.5	682	722	642	1.13		Hörig (1935)
	***F. sylvatica* L.**	**12**	**867**	**977**	**757**	**1.29**	**22**	**This study data**
	F. sylvatica L.	12	870	980	760	1.29		Hearmon and Barkas (1941)
	F. sylvatica L.	12	940	1110	770	1.44		Neumann (1998)
	F. sylvatica L.	12	975	1250	700	1.79		Stamer and Sieglerschmidt (1933)
	F. sylvatica L.	12	1030				23	Bröker and Schwab (1988)
	F. sylvatica L.	11	1360	1640	1080	1.52	24	Huber (1928)
	F. sylvatica L.	6	1870					Günay and Orçan (2007)
	F. sylvatica L.	12					17	Wagenführ (2007)
SHEAR BLOCK	*F. sylvatica* L.	12	735	750	720	1.04		Neumann (1998)
	F. sylvatica L.	12	825					Lagaňa and Rohanová (2011)
	F. grandifolia Ehrh.	12	884	1013	754	1.34		Bodig and Goodman (1973)
	F. purpurea Dum. C.	10.5	1332	1608	1056	1.52		Hörig (1935)
	F. purpurea Dum. C.	10.5			1059			Stamer and Sieglerschmidt (1933)
	F. sylvatica L.	12					8	Kollmann (1951)
	F. sylvatica L.	12					8	Wagenführ (2007)
	F. grandifolia Ehrh.	12					9	ASTM 2555
	F. sylvatica L.	12					12	Perelygin (1965)
	F. sylvatica L.	12					13	Kúdela (1990)
	F. sylvatica L.	12					13	Ugolev (2007)
	F. sylvatica L.	12					14	Požgaj et al. (1997)
	F. sylvatica L.	12					14	Kúdela and Čunderlík (2012)
ULTRASONIC WAVES	*F. sylvatica* L.	12	1068	1280	855	1.50		Hering et al. (2012)
	F. sylvatica L.	12	1120	1320	920	1.43		Bucur and Archer (1984)

Owing to the character of discussed correlation between the ratio G_{LR}/G_{LT} and G_a (Fig. **4.4.3-2**–right) can be true that the sample or a structural element with the higher σ_L exhibits the lower G_a compared to that one with the lower σ_L. This finding is reflected in the low determination coefficient of the linear regression between G_a and σ_L together with the low positive slope of the linear regression model (Fig. **4.4.3-3**–left).

Based on the overall comparison with the reference data, the average shear properties of beech wood determined in this study are in the common ranges reported for the torsion and shear block tests (Tab. 4.4.3-2). Very good agreement of the longitudinal shear moduli with Hearmon and Barkas (1941) was observed; meanwhile, for the σ_L agreement was found with Bröker and Schwab (1988) and Huber (1928). The 2-3 times higher σ_L compared to that one obtained by the standardized shear block test is attributed to the pure shear stress state induced in the sample while twisting. The longitudinal shear moduli measured by using the ultrasonic waves (Bucur and Archer 1984; Hering et al. 2012) are on average about 30 % higher compared to the torsion and shear block tests. In general, such finding applies for all dynamic tests methods when compared to the static test methods. It can be concluded that the presented procedure combining the torsion test and optical measurement is fully applicable for the longitudinal shear moduli determination.

4.4.4 CONCLUSION

The standard torsion test procedure according to EN 408+A1 was sufficiently supplemented by a direct full-field measurement of shear strains and their distribution on the radial and tangential planes accomplished by the optical method based on DIC. The thus obtained experimental shear strain data together with their theoretical predictions computed with the help of torsion stress functions and Hooke's law were used in order to reliably determine both longitudinal shear moduli of European beech (*F. sylvatica* L.). The shear moduli computation is an iterative procedure, in which the apparent longitudinal shear modulus was taken as first parameter estimation. It can be concluded that the proposed procedure is capable of providing the true longitudinal shear moduli of wood. However, its practical and widespread utilization is limited due to the relatively difficult and tedious work with large amount of measured data.

The exploratory analysis of both longitudinal shear moduli determined by the proposed procedure proved about 30 % higher shear modulus determined in the

longitudinal-radial plane compared to one obtained in the longitudinal-tangential plane. Both longitudinal shear moduli were increasingly different as the total torsion angle increased as well as when the apparent longitudinal shear modulus increased. These phenomena are not treated in the apparent longitudinal shear modulus determination according to the standardized procedure, although their knowledge may be helpful in the design of the wood structures, for problems such as torsional buckling and estimating stiffness of floor systems. Based on the regression analyses, it can be concluded that the longitudinal shear moduli cannot be predicted using the torsional longitudinal shear strength and vice versa.

Acknowledgments: This work was funded by the Internal Grant Agency of Faculty of Forestry and Wood Technology at Mendel University in Brno (Grant No. 17/2015) and Ministry of Education, Youth and Sports of the Czech Republic (Grant No. 6215648902) and by the European Social Fund and the state budget of the Czech Republic, project "The Establishment of an International Research Team for the Development of New Wood-based Materials" Reg. No. CZ.1.07/2.3.00/20.0269. This work was also partly supported by the project VEGA 1/0395/16.

4.4.5 REFERENCES

Arcan M, Hashin Z, Voloshin A (1978) A method to produce uniform plane-stress states with applications to fiber-reinforced materials. Exp Mech 18:141-146

ASTM D143 (1994) Standard test methods for small clear specimens of timber. American Society for Testing and Materials, Philadelphia

ASTM D198 (2014) Standard Test Methods of Static Tests of Lumber in Structural Sizes. American Society for Testing and Materials, Philadelphia

ASTM D2555 (2006) Standard Practise for Establishing Clear Wood Strength Values. American Society for Testing and Materials, Philadelphia

Bodig J, Goodman JR (1973) Prediction of elastic parameters for wood. Wood Sci 5:249-264

Boresi AP, Schmidt RJ (2003) Advanced mechanics of materials. Wiley, New York

Bröker FW, Schwab E (1988) Torsionsprüfung von Holz (Torsional testing of wood). Holz Roh Werkst 46:47-52 (in German)

Bucur V, Archer RR (1984) Elastic constants for wood by an ultrasonic method. Wood Sci Technol 18:255-265

Burdzik WMG, Nkwera PD (2003) The relationship between torsional rigidity and bending strength characteristics of SA pine. S Afr For J 198:17-21

Chen Z, Gabbitas B, Hunt D (2006) Monitoring the fracture of wood in torsion using acoustic emission. J Mater Sci 41:3645-3655

Chui YH (1991) Simultaneous evaluation of bending and shear moduli of wood and the influence of knots on these parameters. Wood Sci Technol 25:125-134

Dahl KB, Malo KA (2009a) Linear shear properties of spruce softwood. Wood Sci Technol 43:499-525

Dahl KB, Malo KA (2009a) Nonlinear shear properties of spruce softwood: experimental results. Wood Sci Technol 43:539-558

Davalos JF, Qiao P, Wang J, Salim HA, Schlussel J (2002) Shear moduli of structural composites from torsion tests. J Compos Mater 36:1151-1173

Divos F, Tanaka T, Nagao H, Kato H (1998) Determination of shear modulus on construction size timber. Wood Sci Technol 32:393-402

EN 408+A1 (2012) Timber structures-structural timber and glued lamined timber-determination of some physical and mechanical properties. European Committee for Standardization, Brussels

Gupta R, Heck LR, Miller TH (2002a) Experimental evaluation of the torsion test for determining shear strength of structural lumber. J Test Eval 30:283-290

Gupta R, Heck LR, Miller TH (2002b) Finite-element analysis of the stress distribution in a torsion test of full-size structural lumber. J Test Eval 30:291-302

Gupta R, Siller TS (2005a) A comparison of the shear strength of structural composite lumber using torsion and shear block tests. For Prod J 55:29-34

Gupta R, Siller TS (2005b) Shear strength of structural composite lumber using torsion tests. J Test Eval 33:110-117

Gupta R, Siller TS (2005c) Stress distribution in structural composite lumber under torsion. For Prod J 55:51-56

Günay E, Orçan Y (2007) Experimental investigation of the mechanical behavior of solid and tubular wood species under torsional loading. Turkish J Eng Env Sci 31:89-118

Harrison SK (2006) Comparison of shear modulus test methods. Master Thesis, Virginia Polytechnic and State University

Hearmon RFS, Barkas WW (1941) The effect of grain direction on the Young's moduli and rigidity moduli of beech and sitka spruce. Proc Phys Soc 53:674-680

Heck LR (1998) Evaluation of the torsion test for determining the shear strength of structural lumber. Master Thesis, Oregon State University

Hering S, Keunecke D, Niemz P (2012) Moisture-dependent orthotropic elasticity of beech wood. Wood Sci Technol 46:927-938

Hindman D, Manbeck HB, Janowiak JJ (2005a) Torsional rigidity of rectangular wood composite materials. Wood Fiber Sci 37:283-291

Hindman D, Manbeck HB, Janowiak JJ (2005b) Torsional rigidity of wood composite I-joists. Wood Fiber Sci 37:292-303

Hörig H (1935) Anwendung der Elastizitätstheorie anisotroper Körper auf Messungen an Holz (Application of anisotropic elasticity theory to wooden bodies). Ing.-Arch 6:8-14 (in German)

Hsieh K (2007) Numerical modeling and analysis of composite beam structures subjected to torsional loading. Master Thesis, Virginia State University

Huber K (1928) Verdrehungselastizität und -festigkeit von Hölzern (Torsion stiffness and strength of wood). Wolf, Germany (in German)

Khokhar AM (2011) The evaluation of shear properties of timber beams using torsion test method. Dissertation, Edinburgh Napier University

Koerber H, Xavier JC, Camanho PP (2010) High strain rate characterisation of unidirectional carbon-epoxy IM7-8552 in transverse compression and in-plane shear using digital image correlation. Mech Mater 42:1004-1019

Kollmann F (1951) Technologie des Holzes und der Holzwerkstoffe (Technology of wood and wood-based materials). Springer, Berlin (in German)

Kollmann F, Côté WA (1968) Principles of wood science and technology: I Solid wood. Springer, Berlin

Kúdela J (1990) Vplyv vlhkosti a teploty na mechanické vlastnosti bukového dreva (Influence of moisture and temperature on the mechanical properties of beech wood). Dissertation, Technical University in Zvolen (in Slovakian)

Kúdela J, Čunderlík I (2012) Bukové drevo - štruktúra, vlastnosti, použitie (Structure, properties and utilization of beech wood). Technical University in Zvolen, Zvolen (in Slovakian)

Lagaňa R, Rohanová A (2011) Characteristics values of beech timber for potential construction applications. Ann WULS-SGGW 75:26-29

Liu JY (1984) New shear strength test for solid wood. Wood Fiber Sci 16:567-574.

Liu JY, Ross RJ, Rammer DR (1996) Improved Arcan shear test for wood. In: Proceedings of the international wood engineering conference, New Orleans, pp. 28-31

Majano-Majano A, Fernandez-Cabo JL, Hoheisel S, Klein M (2012) A test method for characterizing clear wood using a single specimen. Exp Mech 52:1079-1096

Moses DM, Prion HGL (2002) Anisotropic plasticity and failure prediction in wood composites. Research Report, University of British Columbia

Müller U, Sretenovic A, Gindl W, Grabner M, Wimmer R, Teischinger A (2004a) Effects of macro-and micro-structural variability on the shear behavior of softwood. IAWA J 25:231-243

Müller U, Sretenovic A, Gindl W, Teischinger A (2004b) Longitudinal shear properties of European larch wood related to cell-wall structure. Wood Fiber Sci 36:143-151

Nafa Z, Araar M (2003) Applied data for modeling the behavior in cyclic torsion of beams in glued-laminated wood: influence of amplitude. J Wood Sci 49:36-41

Neumann AJ (1998) Ermittlung und Bewertung der elastischen Materialkennwerte von Vollholz in Abhängigkeit der Feuchte und der Anisotropie (Identification and evaluation of the elastic properties of solid wood depending on the moisture and anisotropy). Master Thesis, Technische Universität Dresden (in German)

Perelygin LM (1965) Náuka o dreve (Wood Science). Alfa, Bratislava (in Slovakian)

Pierron F, Vautrin A (1998) Measurement of the in-plane shear strengths of unidirectional composites with the Iosipescu test. Compos Sci Technol 57:1653-1660

Požgaj A, Chovanec D, Kurjatko S, Babiak M (1997) Štruktúra a vlastnosti dreva (Wood structure and properties). Príroda, a. s., Bratislava (in Slovakian)

Riyanto DS, Gupta R (1998) A comparison of test methods for evaluating shear strength of structural lumber. For Prod J 48:83-90

Siller TS (2002) Evaluation of the torsion test for determining the shear strength of structural composite lumber. Master Thesis, Oregon State University

Sretenovic A, Müller U, Gindl W, Teischinger A (2004) New shear assay for the simultaneous determination of shear strength and shear modulus in solid wood. Wood Fiber Sci 36:302-310

Stamer J, Sieglerschmidt H (1933) Elastische Formänderung der Hölzer (Elastic deformation of wood). Z Ver Dtsch Ing **77**:503-505 (in German)

Ugolev BN (2007) Drevesinovedenie i lesnoe tovarovedenie (Wood technology and forestry science). Izdovatestvo Moskovskogo Gostdarstvenogo universiteta lesa, Moskva (in Russian)

Ukyo S, Karube M, Harada M, Hayashi T, Murata K (2008) Determination of the shear modulus of wood with standard shear block specimen. J Soc Mater Scie 57:317-321

Ukyo S, Ido H, Nagao H, Kato H (2010) Simultaneous determination of shear strength and shear modulus in glued-laminated timber using a full-scale shear block specimen. J Wood Sci 56:262-266

Vafai A, Pincus G (1973) Torsional and bending behavior of wood beams. J Struct Div 99:1205-1221

Wagenführ R (2007) Holzatlas (Wood atlas). Fachbuchverlag Leipzig im Hanser-Verlag, München (in German)

Xavier JC, Garrido NM, Oliveira M, Morais JL, Camanho PP, Pierron F (2004) A comparison between the Iosipescu and off-axis shear test methods for the characterization of Pinus Pinaster Ait. Compos Part A-Appl Sci 35:827-840

Xavier JC, Oliveira M, Morais J, Pinto T (2009) Measurement of the shear properties of clear wood by the Arcan test. Holzforschung 63:217-225

Yang Z (2012) Torsional shear strength and size effect in structural composite lumber. Master Thesis, University of Massachusetts Amherst

Yoshihara H, Kubojima Y (2002) Measurement of the shear modulus of wood by asymmetric four-point bending tests. J Wood Sci 48:14-19

Yoshihara H, Kubojima Y, Nagaoka M, Ohta M (1998) Measurement of the shear modulus of wood by static bending tests. J Wood Sci 44:15-20

Yoshihara H, Ohsaki H, Kubojima Y, Ohta M (1999) Applicability of the Iosipescu Shear Test on the Measurement of the Shear Properties of Wood. J Wood Sci 45:24-29

Yoshihara H, Ohsaki H, Kubojima Y, Ohta M (2001) Comparison of shear stress and shear strain relations of wood obtained by Iosipescu and torsion tests. Wood Fiber Sci 33:275-283

Yoshihara H, Ohta M (2000) Estimation of the shear strength of wood by uniaxial-tension tests of off-axis specimens. J Wood Sci 46:159-163

4.5 PAPER IV

THE VERIFICATION OF THE ELASTIC MATERIAL CHARACTERISTICS OF NORWAY SPRUCE AND EUROPEAN BEECH IN THE FIELD OF SHEAR BEHAVIOR

Jaromír Milch[1,*], Martin Brabec[1], Václav Sebera[1], Jan Tippner[1]

Holzforschung (2016): Submitted manuscript

[1]Department of Wood Science, Faculty of Forestry and Wood Technology, Mendel University in Brno, Zemědělská 3, 613 00 Brno, Czech Republic; phone: +420 545 134 545

*corresponding author: jaromir.milch@mendelu.cz

ABSTRACT

This paper presents experimental and numerical analyses of uniaxial tensile test parallel to grain in *LR* a *LT* shear of plane meant for verification of elastic material characteristics applicable in FEA. Wood of Norway spruce (*Picea abies* L. Karst.) and European beech (*Fagus sylvatica* L.) was selected in order to describe its behavior when loaded in shear mode. The elastic material models used in the finite element analyses (FEA) were compiled by using in-house experimental characteristics as well as literature data sets. The calibration and verification of material characteristics were performed by 3D numerical models under the same parameters as for the experimental tests. The fully orthotropic elastic material model was applied according to the Hill yield criterion in elastic regions of uniaxial tensile. The digital image correlation (DIC) method was used to verify of numerical models with proposed elastic material characteristics. Great correlation was found between numerically predicted and experimentally measured data. The minor differences between those two data sets could be mainly attributed to certain natural wood characteristics which were neglected in proposed models, i.e., especially variation of early- and latewood density. Proposed elastic material models offer general data sets for evaluation of mechanical response of wood in field of timber structure, especially in timber connections.

KEYWORDS: Beech wood; Digital image correlation; Elastic behavior; Finite element method; Material characteristics; Orthotropic behavior, Shear properties, Spruce wood

4.5.1 INTRODUCTION

The assessing and reconstructing of historical all-wooden structures are increasingly studied topics due to their significance. The structures are commonly investigated by the experimental measurements combined with adequate analytical or numerical solutions (predictions). The numerical analyses have become more sophisticated and practically more usable in comparison with the analytical solutions when the complex issues such as joints are of interest. One of the main advantages of numerical analyses is a parametric modelling, which enables detailed sensitivity analyses. Most often, the impact of changes of the parameters such as specimen geometry, material characteristics, boundary conditions (BC's) etc. are analysed. Therefore, the main authors' effort is devoted to support utilization of the numerical all-wooden structures analyses in the Europe by means of an assembling and multi-calibrating the elasto-plastic material model for most widespread wood species such as Norway spruce (*Picea abies*, L. Karst) and European beech (*Fagus sylvatica*, L). The assembled elasto-plastic material model was already calibrated within the both linear and non-linear compression and bending behavior (Milch et al. 2016a). The present paper contributes to claimed effort by the calibration and verification of the assembled elasto-plastic material model in the field of the linear shear behavior, which stems from two main reasons. At first, the shear characteristics are one of the fundamental parameters describing the mechanical behavior of construction materials and, at second, the shear characteristics are used as an input data beside the normal characteristics and Poisson's ratios for defining the material behavior within the numerical analyses.

There are many possibilities how to induce the shear stresses and strains in the sample. However, to obtain pure shear stress-strain state within a major part of sample volume, only few specific shear tests such as for instance a torsion test may be used. The pure shear strain field takes place within the span along the twisted bar, which is fully constrained at both ends, where well-known st. Venant principle is to be considered (Gupta et al. 2002, Gupta and Siller 2005, Hsieh 2007). Conversely, in most cases the shear strains are accompanied by the non-shear strains such as for instance during the standard shear block test. Prabhakaran (1985), Ukyo et al. (2008 and 2010), Gupta and Sinha (2012) and many others proved overturning moment and a significant normal strains, which occurred in the shear block sample. McNatt (1969) reported the non-shear strains also for a one-rail shear test using the un-notched specimen under tilt

angle of 5°. Nevertheless, Sretenovic et al. (2004) observed the minimal non-shear strains when performing one-rail shear test under tilt angle of 8°.

It was proved, that the pure shear stresses and strains can be induced at least locally by the mutually aligned notches made on the opposite sides of the sample such as in the standard Iosipescu shear test (Iosipescu 1967), Arcan's shear test (Arcan et al. 1978) or one-rail shear test under tilt angle of 0° (Ikeda et al. 1996). While the eccentric opposite forces are applied parallel to the notches, the narrow zone between the opposite notches bottoms containing the almost pure shear stress-strain field was obtained (Prabhakaran 1985, Dumail et al. 2000, Kubojima et al. 2000, Odegard and Kumosa 2000, Xavier et al. 2003, Melin and Neumeister 2006, Melin et al. 2008, Dahl and Malo 2009a and 2009c and Müller et al. 2015). However, the width of such zone reduces as the load increases (Yoshihara et al. 1999). The mentioned pure shear zone is too narrow to be measured by the traditional strain gauges glued onto sample surface. Consequently, the shear characteristics obtained from these tests can be distorted. In order to obtain true shear characteristics by this measurement approach, the correction factors, which take into account the presence of the non-shear strains within the measured strain field, were determined by Dahl and Malo (2009a and 2009b) and Xavier et al. (2009) for the Arcan's shear test as well as by Pierron and Vautrin (1994) and Xavier et al. (2003 and 2004) for the Iosipescu shear test. Despite, Melin and Neumeister (2006), Melin (2008) or Müller et al. (2015) showed that the zone of the pure shear strains, regardless on its dimensions, is fully usable for the true shear characteristics determination within the Arcan's or Iosipescu shear tests when the full-field deformation measurement is employed.

The narrow pure shear strain zone between notches may be obtained also when the notches on opposite sides of the sample are certainly spaced from each other and the opposite forces are applied perpendicularly to the notches. This phenomenon was used by Yoshihara and Ohhata (2003) or Yoshihara (2012) in order to support the shear failure of the beam loaded by an asymmetric four-point bending method. Melin et al. (2000) used similar principle by making double-notch in the rectangular compression sample exactly into the half-depth; they obtained the pure shear strain zone between the notches bottoms. Bonfield and Ansell (1991) as well as Yoshihara and Matsumoto (2005) notched the rectangular tension samples in the same way and they obtained the shear characteristics of the solid wood and wood-based panels.

In order to calibrate the created non-linear elasto-plastic material model (Milch et al. 2016a) by the simple test without using any special sample fixture or equipment, the well-known tension test of the dog-bone shaped sample (Hering et al. 2012 or Niemz et al. 2014) was used. The sample was notched to a depth of half-width onto opposite sample sides. In this manner, the complex strain field consisting of the shear and non-shear strains between the notches was captured and compared with the numerical ones.

4.5.2 MATERIAL AND METHODS

4.5.2.1 MATERIAL

Experimental measurements were carried out on small clear specimens made from Norway spruce (*Picea abies* L. Karst.) and European beech (*Fagus sylvatica* L.). Before the sampling, boards were conditioned in a climate chamber at 20 °C and 65% relative humidity (RH) until the equilibrium moisture content (EMC) was reached. The boards were cut into the well-known dog-bone shaped specimens with the modified dimensions as displayed in Fig. **4.5.2-1** and listed in Tab. **4.5.2-1**. The testing volume (TV) of specimens was tapered from all four sides to a waist with a cross-section of radial (*R*) × tangential (*T*) = 10 × 10 mm^2. In order to obtain the complex strain field including the longitudinal-radial (*LR*) or longitudinal-tangential (*LT*) shear strains, the TV was double-notched by a saw blade to a depth of half-width onto opposite *LR* or *LT* specimen sides (Fig. **4.5.2-1**). In order to prevent the specimen against a crush within the clamping volume (CV), the transverse compression stresses induced by self-locking jaws during tensile loading was reduced by using of end-tabs. They were made from same wood species as the specimens and glued by poly-vinyl-acetate glue onto the opposite surfaces of the CV. In order to improve the image matching during DIC computation, a stochastic and high-contrast speckle pattern was created by a basic matt white paint followed by a finely pigmented black paint. The pattern was sprayed on appropriate side of TV. The moisture absorbed from the glue lines of the end-tabs and from the speckle pattern was reduced by re-conditioning at the standard climate conditions. The final moisture content (MC) and density was measured gravimetrically in compliance with test standard ASTM D2395 (American Society for Testing and Materials 2014).

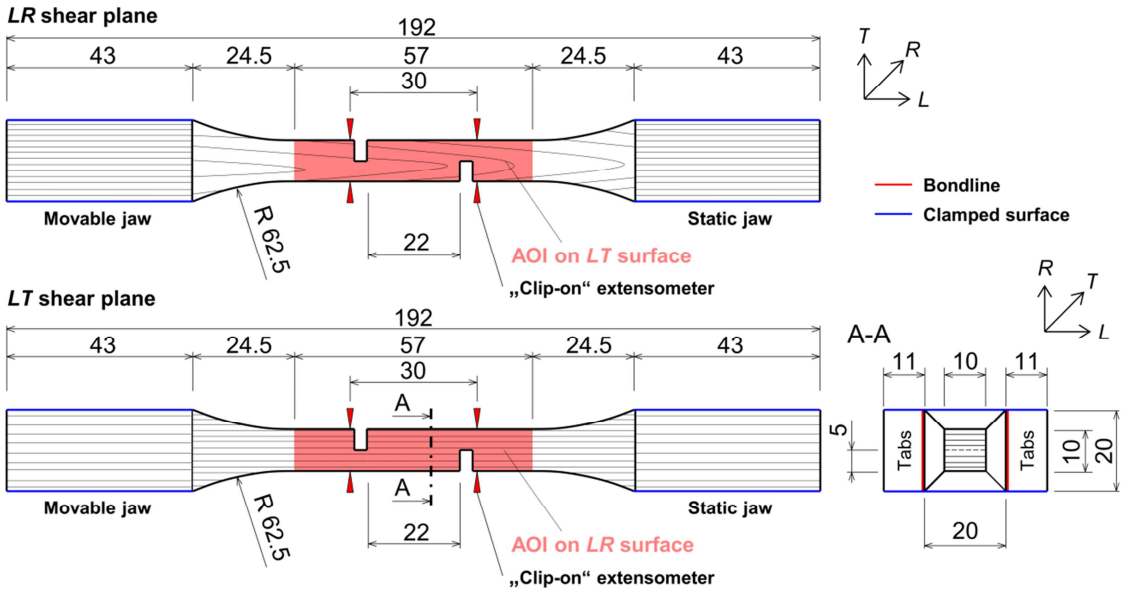

Fig. 4.5.2-1: Scheme of the tensile shear test specimens. Red areas display AOI on *LR* and *LT* plane

Tab. 4.5.2-1: The specimen parameters

	NORWAY SPRUCE (*Picea abies* L. Karst.)		**EUROPEAN BEECH (*Fagus sylvatica* L.)**	
PLANE	***LR***	***LT***	***LR***	***LT***
Number of samples	7	7	7	7
ρ_{12} (kg·m^{-3})	489 (10.86)[a]	477 (6.47)	708 (1.84)	700 (1.76)
Cross section in CV[b] ($R \times T$) (mm)	20 (+12) × 20 (+12)		20 (+12) × 20 (+12)	
Cross section in TV[c] ($r \times t$) (mm)	10 × 10		10 × 10	
Tabs ($L \times R \times T$) (mm)	47 × 20 × 12		47 × 20 × 12	
Shear area ($L \times R$ or T) (mm)	22 × 10		22 × 10	
Area of Interest (AOI)	on *LT*	on *LR*	on *LT*	on *LR*
Total sample length (l_t) (mm)	192		192	
Load direction	*L*		*L*	

[a]Coefficient of Variation [%] in parenthesis, [b]Cross section of clamping volume (CV) + end-tabs, [c]Cross section of testing volume (TV)

4.5.2.2 EXPERIMENTAL ANALYSIS

The tensile loading was performed using universal testing machine Zwick Z050/TH 3A (Zwick Roell AG, Germany) with 50 kN load cell at quasi-static loading rate of 1.8 mm.min^{-1} until the failure. The experiment procedure was set and controlled by TestXpert v.11.02 (Zwick Roell AG, Germany). The mechanical response of the specimens during the tensile loading was evaluated based on the total strain in the

longitudinal direction (ε_L) and *LR*, resp. *LT* shear strains within the TV. The ε_L was calculated based on the relative position of two isolated points, which were mechanically tracked on both opposite specimen sides with help of the conventional "clip on" extensometers (Zwick Roell AG, Germany), see Fig. **4.5.2-2**. The points were spaced 30 mm from each other along the longitudinal direction and positioned in such a way that both notches were located between them (Fig. **4.5.2-1**).

The complex strain field was captured by the full-field optical technique based on DIC. Two CCD cameras (AVT Stingray Copper F-504B, Allied Vision Technologies, Osnabrück, Germany, cell size of 3.45 µm and resolution of 2452×2056 pixels) equipped with lenses (Pentax C2514-M, Pentax Precision Co., Ltd., Tokyo, Japan, focal length of 25 mm) at the stereo-vision configuration (3D) were used (Fig. **4.5.2-2**). The patterned specimens surface was illuminated by two light sources SobrietyCube 360 (Sobriety Ltd. Kuřim, Czech Republic) fitted by LED sensors (Luminus Phlatlight CSM-360, 90 W Luminus Devices Inc., Billerica, MA, USA). The stereo-vision system was centered to the area of interest (AOI), which covered the surface of the straight section from TV (see details in Fig. **4.5.2-1**, Fig. **4.5.2-2** and Fig. **4.5.2-3**). The images together with applied force were synchronously captured in the acquisition interval of 0.25 s (4 Hz) with help of the hardware trigger device. The calculation of the shear strain (ε_{LR} and ε_{LT}) was performed by software Vic-3D v. 2010 (Correlated Solutions Inc., Columbia, SC, USA).

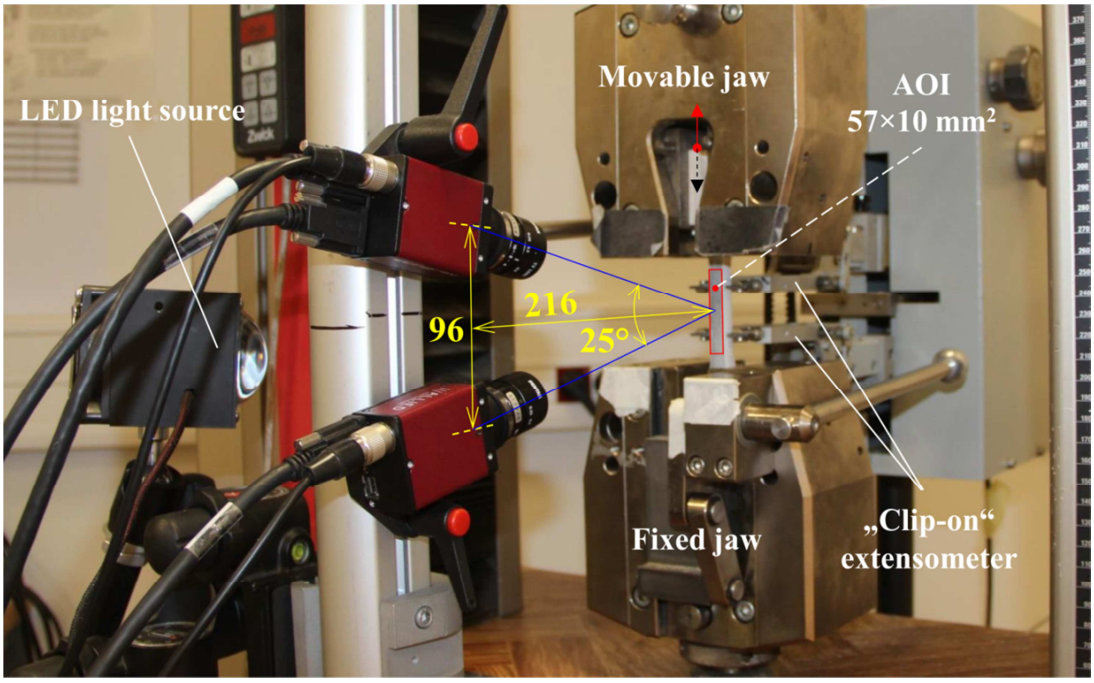

Fig. 4.5.2-2: Experimental test configurations: stereo-vision optical system (3D) for image acquisition of the tests, dimensions in mm

4.5.2.3 NUMERICAL ANALYSIS

The numerical analysis was performed using the FEA in the ANSYS computing system using the ANSYS Parametric Design Language (ANSYS® Mechanical APDL, v.14.5). The specimen models were parametrically built in true scale (1:1) as a 3D solid model. The volume geometry of finite-element (FE) models was meshed using 3D hexahedral 20-node structural solid element SOLID95. The element size was set to 4, 2 and 1 mm for the CV, tapering and straight section of the TV, respectively, thus the total number of elements was approx. 10 500 elements. The numerical analyses were conducted under the BC's that physically reflected experimental testing. Therefore, the force was applied in the longitudinal direction via nodes located onto opposite sides of the clamped surfaces, see Fig. **4.5.2-1**. The all degrees of freedom were fully constrained (all DOF's = 0) at one CV; meanwhile the movement along the load direction of the other one was free.

Fully orthotropic elastic material characteristics for spruce and beech wood were obtained using data sets from in-house experiments (Brabec et al. 2015), namely normal moduli (E_L, E_R, and E_T). The shear moduli (G_{LR}, G_{RT}, and G_{LT}) and Poisson's ratios (v_{LR}, v_{RT}, and v_{LT}) were taken from Kollmann and Côte (1968) and Požgaj et al. (1997). Tab. **4.5.2-2** presents compiled fully orthotropic elastic material models used in FEA.

Tab. 4.5.2-2: Fully orthotropic elastic material characteristics used in FEA

	E_L[a] MPa	E_R[a] MPa	E_T[a] MPa	G_{LR}[b] MPa	G_{RT}[b] MPa	G_{LT}[b] MPa	v_{LR}[b] MPa	v_{RT}[b] MPa	v_{LT}[b] MPa
NORWAY SPRUCE (*Picea abies* L. Karst.)	17850	352	289	573	53	474	0.023	0.557	0.014
EUROPEAN BEECH (*Fagus sylvatica* L.)	13439	1880	1031	1608	460	1059	0.073	0.360	0.043

[a]adopted from in-house experiments by Brabec et al. (2015), [b]adopted from Kollmann and Côte (1968) and Požgaj et al. (1997)

4.5.2.4 CALIBRATION AND VERIFICATION PROCEDURE

The calibration procedure was based on the fitting of the numerically predicted force-displacement curves to the experimental ones obtained using the extensometers and their virtual analogy. It was an iterative procedure based on the changing of the

input material characteristics used in the numerical models. Within each step, the difference between the predicted and measured force-displacement curves was determined, then the input material characteristics were changed to see the response of that difference. This was repeated until the numerically predicted curve was positioned between the experimental ones (Fig. **4.5.3-2**).

A verification procedure was derived from Sebera et al. (2013) who directly compared the deflections of the CLT panel obtained from full-field DIC and FEM data sets. The current numerical model was verified by means of the comparison of the predicted and measured shear strains (ε_{LR} and ε_{LT}) located on the lines at specific positions within the captured surface of the TV (sectional lines 3, 2, 1, M, -1, -2, -3, and H) as depicted on Fig. **4.5.2-3**. The comparison was performed at the end of elastic load level before the proportional limit. The accuracy of the numerical model was determined as the relative difference between the experimental and numerically predicted shear strains.

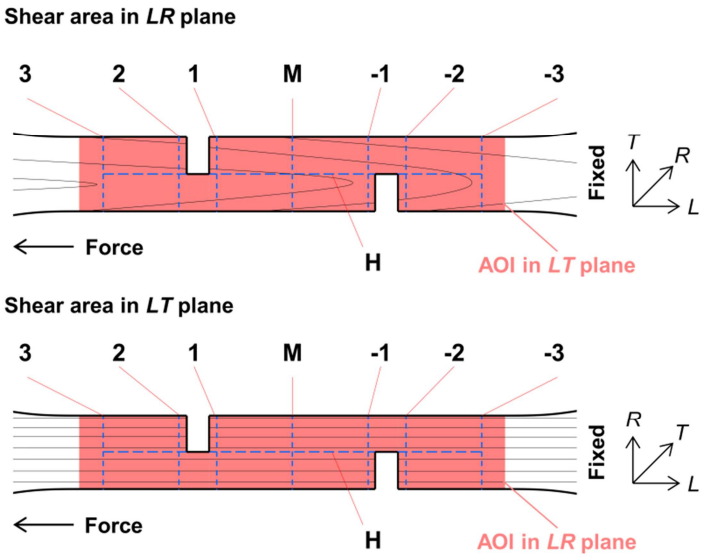

Fig. 4.5.2-3: Positions and paths along the length of the TV in which ε_{LR} and ε_{LT} were analysed; M is the middle level and H is the horizontal level

4.5.3 RESULTS AND DISCUSSION

The full-field strain analysis revealed the narrow close-to-pure shear area between the notch roots, which is consistent with findings reported by Bonfield and Ansell (1991), Hassaini (1998), Melin et al. (2000) as well as by Yoshihara and Matsumoto (2005). Kollmann and Côté (1968) stated that the shear behavior of the wood subjected

to the pure shear strain-strain state is linear to the 90% of F_{max}. Since the force-displacement curves were constructed from the displacement between the points on sample surface located outside the close-to-pure shear area (see location of the mechanical and virtual extensometers in Fig. **4.5.2-1**), it can be expected that the linear shear behavior described by Kollmann and Côté (1968) cannot be captured. As is apparent from the Fig. **4.5.3-1**, this assumption was clearly confirmed. From the Fig. **4.5.3-1** it is also evident that the beech wood exhibits the linearity in the shear behavior up to 80% of F_{max}, whereas the spruce wood to 20% of F_{max} only. This difference could be attributed to the anatomical structure of the both woods. Higher difference between the early- and latewood of the spruce wood may play the important role in this issue.

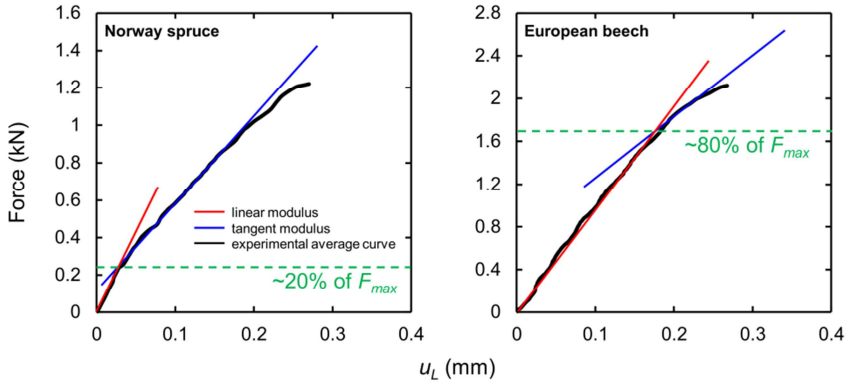

Fig. 4.5.3-1: The determination of the proportional limit (green line) from the average bi-linear curves for both wood species: *left* – Norway spruce, *right* – European beech

The non-linear behavior of wood could be properly described with using of the elasto-plastic material model allowing the hardening or softening. The stress-strain behavior of wood exhibits the non-linear ductile behavior in compression owing to the crushing of wood cell walls and the separation of the fibres. Conversely, the tension and shear stress-strain behavior is linear (or bi-linear) until abrupt brittle failure occurs (Clouston and Lam 2002; Moses and Prion 2002). Owing to the partially plastic shear behavior proved by the force-displacement curves in Fig. **4.5.3-1**, it could be suitable to calibrate and verify the assembled elasto-plastic material model (Milch et al. 2016a) within the fully non-linear behavior including the softening which leads to rupture analysis. However, for the modelling of timber structures it is often sufficient to use only elastic material model for structural assessment (Milch et al. 2016b). Therefore, only the elastic part of the elasto-plastic material model without softening was

calibrated. The full calibration of the assembled material model for beech and spruce wood including the softening with rupture analysis is the next step for the future work.

The calibration procedure was based on the fitting of the numerically predicted force-displacement curves to the experimental ones obtained by the extensometers and their virtual analogy. The final step of this iterative procedure is depicted in Fig. **4.5.3-2**. As is apparent, the force-displacement curves obtained from the FEA do not coincide exactly with the experimental average value of the shear modulus (differences about 12%). However, this is the best possible result of the multi-calibration procedure, which includes calibration within other loading types such as compression and bending load (Milch et al. 2016a).

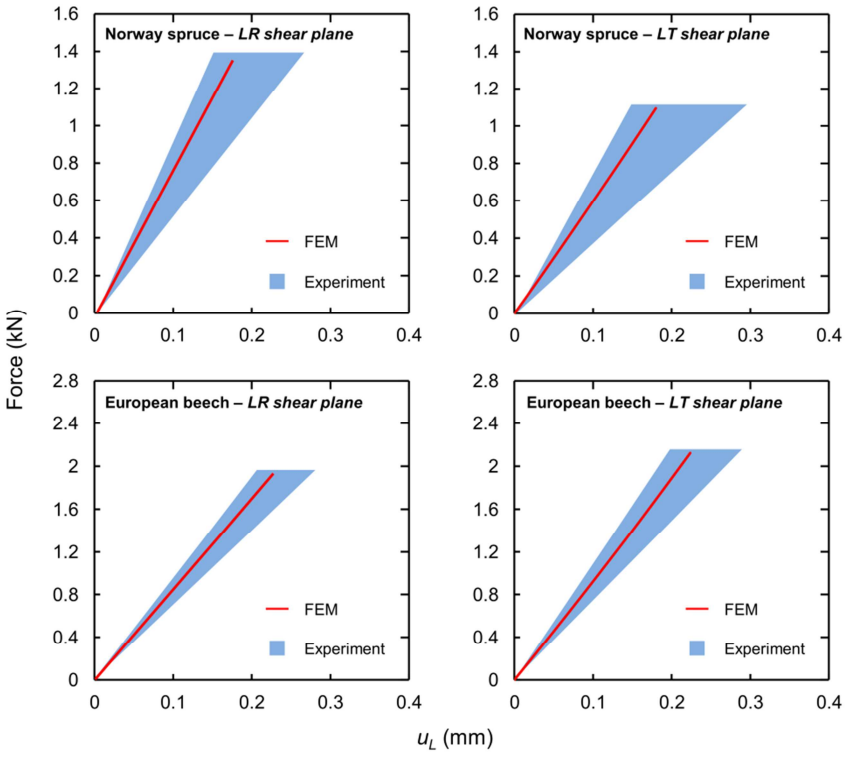

Fig. 4.5.3-2: The relationship between force-displacement curves of tensile tests in *LR* and *LT* shear plane for Norway spruce and European beech wood. Red curves represent FE prediction of elastic behavior and blue areas represent range between minimal and maximal experimental curves

The different shear behavior of the beech and spruce wood is understandable due to the fact that the maximal elastic load level before the proportional limit, which was used for verification of the globally calibrated model, was different for both wood species in respect to respective F_{max}. Fig. **4.5.3-3** presents the comparison of the strain fields ε_{LR} and ε_{LT} obtained by DIC and FEA, which are located at specific positions and mapped

onto sectional lines 3, 2, 1, M, -1, -2, -3, and H within the captured surface of the TV. The experiment and its numerical prediction greatly correlate to each other; nevertheless, the reasonable low differences are observable. These minor differences between experimentally measured and numerically predicted distribution curves of ε_{LR} and ε_{LT} along the sectional lines could be attributed to anatomical structure of wood, i.e. especially to early- and latewood density, which were not considered in proposed numerical models.

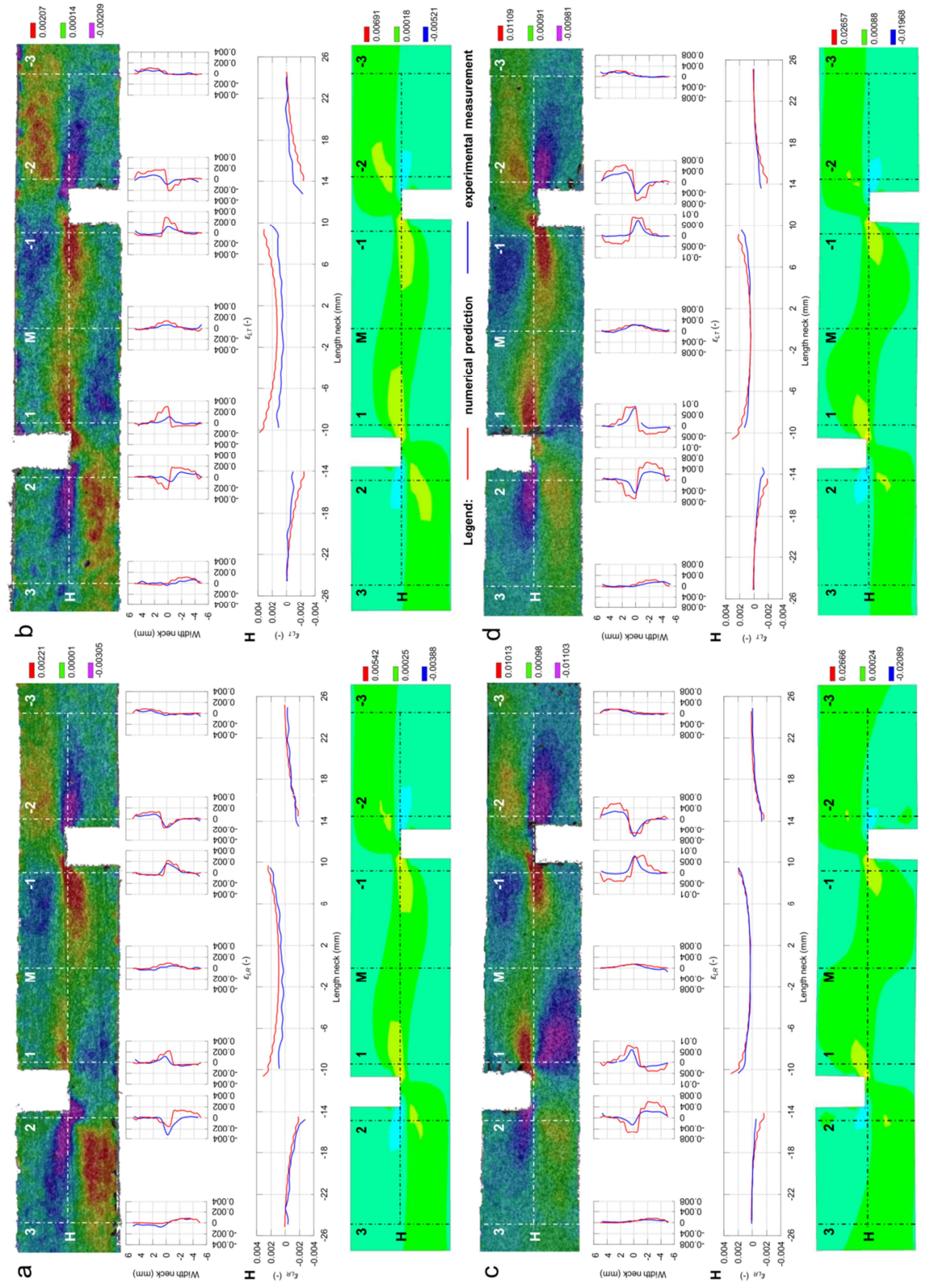

Fig. 4.5.3-3: The ε_{LR} and ε_{LT} comparison between DIC and FEA. Norway spruce tested in *LT* shear plane (a) and *LR* shear plane (b); European beech tested in *LT* shear plane (c) and in *LR* shear plane (d)

4.5.4 CONCLUSION

This paper presents verification of constitutive material characteristics for Norway spruce and European beech wood species, while fully orthotropic elastic material model with linear mechanical behavior are taken into account in FEA. The elastic material models for most commonly used wood species applied in timber constructions in Central Europe were assembled and verified using experimental data sets obtained by DIC technique in the tensile test in *LR* and *LT* shear plane. The total longitudinal strain (ε_L) and shear strain (ε_{LR} and ε_{LT}) indicated great agreement among the data of the experimental and numerical analyses.

The FEA results are in great correlation with the experiments and show a satisfactory implementation of the constitutive law into the finite element code. The verified elastic material characteristics are suitable for the assessment of mechanical response of more complex problems, i.e. timber structure with respect to connection of wooden elements using FE method.

Acknoledgments: This paper was created at the Research Center Josef Ressel in Brno-Utěchov, Mendel University in Brno and was funded by NAKI project " Historical Timber Structures: Typology, Diagnostics and Traditional Wood Working" reg. No, DG16P02M026, provided by the Ministry of Culture of the Czech Republic.

4.5.5 REFERENCES

Arcan, M., Hashin, Z., Voloshin, A. (1978) A method to produce uniform plane-stress states with applications to fiber-reinforced materials. Exp Mech 18:141-146

ASTM D143 (2014) Standard Test Methods for Small Clear Specimens of Timber American Society for Testing and Materials, Philadelphia, PA, USA.

ASTM D2395 (2014) Standard Test Methods for Density and Specific Gravity (Relative Density) of Wood and Wood-Based Materials. American Society for Testing and Materials, Philadelphia, PA, USA.

Bonfield, P.W., Ansell, M.P. (1991) Fatigue properties of wood in tension, compression and shear. J Mater Sci 26:4765-4773

Brabec, M., Tippner, J., Sebera, V., Milch, J., Rademacher, P. (2015) Standard and non-standard deformation behaviour of European beech and Norway spruce during compression. Holzforschung 69:1107-1116

Dahl, K.B., Malo, K.A. (2009a) Linear shear properties of spruce softwood. Wood Sci Technol 43:499-525

Dahl, K.B., Malo, K.A. (2009b) Nonlinear shear properties of spruce softwood: Numerical analyses of experimental results. Compos Sci Technol 69:2144-2151

Dumail, J.F., Olofsson, K., Salmén, L. (2000) An Analysis of Rolling Shear of Spruce Wood by the Iosipescu Method. Holzforschung 54:420-426

Gupta, R., Heck, L.R., Miller, T.H. (2002) Finite-element analysis of the stress distribution in a torsion test of full-size structural lumber. J Test Eval 30:291-302

Gupta, R., Siller, T.S. (2005) Shear strength of structural composite lumber using torsion tests. J Test Eval 33:110-117

Gupta, R., Sinha, A. (2012) Effect of grain angle on shear strength of Douglas-fir wood. Holzforschung 66:655-658

Hering, S., Keunecke, D., Niemz, P. (2012) Moisture-dependent orthotropic elasticity of beech wood. Wood Sci Technol 46:927-938

Hsieh, K. (2007) Numerical Modeling and Analysis of Composite Beam Structures Subjected to Torsional Loading. Master Thesis, Virginia State University

Ikeda, M., Masuda, M., Murata, K., Ukyo, S. (2006) Analysis of in-plane shear behaviour of wood based panels by digital image correlation. J Soc Mater Scie 55:569-575

Iosipescu, N. (1967) New accurate procedure for single shear testing of metals. J Mater 2:537-566

Kollmann, F.F., Côte, W.A. (1968) Principles of Wood Science and Technology I. Solid Wood. In Principles of Wood Science and Technology. Springer-Verlag, New York.

Kubojima, Y., Yoshihara, H., Ohsaki, H., Ohta, M. (2000) Accuracy of shear properties of wood obtained by simplified Iosipescu shear test. J Wood Sci 46:279-283

McNatt, J.D. (1969) Rail shear test for evaluating edgewise shear properties of wood-base panel products. Forest Product Laboratory, Madison

Melin, L.G., Neumeister, J.M., Pettersson, K.B., Johansson, H., Asp, LE. (2000) Evaluation of Four Composite Shear Test Methods by Digital Speckle Strain Mapping and Fractographic Analysis. J Compos Tech Res 22:161-172

Melin, L.N. (2008) The modified Iosipescu shear test for orthotropic materials. Dissertation, Royal Institute of Technology (KTH)

Melin, L.N., Neumeister, J.M. (2006) Measuring constitutive shear behavior of orthotropic composites and evaluation of the modified Iosipescu test. Compos Struct 76:106-115

Milch, J., Tippner, J., Sebera, V., Brabec, M. (2016a) Determination of the elasto-plastic material characteristics of Norway spruce and European beech wood by experimental and numerical analyses. Holzforschung DOI: 10.1515/hf-2015-0267. (in press)

Milch, J., Tippner, J., Sebera, V., Kunecký, J., Kloiber, M. (2016b) The numerical assessment of a full-scale historical truss structure reconstructed with use of traditional all-wooden joints. J Cult Herit 21:759-766

Müller, U., Ringhofer, A., Brandner, R., Schickhofer, G. (2015) Homogeneous shear stress field of wood in an Arcan shear test configuration measured by means of

electronic speckle pattern interferometry: description of the test setup. Wood Sci Technol 49:1123-1136

Niemz, P., Ozyhar, T., Hering, S., Sonderegger, W. (2014) Zur Orthotropie der physikalisch-mechanischen Eigenschaften von Rotbuchenholz. Bautechnik 92:3-8

Odegard, G., Kumosa, M. (2000) Determination of shear strength of unidirectional composite materials with the Iosipescu and 10° off-axis shear tests. Compos Sci Technol 60:2917-2943

Ozyhar, T., Hering, S., Sanabria, S.J., Niemz, P. (2013) Determining moisture-dependent elastic characteristics of beech wood by means of ultrasonic waves. Wood Sci Technol 47:329-341

Pierron, F., Vautrin, A. (1994) Accurate comparative determination of the in-plane shear modulus of T300/914 by the iosipescu and 45° off-axis tests. Compos Sci Technol 52:61-72

Požgaj, A., Chovanec, D., Kurjatko, S., Babiak, M. (1997) Štruktúra a vlastnosti dreva. Priroda a.s., Bratislava

Prabhakaran, R. (1985) Shear testing of composites. J Theor Appl Mech 23:607-615

Sebera, V., Muszyński, L., Tippner, J., Noyel, M., Pisaneschi, T., Sundberg, B. (2013) FE analysis of CLT panel subjected to torsion and verified by DIC. Mater Struct 48:451-459.

Sretenovic, A., Müller, U., Gindl, W., Teischinger, A. (2004) New shear assay for the simultaneous determination of shear strength and shear modulus in solid wood. Wood Fiber Sci 36:302-310

Ukyo, S., Ido, H., Nagao, H., Kato, H. (2010) Simultaneous determination of shear strength and shear modulus in glued-laminated timber using a full-scale shear block specimen. J Wood Sci 56:262-266

Ukyo, S., Karube, M., Harada, M., Hayashi, T., Murata, K. (2008) Determination of the shear modulus of wood with standard shear block specimen. J Soc Mater Scie 57:317-321

Xavier, J.C., Oliveira, M., Morais, J.L., Camanho, P.P., Pierron, F. (2003) Measurement of the shear modulus of wood P. pinaster Ait. by the Iosipescu test: numerical aspects. In: VII Congresso Nacional de Mecânica Aplicada e Computacional. Évora, Portugal

Xavier, J.C., Garrido, N.M., Oliveira, M., Morais, J.L., Camanho, P.P., Pierron, F. (2004) A comparison between the Iosipescu and off-axis shear test methods for the characterization of Pinus Pinaster Ait. Compos Part A-Appl S 35:827-840

Xavier, J.C., Oliveira, M., Morais, J.L., Pinto, T. (2009) Measurement of the shear properties of clear wood by the Arcan test. Holzforschung 63:217-225

Yoshihara, H. (2012) Shear Modulus and Shear Strength Evaluation of Solid Wood by a Modified ISO 15310 Square-Plate Twist Method. Drvna Ind 63:51-55

Yoshihara, H., Matsumoto, A. (2005) Measurement of the shearing properties of wood by in-plane shear test using a thin specimen. Wood Sci Technol 39:141-153

Yoshihara, H., Ohhata, O. (2003) Method of Measuring the Shear Strength of Wood by the Asymmetric Four-Point Bending Test Using a Notched Beam Specimen. J Test Eval 31:1-5

Yoshihara, H., Ohsaki, H., Kubojima, Y., Ohta, M. (1999) Applicability of the Iosipescu Shear Test on the Measurement of the Shear Properties of Wood. J Wood Sci 45:24-29

4.6 PAPER V

NOVEL SANDWICH PANEL WITH INTERLOCKING PLYWOOD KAGOME LATTICE CORE AND GROOVED PARTICLEBOARD FACINGS

Petr Klímek [1,*], Rupert Wimmer [1, 2], Martin Brabec[1], Václav Sebera [1]

BioResources (2016) 11-1: 195-208

[1] Department of Wood Science, Faculty of Forestry and Wood Technology, Mendel University in Brno, Zemědělská 3, 613 00 Brno, Czech Republic; phone: +420 545 134 029

*corresponding author: xklimek@node.mendelu.cz

[2] Institute for Natural Materials Technology, IFA Tulln, University of Natural Resources and Life Sciences

ABSTRACT

A new sandwich composite structure was prepared that utilizes classic wood-based composites as the core and face materials. Particleboards were used as faces, which covered a plywood-made iso-grid core. A new type of core-face fixation was suggested and assessed. The sandwich panels can be regarded as lightweight, as their density was below 400 kg/m^3. Digital image correlation (DIC) was used to determine Poisson's ratios and obtain additional insight into the deformation behavior of the sandwich panel. DIC was also employed to assess the core-face bonding, which was based on imprinted grooves on one side of the particleboard face. The results include strength in edgewise and flatwise compression and flexural properties. The latter were determined through three-point bending tests. Comparable strength properties were found relative to the literature, which means that this new type of sandwich panel demonstrates a competitive property profile. It was concluded that the developed sandwich panel is versatile, and the hollow spaces in the core can be filled with insulation materials such as fibers or foams. Surfaces can also be covered with some overlay, delivering improved bending performance.

KEYWORDS: Wood-based panel; Sandwich structure; Mechanical testing; Digital image correlation; DIC; Imprinted density pattern

4.6.1 INTRODUCTION

Sandwich composite materials that display high strength to low density have been favored for structural and aesthetic applications, e.g., in aerospace, marine, or automotive industries (Davies 2001; Vasiliev et al. 2001; Fan et al. 2007). High stiffness-to-density ratios are obtained by designing suitable core materials, which can be made of foams (Shalbafan 2013), low-density materials such as balsa wood (Bekisli and Grenestedt 2004; Kepler 2011), cork (Král et al. 2014), an iso-grid structure (Vasiliev et al. 2001; Fan et al. 2007; Zhang et al. 2008; Li et al. 2014), or paper-based corrugated structures (Hunt and Gunderson 1988; Hunt et al. 2004; Labans et al. 2011). To obtain a sandwich composite, the core is covered by lamellar top layers made of various materials. The range of possible core structures allows versatile configurations and specifications of the iso-grid core. Interlocking grids have been used in the development of various products (Vasiliev et al. 2001; Fan et al. 2007; Tao et al. 2011). Iso-grid shapes, which have been made with metal and laminate materials (Fan et al. 2007; Li et al. 2014), might also be possible using strips prepared from plywood. Plywood as a corrugated core material has been utilized in sandwich panels (Bhattacharyya et al. 2011; Labans and Kaliniš 2011). Beside stiffness and strength of the material, Poisson's ratios of the material are also important for the assessment of the deformation behavior.

In general, sandwich composite materials require sound numerical models to fully understand the structural and mechanical behavior (Mackerle 2005; Wilczyński and Kociszewski 2010; Labans and Kaliniš 2011; Kanou et al. 2013). Research on robust material models may include non-contact optical techniques such as digital image correlation (DIC), which has been used to analyze wood-based composites on various scales (Zink et al. 1995; Sutton et al. 2009; Hussain et al. 2011; Sebera et al. 2013).

In this research, a new sandwich composite structure is proposed, utilizing classic wood-based composites as core and face materials. As core-face bonding is crucial in manufacturing (Davies 2001), a new type of core-face fixation is suggested using imprinted grooves in the inner sides of the face material. The following research issues are addressed: (1) development of a lightweight sandwich composite having an interlocking iso-grid plywood core, covered by grooved particleboard faces; (2) analysis of bending and compressive performance, (3) qualitative analysis of bondline failures, and (4) determination of Poisson's ratios using DIC.

4.6.2 EXPERIMENTAL

The newly introduced sandwich composite is composed of two components: (1) particleboard face layers that are groove-imprinted on one side, and (2) a 3-layer birch plywood cut in straight strips and intersected to form the iso-grid core. Single-layer particleboards were produced on a laboratory scale with *in-situ* imprinting of self-designed hexagonal patterns, under the conditions listed in Tab. **4.6.2-1**. The grooves imprinted on the inner sides of the particleboard faces provided exact positioning of the plywood strips, which improved the overall core-face bonding (Fig. **4.6.2-1**).

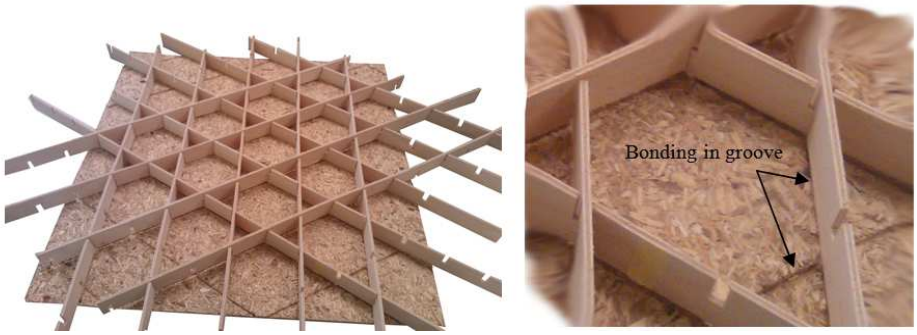

Fig. 4.6.2-1: Particleboard faces with imprinted grooves for iso-grid core positioning and fixation

A single-layer particleboard with an imprinted hexagonal pattern was produced in the laboratory, under the conditions listed in Tab. **4.6.2-1**. The particles were obtained from a local particleboard manufacturer; the average particle size was 1.7 mm in width and 7.5 mm in length. Gluing for the particleboards was done with the urea-formaldehyde resin Prefere 4170 (Dynea™, Lillestrom, Norway) and the hardener Kronoadd HL 100 (Dukol Ostrava s.r.o, Ostrava, Czech Republic). Particles were resinated in a laboratory rotating drum for 10 min, with hardener and distilled water subsequently added. The moisture content was adjusted to 11%. The particle furnish was manually pre-pressed in a rectangular wooden frame 600 × 600 mm in size prior to insertion in the hot-press. Metal distance bars 5 mm in thickness were used on both sides of the particle mat. The stainless steel iso-grid pattern was positioned on top of the pre-pressed particle mat (Fig. **4.6.2-2**). Particleboards were pressed for 50 s at 190 °C, at a specific press-pressure of 3.2 MPa. After pressing, the stainless steel iso-grid pattern was removed and the boards were conditioned for two weeks at 65% relative humidity and 24 °C. Finally, the particleboards were formatted to 500 × 500 mm.

Tab. 4.6.2-1: Parameters for laboratory-produced single-layer particleboards

PARAMETER	VALUE
Thickness	5 mm
Dimensions	600 × 600 mm
Density	800 kg/m^3
Resination ([g] solid to [g] dry wood particles)	8 %
Hardener ([g] solid to [g] solid resin)	1.5 %
Targeted moisture content of particles	11 %

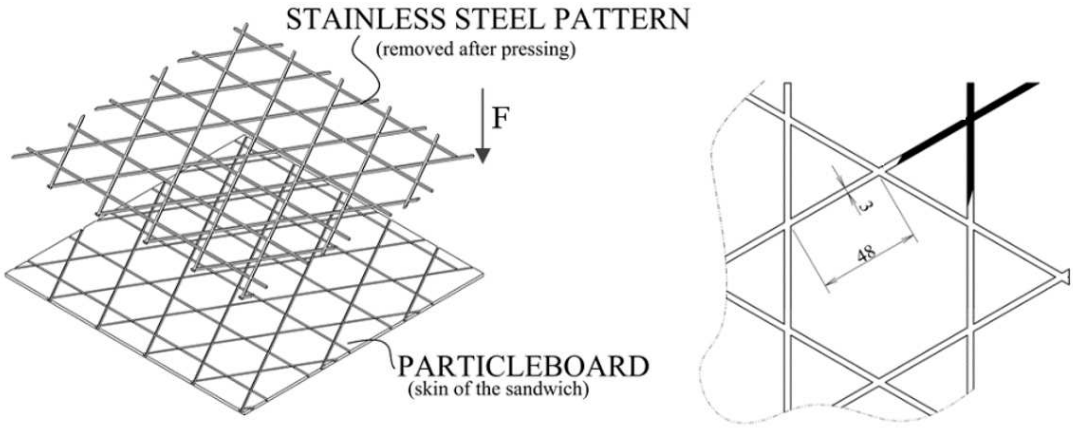

Fig. 4.6.2-2: *left* – particleboard face with inserted stainless steel pattern for imprinting, *right* – stainless-steel iso-grid pattern

Strips 35 mm in width were cut from 3-mm three-layer birch plywood obtained from a local manufacturer. Strips were pre-assembled without adhesive and glued into the imprinted groove pattern (Fig. **4.6.2-1**) by using PVAc adhesive Soudal 67A (INVA Building Materials s.r.o, Praha, Czech Republic), which was equally applied to all the grooves prior to assembling. No adhesive was applied to hold the plywood pieces to each other. The sandwich panel was pressed at a specific pressure of 0.7 MPa for 45 min, followed by conditioning for 24 h at 24 °C and 65% relative humidity to ensure proper curing of the adhesive.

Samples were cut from the particleboard as shown in Fig. **4.6.2-3**. Mechanical properties were measured according to ASTM C365-11 (2011), ASTM C393-06 (2006), and ASTM C297 (2009) standards. Tests were performed on a ZWICK Z050/TH 3A (Zwick Roell AG, Ulm, Germany) universal testing machine.

4.6.2.1 EDGEWISE COMPRESSION TEST

The edgewise compression test followed ASTM C364-07 (2012), which was used to measure the facing compressive panel strength. A loading rate of 2 mm/min was applied to both tested specimens that were cut from the sandwich panel. Because of the symmetrical shape of the core, only one edgewise loading direction was tested. Tab. **4.6.2-2** lists details of all of the tested samples.

4.6.2.2 FLATWISE COMPRESSION TEST

The compressive properties of the panel were measured according to ASTM C365-11 (2011) in a flatwise direction. The panel strength and modulus of elasticity (MOE) were assessed. The loading rate was 2 mm/min. Specimens were cut from the panels in such a way that they covered the entire hexagonal iso-grid units of the core (Tab. **4.6.2-2**).

4.6.2.3 BENDING TESTS

Three-point bending tests followed ASTM C393-06 (2006) to obtain shear stresses in the core as well as in the faces. The sandwich panel width allowed the inclusion of a complete iso-shape core unit (Fig. **4.6.2-3**). The span between the supports (*l)* was 410 mm, and the sandwich panel width (*b*) was 112 mm. The face layer thickness was 5 mm, and the total panel thickness was 38 mm (Tab. **4.6.2-2**). The loading rate was set to 6 mm/min to reach failure within 90 s.

Shear stress τ (Eq. (4.6.2-1) was determined with a three-point bending test, with *P* being the load (N), *d* the sandwich thickness (mm), *c* the core thickness (mm), and *b* the sandwich width (mm).

$$\tau = \frac{P}{(d+c)\cdot b} \tag{4.6.2-1}$$

Flexural facing strength (σ) was determined according to Eq. (4.6.2-2), with *t* being the face thickness (mm), *L* the span length (mm), *d* the sandwich thickness (mm), *c* the core thickness (mm), and *b* the sandwich width (mm).

$$\sigma = \frac{PL}{2t\cdot(d+c)\cdot b} \tag{4.6.2-2}$$

4.6.2.4 FLATWISE TENSION TEST

The bonding strength between faces and the core was determined with the flatwise tensile test following ASTM C297 (2009). The samples were prepared in such a way that a symmetric triangular shape of the core was covered (T1-T3, Fig. **4.6.2-3**). Samples 50 × 50 mm in size were glued with the hot-melt adhesive Siga® N-40 (Siga a.s., Zlín, Czech Republic) onto metal blocks and then tested on a ZWICK Z050/TH 3A (Zwick Roell AG, Ulm, Germany). The loading rate was 1 mm/min, to achieve failure within 60 to 90 s. Three samples per sandwich panel were tested.

Tab. 4.6.2-2: Description of specimens used for testing

SAMPLE	DENSITY kg/m^3	AREAL DENSITY kg/m^2	SPECIMEN DIMENSION mm	FACE THICKNESS mm
FLATWISE COMPRESSION TEST				
FC1	392	14.5	112 ×112 × 37	5
EDGEWISE COMPRESSION TEST				
FW1	385	14.3	112 × 112 × 37	5
FW2	376	14	112 × 112 × 37	5
BENDING TEST				
B1	390	14.5	410 × 112 × 37	5
B2	380	14.1	410 × 112 × 37	5
FLATWISE TENSION TEST				
T1	376	14.5	50 × 50 × 37	5
T2	381	14.1	50 × 50 × 37	5
T3	371	14.1	50 × 50 × 37	5

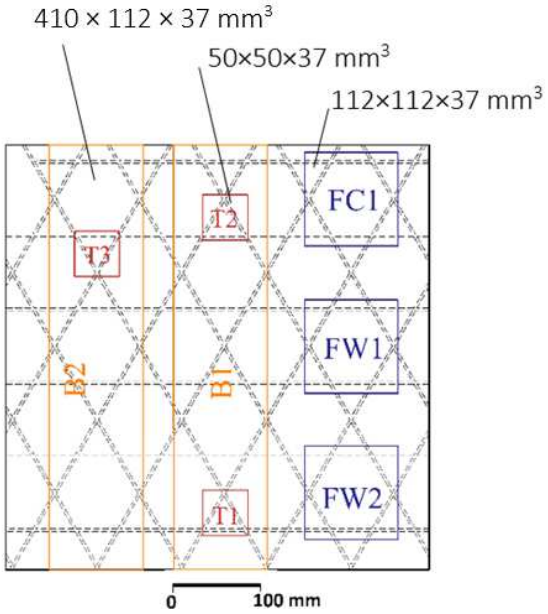

Fig. 4.6.2-3: Samples location on the sandwich panel (FC – sample for flatwise compression test, FW1-FW2 – samples for edgewise compression test, T1-T3 – samples for flatwise tension test, B1-B2 – samples for bending test)

4.6.2.5 DIGITAL IMAGE CORRELATION ANALYSIS

While running the test on the ZWICK Z050/TH 3A (Zwick Roell AG, Ulm, Germany), a stereoscopic camera system was simultaneously installed to acquire images for 3D digital image correlation (3D-DIC) analysis. The goal was to characterize the material's deformation behavior. The stereoscopic system consisted of two CCD video cameras (AVT Stingray Copper F-504B, Allied Vision Technologies, Osnabrück, Germany, cell size of 3.45 μm) with a resolution of 2452 × 2056 px^2. The lenses (Pentax C2514-M, Pentax Precision Co., Ltd., Tokyo, Japan) had a focal length of 25 mm, and all captured images were grey-scale with 256 intensity levels. Observed sample side was covered with stochastic and high-contrast speckle pattern. Firstly the white color was applied onto the surface and after curing the random black spray speckle pattern was manually sprayed. The two-component stochastic and contrast pattern is proposed to enhance image correlation. The surfaces were illuminated by two diffuse lights SobrietyCube 360 (Sobriety s.r.o., Kuřim, Czech Republic) with LED sensors (Luminus Phlatlight CSM-360, 90W, Luminus Devices Inc., Billerica-MA, USA). The images were used to calculate displacement and strain fields using a DIC algorithm implemented in software VIC-3D (Correlated Solutions Inc., Columbia-SC, USA). Poisson's ratios (PR) were calculated from the mean values from the whole area of interest (AOI) according to Eq. (4.6.2-3),

$$\nu_{xy} = \frac{\varepsilon_x}{\varepsilon_y} \tag{4.6.2-3}$$

where v_{xy} is PR, ε_x is strain in the x direction, and ε_y is strain in the y direction. Each compressive test of the panel's main plane resulted in stress-strain diagrams. These diagrams were used to identify elastic regions of deformation that were further used in the DIC calculation. The stereoscopic system was focused on cross-sectional planes of the samples to obtain strain data for the calculation of Poisson's ratios (PR). PRs were examined in the elastic region of the deformation (within 50 to 60 s of testing) and at three main planes. In the case of strain field inconsistency (v_{yx}; v_{xy}) resulting from the strip structure, an alternative approach using a virtual extensometer was chosen as an evaluation tool of VIC-3D (Correlated Solutions Inc., Columbia-SC, USA) software. This provided change of dimension data between two points located on the surface layers of the board (see Fig. **4.6.2-4**).

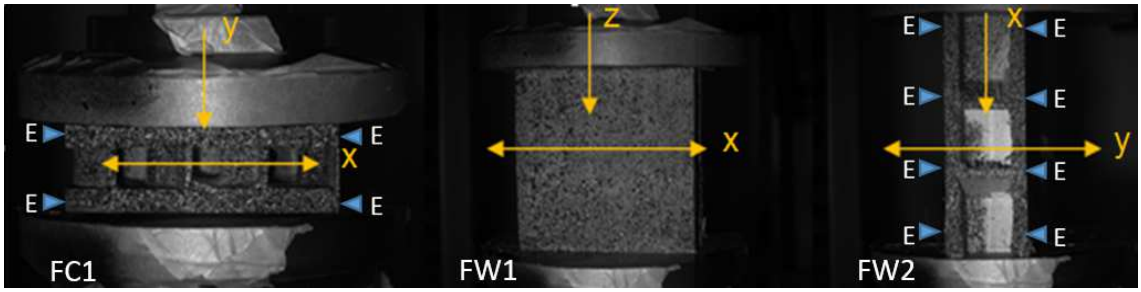

Fig. 4.6.2-4: The examined planes for obtaining Poisson's ratio using DIC with applied pattern: *left* – v_{yx}, *middle* – v_{zx}, *right* – v_{xy}), Es are the positions of virtual extensometers used for obtaining v_{xy} and v_{yx}

4.6.3 RESULTS AND DISCUSSION

4.6.3.1 MECHANICAL BEHAVIOR OF COMPRESSION

In the edgewise compression tests (Fig. **4.6.3-1**), the MOE was derived from the elastic region of the stress-strain curve, and equaled 201 MPa for the FW1 and 220 MPa for the FW2. The compression strength in an edgewise direction was 14.5 MPa. In addition, the obtained data were similar to those reported for spaceboard panel, which also has a hollowed core (Hunt and Gunderson 1988).

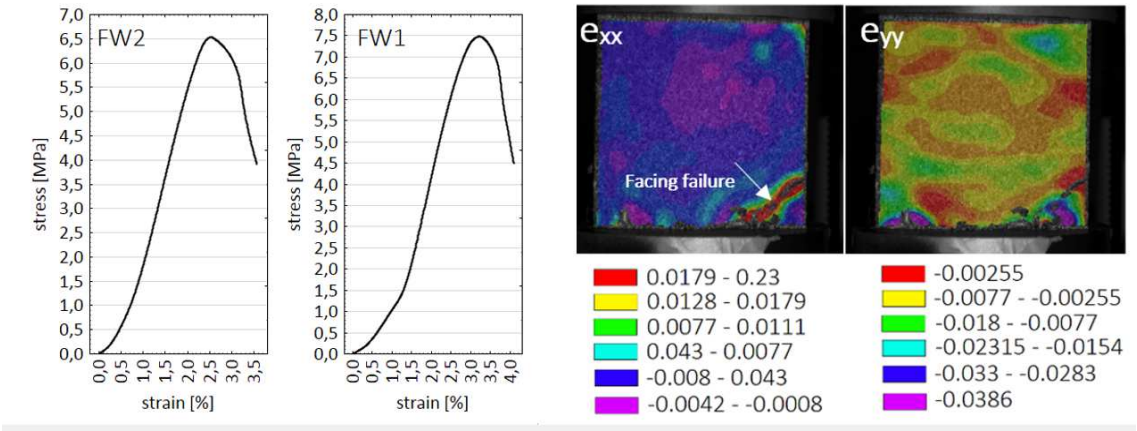

Fig. 4.6.3-1: Compression stress vs. strain diagrams for the novel wood-based sandwich composite and strain situation on the facing in time of failure

In the flatwise direction, a MOE of 112 MPa (FC1, Fig. **4.6.3-2**) was determined, which was lower than the MOE found in the edgewise direction. The same sample had a flatwise compressive strength of 2.64 MPa. Flatwise strength was 3 MPa lower than in work presented by Li et al. (2014). This could be caused by the different geometry of the applied iso-grid pattern, or different materials being utilized. Although core-grid shapes have been used by others (e.g., Fan et al. 2007; Tao et al. 2011), a direct comparison was not possible because different failure mechanisms are in place. Additionally, other materials (e.g., metal, carbon fiber reinforcement) were used. The compressive properties of the new sandwich panel are comparable to honeycomb materials (Bhattacharyya et al. 2011), including polyimide honeycomb structures, as some with lower density reached a comparable flatwise compressive strength of 3 MPa (Hexcel 1999).

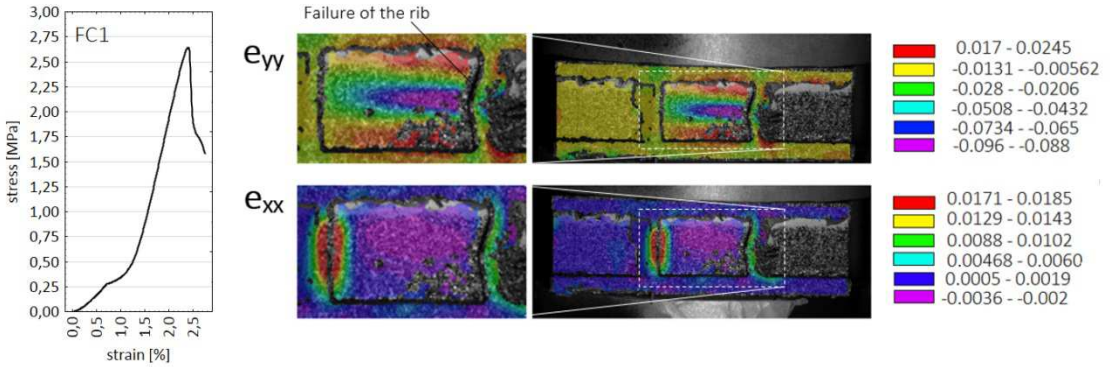

Fig. 4.6.3-2: Compression stress vs. strain for the novel wood-based sandwich composite and strain situation on the cross section of the sample in time of failure

The grid bonding in the impressed grooves is seen as a novel feature of the new sandwich structure. Using digital image correlation, a deformation evaluation was completed (Fig. **4.6.3-3**). As is visible, the regions where the ribs were present showed lower deformation than the rest of the panel. Especially, vertical deformations (e_{yy}) were significantly lower in area of the ribs. The e_{yy} of area with ribs was mostly -0.0005 (-), while in the center of the sample e_{yy} ranged from -0.0018 to -0.0210 (-).

Tab. 4.6.3-1: Flatwise and edgewise compression test

SAMPLE	COMPRESSIVE STRENGTH MPa	PANEL *E* MPa	FAILURE LOAD kN	SPECIFIC MODULUS MPa·m²/kg
FLATWISE COMPRESSION TEST				
FC1	2.64	34.71	33.14	2.40
EDGEWISE COMPRESSION TEST				
FW1	7.48	220.37	31.00	15.41
FW2	6.54	201.46	27.1	14.39

FC1 – flatwise compressive strength sample, N=1; FW1, FW2 – edgewise compressive strength samples, N=2

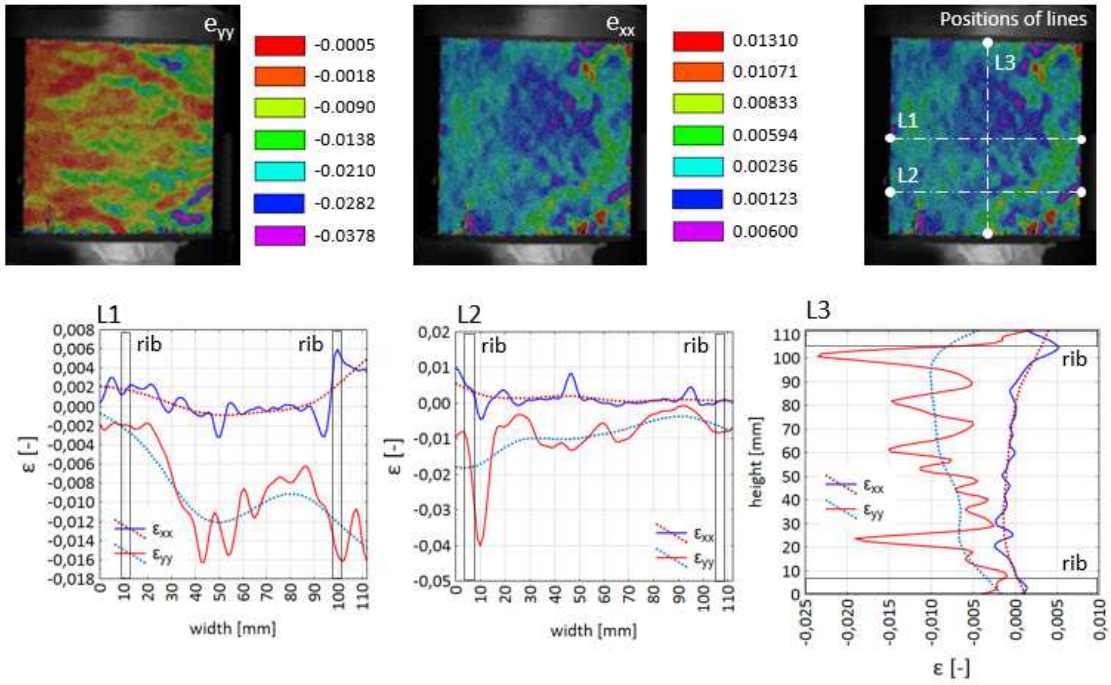

Fig. 4.6.3-3: Deformations (ε) [-] of the facing in *x* and *y* direction in selected regions evaluated by DIC. FW2 sample was evaluated in loading of 7 MPa. L1; L2 and L3 are inspection lines along which deformations were listed in graphs

4.6.3.2 FLEXURAL PROPERTIES

Samples B1 and B2 cut from the sandwich panel were tested to determine the loads at failure, which were 2.14 kN and 1.66 kN, respectively (Tab. **4.6.3-2**, Fig. **4.6.3-5**). The core shear strength values of B1 and B2 were 0.27 MPa and 0.21 MPa, respectively. Flexural facing strength was measured at 11.19 and 8.66 MPa. Samples failed at the outer side of the lower facing. The flexural facing strength was lower than the data reported by Li et al. (2014). Furthermore deformation evaluation (Fig. **4.6.3-4**) by DIC showed that facings are distributing the most of the e_{xx} deformations during the bending. As is common, the top facing was distributing positive strain ($+e_{xx}$), reaching a maximal value of 0.0123 (-), while the bottom facing was distributing negative strain ($-e_{xx}$), which was -0.014 (-). The stress-strain curve is shown in Fig. **4.6.3-5**. For future research, consideration of the application of various surface materials to enhance bending properties is recommended, e.g., veneer overlays (Kawasaki et al. 1999; Král et al. 2013; Král et al. 2014) or fiber glass reinforcement (Li et al. 2014).

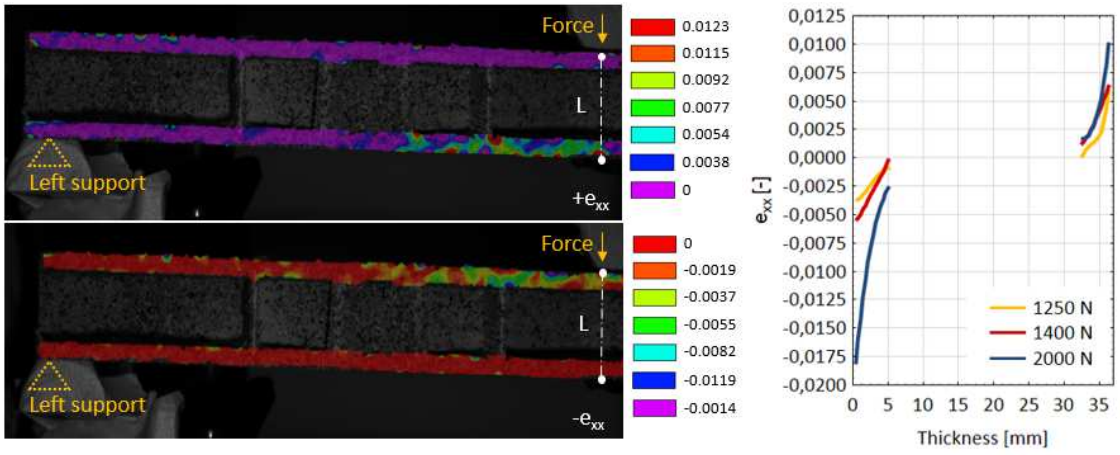

Fig. 4.6.3-4: Positive ($+e_{xx}$) and negative ($-e_{xx}$) strain distribution in the facings measured by DIC; figures on left side are captured when 2000 N force is applied, L – line where strain distribution was listed in graph

Tab. 4.6.3-2: Flexural properties of the sandwich panel

SAMPLE	FAILURE LOAD kN	CORE SHEAR STRENGTH MPa	FLEXURE FACING STRENGTH MPa	SAMPLES DIMENSION mm
B1	2.14	0.27	11.19	410 × 112 × 37
B2	1.66	0.21	8.66	410 × 112 × 37

B1, B2 – three-point bending samples used for determination of the bending properties, N=2

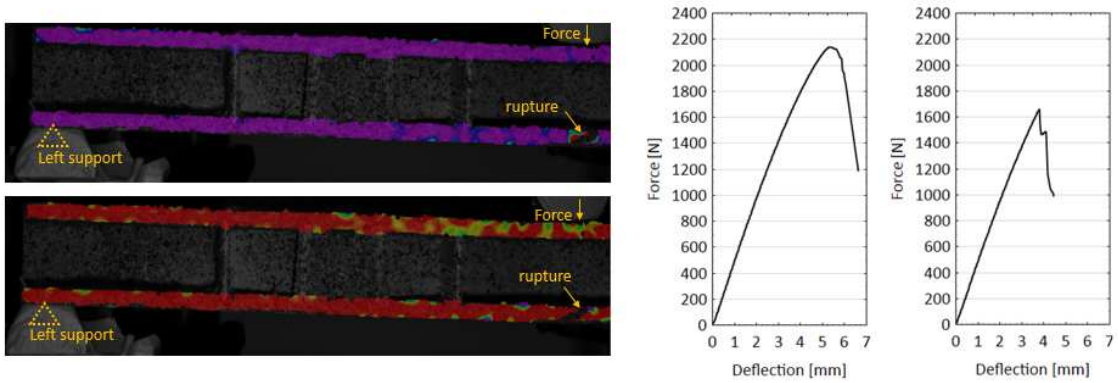

Fig. 4.6.3-5: The loading-deformation curve with respect to applied force and deflection of the sample

4.6.3.3 FLATWISE TENSILE PROPERTIES

The flatwise tensile test delivered an average tensile strength of 0.5 MPa (Tab. **4.6.3-2**). The tested samples revealed that the weakest point of the sandwich construction is the particleboard facing, as particles tended to debond from the remaining layer (Fig. **4.6.3-6**). Interestingly, the flatwise tensile strength of the sandwich panel was similar to the flatwise tensile strength of common particleboards, with strength values ranging from 0.4 to 0.8 MPa (Wimmer and Weigl 2007; Riegler et al. 2013).

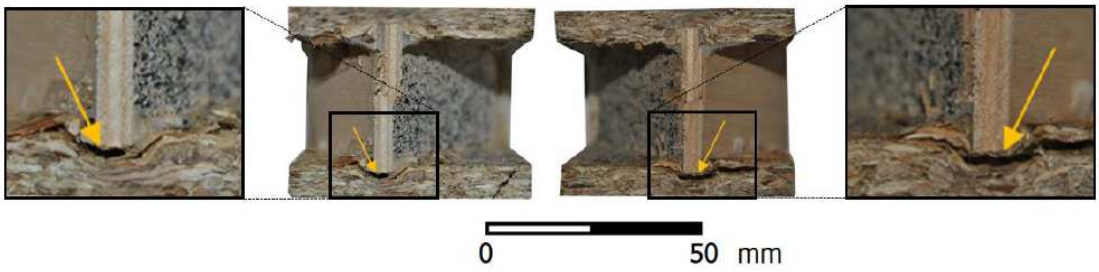

Fig. 4.6.3-6: Failure of the grooved bonding after flatwise tension testing (failure marked with yellow arrows)

Tab. 4.6.3-3: Tensile strength properties of the sandwich panel

SAMPLE	TENSILE STRENGTH MPa	FAILURE LOAD kN
T1	0.42	1.050
T2	0.56	1.400
T3	0.54	1.350

T1-T3 – tensile strength samples

4.6.3.4 DIC EVALUATION AND POISSON'S RATIO DETERMINATION

The linear section of the stress-strain curve was evaluated every second during loading. Four Poisson's ratios were computed every second during testing. Poisson's ratios were statistically evaluated (Tab. 4.6.3-4), and they were determined to be 0.172 in the v_{zx} direction, 0.037 in the v_{xy} direction, and 0.036 in the v_{yx} direction. The Poisson's ratios are displayed as a box-whisker plot in Fig. **4.6.3-7**. The determination of the Poisson's ratios is important especially for finite element modeling. Poisson's ratios are critical in finite element modeling (Mackerle 2005; Labans and Kaliniš 2011; Sebera et al. 2013).

Tab. 4.6.3-4: Poisson's ratios of the sandwich panel

	MEAN	MIN	MAX	SD
v_{zx}	0.172	0.087	0.250	0.035
v_{xy}	0.037	0.001	0.163	0.033
v_{yx}	0.036	0.002	0.075	0.013

v – Poisson's ratio, zx, xy, yx – evaluated strain directions

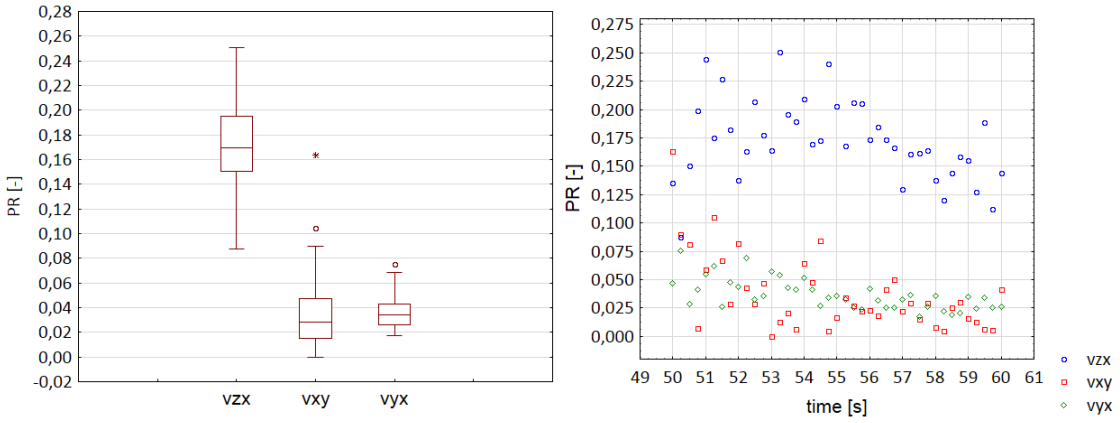

Fig. 4.6.3-7: The variability of the Poisson's ratios in the 50 to 60 sec of the load-deformation curve

4.6.4 CONCLUSION

A novel sandwich panel was successfully assembled that included an iso-grid interlocking core, which was characterized by a flatwise compressive strength of 2.64 MPa, an edgewise compressive strength of 6.4 MPa, a sandwich facing strength of 10 MPa, and a core shear strength of 0.21 MPa. In addition, the panel was lightweight,

having a density of 392 kg/m^3, which compared well with other published findings. The new panel can be defined as lightweight because the density remains below 400 kg/m^3

During mechanical testing, the panel failed in the iso-grid core during flatwise compression, and in the facings when the edgewise compression test was done. It is assumed that the novel grooved bonding into the facings may provide better bonding, as displacement was lower in the area of the groove.

DIC was successfully used to evaluate the Poisson's ratios for all directions. The v_{zx} was 0.172, the v_{xy} was 0.037, and v_{yx} was 0.036.

The sandwich panel is versatile, in that the empty core spaces could be filled with insulation materials such as fibers or foams, which would provide additional insulation capacity. Surfaces could also be equipped with additional overlays, which would deliver better bending performance.

Regarding application, the grooved surface may be produced using common industrial press with a one-side shaped platen. Furthermore in future, the implementation of the insulation material in a core cells such as foams or fibers could be investigated

Acknowledgments: This research was supported the Internal Grant Agency (IGA) of the Faculty of Forestry and Wood Technology, Mendel University in Brno, Project: LDF_VP_2015007.

4.6.5 REFERENCES

ASTM C365-11 (2011). "Standard test method for flatwise compressive properties of sandwich cores," ASTM International, West Conshohocken, PA.

ASTM C393-06 (2006). "Standard test method for core shear properties of sandwich constructions by beam flexure," ASTM International, West Conshohocken, PA.

ASTM C364-07 (2012). "Standard test method for edgewise compressive strength of sandwich constructions," ASTM International, West Conshohocken, PA.

ASTM C297 (2009). "Standard test method for flatwise tensile strength of sandwich constructions," ASTM International, West Conshohocken, PA.

Bekisli, B., and Grenestedt, J. L. (2004). "Experimental evaluation of a balsa sandwich core with improved shear properties," *Composites Science and Technology* 64(5), 667-674. DOI:10.1016/S0266-3538(03)00294-X

Bhattacharyya, D., Kavermann, S., Penneru, P., and Rao, S. (2011). "Veneer-based lightweight sandwich panel for high-end interior applications: Manufacturing, evaluation and cost analysis," *Joint International Symposium on Wood*

Composites and Veneer Processing and Products, Washington State University, Pullman, WA, pp. 1-11.

Davies, J. M. (ed.) (2001). *Lighweight Sandwich Constructions*, Blackwell Science Ltd, Osford, United Kingdoms.

Du, Y., Yan, N., and Kortschot, T. M. (2012). "Light-weight honeycomb core sandwich panels containing biofiber-reinforced thermoset polymer composite skins: Fabrication and evaluation," *Composites Part B: Engineering* 43(7), 2875-2882. DOI:10.1016/j.compositesb.2012.04.052

Fan, H. L., Meng, F. H., and Yang, W. (2007). "Sandwich panels with kagome lattice cores reinforced by carbon fibers," *Composite Structures* 81(4), 533-539. DOI: 10.1016/j.compstruct.2006.09.011

Hexcel Composites (1999). "A comprehensive guide to standard Hexcel honeycomb materials, configurations, and mechanical properties," Industriestrasse 1, A-4061 Pasching, Austria. Available at: http://www.hexcel.com/Resources/DataSheets/Brochure-Data-Sheets/Honeycomb_Attributes_and_Properties.pdf

Hunt, J. F., and Gunderson, D. E. (1988). "DPL spaceboard development," *TAPPI Proceeding of the 1988 Corrugated Containers Conference*, Orlando, FL, TAPPI Press, pp. 11-17.

Hunt, J. F., Harper, D. P., and Friedrich, K. A. (2004). "Three-dimensional engineered fiberboard : Opportunities for the use of low valued timber and recycled material," *38th International Wood Composites Symposium*, Washington State University, Pullman, WA, pp. 207-2016.

Hussain, F., Nairn, J., and Muszyński, L. (2011). "An experimental method for measurement of strain distribution between wood the flour particles and polymer matrix on micro-mechanical level," *Materials Science and Engineering A* 528(18), 6072–6078. DOI: 10.1016/j.msea.2011.04.056

Kanou, H., Nabavi, S. M., and Jam, J. E. (2013). "Numerical modeling of stresses and buckling loads of isogrid lattice composite structure cylinders," *International Journal of Engineering, Science and Technology* 5(1), 42-54. DOI: 10.4314/ijest.v5i1.4

Kawasaki, T., Min, Z., and Shuichi, K. (1999). "Sandwich panel of veneer-overlaid low-density fiberboard," *Journal of Wood Science* 45(4), 291-298.

Kepler, J. A. (2011). "Simple stiffness tailoring of balsa sandwich core material," *Composites Science and Technology* 71(1), 46-51. DOI: 10.1016/j.compscitech.2010.10.002

Král, P., Hrázský, J., Hrapková, L., and Hamšík, P. (2013). "Shape stability of particleboards covered with decorative veneers," *Drvna Industrija* 64(3), 201-220. DOI: 10.5552/drind.2013.1234

Král, P., Klímek, P., Mishra, P. K., Rademacher, P., and Wimmer, R. (2014). "Preparation and characterization of cork layered composite plywood boards," *BioResources* 9(2), 1977-1985. DOI: 10.15376/biores.9.2.1977-1985

Labans, E., and Kaspars, K. (2011). "Numerical *versus* experimental investigation of plywood sandwich panels with corrugated core," *3rd International Conference*

Civil Engineering´11 Proceedings II Materials and Structures, L. Malinovska and Z. Daiga (eds.), Latvia University of Agriculture, Jelgava.

Li, J., Hunt, J. F., Giong, S., and Cai, Z. (2014). "High strength wood-based sandwich panels reinforced with fiberglass and foam," *BioResources* 1(2), 1898-1913. DOI: 10.15376/biores.1.2.1898-1913

Mackerle, J. (2005). "Finite element analyses in wood research: A bibliography," *Wood Science and Technology* 39(7), 579-600. DOI: 10.1007/s00226-005-0026-9

Riegler, M., Spangl, B., Weigl, M., Wimmer, R., and Müller, U. (2013). "Simulation of a real-time process adaptation in the manufacture of high-density fibreboards using multivariate regression analysis and feedforward control," *Wood Science and Technology* 47(6), 1243-1259. DOI: 10.1007/s00226-013-0571-6

Sebera, V., Muszyński, L., Tippner, J., Noyel, M., Pisaneschi, T., and Sundberg, B. (2013). "FE analysis of CLT panel subjected to torsion and verified by DIC," *Materials and Structures* 48(1-2), 451-459. DOI: 10.1617/s11527-013-0195-1

Sebera, V., Tippner, J., Šimek, M., Šrajer, J., Děcký, D., and Klímová, H. (2014). "Poisson's ratio of the MDF in respect to vertical density profile," *European Journal of Wood and Wood Products* 72(3), 407-410. DOI: 10.1007/s00107-014-0780-1

Shalbafan, A. (2013). *Investigation of Foam Materials to be Used in Lightweight Wood-Based Composites*, Ph.D. dissertation, University of Hamburg, Hamburg, Germany.

Sutton, M. A., Orteu, J. J., and Schreier, H. W. (2009). *Digital Image Correlation for Shape and Deformation Measurements: Basic Concepts, Theory and Applications*, Springer Verlag, Heidelberg.

Tao, H. F., Fang, Z. D., and Yang, W. (2011). "Mechanics of advanced fiber reinforced lattice composites," *Acta Mechanica Sinica* 26(6), 825-835. DOI: 10.1007/s10409-010-0390-z

Thoemen, H., Luedtke, J., and Barbu, M. (2007). "Light weight panels: Summary of a new development in Europe," *All Division 5 World Conference*, Oct. 29-Nov. 2, Taipei, Taiwan.

Vasiliev, V. V., Barynin, V., and Rasin, F. (2001). "Anisogrid lattice structures - Survey of development and application," *Composite Structures* 54(2-3), 361-370. DOI: 10.1016/S0263-8223(01)00111-8

Wilczyński, A., and Kociszewski, M. (2010). "Elastic properties of the layers of three-layer particleboards," *European Journal of Wood and Wood Products* 70(1-3), 357-359. DOI: 10.1007/s00107-010-0497-8

Wimmer, R., and Weigl, M. (2007). "A multi-parameter approach to characterize wood quality for particle boards," *All Division 5 World Conference*, Oct. 29-Nov. 2, Taipei, Taiwan.

Zhang, Y. H., Qiu, X. M., and Fang, D. N. (2008). "Mechanical properties of two novel planar lattice structures," *International Journal of Solids and Structures* 45(13), 3751-3768. DOI: 10.1016/j.ijsolstr.2007.10.005

Zink, A. G., Davidson, R. W., and Hanna, R. B. (1995). “Strain measurement in wood using a digital image correlation technique,” *Wood and Fiber Science* 27(4), 346-359.

5. CONCLUSIONS AND REMARKS

The purpose of this work is to exploit the potential of the full-field measurement of the wood response on the mechanical loading in order to obtain more precise and (or) more advanced results. Therefore, the standard mechanical tests of wood and wood-based composites were supplemented by the full-field optical technique applying the principles of the digital image correlation. The supplementation or substitution of the conventional displacement sensors allowed to obtain more precise and (or) more advanced results. The main results are summarized in the subsequent paragraphs. The measurements were carried out on the most wide-spread wood species in the central Europe such as European beech (*Fagus sylvatica*, L.) and Norway spruce (*Picea abies*, L. Karst). Beside the solid wood, the new wood-based sandwich structure was investigated too.

1) The full-field analysis of the deformations during the compression parallel to the grain revealed the reason for the non-standard deformation behaviour detected by the conventional extensometers within spruce and beech wood. It can be characterized by the negative increment of strain in the loading direction. The reason for this consists in the abrupt compression of the damage zones located near the compression plates, which induced the expansion of the middle zone located between them. This phenomenon may resulted in the 3-6 times higher Young's moduli obtained based on the strains measured in the middle (expanded) zone compared to one obtained based on the strains of the damage zones for both wood species, and therefore, should be of concern when measuring wood in such mode.

2) The full-field analysis of the deformations during the three-point bending allowed localizing the neutral axis in the sample. In order to determine the neutral axis position relative to the centroidal sample axis, the additional image processing resulting in the finding of the sample edges was carried out. It was found that the neutral axis and centroidal sample axis are almost coincident. This statement applies for native as well as for thermally modified beech wood. However, the position of the neutral axis locally slightly changed (moved to tension side of the bended sample) as load increases, which has a lot of do with the local compression of wood under the loading head. Therefore, the three-point bending is not efficient for the assessment of the neutral axis position.

3) The full-field analysis of the deformations on both adjacent longitudinal-radial (*LR*) and longitudinal-tangential (*LT*) planes of wood during the twisting the sample provided first input data to determine both longitudinal shear moduli at single torsion test. The other input data were the shear stress distributions on the captured material planes in the radial and tangential directions calculated by torsion stress functions. The coupling of these two input data sets through the Hooke's law is able to provide the true longitudinal shear moduli of beech wood. Both longitudinal shear moduli increasingly mutually differed as the load increases but in average the shear modulus determined in the *LR* plane was higher of about 30 % than one obtained in *LT* plane. However, a large amount of the full-field data is an obstacle to practical use of this procedure.

4) The full-field analysis of the deformations induced around the notches within the dog-bone shaped sample during the uniaxial tension provided the shear strains data of beech and spruce wood for the verification of the elastic material model used in the finite-element analyses. Great correlation was found between the numerically predicted and experimentally measured strain data sets for both *LR* and *LT* shear planes. The verified elastic material characteristics are suitable for the assessment of mechanical response of more complex problems, i.e. timber structure with respect to connection of wooden elements using finite-element method. However, a direct utilization of the shear strains for a calculation of elastic shear characteristics is not suitable because of complex strain field.

5) The full-field analysis of the deformations captured on the face layers and partially on the core cross-section of a new sandwich composite structure delivered the parameters, such as the Poisson's ratios, for the characterization of the elastic behaviour of this new material. Moreover, the full-field displacements and strains provided the additional insight into the deformation behaviour of the new composite structure by means of the assessment of the core-face bonding. The full-field deformation data were also helpful in the detection of the strain concentrations within the composite structure, and thus prediction where the failure occur.

The results shows that a full-field deformation analysis based on the digital image correlation has proved to be a useful tool for the advanced and effective characterization of the deformation behaviour, which open a new ways to the experimental mechanics of wood and wood-based composites.

6. SOUHRN

Stanovení mechanických vlastností materiálu je založeno na kvantifikaci mechanického zatížení ("akce") a odpovídajících deformací ("reakce"). Existuje několik způsobů, jak experimentálně kvantifikovat deformace zkušebních těles; počínaje od základních, které jsou založeny na pozici příčníku vypovídající o průměrné deformaci celého objemu zkušebního tělesa, včetně nežádoucích vůlí zkušebního čelistí; přes externí snímače posunutí jako jsou extenzometry, které bodově měří posunutí na povrchu zkušebního tělesa; až po optické bezkontaktní metody jako je korelace digitálního obrazu, které je schopna plně zachytit přirozenou heterogenitu dřeva.

Cílem předkládané práce je maximálně využít potenciál plno-polního měření odezvy dřeva na mechanické namáhání. Proto byly standardní mechanické zkoušky dřeva a kompozitů na bázi dřeva doplněny o optické bezkontaktní měření deformací, které je založeno na principu korelace digitálního obrazu. Doplnění, příp. nahrazení konvenčních snímačů posunutí optickou metodou umožnilo získat přesnější a (nebo) sofistikovanější výsledky. Hlavní výsledky jsou shrnuty v následujících odstavcích.

Měření byla prováděna na nejpoužívanějších druzích středoevropských dřev, a to na dřevě buku lesního (*Fagus sylvatica*, L.) a smrku ztepilého (*Picea abies*, L. Karst). Kromě masivního dřeva, byly mechanické zkoušky prováděny také na nově vyvinutém kompozitním materiálu na bázi dřeva se sendvičovou strukturou. Tento materiál je tvořen jádrem z břízové překližky, které oboustranně oplášťováno tenkou dřevotřískovou deskou. Zkušební tělesa byla zatěžována pomocí klasických mechanických zkoušek jako je prostý tlak, prostý tah, tříbodý ohyb a krut.

1) Plno-polní analýza deformací v průběhu tlakového zatížení rovnoběžně s vlákny odhalila důvod nestandardního deformačního chování detekovaného pomocí klasických přítlačných extenzometrů u dřeva smrku a buku. Toto nestandardní chování lze charakterizovat jako negativní přírůstek deformací (rozpínání) ve směru zatížení. Příčina této abnormality byla spatřena v náhlém kolapsu (stlačení) kontaktních zón nacházejících se v blízkosti tlačných desek, který umožnil relaxaci napětí ve středové části zkušebního tělesa vlivem jeho rozepnutí. Tento jev může vést až k 3-6 krát vyššímu normálovému modulu pružnosti vypočtenému z deformací středové části ve srovnání s modulem, který byl vypočten na základě deformací v kontaktních zónách.

Podobný rozdíl byl zjištěn pro oba druhy dřev, a proto by měl být brán do úvahy v případech, kdy je dřevo namáháno v tomto módu.

2) Plno-polní analýza deformací v průběhu tříbodého ohybu umožnila definovat pozici neutrální osy ve zkušebním tělese. Za účelem vyjádření pozice neutrální osy v relativních jednotkách (pro porovnání mezi jednotlivými zkušebními tělesy) je potřeba pozici vztáhnout k horní a spodní hraně, příp. ke geometrické ose zkušebního tělesa. Pozice geometrické osy zkušebního tělesa byla získána pomocí několika kroků využívajících se při zpracování digitálního obrazu. Bylo prokázáno, že poloha neutrální osy se téměř neliší od polohy geometrické osy zkušebního tělesa, tento poznatek platí pro přírodní i tepelně upravené dřevo buku. Nicméně, pozice neutrální osy se v průběhu zatížení lokálně mění, s přirůstajícím zatížením se posunuje mírně k tahové straně ohýbaného zkušebního tělesa. Tento lokální posun neutrální osy má co dočinění s lokálním otlačením zkušebního tělesa pod zatěžovací hlavou. Z toho důvodu se použití tříbodé ohybové zkoušky pro stanovení pozice neutrální osy jeví jako nevhodné.

3) Plno-polní analýza deformací na obou přilehlých podélných rovinách dřeva (podélně-radiální – *LR* a podélně-tangenciální – *LT*) v průběhu kroucení zkušebního tělesa poskytla první vstupní data pro stanovení obou podélných smykových modulů pružnosti dřeva buku v rámci jedné krutové zkoušky. Druhými vstupními daty byly distribuce smykových napětí na snímaných plochách zkušebního tělesa v radiálním a tangenciálním směru vypočtené pomocí funkcí krutového napětí ("torsion stress functions"). Propojení těchto dvou vstupních dat přes Hookův zákon umožní stanovit skutečné podélné smykové moduly. Rozdíl mezi oběma smykovými moduly se postupně zvyšuje s přirůstajícím zatížením. V průměru je smykový modul stanovený v *LR* rovině o 30 % vyšší než smykový modul stanovený v *LT* rovině. Nicméně, velký rozsah plno-polních dat se může ukázat jako překážka v praktickém používání této procedury stanovení smykových modulů.

4) Plno-polní analýza deformací vyvolaných kolem hrotů zářezů, kterými bylo opatřeno zkušební těleso ve tvaru psí kosti, v průběhu jednoosého tahu, poskytla smykové poměrné deformace buku a smrku, které byly následně použity pro verifikaci (ověření) elastického materiálového modelu používaného v konečně-prvkových analýzách. Mezi numericky predikovanými a experimentálně naměřenými smykovými deformacemi byla nalezena velmi dobrá shoda pro obě podélné smykové roviny

(*LR* + *LT*). Ověřené materiálové charakteristiky jsou vhodné pro posouzení mechanické odezvy složitějších struktur, tj. dřevěných konstrukcí s ohledem na spojení jednotlivých dřevěných prvků, pomocí konečně-prvkové metody. Nicméně, přímé použití smykových poměrných deformací pro stanovení elastických smykových charakteristik není vhodné z důvodu komplexního deformačního pole vyskytujícího se kolem hrotů zářezů, které zahrnuje i normálové deformace.

5) Plno-polní analýza deformací snímaných na krycích deskách a částečně také na jádře nově vyvinutého kompozitního materiálu na bázi dřeva se sendvičovou strukturou poskytla parametry, jako jsou Poissonovy čísla, pro charakteristiku elastického chování tohoto nového materiálu. Navíc, plno-polní data posunutí a poměrných deformací poskytla hlubší náhled na deformační chování nové kompozitní struktury prostřednictvím posouzení spojení mezi jádrem a krycími deskami. Plno-polní data deformací byla také užitečná pro detekci míst, kde dochází k lokální koncentraci deformací, což je obvykle spojeno se vznikem trhliny a porušením zkušebního tělesa.

Výsledky této práce napovídají tomu, že plno-polní analýza deformací založená na principu korelace digitálního obrazu se ukázala jako užitečný nástroj pro sofistikovanou a efektivní charakteristiku deformačního chování, který otevírá nové cesty pro experimentální mechaniku dřeva a kompozitních materiálů na bázi dřeva.

7. LIST OF REFERENCES

Aicher, S., Dill-Langer, G., Höfflin, L. (2001) Effect of polar anisotropy of wood loaded perpendicular to grain. Journal of materials in civil engineering 13(1): 2-9.

Adler, R., Korpel, A., Desmares, P. (1968) An Instrument for Making Surface Waves Visible. IEEE Transactions on Sonics and Ultrasonics 15(3): 157-160.

Antonelli, G.A., Maris, H.J., Malhotra, S.G., Harper, J.M.E. (2002) Picosecond ultrasonics study of the vibrational modes of a nanostructure. J Appl Phys 91(5): 3261-3267.

ASTM C297 (2009) Standard test method for flatwise tensile strength of sandwich constructions. American Society for Testing and Materials, Philadelphia, PA, USA.

ASTM C364 (2012) Standard test method for edgewise compressive strength of sandwich constructions. American Society for Testing and Materials, Philadelphia, PA, USA.

ASTM C365 (2011) Standard test method for flatwise compressive properties of sandwich cores. American Society for Testing and Materials, Philadelphia, PA, USA.

ASTM C393 (2006) Standard test method for core shear properties of sandwich constructions by beam flexure. American Society for Testing and Materials, Philadelphia, PA, USA.

ASTM D143 (1994) Standard test methods for small clear specimens of timber. American Society for Testing and Materials, Philadelphia, PA, USA.

ASTM D198 (2014) Standard Test Methods of Static Tests of Lumber in Structural Sizes. American Society for Testing and Materials, PA, USA.

ASTM D2395 (2014) Standard Test Methods for Density and Specific Gravity (Relative Density) of Wood and Wood-Based Materials. American Society for Testing and Materials, Philadelphia, PA, USA.

Bachtiar, E.V., Sanabria, S.J., Mittig, J.P., Niemz, P. (2016) Moisture-dependent elastic characteristics of walnut and cherry wood by means of mechanical and ultrasonic test incorporating three different ultrasound data evaluation techniques. Wood Sci Technol (in press): DOI: 10.1007/s00226-016-0851-z.

Bay, B.K. (1995) Texture correlation: A method for the measurement of detailed strain distributions within trabecular bone. J Orthop Res 13(2): 258-267.

Bay, B.K., Smith, T.S., Fyhrie, D.P., Saad, M. (1999) Digital volume correlation: Three-dimensional strain mapping using X-ray tomography. Exp Mech 39(3): 217-226.

Belgen, M.H. (1967) Structural stress measurements with an infrared radiometer. ISA T 6: 49–53.

Besnard, G., Hild, F., Roux, S. (2006) “Finite-Element” Displacement Fields Analysis from Digital Images: Application to Portevin–Le Châtelier Bands. Exp Mech 46(6): 789-803.

Berthelot, J.M., (1998) Composite materials: Mechanical behaviour and structural analysis, Springer Science & Business Media, New York.

Betts, S.C., Miller, T.H., Gupta, R. (2010) Location of the neutral axis in wood beams: A preliminary study. Wood Material Science and Engineering 5(3-4): 173-180.

Bigorgne, L., Brunet, M., Maigre, H., Simon, P., Chaudet, P. (2011) Softwood fracture characterisation at the mesoscopic scale. Procedia Engineering 10: 2707-2712.

Biot, M.A. (1954) On anisotropic viscoelasticity. J Appl Phys 25: 1385–1391.

Biot, M.A. (1955) Plasticity and consolidation in a porous anisotropic solid. J Appl Phys 26: 182–185.

Biot, M.A. (1956) Thermoelasticity and irreversible thermodynamics. J Appl Phys 27: 240–253.

Bodig, J., Jayne, B.A. (1993) Mechanics of wood and wood composites. Krieger Publishing Company, Malabar.

Boresi, A.P., Schmidt, R.J. (2003) Advanced mechanics of materials. Wiley, New York.

Brdička, M., Samek, L., Sopko, B. (2000) Mechanika kontinua. Academia, Praha, Czech Republic.

Brewster, D. (1816) On the communication of the structure of doubly refracting crystals to glass, muriate of soda, flour spar and other substances by mechanical compression and dilatation. Philosophical Transactions of the Royal Society 106: 156–178.

Brooks, R.E., Heflinger, L.O., Wuerker, R.F. (1965) Interferometry with a holographically reconstructed comparison beam. Appl Phys Lett 7(9): 248-249.

Bruck, H.A., McNeill, S.R., Sutton, M.A., Peters, W.H. (1989) Digital image correlation using Newton-Raphson method of partial differential correction. Exp Mech 29(3): 261-267.

BS 373 (1957) Methods of testing small clear specimens of timber. British Standard Institution, London, UK.

Burger, C.P. (1980) Nonlinear photomechanics. Exp Mech 20(11): 381-389.

Chen, D.J., Chiang, F.P., Tan, Y.S., Don, H.S. (1993) Digital speckle-displacement measurement using a complex spectrum method. Appl Optics 32(11): 1839-1849.

Clauß, S., Pescatore, C., Niemz, P. (2014) Anisotropic elastic properties of common ash (*Fraxinus excelsior* L.). Holzforschung 68(8): 941-949.

Cloud, G. (2008) Basics of Optics. Springer handbook of experimental solid mechanics. W.N. Sharpe Jr. Berlin: Springer, pp 447-480.

Compton, K.T., Webster, D.B. (1915) Temperature changes accompanying the adiabatic compression of steel: verification of W. Thomson's theory to a very high accuracy. Physical Review 5: 159–166.

Dahl, K.B. (2009) Mechanical properties of clear wood from Norway spruce. Norwegian University of Science and Technology, Trondheim, Norway.

Daniel, I.M., Ishai, O. (2006) Engineering mechanics of composite materials, Oxford University Press, New York.

Davis, C.Q., Dennis, M.F. (1998) Statistics of subpixel registration algorithms based on spatiotemporal gradients or block matching. Opt Eng 37(4): 1290-1298.

Davis, P.M., Gupta, R., Sinha, A. (2012) Revisiting the neutral axis in wood beams. Holzforschung 66(4): 497–503.

Denisyuk, Y.N. (1962) Photographic reconstruction of the optical properties of an object in its own scattered radiation field. Soviet Physics Doklady 7: 543.

Derome, D., Rafsanjani, A., Hering, S., Dressler, M., Patera, A., Lanvermann, C., Sedighi-Gilani, M., Wittel, F.K., Niemz, P., Carmeliet, J. (2013) The role of water in the behavior of wood. J Build Phys 36(4): 398-421.

Dewhurst, R.J., Shan, Q. (1999) Optical remote measurement of ultrasound. Meas Sci Technol 10(11): 139-168.

Every, A., Sachse, W. (1990) Determination of the elastic constants of anisotropic solids from acoustic-wave group-velocity measurements. Phys Rev B 42(13): 8196-8205.

Gabor, D. (1948) A New Microscopic Principle. Nature 161(4098): 777-778.

Garab, J., Keunecke, D., Hering, S., Szalai, J., Niemz, P. (2010) Measurement of standard and off-axis elastic moduli and Poisson's ratios of spruce and yew wood in the transverse plane. Wood Sci Technol 44(3): 451-464.

Gaudette, G.R., Todaro, J., Krukenkamp, I.B., Chiang, F. (2001) Computer Aided Speckle Interferometry: A Technique for Measuring Deformation of the Surface of the Heart. Ann Biomed Eng 29(9): 775-780.

Gerhards, C.C. (1982) Effect of moisture and temperature on the mechanical properties of wood. An analysis of immediate effects. Wood Fiber Sci 14(1):4-36.

Giachetti, A. (2000) Matching techniques to compute image motion. Image Vision Comput 18(3): 247-260.

Gonzalez, R.C., Woods, R.E., Eddins, S.L. (2004) Digital Image processing using MATLAB. Prentice Hall, New Jersey.

Greene, R.J., Patterson, E.A., Rowlands, R.E. (2008) Thermoelastic Stress Analysis. Springer handbook of experimental solid mechanics. W.N. Sharpe Jr. Berlín: Springer, pp 743-768.

Güntekin, E., Aydin, T.Y., Niemz, P. (2016) Some orthotropic elastic properties of fagus orientalis as influenced by moisture content. Wood Res-Slovakia 61(1): 95-104.

Gusev, V., Karbutov, A. (1993) Laser optoacoustics. American Institute of Physics, New York.

Gustafsson, P.J. (2003) Fracture Perpendicular to Grain - Structural Applications. Ch.7 in Timber Engineering ed. by Thelandersson, S., Larsen, H., Wiley, Chichester West Sussex, UK.

Haldar, S., Bruck, H.A. (2013) Mechanics of fiber-reinforced porous polymer composites. In: Conference Proceedings of the Society for Experimental Mechanics Series. Costa Mesa, CA, pp 99-105.

Haldar, S., Gheewala, N., Grande-Allen, K.J., Sutton, M.A., Bruck, H.A. (2011) Multi-scale Mechanical Characterization of Palmetto Wood using Digital Image

Correlation to Develop a Template for Biologically-Inspired Polymer Composites. Exp Mech 51(4): 575-589.

Han, B. (1993) Interferometric methods with enhanced sensitivity by optical/digital fringe multiplication. Appl Optics 32(25): 4713-4718.

Han, B., Post, D. (2008) Geometric Moiré. Springer handbook of experimental solid mechanics. W.N. Sharpe Jr. Berlín: Springer, pp 601-626.

Han, C. (2005) Contrast of shadow moiré at high-order Talbot distances. Opt Eng 44(2): 1-6.

Han, C., Han, B. (2006) Error analysis of the phase-shifting technique when applied to shadow moiré. Appl Optics 45(6): 1124-1133.

Harwood, N., Cummings, W.M. (1986) Applications of thermoelastic stress analysis. Strain 22(1): 7-12.

Helm, J.D. (1996) Improved three-dimensional image correlation for surface displacement measurement. Opt Eng 35(7): 1911-1920.

Helm, J.D., Deaner, J.R. (2004) Off-axis two-dimensional digital image correlation. In: *Proccedings of 2004 SEM X International Congress & Exposition on Experimental and Applied Mechanics, Costa Mesa*, pp 6-7.

Hering, S., Keunecke, D., Niemz, P. (2012) Moisture-dependent orthotropic elasticity of beech wood. Wood Sci Technol 46(5): 927-938.

Hild, F., Roux, S. (2006) Digital Image Correlation: from Displacement Measurement to Identification of Elastic Properties - a Review. Strain 42(2): 69-80.

Hopperstad, O.S. (2003) Lecture notes Nonlinear Finite Element methods. Basic Principles TKT 8207. Seminar 4: Linear Elasticity. Trondheim, Dept. of Structural Engineering, NTNU.

Huntley, J.M. (1998) Automated fringe pattern analysis in experimental mechanics: a review. J Strain Anal Eng 33(2): 105-125.

Hurley, D.C., Tewary, V.K., Richards, A.J. (2001) Surface acoustic wave methods to determine the anisotropic elastic properties of thin films. Meas Sci Technol 12(9): 1486-1494.

Hutchins, D.A. (1988) Ultrasonic Generation by Pulsed Lasers. Physical Acoustics V18: Principles and Methods. W.P. Mason, R.N. Thurston. Elsevier Science, Oxford, UK.

Hwang, S., Horn, J., Wang, H. (2008) Strain measurement of SU-8 photoresist by a digital image correlation method with a hybrid genetic algorithm. Opt Laser Eng 46(3): 281-289.

Jeong, G.Y., Park, M.J. (2016) Evaluate orthotropic properties of wood using digital image correlation. Constr Build Mater 113: 864-869.

Jin, G., Meng, L., Chen, J., Ma, S., Zhang, J. (2006) The Progress and Application of Digital Speckle Correlation Method. Journal of Experimental Mechanics 21(6): 689–702.

Ju, S.H., Rowlands, R.E. (2007) Thermoelastic determination of crack-tip coordinates in composites. Int J Solids Struct 44(14-15): 4845-4859.

Kang, H.Y., Muszyński, L., Milota, M.R. (2011) Optical Measurement of Deformations in Drying Lumber. Dry Technol 29(2): 127-134.

Kang, H.Y., Muszyński, L., Milota, M.R., Kang, C.W., Matsumura, J. (2011) Preliminary tests for optically measuring drying strains and check formation in wood. Journal of the Faculty of Agriculture 56(2): 313-316.

Kang, H.Y., Rang, S.G., Kang, C.W., Matsumura, J. (2013) Measurement of Strain Distributions in White Oak Boards during Drying Using a Digital Image Correlation Method. Journal of the Faculty of Agriculture 58(1): 55-59.

Kaw, A.K. (1997) Mechanics of composite materials. Taylor and Francis, New York.

Keunecke, D., Hering, S., Niemz, P. (2008) Three-dimensional elastic behaviour of common yew and Norway spruce. Wood Sci Technol 42(8): 633-647.

Keunecke, D., Niemz, P., Zürich, E.T.H., Tollert, M., Hansel, A. (2012) Mechanical properties and failure behaviour of yew and spruce determited with a compact tension testand digital image correlation. Wood Res-Slovakia 57(4): 669-676.

Keunecke, D., Novosseletz, K., Lanvermann, C., Mannes, D., Niemz, P. (2012) Combination of X-ray and digital image correlation for the analysis of moisture-induced strain in wood: opportunities and challenges. Eur J Wood Wood Prod 70(4): 407-413.

Knauss, W.G., Chasiotis, I., Huang, Y. (2003) Mechanical measurements at the micron and nanometer scales. Mech Mater 35(3-6): 217-231.

Knorz, M., Niemz, P., van de Kuilen, J.W. (2016) Measurement of moisture-related strain in bonded ash depending on adhesive type and glueline thickness. Holzforschung 70(2): 145-155.

Kojiro, K., Furuta, Y., Ishimaru, Y. (2008) Effects of Heating from 100°C to 200°C on Dynamic Viscoelastic Properties of Dry Wood. Journal of the Society of Materials Science 57(4): 350-355.

Kollmann, F., Côté, W.A. (1968) Principles of wood science and technology: I Solid wood. Springer-Verlag, Berlin.

Krishnaswamy, S. (2008) Photoacoustic Characterization of Materials. Springer Handbook of Experimental Solid Mechanics. W.N. Sharpe Jr. Berlín: Springer, pp 769-800.

Kwon, O., Hanna, R. (2010) The Enhanced Digital Image Correlation Technique for Feature Tracking During Drying of Wood. Strain 46(6): 566-580.

Lanvermann, C., Sanabria, S.J., Mannes, D., Niemz, P. (2014b) Combination of neutron imaging (NI) and digital image correlation (DIC) to determine intra-ring moisture variation in Norway spruce. Holzforschung 68(1): 113-122.

Lanvermann, C., Wittel, F.K., Niemz, P. (2014a) Full-field moisture induced deformation in Norway spruce: intra-ring variation of transverse swelling. Eur J Wood Wood Prod 72(1): 43-52.

Larsen, F., Ormarsson, S., Olesen, J.F. (2010) Experimental investigation of moisture driven fracture in solid wood. In: 11th World Conference on Timber Engineering. Trentino; Italy, pp 3525-3532.

Laš, V. (2004) Mechanika kompozitních materiálů. Západočeská univerzita v Plzni, Plzeň, Czech Republic.

Lecompte, D., Smits, A., Bossuyt, S., Sol, H., Vantomme, J., Van Hemelrijck, D., Abraken, A.M. (2006) Quality assessment of speckle patterns for digital image correlation. Opt Laser Eng 44(11): 1132-1145 .

Lin, S.T., Rowlands, R.E. (1995) Thermoelastic stress analysis of orthotropic composites. Exp Mech 35(3): 257-265.

Lippmann, M.G. (1891) La photographie des couleurs. In: Comptes Rendus Hebdomadaires des Séances de l'Academie des sciences. 274 p.

Lu, H., Cary, P.D. (2000) Deformation measurements by digital image correlation: Implementation of a second-order displacement gradient. Exp Mech 40(4): 393-400.

Luo, P. F., Chao, Y.J., Sutton, M.A., Peters, W.H. (1993) Accurate measurement of three-dimensional deformations in deformable and rigid bodies using computer vision. Exp Mech 33(2): 123-132.

Mackenzie, A.K. (1989) Effects of surface coating on infrared measurements of thermoelastic response. In: Stress and Vibration: Recent Developments in Measurement and Analysis. International Society for Optics and Photonics 1084: 59–71.

Majano-Majano, A., Fernandez-Cabo, J.L., Hoheisel, S., Klein, M. (2012) A Test Method for Characterizing Clear Wood Using a Single Specimen. Exp Mech 52(8): 1079-1096.

Maldague, X. (2001) Theory and practice of infrared technology for nondestructive testing. Wiley, New York.

Mandát, D. (2012) Optické bezkontaktní topografické metody. Univerzita Palackého v Olomouci, Olomouc.

Maznev, A.A., Akthakul, A., Nelson, K.A. (1999) Surface acoustic modes in thin films on anisotropic substrates. J Appl Phys 86(5): 2818-2824.

McNeill, S.R., Paquette, M. (1988) Initial Studies of Stereo Vision for Use in 3-D Deformation Measurements. Univ. South Carolina, USA.

Méité, M., Dubois, F., Pop, O. Absi, J. (2013) Mixed mode fracture properties characterization for wood by Digital Images Correlation and Finite Element Method coupling. Eng Fract Mech 105: 86-100.

Meng, L., Jin, G., Yao, X. (2006) Errors caused by misalignment of the optical camera axis and the object surface in the DSCM. Qinghua Daxue Xuebao/Journal of Tsinghua University 46: 1930-1932.

Minster, J., Drdácký, M., Jirovský, I., Kloiber, M., Micka, M., Slížková, Z., Václavík, P. (2006) Diagnostic techniques to assess mechanical characteristics of historical timber. In: Proceedings of the International Conference on Heritage, Weathering and Conservation, HWC 2006. Madrid; Spain, pp 667-673.

Miyauchi, K., Murata, K. (2007) Strain-softening behavior of wood under tension perpendicular to the grain. J Wood Sci 53(6): 463-469.

Mott, L., Shaler, S.M., Groom, L.H. (1996) A technique to measure strain distributions in single wood pulp fibers. Wood Fiber Sci 28(4): 429-437.

Mouchalin, J.P. (1986) Optical detection of ultrasound. IEEE Transactions on Ultrasonics Ferroelectrics and Frequency Control 33(5): 485-499.

Murata, K., Ito, M., Masuda, M. (2001). An analysis of the swelling behavior of various woods using an optical microscope and a digital image correlation method (DIC). Journal of Society of Materials Science Japan, 50:397-402.

Murata, K., Masuda, M. (2003) Analysis of strain distribution of softwood in transverse compression measured by digital image correlation method. Zairyo/Journal of the Society of Materials Science, Japan, 52(4): 347-352.

Murata, K., Masuda, M. (2006) Microscopic observation of transverse swelling of latewood tracheid: effect of macroscopic/mesoscopic structure. J Wood Sci 52(4): 283-289.

Murata, K., Masuda, M., Ichimaru, M. (1999) Analysis of radial compression behavior of wood using digital image correlation method. Mokuzai Gakkaishi/Journal of the Japan Wood Research Society 45(5): 375-381.

Murata, K., Nagai, H., Nakano, T. (2011) Estimation of width of fracture process zone in spruce wood by radial tensile test. Mech Mater 43(7): 389-396.

Murata, K., Nakao, S. (2007) Transverse compression behavior of softwood and alternately laminated lumber of rubberwood veneer and falcata veneer. Zairyo/Journal of the Society of Materials Science, Japan 56(4): 316-320.

Murata, K., Tanahashi, H. (2010) Measurement of young's modulus and poisson's ratio of wood specimens in compression test. Zairyo/Journal of the Society of Materials Science, Japan, 59(4): 285-290.

Muszyński, L., Lagaňa, R., Shaler, S.M. (2006) Hygro-mechanical behavior of red spruce in tension parallel to the grain. Wood Fiber Sci 38(1): 155-165.

Nagai, H., Murata, K., Nakamura, M. (2007) Defect Detection of Lumber Including Knots Using Bending Deflection Curve. Journal of the Society of Materials Science, Japan 56(4): 326-331.

Nagai, H., Murata, K., Nakano, T. (2009) Defect detection in lumber including knots using bending deflection curve: comparison between experimental analysis and finite element modeling. J Wood Sci 55(3): 169-174.

Nagai, H., Murata, K., Nakano, T. (2011) Strain analysis of lumber containing a knot during tensile failure. J Wood Sci 57(2): 114-118.

Niemz, P., Brunner, A.J., Walter, O. (2009) Investigation of the mechanism of failure behaviour of wood-based materials using acoustic emission analysis and image processing. Wood Res-Slovakia 54(2): 49-62.

Oscarsson, J., Olsson, A., Enquist, B. (2012) Strain fields around knots in Norway spruce specimens exposed to tensile forces. Wood Sci Technol 46(4): 593-610.

Ozarska, B., Burvill, C., Juniper, L. (2013) Strain measurement of softened Eucalyptus regnans wood during bending operation using a low-cost single camera optical method. International Wood Products Journal 4(1): 4-14.

Ozyhar, T., Hering, S., Niemz, P. (2012) Moisture-dependent elastic and strength anisotropy of European beech wood in tension. J Mater Sci 47(16): 6141-6150.

Ozyhar, T., Hering, S., Niemz, P. (2013) Viscoelastic characterization of wood: Time dependence of the orthotropic compliance in tension and compression. J Rheol 57 (2): 699-717.

Ozyhar, T., Mohl, L., Hering, S., Hass, P., Zeindler, L., Ackermann, R., Niemz, P. (2016) Orthotropic hygric and mechanical material properties of oak wood. Wood Material Science & Engineering 11(1): 36-45.

Pan, B., Qian, K., Xie, H., Asundi, A. (2009) Two-dimensional digital image correlation for in-plane displacement and strain measurement: a review. Meas Sci Technol 20(6): 1-17.

Pan, B., Xie, H., Wang, Z., Qian, K, Wang, Z. (2008) Study on subset size selection in digital image correlation for speckle patterns. Opt Express 16(10): 7037-7048.

Peng, M., Ho, Y-C., Wang, W-C., Chui, Y.H., Gong, M. (2012) Measurement of wood shrinkage in jack pine using three dimensional digital image correlation (DIC). Holzforschung 66(5): 639–643.

Peng, M., Kershaw, J.A., Chui, Y.H., Gong, M. (2013) Modelling of tangential, radial, and longitudinal shrinkage after drying in jack pine and white spruce. Can J Forest Res 43(8): 742-749.

Perelygin, L.M. (1965) Náuka o dreve. Alfa, Bratislava, Slovak Republic.

Pereira, J., Xavier, J., Morais, J., Lousada, J. (2014) Assessing wood quality by spatial variation of elastic properties within the stem: Case study of Pinus pinaster in the transverse plane. Can J Forest Res, 44(2): 107-117.

Peters, W.H., Ranson, W.F. (1982). Digital Imaging Techniques In Experimental Stress Analysis. Opt Eng 21(3): 427-431.

Pih, H., Knight, C.E. (1969) Photoelastic Analysis of Anisotropic Fiber Reinforced Composites. J Compos Mater 3(1): 94-107.

Post, D., Han, B. (2008) Moiré Interferometry. Springer handbook of experimental solid mechanics. W.N. Sharpe Jr. Berlín: Springer, pp 627-654.

Post, D., Han, B. Ifju, P. (1994) High Sensitivity Moiré: Experimental Analysis for Mechanics and Materials. Springer, New York.

Post, D., Han, B., Ifju, P. (2000) Moiré methods for engineering and science – moiré interferometry and shadow moiré. Photomechanics. P.K. Rastogi. Springer, New York.

Požgaj, A., Chovanec, D., Kurjatko, S., Babiak, M. (1997) Štruktúra a vlastnosti dreva. Príroda, a. s., Bratislava.

Pratt, W.K. (2007) Digital image processing PIKS Scientific inside. Wiley-Interscience, New York.

Press, W.H. (2003) C++ numerical algorithms. Publishing House of Electronics Industry, Beijing.

Pryputniewicz, E.J., Miller, S.L., Deboer, M.P., Brown, G.C., Biederman, R.R., Pryputniewicz, R.J. (2000) Experimental and analytical characterization of

dynamic effects in electrostatic microengines. In: Proc. Internat. Symp. on Microscale Systems. Orlando, FL, pp 80-83.

Pryputniewicz, R.J. (1992) Holographic Numerical Analysis. Worcester Polytechnic Institute, Worcester, UK.

Pryputniewicz, R.J. (1995) Hologram interferometry from silver halide to silicon and-- beyond. SPIE Proceedings 2545: 405-417.

Pryputniewicz, R.J. (2008) Holography. *Springer handbook of experimental solid mechanics*. W.N. Sharpe Jr. Berlín: Springer, pp 675-700.

Pryputniewicz, R.J., Stetson, K.A. (1990) Measurement of vibration patterns using electro-optic holography. In: 33rd Annual Techincal Symposium. International Society for Optics and Photonics. pp 456-467.

Quinn, S., Dulieu-Barton, J.M., Langlands, J.M. (2004) Progress in Thermoelastic Residual Stress Measurement. Strain 40(3): 127-133.

Ramesh, K. (2008) Photoelasticity. Springer handbook of experimental solid mechanics. W.N. Sharpe Jr. Berlín: Springer, pp 701-742.

Ramesh, K., Kasimayan, T., Neethi Simon, B. (2011) Digital photoelasticity - A comprehensive review. The Journal of Strain Analysis for Engineering Design 46(4) 245-266.

Rastogi, P.K. (2000) Photomechanics. Topics in Applied Physics. Springer-Verlag, Berlin.

Reu, P.L., Sutton, M., Wang, Y., Miller, T.J. (2009) Uncertainty quantification for digital image correlation. In: Society for Experimental Mechanics - SEM Annual Conference and Exposition on Experimental and Applied Mechanics. Albuquerque, NM, pp 368-374.

Riley, W., Sturges, L., Morris, D. (2007) Mechanics of materials. John Wiley & Sons, New York.

Ritschel, F., Zhou, Y., Brunner, A. J., Fillbrandt, T., Niemz, P. (2014) Acoustic emission analysis of industrial plywood materials exposed to destructive tensile load. Wood Sci Technol 48(3): 611-631.

Rossmanith, H.P., SHUKLA, A. (1981) Dynamic photoelastic investigation of interaction of stress waves with running cracks. Exp Mech 21(11): 415-422.

Rowlands, R.E. (2008) Stress analysis by synergizing experimental, analytical and numerical techniques. In: International Conference on Experimental Mechanics. Nanjing, China.

Samarasinghe, S., Kulasiri, D. (2004) Stress intensity factor of wood from crack-tip displacement fields obtained from digital image processing. Silva Fenn 38(3): 267-278.

Schreier, H.W., Braasch, J.R., Sutton, M.A. (2000) Systematic errors in digital image correlation caused by intensity interpolation. Opt Eng 39(11): 2915-2921.

Schreier, H.W., Garcia, D., Sutton, M.A. (2004) Advances in light microscope stereo vision. Exp Mech 44(3): 278-288.

Schreier, H.W., Sutton, M.A. (2002) Systematic errors in digital image correlation due to undermatched subset shape functions. Exp Mech 42(3): 303-310.

Schumann, W., Zürcher, J., Cuche, D. (1985) *Holography and deformation analysis*. Springer-Verlag, New York.

Schwarzkopf, M., Muszyński, L. (2015) Stereomicroscopic optical method for the assessment of load transfer patterns across the wood-adhesive bond interphase. Holzforschung 69(5): 653-660.

Scruby, C., Drain, L. (1990). *Laser ultrasonics: techniques and applications*. A. Hilger, Philadelphia, USA.

Sebera, V., Muszyński, L. (2011). Determination of local material properties of OSB sample by coupling advanced imaging techniques and morphology-based FEM simulation. Holzforschung 65(6): 811–818.

Serrano, E., a Enquist, B. (2005) Contact-free measurement and non-linear finite element analyses of strain distribution along wood adhesive bonds. Holzforschung 59(6): 641-646.

Sfarra, S., Theodorakeas, P.N., Avdelidis, P., Koui, M. (2013) Thermographic, ultrasonic and optical methods: A new dimension in veneered wood diagnostics. Russ J Nondestruct+ 49(4): 234-250.

Shipsha, A., Berglund, L. (2007). Shear coupling effects on stress and strain distributions in wood subjected to transverse compression. Compos Sci Technol 67(7-8): 1362-1369.

Silva, F.G.A., Morais, J.J.L., Dourado, N., Xavier, J., Pereira, F.A.M., de Moura, M.F. S.F. (2014) Determination of cohesive laws in wood bonded joints under mode II loading using the ENF test. Int J Adhes Adhes, 51: 54-61.

Sjödahl, M. (1994) Electronic speckle photography: increased accuracy by nonintegral pixel shifting. Appl Optics 33(28): 6667-6673.

Sjödahl, M. (1997) Accuracy in electronic speckle photography. Appl Optics 36(13): 2875-2885.

Sjödahl, M., Benckert, L.R. (1993) Electronic speckle photography: analysis of an algorithm giving the displacement with subpixel accuracy. Appl Optics 32(13): 2278-2284.

Sjödahl, M., Benckert, L.R. (1994) Systematic and random errors in electronic speckle photography. Appl Optics 33(31): 7461-7471.

Stetson, K.A., Powell, R.L. (1965) Interferometric Hologram Evaluation and Real-Time Vibration Analysis of Diffuse Objects. Journal of the Optical Society of America 55(12): 1694-1695.

Sutton, M.A. (2008) Digital Image Correlation for Shape and Deformation Measurements. Springer handbook of experimental solid mechanics. W.N. Sharpe Jr. Berlín: Springer, pp 565-600.

Sutton, M.A., Mcneill, S.R., Helm, J.D., Chao, Y.J. (2000). Advances in Two-Dimensional and Three-Dimensional Computer Vision. Photomechanics Berlin, Heidelberg: Springer Berlin Heidelberg, 77: 323-372.

Takasaki, H.M. (1970) Topography. Appl Optics 9(6): 1467-1472.

Testorf, M., Jahns, J., Khilo, N.A., Goncharenko, A.M. (1996). Talbot effect for oblique angle of light propagation. Opt Commun 129(3-4): 167-172.

Thomson, W. (1853) On dynamical theory of heat. Trans. R. Soc. Edinburgh. 20: 261-283.

Tong, W., Tao, H., Zhang, N., Hector, L.G. (2005) Time-resolved strain mapping measurements of individual Portevin–Le Chatelier deformation bands. Scripta Mater 53(1): 87-92.

Trebuna, F. (1990) Some problems of accelerating the measurements and evaluating the stress fields by the photostress method. Exp Techniques 14(2): 36-40.

Tukiainen, P., Hughes, M. (2016) The cellular level mode I fracture behaviour of spruce and birch in the RT crack propagation system. Holzforschung 70(2): 157-165.

Ugolev, B.N. (2007) Drevesinovedenie i lesnoe tovarovedenie. Izdovatestvo Moskovskogo Gostdarstvenogo universiteta lesa, Moskva.

Ukyo, S., Karube, M., Harada, M., Aoi, H. (2010) Damage Detection in Bolted Timber Connections Using Acoustic Emission Monitoring. In: 11th World Conference on Timber Engineering. Trentino; Italy, pp 498-505.

Ukyo, S., Karube, M., Harada, M., Hayashi, T. (2008) Strain Analysis of Traditional Japanese Timber Joints under Tensile Loading. In: 10th World Conference on Timber Engineering. Miyazaki; Japan, pp 1214-1221.

Ukyo, S., Masuda, M. (2006) A new method for measuring the true shear strength of wood. In: 9th World Conference on Timber Engineering. Portland, OR, pp 1657-1663.

Vable, M. (2002) Mechanics of materials. Oxford University Press, New York.

Vable, M. (2007) Intermmediate mechanics of materials. Oxford University Press, New York.

Vable, M. (2015) Advanced mechanics of materials. Expanding Educational Horizons, LLC, Houghton, Michigan, USA.

van Beerschoten, W.A., Carradine, D.M., Carr, A. (2014) Development of constitutive model for laminated veneer lumber using digital image correlation technique. Wood Sci Technol 48(4): 755-772.

Vasic, S., Ceccotti, A (2009). Influence of intermediate deformation rates in softwoods characterized with fracture resistance R-curves. Wood Sci Technol 43(7-8): 591-614.

Vendroux, G., Knauss, W.G. (1998) Submicron deformation field measurements: Part 2. Improved digital image correlation. Exp Mech 38(2): 86-92.

Vessby, J., Olsson, A., Enquist, B. (2008) Contact-free strain measurement of bi-axially loaded sheathing-to-framing connection. In: 10th World Conference on Timber Engineering. Miyazaki; Japan, pp 1447-1454.

Vest, C.M., Pryputniewicz, R.J. (2007) Applications of Holography. In: SPIE Milestone Series.

Wagenführ, R. (2007) Holzatlas. Fachbuchverlag Leipzig im Hanser-Verlag, München.

Wagner, J.W. (1990) Optical Detection of Ultrasound. Ultrasonic measurement methods. R.N. Thurston, A.D. Pierce. Boston: Academic Press, pp 201-266.

Walker, C.A. (1994) A historical review of moiré interferometry. Exp Mech 34(4): 281-299.

Wang, L., Lu, Z., Zhao, D. Wang, S. (2002) Crack initiation and propagation in LT specimens of betula platyphylla Suk. Beijing Linye Daxue Xuebao/Journal of Beijing Forestry University 24(2): 59-61.

Wang, Z.Y., Li, H.Q., Tong, J., W., Ruan, J.T. (2007) Statistical Analysis of the Effect of Intensity Pattern Noise on the Displacement Measurement Precision of Digital Image Correlation Using Self-correlated Images. Exp Mech 47(5): 701-707.

Watanabe, K., Lazarescu, C., Shida, S., Avramidis, S. (2012) A Novel Method of Measuring Moisture Content Distribution in Timber During Drying Using CT Scanning and Image Processing Techniques. Dry Technol 30(3): 256-262.

Weber, W. (1830) Über die spezifische Wärme fester Körper insbesondere der Metalle. *Ann. Phys. Chem.* 96: 177-213.

White, R.M. (1963) Generation of Elastic Waves by Transient Surface Heating. J Appl Phys 34(12): 3559-3567.

Wolfe, R.W., Rowlands, R.E., Lin, C.H. (1994) Full Field Stress/Strain Analysis: Use of Moiré and TSA for Wood Structural Assemblies. In: Experimental Mechanics Plenary Session at the Forest Products Research Society Annual Meeting. Portland, ME, pp 23-30.

Xavier, J., de Jesus, A.M.P., Morais, J.J.L., Pinto, J.M.T. (2012) Stereovision measurements on evaluating the modulus of elasticity of wood by compression tests parallel to the grain. Constr Build Mater 26(1): 207-215.

Xavier, J., Oliveira, M., Morais, J.J.L., de Moura, M.F.S.F. (2014a) Determining mode II cohesive law of Pinus pinaster by combining the end-notched flexure test with digital image correlation. Constr Build Mater 71: 109-115.

Xavier, J., Oliveira, M., Morais, J.J.L., de Moura, M.F.S.F. (2015) Determining mode I cohesive law of Pinus pinaster by coupling double cantilever beam test with digital image correlation. Frattura ed Integritá Strutturale 31: 13-22.

Yang, F., Xiaoyuan H.E., QUAN, C. (2006) Characterization of dynamic microgyroscopes by use of temporal digital image correlation. Appl Optics 45(30): 7785-7790.

Yaofeng, S., Pang, J.H.L. (2007) Study of optimal subset size in digital image correlation of speckle pattern images. Opt Laser Eng 45(9): 967-974.

Yoneyama, S., Morimoto, Y., Takashi, M. (2006) Automatic Evaluation of Mixed-mode Stress Intensity Factors Utilizing Digital Image Correlation. Strain 42(1): 21-29.

Zandman, F., Redner, S.S., Riegner, E.I. (1962) Reinforcing effect of birefringent coatings. Exp Mech 2(2): 55-64.

Zauner, M., Niemz, P. (2014) Uniaxial compression of rotationally symmetric Norway spruce samples: surface deformation and size effect. Wood Sci Technol 48(5): 1019-1032.

Zhang, D., Luo, M., Arola, D.D. (2006) Displacement/strain measurements using an optical microscope and digital image correlation. Opt Eng 45(3):1-9.

Zhang, D., Zhang, X., Cheng, G. (1999) Compression strain measurement by digital speckle correlation. Exp Mech 39(1): 62-65.

Zhang, J., Jin, G., Ma, S., Meng, L. (2003) Application of an improved subpixel registration algorithm on digital speckle correlation measurement. Opt Laser Technol 35(7): 533-542.

Zhou, P., Goodson, K.E. (2001) Subpixel displacement and deformation gradient measurement using digital image/speckle correlation (DISC). Opt Eng 40(8): 1613-1620.

Zink, A.G., Davidson, R.W., Hanna, R.B. (1995) Strain measurement in wood using a digital image correlation technique. Wood Fiber Sci 27(4): 346-359.